Universitat Politècnica de València
Departamento de Máquinas y Motores Térmicos

UNIVERSITAT
POLITÈCNICA
DE VALÈNCIA

Doctoral Thesis

Acoustic and Fluid-Dynamic Characterization of State-of-the-Art Exhaust After-treatment Systems

Presented by:

Mr. Álvaro Rafael Redondo Navarro

Supervised by:

Dr. Antonio José Torregrosa Huguet

In fulfillment of the requisites for the degree of
Doctor of Philosophy

València, May 2023

Ph.D. Thesis

Acoustic and Fluid-Dynamic Characterization of State-of-the-Art Exhaust After-treatment Systems

Presented by: Mr. Álvaro Rafael Redondo Navarro
Supervised by: Prof. Antonio José Torregrosa Huguet

Defense Committee:

Chairman: Dr. Alberto González Salvador
Secretary: Dr. María Dolores Redel Macías
Member: Dr. Angelo Onorati

Reviewing board:

Dr. Angelo Onorati
Dr. Augusto Della Torre
Dr. Antonio Jose Cubero Atienza

València, May 2023

Acoustic and Fluid-Dynamic Characterization of State-of-the-Art Exhaust After-treatment Systems

Álvaro R. Redondo N.

Abstract

Continuously tightening pollutant and noise emission regulations have been the key motivation for engine –and engine related technology– research, development and optimization. Such trend gave rise to the gradual introduction of after-treatment systems to reduce pollutant emissions in automotive applications. However, in the last two decades the level of restrictions have made the use of after-treatment systems intensive and mandatory, evolving from small individual devices to very complex systems often including more than one device.

Even though the main purpose of after-treatment systems is pollutant emissions abatement, they also exert a strong influence on wave dynamics, back-pressure and acoustic behaviour of the exhaust line, therefore changing the flow, acoustic and pressure characteristics of the exhaust flow. This in turn redefines the boundary conditions for the main silencing device (muffler) placed downstream. A better understanding of the sound attenuation and pressure drop due to the presence of after-treatment systems could have beneficial impacts, allowing the optimized design of the devices and the complete exhaust lines, especially the muffler. It was considered that a promising approach to reach a better understanding on the matter would be to account for the influence that usual components and characteristics of after-treatment systems have on their actual behaviour.

Experimental and modelling approaches were used to study and characterize the acoustic and fluid-dynamic behavior of a diverse set of state-of-the-art after-treatment systems and devices, covering a wide range of elements and characteristics representative of after-treatment applications of commercial use. Transmission loss and pressure drop were selected as the key parameters to account for the sound attenuation and back-pressure generated by each device. Well established measurement facilities and procedures were used for the experimental characterization. In parallel, 1D, 3D CFD and even coupled 1D-3D simulation approaches on the basis of the "virtual twinning" concept were implemented on commercial software, aiming to replicate the experimental results in order to provide additional information and help deepen the understanding of internal phenomena, three-dimensional flow and acoustic effects.

Prior to the thorough characterization of the devices, the validity and significance of acoustic cold (ambient) condition measurements, as those to be taken, to represent the devices in their actual operating condition, i.e. hot and pulsating-flow as in the hot-end of exhaust lines were after-treatment systems are usually placed, was verified. Once such validation was done, for each system or device pressure drop measurements were performed for a range of mass flow rates, usually between 0 to 800 kg/h. Similarly, transmission loss measurements were performed at no-flow condition and with three different superimposed mean mas flow rates, commonly 100, 200 and 300 kg/h. The information produced, with some post-processing, decomposition and comparative analysis, and the use of inductive reasoning were used to account and relate each element with their effects.

Additionally, some other topics were assessed, such as the compliance of the additivity property of pressure drop and the transmission loss when several after-treatment devices are arranged together as an after-treatment system, the actual importance of auxiliary devices often overlooked, the changes in the early service life of a device with a GPF monolith, the benefits of performing decomposition analysis to the transmission loss, the capabilities of 1D and 3D CFD to produce useful information and the eventual benefits of 1D-3D co-simulation.

Overall, a comprehensive database on the pressure drop and transmission loss of state-of-the-art after-treatment devices and systems was produced. The experimental methodologies used, with their corresponding post processing, proved to be adequate and to produce significant information, especially after the validation of ambient condition acoustic measurements regarding engine-like conditions. The computational modelling approaches were also found capable of producing significant results; the 1D models were found to be very indicative with proper tuning and to produce fairly useful information on both pressure drop and transmission loss while mimicking the geometry and working principles of the measurements. 3D modelling allowed to further analyze the internal and three-dimensional effects, and 1D-3D integration, while demanding in terms of preparation, produced significant improvements. By using the proposed methodologies and guidelines excellent pressure drop and good transmission loss results (up to the 500-700 Hz at least) can be produced with the models being fed only with geometrical data,

i.e. without the need of experimental measurements for tuning. Additionally, the decomposition analysis approaches presented proved to be a versatile and profitable tool, as valuable information was produced for the analysis of all the specific topics assessed.

Regarding those topics, the check of the additivity property confirmed that pressure drop is essentially additive, whereas in the case of transmission loss, the additivity varies with the frequency: at low to mid frequencies dominated by reactive effects it is not additive, whereas mid to high frequencies where the dissipative effects dominate have a considerable level of additivity. The study of an auxiliary device, with a static swirl mixer inducer as representative part, lead to determine that, while usually overlooked, auxiliary elements in fact contribute significantly to pressure drop and may have a significant influence on the acoustic attenuation of the after-treatment system. It also filled a knowledge gap as these are the first reference results published for the kind of mixer element characterized. Finally, both experimental and modelling approaches helped identify the influence of in-pore soot deposition during the first few uses of a GPF on reactive and dissipative effects.

Overall, it was found that taking special care in certain aspects, the models can be used to provide adequate inlet conditions for the design of the exhaust line. This thesis and the data produced contribute to fill the knowledge gap in the acoustics of after-treatment systems and related elements. It also provides several tools and approaches useful for the improvement and optimization of exhaust line design procedures, which eventually could also be transferred to other applications.

Resumen

Las normativas sobre emisiones contaminantes y sonoras, cada vez más estrictas, han sido la principal motivación para la investigación, el desarrollo y la optimización de los motores de combustión y demás tecnologías relacionadas. Esta tendencia ha dado lugar a la introducción paulatina de sistemas de postratamiento para reducir las emisiones contaminantes provenientes de la automoción. Sin embargo, en las dos últimas décadas el nivel de restricciones impuestas ha hecho que el uso de sistemas de postratamiento sea intensivo y obligatorio, pasando de ser pequeños dispositivos individuales a sistemas muy complejos que a menudo incluyen más de un dispositivo.

Aunque el objetivo principal de los sistemas de postratamiento es la reducción de las emisiones contaminantes, estos también ejercen una gran influencia en la dinámica de las ondas, la contrapresión y el comportamiento acústico de la línea de escape, por lo que modifican las características del flujo, la acústica y la presión del flujo de escape. Lo que a su vez redefine las condiciones de diseño para el silenciador (mofle) situado aguas abajo. Una mejor comprensión de la atenuación acústica y la caída de presión debidas a la presencia de sistemas de postratamiento podría tener repercusiones beneficiosas, ya que permitiría optimizar el diseño de los mismos dispositivos y de las líneas de escape completas, especialmente del silenciador. Se consideró que un enfoque prometedor para obtener una mejor comprensión del tema sería tener en cuenta la influencia que los componentes individuales y las características más frecuentes de los sistemas de postratamiento tienen en su desempeño final.

Se emplearon diferentes enfoques experimentales y de modelado computacional para estudiar y caracterizar el comportamiento acústico y fluidodinámico de un conjunto diverso de sistemas y dispositivos de postratamiento, abarcando así una amplia gama de elementos y características representativos de las aplicaciones de postratamiento más avanzadas de uso comercial. La pérdida por transmisión y la caída de presión fueron seleccionadas como parámetros clave de estudio para cuantificar la atenuación acústica y la contrapresión generada por cada dispositivo. Para la caracterización experimental se utilizaron instalaciones y procedimientos de medición bien establecidos. Por su parte,

para el modelado computacional se emplearon distintos enfoques de simulación, tales como el unidimensional, el CFD (tridimensional) e incluso la co-simulación 1D-3D, siguiendo en la medida lo posible el concepto o principio "gemelos digitales" (virtual twinning), en programas comerciales con el objetivo de replicar los resultados experimentales, a fin de obtener información complementaria y ayudar a profundizar en la comprensión de los fenómenos internos, los efectos tridimensionales del flujo y los efectos acústicos.

Previo a la caracterización minuciosa de los dispositivos, se verificó la validez y significancia de las medidas acústicas en condiciones frías (ambiente), como las que se iban a tomar, para representar los dispositivos respecto a sus condiciones reales de funcionamiento, es decir, expuestos a flujo caliente y pulsante como en el extremo caliente de las líneas de escape donde habitualmente se sitúan los sistemas de postratamiento. Una vez realizada esta validación. Comenzó se dio paso a la caracterización experimental, para cada sistema o dispositivo se registraron mediciones de caída de presión para un rango de caudales másicos, normalmente entre 0 y 800 kg/h. Del mismo modo, se efectuaron mediciones de pérdida de transmisión en condiciones de ausencia de flujo y con tres caudales másicos diferentes superpuestos, por lo general 100, 200 y 300 kg/h. La información producida, tras cierto post-procesamiento, análisis por descomposición y comparativo, sumado al uso del razonamiento inductivo fueron empleados para cuantificar y relacionar cada elemento con sus efectos.

Adicionalmente otros temas fueron evaluados, como el cumplimiento de la propiedad aditiva en los resultados de caída de presión y pérdida por transmisión cuando varios dispositivos de postratamiento se disponen juntos formando un sistema, la importancia real de los dispositivos auxiliares que a menudo son pasados por alto , los cambios en los inicios de la vida útil de un dispositivo con filtro de partículas tipo GPF, las ventajas de realizar análisis por descomposición en los resultados de pérdida por transmisión, las capacidades de 1D y 3D CFD para producir información útil y los beneficios eventuales de la co-simulación 1D-3D.

En conjunto, se elaboró una base de datos exhaustiva sobre la caída de presión y la pérdida de transmisión de los dispositivos y sistemas de postratamiento más avanzados. Las metodologías experimentales utilizadas, con su correspondiente posprocesado, demostraron ser ade-

cuadas y producir información significativa. Especialmente tras la validación realizada con las mediciones acústicas en condiciones ambientales relativas a condiciones similares a las reales en el motor. Los modelos 1D resultaron ser muy indicativos, dado un ajuste adecuado, y produjeron información bastante útil sobre la caída de presión y la atenuación acústica, al tiempo que imitaban la geometría y los principios de funcionamiento de las mediciones. El modelado computacional 3D permitió analizar más a fondo los efectos internos y tridimensionales, entre tanto la integración 1D-3D, aunque más exigente en términos de preparación, produjo mejoras significativas. Utilizando las metodologías y directrices propuestas se pueden obtener excelentes resultados de caída de presión y buenos resultados de atenuación acústica (como mínimo hasta los 500-700 Hz) alimentándose únicamente de datos geométricos, es decir, independientemente de cualquier medición experimental. Además, los enfoques de análisis por descomposición presentados demostraron ser una herramienta versátil y provechosa, ya que se produjo información valiosa para el análisis de todos los temas específicos evaluados.

Con respecto a dichos temas, la comprobación de la propiedad aditiva confirmó que la caída de presión es esencialmente aditiva, mientras que, en el caso de la pérdida de transmisión, la aditividad varía con la frecuencia, para frecuencias entre bajas y medias, dominadas por efectos reactivos no se encontró aditividad, mientras que de frecuencias medias a altas donde dominan los efectos disipativos si se evidencio un nivel considerable de aditividad. El estudio de un dispositivo auxiliar con un inductor de mezclado estático tipo "swirl" como pieza representativa, llevó a determinar que, aunque normalmente se pasan por alto, los elementos auxiliares contribuyen de forma significativa a la caída de presión y pueden tener una influencia notable en la atenuación acústica del sistema de postratamiento. Este último estudio también contribuyó a llenar una brecha de conocimiento, ya que se trata de los primeros resultados publicados para el tipo de elemento mezclador caracterizado. Finalmente, ambos enfoques, experimental y de modelado computacional, ayudaron a identificar la influencia de la deposición de hollín en los poros de un filtro de partículas GPF durante los primeros ciclos de uso sobre los efectos reactivos y disipativos.

En general, se encontró que, prestando especial atención a determinados aspectos, los modelos computacionales pueden utilizarse para

proporcionar condiciones iniciales adecuadas para el diseño de la línea de escape. Esta tesis y los datos producidos contribuyen a llenar la brecha de conocimiento en la acústica de sistemas postratamiento y elementos relacionados, también proporciona varias herramientas y enfoques útiles para mejorar el procedimiento de diseño de las líneas de escape y por lo tanto su optimización, las cuales eventualmente podrían ser transferidas a otras aplicaciones.

Resum

Les normatives sobre emissions contaminants i sonores, cada vegada més estrictes, han sigut la principal motivació per a la investigació, el desenvolupament i l'optimització dels motors de combustió i altres tecnologies relacionades. Aquesta tendència ha donat lloc a la introducció gradual de sistemes de post-tractament per a reduir les emissions contaminants provinents de l'automoció. No obstant això, en les dues últimes dècades el nivell de restriccions imposades ha fet que l'ús de sistemes de post-tractament siga intensiu i obligatori, passant de ser xicotets dispositius individuals a sistemes molt complexos que sovint inclouen més d'un dispositiu.

Encara que l'objectiu principal dels sistemes de post-tractament és la reducció de les emissions contaminants, aquests també exerceixen una gran influència en la dinàmica de les ones, la contrapressió i el comportament acústic de la línia de escapament, per la qual cosa modifiquen les característiques del flux, l'acústica i la pressió del flux de escapament. El que al seu torn redefineix les condicions de disseny per al silenciador situat aigües avall. Una millor comprensió de l'atenuació acústica i la caiguda de pressió degudes a la presència de sistemes de post-tractament podria tindre repercussions beneficioses, ja que permetria optimitzar el disseny dels mateixos dispositius i de les línies de escapament completes, especialment del silenciador. Es va considerar que un enfocament prometedor per a obtindre una millor comprensió del tema seria tindre en compte la influència que els components individuals i les característiques més freqüents dels sistemes de post-tractament tenen en el seu compotarment final.

Es van emprar diferents enfocaments experimentals i de modelatge computacional per a estudiar i caracteritzar el comportament acústic i fluidodinàmic d'un conjunt variat de sistemes i dispositius de post-tractament, abastant així una àmplia gamma d'elements i característiques representatius de les aplicacions de post-tractament més avançades d'ús comercial. La pèrdua per transmissió i la caiguda de pressió van ser seleccionades com a paràmetres clau d'estudi per a quantificar l'atenuació acústica i la contrapressió generada per cada dispositiu. Per a la caracterització experimental es van utilitzar instal·lacions i procediments de mesura ben establits. Per part seua, per al modelatge computacional es

van emprar diferents enfocaments de simulació, com ara l'unidimensional, el CFD (tridimensional) i fins i tot la co-simulació 1D-3D, seguint en la mesura del possible el concepte o principi "bessons digitals" (virtual twinning), en programes comercials amb l'objectiu de replicar els resultats experimentals, a fi d'obtindre informació complementària i ajudar a aprofundir en la comprensió dels fenòmens interns, els efectes tridimensionals del flux i els efectes acústics.

Previ a la caracterització minuciosa dels dispositius, es va verificar la validesa i significança de les mesures acústiques en condicions fredes (ambient), com les que s'anaven a prendre, per a representar els dispositius respecte a les seues condicions reals de funcionament, és a dir, exposats a flux calent i periòdic com en l'extrem calent de les línies de escapament on habitualment se situen els sistemes de post-tractament. Una vegada realitzada aquesta validació, per a cada sistema o dispositiu es van registrar mesures de caiguda de pressió per a un rang de cabals màssics, normalment entre 0 i 800 kg/h. De la mateixa manera, es van efectuar mesures de pèrdua de transmissió en condicions d'absència de flux i amb tres cabals màssics diferents superposats, en general 100, 200 i 300 kg/h. La informació produïda, després d'un cert post-processament, anàlisi per descomposició i comparatiu, sumat a l'ús del raonament inductiu van ser emprats per a quantificar i relacionar cada element amb els seus efectes.

Addicionalment altres temes van ser avaluats, com el compliment de la propietat additiva en els resultats de caiguda de pressió i pèrdua per transmissió quan diversos dispositius de post-tractament es disposen junts formant un sistema, la importància real dels dispositius auxiliars que sovint són passats per alt, els canvis en els inicis de la vida útil d'un dispositiu amb filtre de partícules tipus GPF, els avantatges de realitzar anàlisis per descomposició en els resultats de pèrdua per transmissió, les capacitats dels models 1D i 3D CFD per a produir informació útil, i els beneficis eventuals de la co-simulació 1D-3D.

En conjunt, es va elaborar una base de dades exhaustiva sobre la caiguda de pressió i la pèrdua de transmissió dels dispositius i sistemes de post-tractament més avançats. Les metodologies experimentals utilitzades, amb el seu corresponent post-processament, van demostrar ser adequades i produir informació significativa. Especialment després de la validació realitzada amb les mesures acústiques en condicions ambien-

tals relatives a condicions similars a les reals en el motor. Els models 1D van resultar ser molt indicatius, donat un ajust adequat, i van produir informació prou útil sobre la caiguda de pressió i l'atenuació acústica, al mateix temps que imitaven la geometria i els principis de funcionament dels mesuraments. El modelatge computacional 3D va permetre analitzar més a fons els efectes interns i tridimensionals, mentre que la integració 1D-3D, encara que més exigent en termes de preparació, va produir millores significatives. Utilitzant les metodologies i directrius proposades es poden obtindre excel·lents resultats de caiguda de pressió i bons resultats d'atenuació acústica (com a mínim fins als 500-700 Hz) alimentant-se únicament de dades geomètriques, és a dir, independentment de qualsevol mesurament experimental. A més, els enfocaments d'anàlisis per descomposició presentats van demostrar ser una eina versàtil i profitosa, ja que es va produir informació valuosa per a l'anàlisi de tots els temes específics avaluats.

Respecte a aquests temes, la comprovació de la propietat additiva va confirmar que la caiguda de pressió és essencialment additiva, mentre que, en el cas de la pèrdua de transmissió, la additivitat varia amb la freqüència: per a freqüències entre baixes i mitjanes, dominades per efectes reactius no es va trobar additivitat, mentre que de freqüències mitjanes a altes on dominen els efectes dissipatius si es fa palès un nivell considerable d'additivitat. L'estudi d'un dispositiu auxiliar amb un inductor de mescla estàtic tipus "swirl" com a peça representativa, va portar a determinar que, encara que normalment es passen per alt, els elements auxiliars contribueixen de manera significativa a la caiguda de pressió i poden tindre una influència notable en l'atenuació acústica del sistema de post-tractament. Aquest últim estudi també va contribuir a omplir una bretxa de coneixement, ja que es tracta dels primers resultats publicats per al tipus d'element mesclador caracteritzat. Finalment, tots dos enfocaments, experimental i de modelatge computacional, van ajudar a identificar la influència de la deposició de sutge en els porus d'un filtre de partícules GPF durant els primers cicles d'ús sobre els efectes reactius i dissipatius.

En general, es va trobar que prestant especial atenció a determinats aspectes, els models computacionals poden utilitzar-se per a proporcionar condicions inicials adequades per al disseny de la línia de escapament. Aquesta tesi i les dades produïdes contribueixen a omplir

la bretxa de coneixement en l'acústica de sistemes de post-tractament i elements relacionats; també proporciona diverses eines i enfocaments útils per a millorar el procediment de disseny de les línies de escapament i per tant la seua optimització, les quals eventualment podrien ser transferides a altres aplicacions.

Publications

List of Related Publications

The following correspond to articles produced within the framework of this research, and therefore directly related to the hereby presented doctoral thesis, consequently some of the results and discussion written down here can also be found in them:

- Torregrosa, A. J., Broatch, A., Quintero, P., Redondo, Á. & Morin, F. (2022). Assessment of the fluid-dynamic and acoustic behaviour of a swirl static mixer for after-treatment systems. Applied Acoustics, 186, 108446.
  DOI : 10.1016/$j.apacoust$.2021.108446 [1].

- Torregrosa, A.J., De la Morena, J., Sanchis, E.J., Redondo, Á. & Servetto, E. (2022). A study of the early life of Gasoline Particulate Filters: Reactive and dissipative acoustic effects. Proceedings of the Institution of Mechanical Engineers, Part D: Journal of Automobile Engineering.
  DOI : 10.1177/09544070221127330 [2].

- Torregrosa, A. J., Piqueras, P., Sanchis, E.,J., Redondo, Á. (2023). On the Applicability of Cold Acoustic Measurements to High-Amplitude Hot Pulsating Flows. Acoustics Australia, 51, 115–128.
  DOI : 10.1007/$s40857 - 022 - 00282 - 5$ [3].

Division of work between authors

These publications have been done in collaboration with other researchers, being the author signatures in order of seniority. The respondent performed most of the post-processing of experimental measurements, most of the modelling work, the repair and preparation of CAD files, most of the 3D models (Star CCM+), all the 1D models (GT-ise), and the 1D-3D coupled simulations (Star-GT). Methodologies, result discussions and analysis were done in collaboration with the supervisor, Dr. Antonio Torregrosa, as well as with the rest of co-authors.

Other publications by the respondent

Prior to this doctoral research the author has been involved in the publications detailed below. The first was developed during the time working in engineering consultancy services prior to incorporation to UPV. The other is the final project of the Master, which is considered as the previous academic and research period to this doctoral program. The late served as a preparation and previous steps needed to properly conduct this research.

- Corredor, L., Avendaño, J., Bello, R., Redondo, Á., Calle, J., & Viloria, J. (2018). Industrial Energetic Districts: Impact Analysis on the Global Energy Efficiency and Business Competitiveness. In E3S Web of Conferences (Vol. 64, p. 08007). EDP Sciences. DOI : 10.1051/$e3sconf$/20186408007 [4].

- Redondo Navarro, Á.R. (2020). Experimental Characterization and Improved Modelling Methodology for Simple Geometry After–treatment Devices Focused on Pressure Drop and Transmission Loss. Universitat Politècnica de València.
  $http$: //$hdl.handle.net$/10251/158904 (Master's Thesis / Final degree project) [5].

Acknowledgements

Dedicatoria especial para Mami Ruth, por todo el amor y enseñanzas recibidos, por cultivar en mi la curiosidad, el gusto por la lectura y el hambre de conocimiento. Esta tesis y todo esfuerzo académico realizado desde pequeño son dedicados a mi abuela. Mi Ángel, este trabajo y el título son tuyos. Por siempre en mi corazón Ruth Lechuga Consuegra.

Dedicado a Pamela Alva, Mi Pameluki, mi girasol, mi compañera de vida, mi prometida y muy pronto esposa, mi compañía en todo este proceso y por el resto de la vida, ¡por todo lo vivido y lo que viviremos! Agradecido contigo por todo tu apoyo y respaldo en los momentos duros, por ayudarme a sacar lo mejor de mí, por entregarme tu amor incondicional y por ser mi oasis de descanso y felicidad en todo momento. Vamos juntos por los siguientes pasos de nuestro proyecto.

Dedicado también a Ana Isabel, mi incansable madre, por forjarme en el hombre que soy, siendo siempre ejemplo y guía para perseverar y luchar contra las adversidades. ¡Gracias por respaldarme siempre en todo cuanto puedes y mucho más! y gracias por siempre ver y hacerme ver mi potencial y capacidades.

Agradecimiento eterno para toda mi familia, mi abuelo Adalberto, mis tíos Edgar y Freddy, mis tías Mirella y Jenice, a mis primos que son mis hermanos, Angie, Edgard, Emmanuel, Marianna, a baby Jero, a la abue Nazly y a todos en la familia extendida de los Lechuga y los enlechugados. A mi padre Álvaro Enrique, mi hermanito Samuel, Lizeth y familia. A Don Rubér, Karen, Gaby (que además me diseño la imagen de la portada) y Daniela por acogerme en la familia.

Agradecimientos para amigos entrañables en Colombia, Simón, Pipe, Yosuira, Rafa, Diana, Gabo, Leo, Rubén y demás amigos de Colombia. Al ingeniero Lesmes por su legado, por su visión, y por motivarnos a

sus estudiantes a aspirar más alto, hay que apuntarle a lo difícil porque para lo fácil hay fila. También para mis amigos en España que han llegado a sentirse como familia Ivis, Karel, Isaac, Edu, Aryani, Arturo, Rubén, Reme y mis sobrinitos Thiago y Andrea.

Al Profe Tono, Dr. Antonio Torregrosa, por siempre estar disponible, guiarme y acompañarme en la investigación dándome mi margén de maniobra, y brindarme un trato tutor-alumno muy cordial y ameno. A mis diferentes compañeros de despacho a lo largo de estos años, en especial a Amín Dreif por ser ese saludo amigable, conversación casual y compañero para las clases, ratos de estudio y de exámenes.

Technical Acknowledgements

I wish to thank Pedro Piqueras, Enrique Sanchis and Pedro Quintero; CMT colleagues, helpful and willing paper co-authors. I also wish to thank Adolfo Guzmán and Bernardo Planells for their valuable assistance with the experiments and their willingness to share with me many clarifying ideas from the practical and experimental point of view. To Amparo Cutillas, always helpful, efficient and willing to guide in all administrative procedures, and finally to all members of Instituto Universitario CMT-Motores Térmicos.

I also wish to express my gratitude to Florent Morin, Maxime Dubarry and Sebastien Baert, from Renault Paris, as they provided the studied devices, technical information, continuous feedback, and so many fruitful exchanges of ideas. Also my gratefulness to POWERTECH Engineering s.r.l (PWT) for accepting me for my research placement, even though it had to be a virtual stay it was profitable as any, thanks to my advisor Mr. Emanuele Servetto and Mr. Andrea Bianco, for their obliging at sharing their experience with me.

Funding Acknowledgements

This research has been funded by the Programa de Ayudas de Investigación y Desarrollo PAID-01-19, from Universitat Politècnica de València (UPV), which granted my pre-doctoral contract.

"Investigar es ver lo que todo el mundo ha visto, y pensar lo que nadie más ha pensado".

"Research is to see what everybody else has seen, and to think what nobody else has thought".

- Albert Szent-Györgyi

Contents

List of Figures

List of Tables

Nomenclature

Latin, Mathematical and Special Characters

Character	Meaning	Units
a	Wave propagation speed	$[ms^{-1}]$
a_k *and* b_k	Fourier series constants	[-]
A	Amplitude	$[dB]$
c	Speed of Sound	$[ms^{-1}]$
D	Diameters	$[mm]$
f	Frequency	$[Hz]$
H	Engine Order	[-]
He	Helmholtz number	[-]
k	Turbulent Kinetic Energy	$[m^2s^{-2}]$
k	Wave number	[-]
K	Pressure Drop Factor	[-]
l	Length	$[m]$
M	Mach Number	[-]
$\dot{m}$	Mass Flow Rate	$[kgs^{-1}]$
p	Pressure	$[Pa]$
P	Pressure Spectrum	$[Pa]$
r_1, r_2	Refflection Coefficient	[-]
Re	Reynolds Number	[-]
S	Cross-sectional Area	$[m^2]$
t	Time	$[s]$
t_12, t_21	Transmission Coefficient	[-]
T	Temperature	$[^\circ C]$
u	Velocity	$[ms^{-1}]$
W	Acoustic Power	$[W]$

Greek Characters

Character	Meaning	Units
Δ	Variation of a variable	[-]
ϵ	Turbulent dissipation rate	$[m^2 s^{-3}]$
ε	Fourier series fitted to differences	[-]
γ	Ratio of specific heats	[-]
λ	Wavelength	$[m]$
μ	Micro multiplier (10^{-6})	[-]
φ	Fourier series fitted to baseline operating point	[-]
ψ	Real or imaginary parts	[-]
ρ	Mass Density	$[kgm^-3]$
τ	Characteristic period	$[s]$
ξ	Defined in Chapter 3	[-]

Superscripts and Subscripts

Kind	Symbol	Meaning
Subscript	*0*	Reference
Subscript	*1,2*	Position reference
Subscript	*ATS*	Estimated for the device or system
Subscript	*comp*	Composed
Subscript	*d, diss*	Dissipated
Subscript	*i, inc*	Incident
Subscript	*gen*	Generated
Subscript	*r, ref*	Reflected
Subscript	*t, tran*	Transmitted
Superscript	+	Forward
Superscript	-	Backward
Superscript	ND	No Dissipation Assumption
Sub- and Superscript	duct	Measure of test rig ducts
Sub- and Superscript	fric	Due to friction
Sub- and Superscript	in	Inlet
Sub- and Superscript	out	Outlet
Sub- and Superscript	test	Measure of rig and device bundle

Acronymns and Abbreviations

Item	Meaning
0D	Zero-dimensional
1D	One-dimensional
1D-3D	Co-simulation
2D	Two-dimensional
3D	Three-dimensional
A,D1,D2,AD1,D1D2	Abreviations of SG devices and combinations
ACT	Advanced Combustion Technologies
APS	Announced Pledged Scenario
ASC	Ammonia Slip Catalyst
ATD	After-treatment Device
ATS	After-treatment System
BEM	Boundary Element Method
BEV	Battery Electric Vehicles
CAD	Computer Assisted/Aided Design/Drawing
CC	Catalytic Converter
C-C	Close-Coupled
CFD	Computational Fluid Dynamics
CFTB	Cold Flow Test Bench
CG	Complex Geometry
CI	Compression Ignition
CMT	Instituto Universitario Motores Termicos
CUC	Clean-Up Catalyst
DEF	Diesel Exhaust Fluid
DOC	Diesel Oxidation Catalyst
DOE	Design of Experiments
DPF	Diesel Particulate Filter
DPFc	Catalyst-coated DPF
EATS	Exhaust ATS
EGR	Exhaust Gas Recirculation
FEA	Finite Element Analysis
FEM	Finite Element Method
FESEM	Field Emission Scanning Electron Microscope
FLC	Forward Loss Coefficient

Item	Meaning
FSG	FlowSplitGeneral
FT	Flow-Through
FVM	Finite Volume Element
GDI	Gasoline Direct Injection
GHG	Greenhouse Gas
GPF	Gasoline Particulate Filter
GPFc	Catalyst-coated GPF
HC	Hydrocarbon
HCCI	Homogeneus Charge Compression Ignition
ICE	Internal Combustion Engine
IG	Intermediate Geometry
IL	Insertion Loss
ITR	Impulse Test Rig
JCR	Journal Citation Reports
$k-\epsilon$	Turbulence Model
LNT	Lean NOx Trap
LP	Lumped Parameter
MFR	Mass Flow Rate
NEDC	New European Driving Cycle
NM	No Monolith
NR	Noise Reduction
NZE	Net Zero Emission
OBD	On-Board Diagnostics
OEM	Original Equipment Manufacturer
PD	Pressure Drop
PF	Particulate Filter
PM	Particulate Matter
PN	Particulate Number
PR	PipeRound
PWT	POWERTECH Engineering s.r.l
Q3D	Quasi-3D (Quasi-Three-Dimensional)
RANS	Reynolds Avaraged Navier-Stokes
RDE	Real Driving Emissions
SCR	Selective Catalytic Reduction
SCRf	SCR particulate filter

Item	Meaning
SG	Simple Geometry
SI	Spark Ignition
SPL	Sound Pressure Level
STEPS	Stated Policies Scenario
SUV	Sport Utility Vehicle
TL	Transmission Loss
TWC	Three Way Catalyst
UF	Under-floor
UFGS	Unsteady Flow Gas Stand
UPV	Universitat Politecnica de Valencia
URANS	Unsteady RANS
UWS	Urea-Water Solution
WF	Wall Flow
WLTC	World-Harmonized Light-duty Vehicle Test Cycle/Procedure

Chapter 1

Introduction

This chapter serves as the introduction to the research work developed; it first contextualizes the *Background* and *Motivation* of the research, then presents the *Research Objectives and Scope* to delimit what was assessed; afterwards, details on the overall *Research Methodology* followed in the development of the study are commented, and finally an overall view of the document is given in the *Thesis Outline*.

1.1 Background

Environmental awareness has been on the rise for decades, driving the development of technologies and impacting on consumer preferences in response for the need to ensure energy security, by protecting and giving proper administration to natural resources, and to control pollution, in particular to minimize the greenhouse gases (GHG) emissions associated with climate change and to improve air quality for the sake of public health [6, 7]. Reducing oil dependence is currently one of the key objectives of governments around the world, as it directly impacts in both the energy security and pollutant emissions derived from its use. Latest update of bp Statistical Review of World Energy, published in 2022 with data up to 2021, reports a world overall energy demand of about 595.15 exajoules, with an increase of 5.8% to 2020, bouncing back from the COVID pandemic decrease, and an average yearly increase of 1.3% in the last decade, being oil the source of up to 33% of the global energy demand [8]. In spite of environmental concerns, worldwide en-

ergy consumption is growing alongside population and living standards, and an overall 15% increase is expected for 2050 if current trends and policies are kept [7, 9]. Fig. 1.1 shows such a projection detailed by sector.

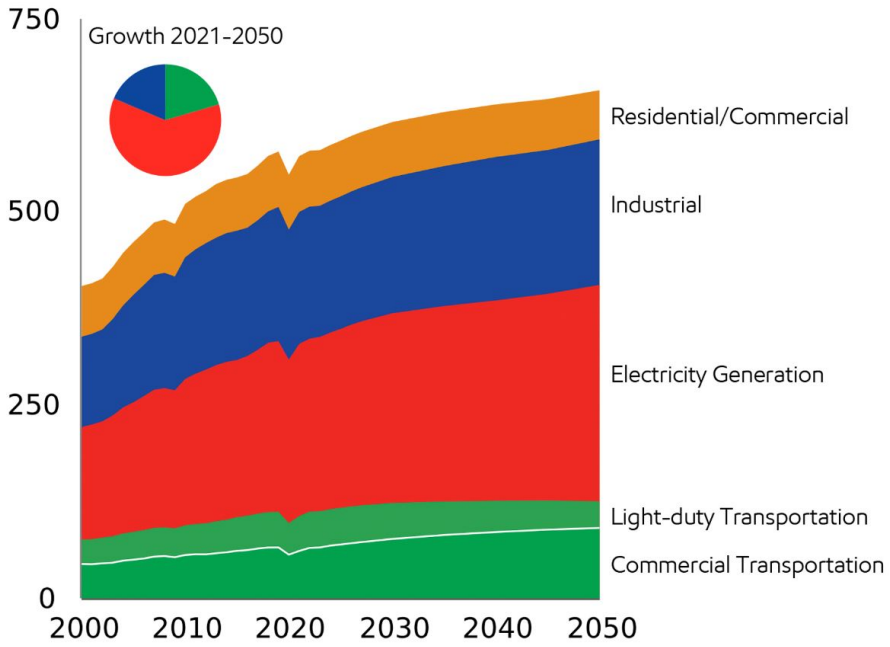

Figure 1.1: Global energy demand by sector, projection for 2050 expressed in quadrillion Btu, took from [7]

As shown, the transport sector is expected to increase its energy demand in about 30% driven by the rise in population and prosperity. This increase internally has two opposing trends, the demand from light-duty passenger transport would decrease as more efficient technologies and electrification (either partial or total) are implemented even though of expected increase in the access to personal mobility. In the opposite side, commercial transport (heavy-duty land, aviation, marine and rail) energy demand would increase due to the increased acquisition power of population acquiring goods or travelling carrying the overall sector increase [7, 9].

Regarding the transportation sector, the International Energy Agency have recently published their World Energy Outlook 2022 [9], where three main scenarios for 2050 were considered: STEPS (Stated Policies Scenario) considering the prevalence of current policy settings, APS (Announced Pledged Scenario) considering the full completion of all aspirational targets announced by governments, and the NZE (Net Zero Emissions) scenario which, optimistically, projects a way to achieve a 1.5°C stabilization in the rise in global average temperature, alongside universal access to modern energy by 2030. Fig. 1.2 shows the three scenarios. In the STEPS [7] oil and natural gas would account for about 55% of the world energy mix in 2050, and even in the NZE scenario, for the transportation sector oil would still be a considerable energy source as of 2040 and still residual for 2050.

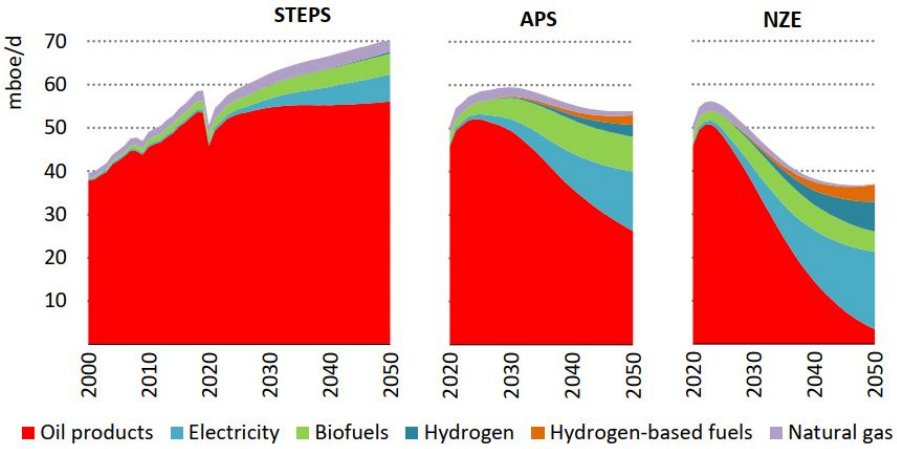

Figure 1.2: Energy use in transportation by scenario, 2000 – 2050, taken from [9]

Nowadays the transportation sector (both commercial and light-duty) accounts for about 25% of the global energy demand, is responsible of around 40% of the emissions from end-use sectors (23% of global carbon dioxide emissions) and about 90% of the energy used comes from oil [9, 6]. Roughly 60% of crude oil production is used to make petroleum-derived liquid fuels for transportation: diesel, gasoline and

jet fuel [7, 10, 8, 9]. To be precise, it is estimated that the global daily demand of these fuels is at around 4.9 billion litres each for gasoline and diesel and 1.3 billion liters for jet fuel [11], with an expected yearly growth of around 1% [7, 9].

Powerplants for transportation are almost entirely ($> 99.9\%$) internal combustion engines (ICEs), with reciprocating engines powering land and marine transport, and jet engines powering air transport [6]. Spark ignition (SI) engines power around 80% of all passenger cars across the world [8], while diesel engines dominate the commercial sector (road and marine use). Light-duty Vehicles use around 44% of the global transportation energy [9] although they are much greater in number compared to commercial vehicles [6].

Alternatives to fossil-fueled ICE powertrains have been on the rise and receiving lots of attention, for example, battery electric vehicles (BEV) and fuel cell technology. There have been also efforts to establish other fuels such as natural gas, biofuels and e-fuels [6]. However, two points need to be considered; firstly, that every alternative must be analyzed on a complete life-cycle basis to be sure that environmental and other benefits are real, as otherwise the problems are just being moved from the tailpipe to somewhere else without solution [12, 13, 14]. Secondly, these alternatives start from scratch in terms of massive supportive infrastructure and face significant barriers to fast and unrestrained growth in comparison to the deep-rooted fossil fuel based ICEs and all the decades of technological maturity and consolidated infrastructure.

In this light, one may expect that most of the transportation will continue to rely on ICE-powered vehicles for several years or decades to come [6, 7, 9, 10]. Projections suggest that, within this transition period, shortage of crude oil should not constrain growth in transportation as known reserves of oil have increased faster than consumption for several years, and the current reserves should last for at least the next 50 years even if current consumption rates are maintained [11, 8].

Therefore, the safest path to ensure the compliance of environmental policies and guarantee in the short-run the sustainability of transportation, in terms of availability, reliability and emissions, is by improving the efficiency and fuel consumption of current ICEs and related technology, for example, through improvements in combustion, control, and after-treatment systems, assisted by partial electrification in the form

of hybridization [15, 16, 17, 18, 19, 20]. For instance, advanced combustion technologies (ACTs), such as pre-chambered lean burn combustion and homogeneous charge compression ignition (HCCI), have been researched for long as new options to evolve or replace conventional diesel and gasoline engines, evidencing a great potential for NOx and PM reduction [21].

Examples of ICE related technology already helping ICEs to comply with regulations include the broad use of Direct Injection in gasoline engines, "downsizing" or "right-sizing" thanks to turbochargers and superchargers, and the standard approach of incorporating ATS into the exhaust line to eliminate the pollutant species before they are emitted into the atmosphere [22]. Particularly ATS development has been delivering new combinations or improvements of pre-existing after-treatment devices (ATD) on a regular basis to match the ever increasingly restrictive emission regulations [15, 16, 17, 18, 19, 20].

1.2 Motivation

As exposed in the *Background*, still a few decades will pass before ICE can be fully replaced; meanwhile current and upcoming ICE powered means of transportation are equipped in their intake and exhaust lines with numerous elements whose main function is related to regulate or improve engine performance or to reduce pollutant emissions, see Fig. 1.3 for reference. However, all these elements change the conditions for the flow passing-by, affecting the back-pressure and propagation of waves, which translates into secondary but non-negligible silencing effects, either by dissipation or absorption means, which are seldom considered [23].

This research is focused on ATS, elements placed in the exhaust line whose main function is emissions abatement, but whose presence defines the effective boundary conditions perceived by any silencing element (muffler) located downstream. It is considered that understanding the effects of the presence of ATS on acoustics and back-pressure, and the possibility to include the consideration of such effects as an integral part of the design of the noise control system, can lead to improvements in the design of the complete exhaust line, for example requiring a smaller, simpler, and cheaper silencing element by optimizing the design

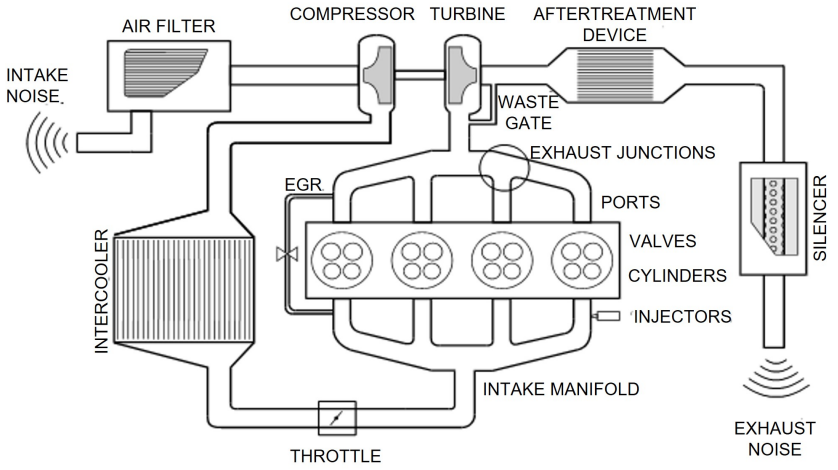

Figure 1.3: General scheme showing most common elements in intake and exhaust systems for automotive engines, adapted from [23].

and arrangement of the ATS elements, or even possibly not requiring a muffler any more.

There is a large amount of literature and research focused on ATS and ATD in terms of their effectiveness in emission control, their main function, alongside with their pressure drop, chemical reactivity and thermal behaviour, allowing for a considerably high understanding of the mechanisms involved. In the opposite end, there is comparatively scarce literature on their acoustic effects. Some of the first publications assessing the influence of ATDs on exhaust noise date back to the 90's. These first studies were focused on the acoustics of catalytic converters [24, 25, 26, 27]. By this time, all the articles published addressed the study necessarily by experimental methodologies as in [28, 29, 30], given the lack of mathematical models and specialized software dealing with the acoustics of these elements.

The research publications focused on the acoustics of these systems present a pattern of appearance that closely follows the development of each device on which they focus; for this reason in the period between 2005 and 2006 there was much research interest focused on particulate filters [31, 32, 33]; later, from 2010 on, publications covering various

types of devices began to be found as exhaust lines with multiple after-treatment systems arranged together became more common [34, 35, 36]. More recent publications have resumed the trend of studying particular devices, but now focusing on the use of software and the development of models and tools that allow the study of the acoustics of these devices making use of numerical and computational tools [37, 38, 39, 40].

This research intends to help fill the knowledge gap in the acoustic effects of several *State-of-the-Art Exhaust After-treatment Systems*, specially in the effects of some specific aspects, as well as the experimental and computational approaches to characterize the acoustic and wave-dynamic behaviour as a whole.

The opportunity and convenience of developing this research is justified because the CMT University Institute has had lots of projects with companies and manufacturers that open the possibility of accessing a great variety of ATDs, as well as information from previous projects that can still be taken advantage of by revisiting it with a different approach. This wide range of information would make it possible to study the influence of various aspects of ATDs on wave dynamics and exhaust line acoustics, most notably of:

- Geometric aspects such as length, diameter, bends, shapes, etc.
- Presence and configuration of cavities.
- Presence and configuration of sensors, mixers and other obstacles.
- Types of monolithic elements and their order.
- Particle accumulation in filter elements.

A secondary benefit of this research is the opportunity to propose and validate changes in the test benches, or the development of new experimental installations that allow the measurement of the acoustic behaviour and pressure drop of the systems in pressure amplitude and temperature conditions that are more representative of the real operating conditions that occur in the exhaust lines of current internal combustion engines.

1.3 Research Objectives and Scope

Considering the aforementioned context and motivation, the objectives for this research were set as follows:

- To generate a comprehensive experimental database concerning the acoustic and fluid-dynamic behaviour of after-treatment devices, using the three characterization facilities available: cold flow bench, hot and pulsating flow bench (unsteady gas stand) and impulse test bench.
- To develop and refine modelling methodologies and models, using different computational tools, of various levels of complexity, mainly one-dimensional (1D), three-dimensional (3D), and coupled (1D-3D), as required by the cases studied for the interpretation and simulated reproduction of experimental results.
- To perform the joint evaluation of experimental and modelling results to narrow down the impact of these devices on back-pressure (pressure drop) and engine exhaust noise in real conditions and the potential implications on exhaust line design to reduce undesired effects or incorporate improvements.

These objectives were applied within certain scope: as stated in the thesis title, the idea was to cover a wide range of the existing, *State-of-the-art after-treatment systems* or technologies, specifically to the device level. Therefore, what is understood as a system and as a device within this research has to be defined:

- **System:** Refers to the complete array of devices that work together to accomplish the emission abatement function, i.e. the exhaust line downstream of the manifold, or of the turbine if present, and down to the silencing element but excluding it.
- **Device:** Refers to a component composed by inlet and outlet sections (usually pipework) with some special non-pipe elements in between which are the ones with a definite function in terms of the ATS operation.

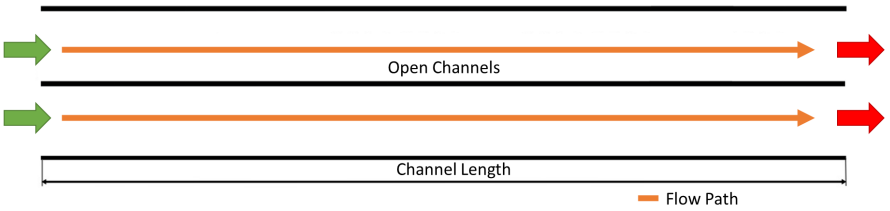

Figure 1.4: Scheme of the flow path in the open channels of flow-through monoliths.

The main group of after-treatment devices includes all those that have monoliths, whose main function is related to emission abatement. There are two main kinds of monoliths in terms of their constructive and fluid-dynamic characteristics, namely flow-through (FT) and wall-flow (WF) monoliths. A scheme representing the flow path through FT monoliths is shown in Fig. 1.4; similarly, the typical flow path in WF monoliths is shown in Fig. 1.5. These figures illustrate how each kind of monolith imposes different conditions to the passing flow, so that different wave dynamics, back-pressure and acoustic effects arise.

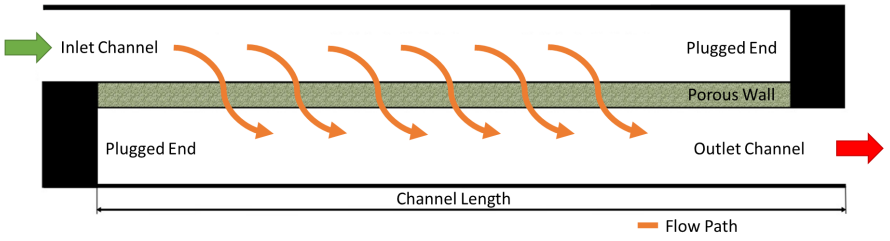

Figure 1.5: Scheme of the flow path in the alternatively plugged channels of wall-flow monoliths.

ATDs containing monoliths often require some specific conditions in order to accomplish their function effectively, and there are several kinds of auxiliary devices that help fulfil those conditions; for example, injectors to supply certain chemicals or fuel, heaters to control temperature, mixing inducers to guarantee homogeneity of mixtures or sensors

to monitor parameters that may be the signal to activate other systems only under preset conditions.

Devices studied here include different combinations of all the aforementioned ones, with several levels of "geometrical complexity", this is: presence or absence of bends, flexible elements, irregular shapes and tapered elements. The specific details on each device is presented in Section 3.1, but all of the following elements or characteristics are covered in at least one device.

- Flow-Through monoliths.
  - DOC.
  - TWC.
  - SCR.
  - SCR-CUC.
- Wall-flow monoliths.
  - DPF.
  - DPFc/SCRf.
  - GPFc.
- Mixers.
  - Static Swirl Mixer.
  - Perforated Tunnel.
  - Perforated Plate.
- Injectors.
- Sensors.
- Separator.

1.4 Research Methodology

Fig. 1.6 summarizes in a flowchart the overall methodology used to develop the research. Three work fronts were defined: A passive one, the review of the state-of-the-art, and two active ones, the data collection and the development of computational models. The experimental measurements were the main source of information within the data collection, and 1D modelling the most exhaustively used approach in the computational modelling.

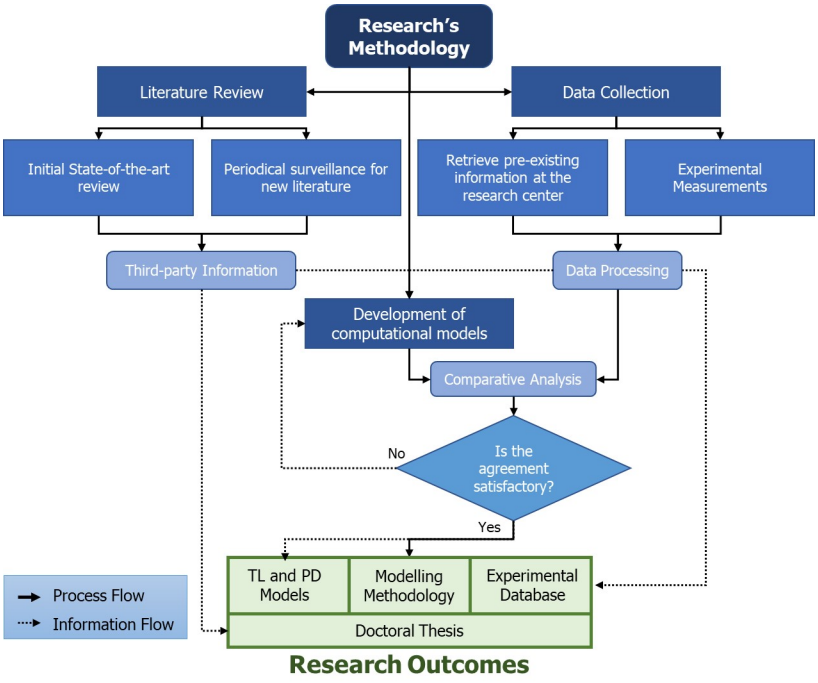

Figure 1.6: Research's methodology flowchart.

The review of the state-of-the-art is considered as a passive, yet relevant, work front, as third party information available in the literature served well as guidance in the preliminary and early steps of the active work fronts, and it also allowed for the identification of certain knowledge gaps that this research seeks to help fill. An initial exhaustive

literature review was made, and periodic literature searches, approximately twice per year, helped keep the initial revision updated.

Data collection in turn also started by retrieving pre-existing relevant information available, as previous projects with OEMs had already produced reference information, and helped improve the experimental test facilities and acquire know-how in their usage. For instance, the initial validation on the significance of cold condition measurements in regards to actual operating conditions presented in Chapter 4, responds to one of the knowledge gaps identified in the Literature Review and also integrates in a new methodology experimental test rigs, procedures and concepts previously developed. Even the device was readily available from the start of the research as it was used in a preceding project. Then, a partner OEM supplied a complete prototype ATS, several individual ATDs, alongside their corresponding CAD files and information on the monoliths contained. The information on these devices is presented in Section 3.1.

Later on, the measurement campaign started with the reception of devices and information from the OEM, the preparation of devices for their testing, which includes preparing adapters to fit each device into the test facilities, to cut-off pipe sections in excess to the interest of the research, soot loading for some devices containing PF, and finally performing all the required measurements. All of these were performed with the valuable help of the technicians. The information produced was then post-processed as required in each case (e.g. corrections, smoothing, wave decomposition). Details on the measurements, experimental test facilities, and post-processing are presented in Section 3.2.

The computational modelling performed pursued the vision of assessing the possibility of developing 1D models in a commercial gas dynamic code, that can replicate as accurately as possible the characteristics of the devices, as well as the logic and methodology of the experimental study, using the approach of digital or simulated twinning, validating in case of success the possibility of using the simpler level of modelling with a high level of confidence as sources of information and convenient tools to be incorporated into the design process of complete exhaust lines. The most suitable approach, the one recommended by experts, for reference, PWT CFD and powertrain simulation experts consulted within the doctoral research placement, is to use post-processed

experimental data as the benchmark for 3D CFD models using CAD files as the input, then use 3D CFD results as the benchmark to develop and evaluate 1D models. Then if the complexity of a device results to be beyond base 1D simulations, an additional 1D-3D coupled simulation can be used to assess it. In any case, most of the work was focused on the use of 1D models, which produced satisfactory results even when compared directly to the post-processed (smoothed) experimental data.

The computational workfront also had three separated stages: the preliminary steps, the 3D modelling, and the 1D modelling, considering the 1D-3D coupling as a last resource to further improve 1D modelling when needed. The preliminary steps include the CAD file preprocessing, which includes from removing elements out of the research interest, to repairing gaps or filling sensor holes, to the preparation of simplified copies for the 1D modelling discretization and meshing for the 3D modelling. In the 1D modelling, the preparations included sensitivity studies and parameter definition, and the preparation of Virtual Twins for the Experimental Facilities in order to be used as templates. Then the 3D modelling started from the post-processed CAD files, and the 1D modelling by preparing models in the PD digital twin template. This was based on previous experience from the research institution that models validated in the PD aspect are the best starting point to assess the acoustic behaviour. Both 3D and 1D required an iterative optimization process until both the acoustic and the pressure drop behaviour were satisfactorily represented. The comparative analysis is not considered a workfront on its own, as it is a continuous process with experimental data serving as benchmark for the iterative improvement of computational models.

It was decided that the computational modelling was to be assessed in the order of increasing complexity of the devices. The subject devices were classified into three categories: simple, intermediate and complex geometry. This choice is justified on the grounds of previous research, in which the consideration of only complex realistic systems did not allow to obtain conclusive results. In fact, the experimental results did not provide sufficient information about the eventual source for the discrepancies observed between the results of the experiments and the results of the models developed.

Starting with the assessment of a complete ATS which consisted of

three geometrically simple devices, which only had practically straight and aligned pipe sections, flow-through monoliths, straight tapered elements and common auxiliaries such as injector and sensor ports and a static swirl mixer. This initial limitation in complexity allowed to focus on structuring the base of the methodology, to test software capabilities under a theoretically understood situation and to adjust the virtual twin templates previously prepared. The opportunity of these ATDs being part of a unique ATS, also enabled to assess their interactions when put together. From this point on, the assessment moved into increasingly complex geometries and traits until the full set of ATDS was characterized, delivering a depurated and validated methodology.

Following is the breakdown of tasks and activities developed in the research carried out:

Review of the state-of-the-art:

- Initial exhaustive literature review.
- Periodical (six months) complementary updates.

Data collection:

- Gathering of available experimental information from previous projects.
- Validation of cold measurement significance (Unsteady Flow Gas Stand).
- Conducting experimental characterization.
  - Reception and preparations of subject devices.
  - Make required measurements in the experimental facilities available.
    - Pressure drop measurements in the cold flow test bench.
    - Transmission loss measurements in the impulse test rig.
- Post-processing of experimental data.

Development of computational models:

- Sensitivity studies and parameter definition.
- Preparation of virtual twins of experimental facilities (templates).
- CAD files pre-processing.
- Development of models in specialized software packages.
  - 3D Modelling.
  - 1D Modelling (Iterative).
    - First round on simple geometry devices.
    - Second round on intermediate complex geometry devices.
    - Final round (validation) on highly complex geometry devices.

Development of research outcomes:

- Related articles published during the research period.
- Exhaustive state-of-the-art ATS acoustic and fluid-dynamic characterization:
  - Depurated ATS modelling methodology, with best practices and discretization guidelines.
  - Experimental database.
  - PD and TL validated models and results (Computational characterization outcome).

Finally, all the process and results are consigned in this doctoral thesis.

1.5 Thesis Outline

The following is a brief summary on the outline followed in this document. The current chapter, *Chapter 1*, was devoted to the Introduction, presenting some background information, the motivation for developing this research, stating the objectives set, some insights on the methodology and this summary of the thesis structure. Immediately after *Chapter 2* presents the literature review, covering general information relevant to the field of research, and then in further detail an introduction to the state-of-the-art in automotive acoustics, after-treatment systems, and research and methodologies applied to the fluid-dynamic and acoustic characterization of such systems.

Then *Chapter 3* is devoted to presenting the materials and methods used. This includes relevant information on the devices studied, the experimental test facilities and their usage and related post-processing, the various modelling and computational tools and approaches applied for the simulated reproduction of experimental results and their processing, and special attention is given to the decomposition analysis applied to some of the transmission loss results. Several examples are presented in this chapter to illustrate the application and results obtained by each procedure.

Subsequently, three chapters are devoted to the main body of the research: *Chapter 4* assesses the significance of cold condition measurements to actual in-engine conditions and some other aspects in order to ensure that the measurements used to characterize the devices actually generate relevant and useful information for the pursued characterization. *Chapter 5* presents the first detailed characterization performed, the case study of a complete SCR exhaust line with static swirl mixer, which includes the characterization of individual monolithic devices with one and two monoliths, and shed light on the interaction between different elements on a unique exhaust line, and the effects of auxiliary elements, in this case a static swirl mixer, which are usually neglected in these kind of studies, thus covering the simple geometry category. *Chapter 6* continues with the characterization of several other individual after-treatment devices from the intermediate and complex geometry categories, allowing to investigate the effects of special features, such as intricate geometries, flexible elements, additional kinds of

mixer inducers, the presence of wall-flow monoliths and a novel check on the changes that take place in the first few load-regeneration cycles of a device containing a GPF.

Finally, *Chapter 7* summarizes the main findings and contributions of this research in the conclusions, and presents some insights on the possibilities of related future work, and *Chapter 8* condenses the complete references and bibliography cited.

Chapter 2

Literature Review

In this chapter, the first part is dedicated to introduce the theoretical framework and background knowledge needed to contextualize the research here presented. Afterwards, the state-of-the-art description is focused on the acoustic and fluid-dynamic characterization of exhaust systems, devices or components, either by experimental or computational approaches.

2.1 Theoretical Framework

Several key concepts relevant to the research hereby presented are introduced briefly, starting with some concepts on acoustics.

General Acoustic Concepts

Acoustics is the branch of science, in concrete of physics, dedicated to the study of sound; including its generation, propagation, control, reception and perception [41]. Sound is always originated by the vibration of an object or an unsteady flow, which in turn creates pressure waves that travel through the air or other mediums. Sound is a form of energy that is transmitted as mechanical waves; this means it needs a physical medium to propagate, particularly as vibrations in the particles of the medium itself. The medium can be gaseous, liquid or solid. Sound is audible, and this refers to the fact that it can be detected, at least certain sounds, by the human ear or other types of sound sensors.

The basic properties of sound are:

- Frequency, usually denoted as f, refers to the number of vibrations per second, measured in Hertz (Hz).
- Wavelength (λ), is the distance between two successive points on the wave that are in phase, for example two consecutive peaks or troughs; it is inversely proportional to frequency.
- Amplitude (A), refers to the intensity or loudness of a sound wave, and is related to the amount of energy carried by the wave, measured usually in decibels (dB).
- Velocity (a or c, usually), also known as propagation speed, is the speed at which sound waves travel through a medium, and is determined by the properties of the medium itself.

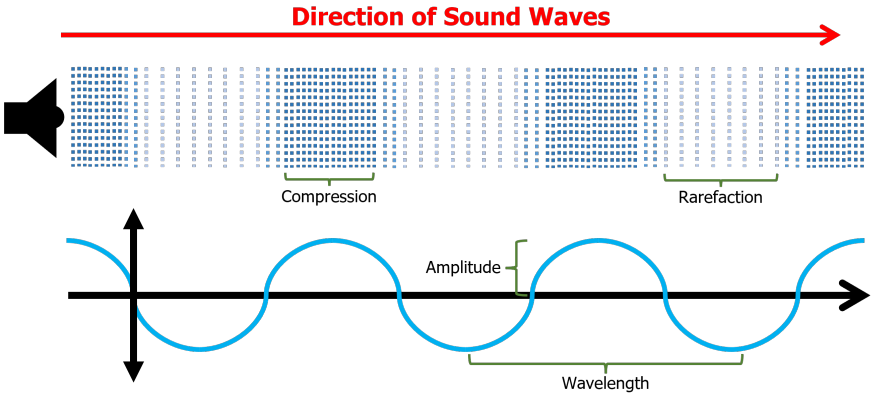

Figure 2.1: Properties of acoustic waves.

As the acoustics waves, in the form of pressure waves, travel through the propagation medium, they cause its molecules to vibrate back and forth, thus changing the local density of the medium. Regions were the local density is increased are called compressions, whereas regions with decreased density (molecules spread apart) are rarefactions. The

frequency of these compressions and rarefactions is what determines the frequency of the sound wave.

There are several aspects of sound that can be measured, for example the energy transferred by an acoustic wave can be defined as the pressure difference over a given period of time. Pressure is another important quantity as certain levels of sound pressure can cause actual pain; given the previously presented properties of sound, sound pressure is basically the amplitude of the sound wave. Sound pressure level is a quantification of the pressure variations in the air due to sound waves.

Noise is a denomination usually given to any sound that is unwanted or considered unpleasant, usually because it disrupts or interferes with communication or other activities. Noise can be generated by a wide range of sources, including industrial processes, transportation, construction, equipment, appliances, music, and people. In acoustics, noise is defined as any sound that is not related to the intended signal or source. Additional to sound properties it is also characterized by duration, and spectral content.

Both sound pressure level and noise are commonly measured in decibels (dB). The decibel is a unit of measurement that expresses the ratio between two physical values, this means it always expresses the measurement of something compared to a reference. Even though its most common uses are related to acoustics, as to express the acoustic power and the sound pressure level of sound waves, it has other uses, for example to account for the gain or loss or a signal in electronic systems. In acoustics, the usual reference level is the threshold of human hearing, which is defined as the 0 dB. As the scale of the unit is logarithmic, small values can represented a significant difference. A 3 dB is equivalent to double the sound energy, and a about 23% increase in perceived loudness, while a 10 dB increase is about 10 times the sound energy and twice as loud. Table 2.1 illustrates some everyday examples for some decibel levels. [42]

The lowest sound pressure which can be heard by humans is called the hearing threshold, whereas the highest that can be endured is known as the pain threshold. Additionally human sound perception is also limited in frequency: the average audible spectrum for human adults goes between 20 Hz to 20 kHz.

Table 2.1: Everyday examples of the decibel scale.

Reference Sound Level	**Everyday example**	**Reference Sound Level**	**Everyday example**
0 dB	Silence	90	Motorcycle
10 dB	Normal breathing	100	Lively audience at sportgame
20 dB	Leaves rusting	110	Maximum level of personal listening devices
30 dB	Whispering	120	Siren
40 dB	Average home noise	130	Jet engine
50 dB	Bird calls	140	Fireworks
60 dB	Normal conversation	150	Shotgun
70 dB	Dishwasher	160	Loud concert near speakers
80 dB	City traffic	170	Rocket launch
85 dB	Lawnmowers	180	Explosion

Continuous exposure to noise can have prejudicial effects on human health and well-being including physical disability in the way of hearing damage[42], cardiovascular and pulmonary illness and sleep disturbances. It also has been found to increase levels of stress, anxiety and depression, cognitive impairment ranging from difficulties with attention up to memory loss and several other effects. [43]. The World Health Organization recommends that average noise levels should not exceed 53 dB during the day and 45 dB at night to avoid adverse health effects.

Acoustic power refers to the rate at which sound energy is transmitted through a medium, typically air. It is a measure of the total amount of sound energy produced by a sound source per unit time. The unit of measurement for acoustic power is watt (W). It relates the sound pressure, the area over which the wave have propagated and the speed of the vibration of particles due the sound wave. It is often used to describe the sound output of a source.

Noise control encompasses all actions and strategies aimed to reduce the level of noise in a given environment or from a given source. Noise control techniques can either be centred on the source, for example making improvements to a noisy machine, applying sound insulation, or applying active noise cancellation, or centred on the receiver as when masking noise with ambient sound or personal protective equipment which indirectly reduces the noise perceived.

Sound attenuation refers to the process in which the intensity or amplitude of the sound wave is reduced as it propagates. The attenuation occurs because the kinetic energy being transferred is either absorbed, reflected, or dispersed as it travels through the medium. Several factors contribute to such attenuation:

1. The distance travelled: the longest the distance the greater the attenuation as energy is dispersed, i.e. its density is in decrease.

2. The absorption coefficient of the medium, as it represents the amount of energy that it can absorb, by converting it into other forms of energy, usually heat.

3. Reflection and diffraction: Sound waves impinging into an obstacle or a medium change can be partially reflected, or diffracted. The first phenomena correspond to the wave bouncing back and the latter to the wave being scattered in all directions.

Transmission Loss

The most common metrics to quantify the acoustic attenuation of devices, usually mufflers –as attenuation is their main function–, are insertion loss (IL), transmission loss (TL), and noise reduction (NR) [37]. TL represents the difference of acoustic energy between that reaching the device, and that emitted into an anechoic environment or termination.

In other words, it represents the capability of the measured system to attenuate sound if both the source and termination are assumed to be anechoic [44]. It has the advantage that it can be reliably measured and numerically simulated without the need of having the system connected to an acoustic source [37].

Pressure drop

Pressure drop (PD) refers to the decrease in the pressure of a fluid as it flows through a given system. Such decrease is caused by the resistance of the system to permit flow, which depends on several aspects including: the geometry of the system, the properties of the fluid, and the flow rate.

The magnitude of PD has to be measured by comparing to a reference level, which can be either ambient or another point on the flow. In general, pressure drop magnitude exhibits a direct relation to the flow rate, viscosity, and length of the system. Some other factors that could affect it are changes in temperature and the presence of obstacles.

PD is an important factor to consider in the design, operation and analysis of fluid systems, as excessive PD can lead to reduced efficiency, increased energy consumption, and other operational issues. Given its relevance it is commonly used to evaluate, study and optimize the design and operation of fluid systems.

Pressure drop coefficient

Pressure drop coefficient, also known as pressure loss coefficient or loss factor, is a dimensionless factor that characterizes the PD through a specific element or component in a fluid system, such as a valve, pipe, or fitting. It is expressed as the ratio of the pressure loss across the component to the dynamic head of the fluid. The pressure drop coefficient is an important parameter in fluid flow analysis, commonly used to predict the PD across various components in a fluid system. It is often used to evaluate the efficiency and performance of pumps, valves, and other fluid system components.

Scattering Matrix

In acoustics, the scattering matrix is a mathematical tool used to describe the scattering of sound waves in a system. The scattering matrix relates the incident and scattered sound waves in terms of their amplitude and phase. The scattering matrix is typically represented as a square matrix with elements that describe the amplitude and phase shift of the scattered wave relative to the incident waves for each possible scattering event. The number of rows and columns in the matrix correspond to the number of incident and scattered waves, respectively.

Within acoustic characterization, the scattering matrix is often used to calculate the acoustic scattering properties of objects, this is, the reflection and transmission coefficients. These properties are important for predicting the behaviour of sound waves in complex acoustic environments; nowadays such predictions are made by using the scattering matrix alongside numerical methods or simulation tools.

Transfer Matrix

The transfer matrix is a mathematical formulation used to relate inlet and outlet acoustic pressure and velocity (or volume velocity or mass velocity), as seen in the equation below. It contains exactly the same information as the scattering matrix, but with these magnitudes in the state vectors instead of pressure components. [44]

2.2 Background

Moving into more specific topics of the thesis, first a brief introduction to automotive acoustics centred in the exhaust noise source is presented, and then complementary general information on after-treatment systems, with special attention to those studied in this research, is provided.

2.2.1 Automotive Acoustics

Alongside pollutant emissions and dependence on fossil fuels, probably the third major issue of internal combustion engines (ICE) is that of noise emission. The extended use of vehicles, specially in urban areas,

has given rise to awareness of the impact of vehicle noise on public health. For that reason, many countries have started enforcing specific regulations to establish noise limits for different types of vehicles and environments (countryside or urban, day or night) and requiring manufacturers to develop vehicles that meet those standards.

Noise emissions from vehicles are directly linked to their operation; as vehicles are very complex systems the overall noise emission comes from several sources, including the engine, the interactions of component of the vehicle body with the surroundings, and ancillary systems like the air conditioning. Engine related noise is the major source, and regarding it in detail two physical mechanisms of transmission and two noise sources can be identified. The mechanisms are the vibration of components, called structure-borne sound transmission, and air-borne sound transmission. On the other hand, the two noise sources are the engine block, and the intake and exhaust systems. Fig. 2.2 illustrates hot these noise sources and transmission mechanisms relate.

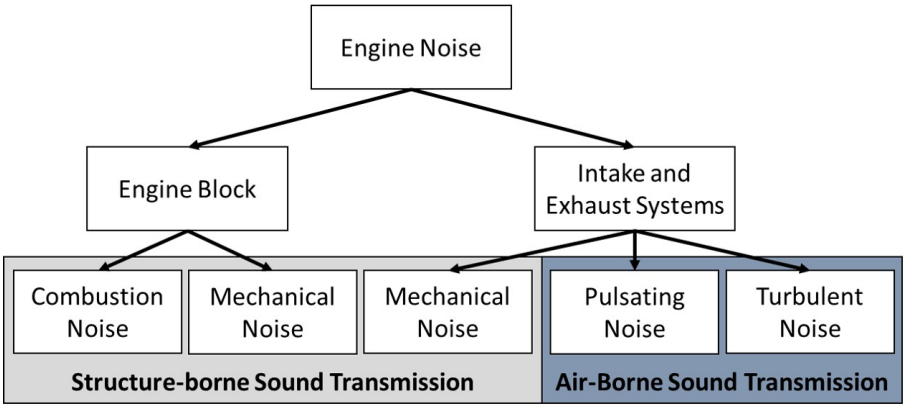

Figure 2.2: Engine noise transmission map. Took from [45]

To reduce the noise generated, solutions and palliative strategies implemented by manufacturers range from traditional ones as the use sound insulation materials and the inclusion of silencing systems (mufflers) in the exhaust line, to design considerations as improving the aerodynamics and system operation by including acoustic criteria to

the design process, and some top notch vehicles are even equipped with active noise-cancelling technologies that use microphones and speakers to cancel out unwanted noise.

Exhaust Noise

Back in Chapter 1, Fig. 1.3 already presented a scheme of a typical engine, with the intake and exhaust system indicating also the noise emissions. As this research is devoted to exhaust ATS, this noise source is presented with some more detail. Fig. 2.3 portrays a schematic representation of exhaust noise source and emission. It is to mention that even if intake and exhaust system are similar in nature as noise sources for being ancillary systems to the engine itself, and share the contributions of mechanical, pulsating and turbulent noise, the exhaust is considerably noisier than the intake.

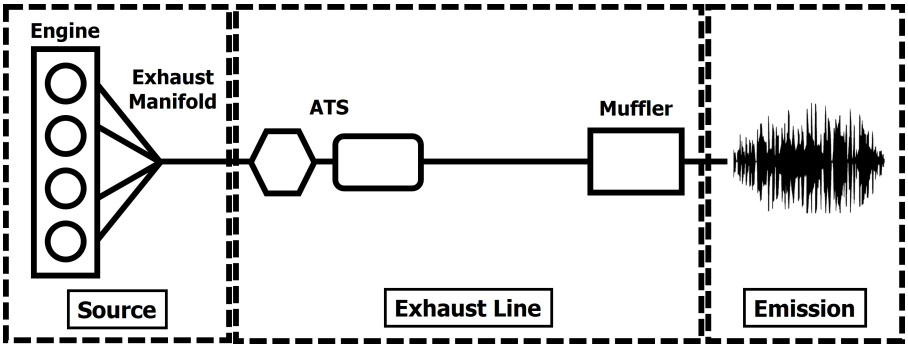

Figure 2.3: Sources of exhaust noise emission. Adapted from [45]

Even though the exhaust line is regarded as the integral noise source, the noise originates in the rapid discharge of hot gases as they exit the engine through the exhaust valves and pass through the exhaust system. Such discharge creates pressure waves that travel along the exhaust pipes and eventually are emitted at the tailpipe open end as sound waves.

The level of exhaust noise emitted depends on the type of engine, particularly on its power output, but also to an important extent on

the design of the exhaust system in terms of geometry and silencing elements (if any). Due to regulations, the baseline noise from a commercial vehicle should fall within the acceptable levels of its year of production, and therefore sudden or excessive exhaust noise might indicate problems with either the engine or the elements of the exhaust line, such as leaks or damaged components.

2.2.2 After-treatment Systems

After-treatment systems comprise a wide variety of technological applications designed to reduce in-situ, by direct (trapping and catalysing) or indirect (gas recirculation of EGR) the pollutant emissions that would otherwise be directly discharged into the atmosphere. Different after-treatment systems are able to abate different pollutant emissions to levels admitted by policies; the main pollutants are of course the main ones to be reduced: nitrogen oxides (NOx), particulate matter (PM), unburnt hydrocarbons (HC), and carbon monoxide (CO). Even thought it is not their main purpose, these systems usually have non-negligible contributions to both back-pressure and sound attenuation.

The most common ATS are:

- Catalytic converters (CC) consist of a substrate in the form of extruded ceramic monoliths, usually with a honeycomb structure of square channels open at both ends, through which the fluid passes (flow-through construction), that have a washcoat with certain catalytic material which reacts with the exhaust flow to convert harmful pollutants into less harmful substances, such as nitrogen, water vapour, and carbon dioxide. Three-way catalyst (TWC) is the standard application for gasoline engines, whereas the Diesel oxidation catalyst is the equivalent for diesel engines.

- Particulate filters (PF), also called particulate traps, including gasoline PF (GPF) and diesel PF (DPF), consist also of an extruded substrate but in this case neighbouring channels are closed (plugged) on opposite ends, what forces the flow path through the walls of the channels (wall-flow construction); these are designed to trap and remove particulate matter from the exhaust flow.

- Selective catalytic reduction (SCR) systems, are more advanced ATS that have monoliths but also incorporate a reductant chemical, externally supplied by an injector placed upstream, to convert NOx into nitrogen and water vapour. There are both WF and FT versions of this technology, SCRf the WF version and slow SCR the FT one.

- Lean NOx traps (LNTs) which are quite similar in operation to SCR systems, but they use a chemical process in the catalyst to trap NOx during lean-burn operation, and then release it during rich-burn operation when the catalyst is regenerated.

- Exhaust gas recirculation (EGR) systems, which is different in the sense that no monolitha are used and the action is indirect: it is a by-pass with a throttle that redirects part of the exhaust flow to recirculate back into the intake, reducing the amount of oxygen available for combustion and thus reducing the formation of NOx.

A brief summary on the most important milestones of historical apparition of these devices, motivated by increasingly stricter emissions, is given in the following:

1970s: The CC was the first ATS to be introduced; its implementation started in response to the Clean Air Act of 1970, which mandated a reduction in emissions from vehicles. Its introduction revolutionized the way automotive exhaust emissions were controlled, though it suffered from several problems such as breakage and thermal shock, and no know-how to solve them; however, research and development helped mature the technology leaving behind those problems. The addition and advances on fuel injection also improved the efficiency of catalytic converters.

1980s: The rising trend of electronic engine management systems became more widespread, allowing for more precise control of fuel injection and ignition timing. This in turn led to better combustion and reduced emissions. In this decade, the TWC appeared improving previous CC, which were only effective at reducing one or two types of pollutants.

1990s: The introduction of on-board diagnostic (OBD) systems allowed for the monitoring of emissions-related components and the detection of malfunctions. In this decade, DOC made their first appearence, with notable effects on the reduction of HC and CO.

2000s: DPFs became a standard ATS to handle particulate matter emission from diesel engines. In parallel, advances in fuel injection systems and exhaust gas recirculation (EGR) helped to reduce NOx emissions from diesel engines. Alongside PF implementation, the use of ATS with several monolithic ATDs became frequent, a tendency that has remained since then.

2010s: Selective catalytic reduction (SCR) systems were introduced to further reduce NOx emissions from diesel engines. In parallel, lean NOx traps (LNTs) were developed to reduce NOx emissions from gasoline engines. Then at mid to late 2010's the GPF started to be implemented. Over the end of the decade a new technology, ammonia slip catalysts (ASCs), was developed to reduce emissions of ammonia, which are in part a side effect of SCR systems.

Latest: The development of ATS technologies, mainly the most recent ones like GPFs, LNTs and ASCs, continues as well as their use in new vehicles, even though ATS requirements of the increasingly widespread hybrid vehicles are much reduced.

Overall, the presence of devices has evolved from individual applications into very complex arrangements implementing more than one technology and electronic controls. These implementations have been sufficient to comply regulations so far, but have also added significant cost and complexity to vehicle design, not to mention that depending on the technology their maintenance and replacement can also be relatively frequent or costly.

Monoliths after-treatment systems

A little further detail is to be presented in FT and WF monoliths.

Flow-through monolith are catalytic converter designs that use a honeycomb-shaped ceramic or metal structure with a large number of small channels or passages to enable exhaust gases to pass through.

The walls of the channels are coated with a thin layer of catalyst material, such as platinum, palladium, or rhodium, which reacts with and reduces the harmful emissions present in the exhaust gas. The channels are designed to create a large surface area for the catalyst to interact with the exhaust gases, which increases the conversion efficiency of the catalytic converter. Flow-through monoliths are commonly used in automotive exhaust systems, as they are compact and lightweight, and can be easily integrated into the exhaust system of a vehicle. These catalytic converters are also relatively low-cost to produce and have been effective in reducing the emissions of harmful pollutants from vehicles.

The current state of diesel engine technology and the prominence of the gasoline direct injection (GDI) technology over other spark-ignited engine technologies have made that particulate matter (PM) has become a major issue in all automotive applications. The use of wall-flow particulate filters (PFs), namely Diesel particulate filters (DPF) for all Diesel vehicles and gasoline particulate filters (GPF) for GDI vehicles [46, 47, 48, 49], has become the standard and most reliable approach to abate PM emissions; both technologies usually consist of filters with honeycomb structure made of extruded porous ceramic materials as the substrate, with or without different catalytic washcoats, and with a similar cell density, through which the exhaust gases are forced to flow, trapping the PM in the process.

The complete cycle of operation of a PF, either DPF or GPF, consist of a continuous succession of loading and cleaning processes; even though specific characteristics of each process vary, the overall principles are essentially the same. Both kinds of filter are made of materials specifically designed to hold a certain quantity of PM, and during the loading process the accumulation of PM slowly creates a restriction to the flow, increasing the pressure drop across the filter, which could eventually result in clogging of the filter and have a negative impact on engine operation [50, 51, 52]. Therefore, PF systems need a cleaning process to remove trapped PM and rehabilitate their soot collection capability so that proper engine operation is guaranteed. In that process, called regeneration, the trapped soot is incinerated, and the process can occur discretely when a certain quantity of soot has been captured, or continuously over regular operation [51, 52, 53].

In the loading process, two internal phenomena occur simultaneously: soot accumulation and ash accumulation. Soot accumulation occurs over short periods, within the time scale of a few hours, and ends with the regeneration process. However, not all the trapped material is burned, as a small amount of inorganic ash is left behind each time, which in turn accumulates over much longer time scales, typically of the order of several thousand operation hours, due to the small amount contained in the soot which is in the range of 0.5% to 1.0% [54]. The accumulated ash is immune to regeneration, therefore poisoning and deteriorating the PF useful life, while also impacting fuel-economy and potentially complicating on-board control [55]. Both soot and ash accumulation increase backpressure within their own time scales, compromising and modifying efficiency, acoustics and gaseous emissions.

Two main different mechanisms of soot filtration may be distinguished during the loading process. First, particle deposition fills material pores changing the substrate microstructure. This initial mechanism is called "deep-bed" filtration [56] and causes a steep increase in pressure drop [57]. Later, as all the available space within the substrate pores is filled, particles start to agglomerate on top of the channel walls, leading to the formation of a continuous and consistent layer, which is called soot cake, and accordingly the mechanism is known as "soot cake" filtration; this is accompanied by a modest pressure drop increase, when compared to the previous mechanism, and almost 100% filtration efficiency [57, 58]. Most of the soot captured resides in the soot cake layers [59, 60]. The much slower and regeneration-immune ash particles that are trapped can be found in one or both of the following forms: as an ash layer on top of the filter walls or as a more compact plug at the closed end of the channels. A simplified representations of the different ash and soot formation processes described can be seen in Fig. 2.4. As a complement, Fig. 2.5 shows further detail on the stages of soot cake formation.

Once accumulation during the loading process has reached a certain level, the regeneration process takes place, and trapped soot particles are oxidized either by O_2 or NO_2 for sufficiently high temperatures, producing a variety of gaseous products, being CO_2 that most abundant. If all the required conditions are fulfilled naturally during operation, either continuously as in GPF, or discretely as in some DPF, the process

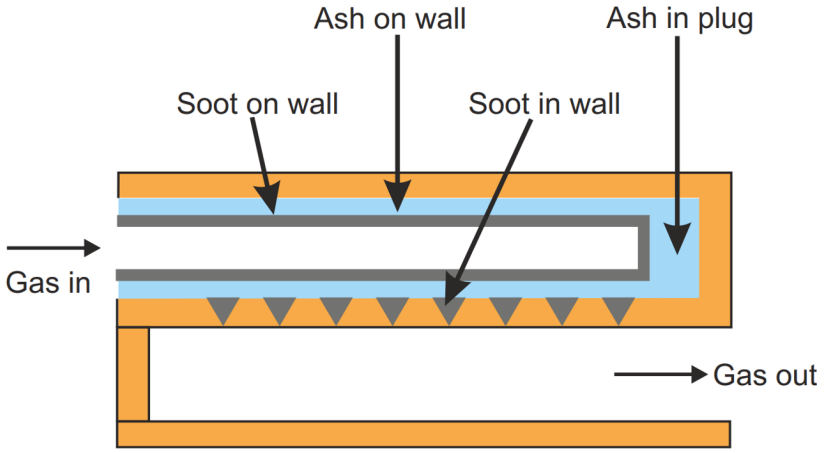

Figure 2.4: Simplified representation of soot and ash deposition in a wall-flow particulate filter.

is called Passive Regeneration; on the contrary, if additional auxiliary systems are used to promote the regeneration it is called Active Regeneration [50, 61], this latter also entailing around 2%-3% extra fuel consumption penalty, whereas passive regeneration strategies can drop this penalty by about 80% [62]. A proper performance of the regeneration mechanism sustains a stable cycle of soot capture and oxidation in the filter [63, 61]. Several operation conditions determine filter regeneration performance, temperature being the most important [64], followed by the soot load in the filter.

As there are similarities between DPFs and GPFs, there are also differences, both in engine operation and in the filter devices themselves. For instance, Diesel engines run on excess of oxygen, whereas gasoline engines run with closer to stoichiometric mixtures, thus changing the availability of air in the exhaust, which in turns facilitates or complicates the conditions for regeneration. The higher temperatures allow for frequent, almost continuous regeneration in GDI engines, whereas in diesel engines additional adjustments are needed, either increasing exhaust gas temperature or lowering the soot ignition temperature via the inclusion of a catalyst. Thermal passive regeneration is undoubtedly the cleanest and most attractive method for regenerating DPFs [50, 63].

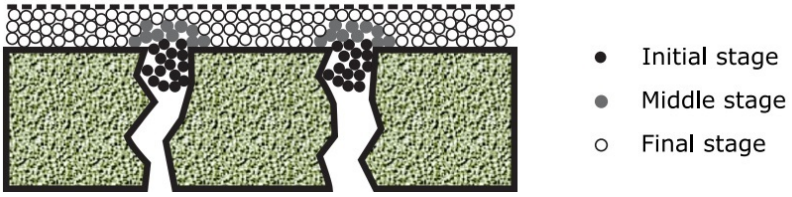

Figure 2.5: Schematic representation of the stages in cake-layer formation.

2.3 Historical Evolution of Studies in Atfertreatment Systems

The presence of after-treatment systems and the dissipative effects imposed by them, modify the boundary conditions for muffler desing, which usually leads to a substantial reduction in volume or even its elimination [65]. For this reason, the determination of the acoustic effects of the ATS is essential to guarantee the correct design of this element [66]. Experimental measurements and acoustic modelling tools are of fundamental help for this task, covering a broad spectrum of solution approaches. Currently, among computational tools one can find those based on linear and non-linear methods, with different levels of spatial resolution, from the most complex and computationally expensive, with a 3D approach [67], to simple models based on phenomenological solutions [39], going through those with an intermediate complexity such as quasi-3D cells models [68] and 1D/2D models [31]. There is also variety in the numerical schemes used, comprising models that use finite element methods (FEM) [25] for the analysis of wave propagation along monolith channels, and boundary element methods (BEM) to account for 3D effects in the inlet and outlet canning volumes [66]. Otherwise, PF modelling requires specific tools capable of predicting its operation under different unsteady flow conditions and with different PM loading.

In the literature, there is a wide variety of experimental techniques that can be use to measure the acoustic behaviour of after-treatment systems [69]. These techniques range from those with external sound level meters [70] to techniques using multiple sensors in the ducts [71],

typically condenser (pressure) microphones. In this last approach, it is possible to find methods with different degrees of complexity, from those that use two sensors located at the inlet and outlet of the element to be analysed [72], to those that use multiple sensors at the inlet and outlet and allow systems to be characterized with greater complexity, both at the structural level and regarding flow conditions [69].

Assessing the literature of experimental and modelling studies to characterize ATS in historical apparition the following was found:

Even though the WF PF devices have been around since the second half of the 70's, up to 2000's due to market being mostly covered by non-direct injection gasoline engines, studies in ATD were mostly focused in FT monoliths, the CC was the direct or indirect focus of researchers, yet all that literature and knowledge constitutes background for the later studies on WF monoliths, specially since most ATS combine both kind of monoliths, usually placing a WF immediately downstream of a FT which thus define the flow conditions at the inlet of the WF.

The first attempts to model unsteady flow in catalytic honeycomb structures were restricted to the linear regime and date back to the work of Glav et al. [73].

Some of these previous studies on wave dynamics, flow characteristics, PD and acoustics on PFs or ATDs with PF included are an early attempt on the acoustics in capillary tubes and the effect of superimposed flow, relatable to FT monolithic ATD by Peat et al. [74]. Another study, this one by Selamet et al was one of the first to cover a "whole" ATD, with FT monoliths, this compares circular and oval catalyst, considers inlet and outlet tapers, considers analytical and finite element approaches, and attempts to consider separation of reactive and dissipative effects by comparing results with and without monolith [75].

Up to late 2000's diesel engines were capable to meet emission standards without PF ATDs or any other special ATS through advanced engine design and in cylinder engineering, later tightening emission standards promote/force the study, development and use of NOx adsorbers and urea selective catalytic reduction for NOx emissions and DPF for PM/PN emissions. Early DPF designs lacked reliability and durability, then continued development improved their design [50]. From this point on, research interest in DPF monolith and ATDs containing PF elements started to increase in quantity and frequency. In 2004 Katari

et al studied aspects such as monolith's aspect ratio, and the effects of inlet and outlet tapers at each side, acoustic attenuation (TL) were also accounted [76]. Later in 2006 several studies approached the simulation of DPFs among other ATDs, studying the filtering efficiency and position effects (exhaust line layout) [77], loading and regeneration processes under steady state engine operating conditions, the back-pressure, its variation with soot load and its side effects on fuel consumption and emissions [78, 79].

Among the first PF models is the one presented by Allam and Abom, based on a linear 1D solution [32]. This model is the basis for the definition of the transfer matrix in other more complex linear models, based on 3D-FEM solutions that provide a better prediction of the PF response at high frequencies [80]. While all these theoretical tools are fundamental to the analysis and optimization of the acoustic response of ATS, their validity is highly dependent on the availability of reliable experimental data.

An special DPF with no washcoat and a modified substrate composition for improved thermal durability of the catalyst layer was studied in terms of soot loading and PD [81].

Starting in 2009 there is a noticeable increase in the presence of Diesel Engines in car pool market and the tightening Emission Standards shot up the use of DPFs, thus the number of studies on the topic rose accordingly. With the increasing share of diesel engines in the vehicle market, air pollution and environmental impacts such as noise began to be the subject of examination.

That year, Bensaid et al addressed the soot deposition under different operating conditions via CFD, some of the findings include correlating the flow field and velocity profiles inside the filter with the soot distribution along the axial coordinate, that the fraction of particles that impact the wall surface and are trapped by the porous media is sensitive to the particle size (most penetrating from 200 nm to 500 nm), the depth filtration and the soot cake formation (cake filtration) generates an additional PD [82].

Mukherjee et al covered the noise control effects of the DPF by the TL parameter using a code in FORTRAN-77 based on previous literature, considering the mean flow effect [83].

DPF controls and maintains around a stable PD across the filter

by repeating the regeneration process to burn accumulated PM, but after each regeneration a little incombustible ash is left behind, slowly accumulating and this eventually causes increased PD which affects the product life of the PF. Ash accumulates differently depending on the regeneration system. With passive ash accumulates uniformly on the filter wall, with active ash accumulates near the outlet of the filter, yet the amount of ash collected is the same regardless of the regeneration method, the difference in the way ash accumulates affects the PD across the filter. Ash is different in particle size depending on temperature of PM combustion during regeneration. Smaller at lower combustion temperatures (passive) and larger at higher combustion temperatures (active) [84, 85, 86].

Ishizawa et al took that starting point and studied the effect of the regeneration system on ash accumulation in the DPF taking a few DPFs as sample from a high-mileage fleet and evaluated for both PD and PM filtering performance (post-mortem analysis) Artificial Accelerated Ash loading to create various patterns of ash collection. Results let them to propose a DPF regeneration system that produces an ideal accumulation pattern of ash to keep PM filtering performance at the optimal level for useful life [87].

The loading of DPFs entails the need of regeneration, whose efficiency and frequency are affected by the way soot is deposited along the channels. Relationship between engine performance and filter loading is studied to take advantage of this during DPF design and optimization. DPF samples were loaded downstream the DOC in an ad hoc designed reactor coupled to a rig that reproduced conditions of an automotive diesel engine at a critical operating condition from the NEDC. A proposed methodology using FESEM observations enable estimation of the actual soot thickness along the channel length [88].

In parallel, complimentary studies centred on the soot itself appeared along, these include; an early characterization of soot itself in terms of composition, structure and fractal dimension, under different operating conditions from 2006 [89]. A characterization of soot morphology in terms of radii of gyration and fractal diameters via lumped parameter (LP) model considering operating conditions in 2009. This study also covered global soot production, loading and regeneration processes. The performance of the DPF during loading is evaluated

according to soot layer thickness and PD; the characteristics of soot morphology and particulate deposit during the regeneration. Results were validated by comparison to experimental measures and 3D CFD simulations [90].

In 2010, Jiang et al presented a different approach on a complete exhaust line with a built-in DPF, which was studied in terms of TL, using two parallel approaches, modelling the DPF as a block of bulk-reacting material and using the element-to-element four-pole connection between two BEM substructures. Four-pole parameters of DPF were obtained from a measurement [66].

Hicks et al approached the acoustic and performance effects of having a DPF in the ATS, the acoustic performance of the DPF changes with increasing soot density and exhaust back-pressure, the acoustic response was measured at multiple soot load densities [91].

Otzurk and Erol approached with FEM analysis the modelling of the full DPF and its acoustic performance. TL is chosen as the parameter that defines the acoustic performance, frequency-dependent sound TL was simulated under the idle condition (diesel engine) and plotted in the entire plane wave range [36].

Navratil et al. presented a 1D modelling methodology based on experimental test set up, on the Ricardo Wave software, studying IL, TL and Noise Reduction (NR) to evaluate the acoustical performance, as this are commonly used for mufflers, this was applied to a DOC (Catalyst) and a DPF and validated against TL measurements. Differences were identified, and model sensitivity-studies conducted resulting in revised modelling recommendations for DOC's and DPF's modeling. This resulted in more accurate modelling of TL before any hardware is procured [37].

Depcik et al presented an updated model for pseudo compressible flow shows improvement in the predictions under varying PF temperature profiles when compared to dynamically incompressible flow. A computation of the PD for non-isothermal flow is done by a single algebraic equation, reducing computational costs in comparison to the previous compressible numerical approaches. [92].

Chapter 3

Materials and Methods

This chapter is devoted to present all the *Materials* or resources involved in the development of this research, namely the studied devices, the experimental installations used, and also the software and computational tools used to handle the information. Complementarily, the *Methods*, i.e. the measurement procedures, the data collection process, and the post-processing and decomposition analysis applied are also described. Each of these is accompanied by examples of application or results, in order to illustrate the core of the process and avoid subsequent repetition of steps in the following chapters.

As a disclaimer, information of the experimental installations and their usage have been featured several times as part of the Materials and Methods sections of thesis related publications listed in the publications section, as well as several other publications from the hosting research centre as all have used the same experimental installations at different stages of development, of course adapting the installation or the procedure to the specific needs of each research.

3.1 Studied Devices: Exhaust Systems

As stated in the scope, Section 1.3, this research aimed to achieve a comprehensive characterization of the fluid-dynamic and acoustic behaviour that different after-treatment and auxiliary devices induce in exhaust lines; therefore it is required to address several kinds and combinations of such devices. For this end, the research started with a

unique device labelled ATD0 which was already in the research centre from a previously developed project. Afterwards, the collaboration with an OEM granted access to a complete exhaust line which integrates an ATS consisting of three devices, two with monoliths and the other one comprising auxiliary elements, and also other six individual ATDs with different configurations and characteristics representative of ATS in current commercial use. These were classified into groups in order to assess them in order of increasing complexity as advanced in Section 1.4.

- **Initial Validation**
  - *ATD*0*:* DOC-DPF Small device with bent pipes.
- **Simple Geometry Category**
  - *ATS*1*:* Complete exhaust line with SCR technology.
    - *ATS*1*-A:* Auxiliary package including DEF Injection port and static swirl mixer.
    - *ATS*1*-D*1*:* Double SCR device.
    - *ATS*1*-D*2*:* Single SCR device.
- **Intermediate Geometry Category**
  - *ATD*1*:* Compact packed TWC-GPFc device.
  - *ATD*2*:* Compact packed Double TWC device.
  - *ATD*3*:* Fuel-Nozzle shaped Double TWC device.
  - *ATD*4*:* Straight disposition DOC-DPF device.
- **Complex Geometry Category**
  - *ATD*5*:* SCR SCR-CUC Underfloor device.
  - *ATD*6*:* DOC SCRf SCR-CUC Close Coupled device.

3.1.1 Devices in detail

Detailed descriptions, pictures, and tables with relevant monolith information are presented for each device. Detailed CAD files were also available for all of them, whose processing is explained in Section 3.3.3.

ATD0: DOC-DPF Small device with bent pipes

This ATD designed for a Diesel powered vehicle consists of a DOC and a DPF contained in a unique canning, as shown in Fig. 3.1. It has a relatively long and curved inlet pipe section which connects eccentrically with the canning, while the outlet side has a slightly rounded lid with a short and straight outlet pipe section also projected eccentrically. The main characteristics of its monoliths are summarized in Table 3.1.

Figure 3.1: DOC-DPF Small bent pipes device.

Table 3.1: Characteristics of ATD0 monoliths. (*) marked values are estimated or assumed.

Characteristic	DOC Monolith	DPF Monolith
Length [mm]	85	105
Diameter [mm]	170	170
Monolith volume [l]	1.605	1.965
Cell size* [mm]	1.27	1.795
Channel size* [mm]	1.16	1.39
Wall thickness [μm]	110	405
Cell density [cpsi]	400	200
Number of channels* [#]	14540	7270
Porosity* [%]	-	50
Catalytic area [m^2]	5.54	-
Filtration area [m^2]	-	2.215

ATS1: Complete Exhaust Line

This ATS prototype corresponds to a complete Selective Catalytic Reduction (SCR) system to be used in diesel engines to handle nitrogen oxide (NO_x) emissions. It has three identical SCR FT monoliths whose main characteristics are given in 3.2, the first two in the downstream direction share canning with a small empty gap between them, and the third one has its own canning. As SCR requires the injection of DEF, upstream of the first canning there is a lateral side chamber with a DEF injection port followed by a static swirl mixer inducer and a mixing pipe section in order to guarantee a uniform distribution of the injected fluid stream.

Figure 3.2: Complete exhaust line as received from OEM.

The ATS was classified in the "simple geometry category" due to its overall configuration, being the devices practically straightly aligned, and the fact that the two cans are almost ideal/theoretical expansion chambers with tapered elements in both the inlet and the outlet side. This ATS offered the opportunity to perform a split and rejoin assessment, therefore allowing to assess the eventual additivity of their effects and any other potential interaction between the ATDs. With that purpose, each device was characterized individually and then recombined with the others; this corresponds to the second step of the research and details are presented in Chapter 5. Further detail on each device is given in the following paragraphs.

Table 3.2: Characteristics of ATS1 SCR monoliths. (*) marked values are estimated.

Characteristic	SCR Monolith
Length [mm]	136
Diameter [mm]	144
Volume [l]	1.34
Cell size* [mm]	1.037
Channel size* [mm]	0.95
Wall thickness [μm]	87
Cell density [cpsi]	600
Number of channels* [#]	15100
Catalytic area [m^2]	6.615

ATS1-A: Auxiliary elements

The section containing the DEF Injection port, the static swirl mixer and half of the mixing pipe was split and considered as a device. Fig. 3.3 shows it when mounted with its adapters into one of the experimental facilities during its individual characterization. This section of ATS1 was labelled ATS1-A and it was considered of special interest as the fluid dynamic and, more importantly, the acoustic effects of the presence of a static swirl mixer are usually neglected in ATS studies. Filling such a gap in knowledge was another of the purposes of Chapter 5, and also the main topic assessed in the related paper [1].

Figure 3.3: ATS1-A and its adapters.

ATS1-D1: Double SCR Device

This ATD has the downstream half of the mixing pipe as inlet section, the canning that contains the first two SCR monoliths of the system with a small gap in between, tapered elements at both sides and a short outlet pipe section. In general terms, it is almost identical to ATS1-D2, but longer and with a second monolith; this similarity allowed to assess the differences due to the presence of the second monolith and the empty gap.

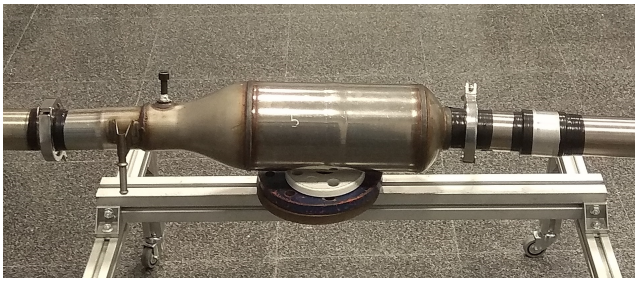

Figure 3.4: ATS1-D1 and its adapters.

ATS1-D2: Single SCR Device

This ATD includes short inlet and outlet pipe sections, and the canning that contains the third SCR monolith with tapered elements at both sides. This geometrical configuration almost matches that of an ideal expansion chamber, which opens the possibility to account precisely for the effects induced by the monolith.

Figure 3.5: ATS1-D2 as split.

ATD1: Compact packed TWC-GPFc device

This device for gasoline engines was designed to meet Euro 6d-Temp regulation, and includes two monoliths, a FT TWC followed by a WF catalyst-coated gasoline particulate filter (GPFc); details on the monoliths are presented in Table 3.3. As shown in Fig. 3.6, the inlet and outlet sections are both eccentrical, of irregular shape and connected to open volumes before and after the monoliths, respectively. This device was classified into the "intermediate geometry" group and assessed exhaustively as a knowledge gap was identified about the changes occurring during the first few load-regeneration cycles; this analysis is presented in Chapter 6 and in the related paper [2].

Figure 3.6: Compact packed TWC-GPFc device.

Table 3.3: Characteristics of ATD1 monoliths. (*) marked values are estimated or assumed.

Characteristic	TWC Monolith	GPF Monolith
Length [mm]	45	120
Diameter [mm]	120	120
Monolith volume [l]	0.331	1.133
Cell size* [mm]	1.037	1.467
Channel size* [mm]	0.948	1.265
Wall thickness [μm]	89	205
Cell density [cpsi]	600	150 (open) 300 (total)
Number of channels* [#]	10240	2560 (open) 5120 (total)
Porosity* [%]	-	50
Catalytic area [m^2]	1.564	-
Filtration area [m^2]	-	1.528

ATD2: Compact packed Double TWC device

Figure 3.7: Compact packed Double TWC device.

This device was designed for gasoline engines to meet Euro 6b emission standard and it has two FT TWC monoliths, whose characteristics are presented in Table 3.4. As shown in Fig. 3.7, the inlet and outlet sections are both eccentric, with circular cross-section, bent and connected to open volumes upstream and downstream of the monoliths. This device was classified into the "intermediate geometry" group. As this device has a similar shape and size as ATD1 but with both monoliths of the FT kind, comparison of their respective results allowed for the analysis of the differences related to presence of the WF monolith. This device was also cycled to check for any relevant differences in the first few hours of use but no significant effect was found.

Table 3.4: Characteristics of ATD2 monoliths. (*) marked values are estimated.

Characteristic	TWC Monolith	TWC Monolith
Length [mm]	50	90
Diameter [mm]	120	120
Monolith volume [l]	0.36	0.65
Cell size* [mm]	1.037	1.037
Channel size* [mm]	0.972	0.927
Wall thickness [μm]	65	110
Cell density [cpsi]	600	600
Number of channels* [#]	10240	10240
Catalytic area [m^2]	1.646	3.119

ATD3: Fuel-Nozzle shaped Double TWC device

Figure 3.8: Fuel-Nozzle shaped Double TWC device

The device shown in Fig. 3.8 was designed for gasoline engines. It has two TWC monoliths of different volumes, but these are not placed in a unique canning; instead, an irregular volume connects them. Specific characteristics of the monoliths are shown in Table 3.5. The inlet and outlet pipes are both straight and round, but the tapered elements are irregular: the one in the inlet side resembles a cone but it is also bent, whereas the one in the outlet is a eccentric toricone with knuckles at both ends. It was classified in the "intermediate geometry" group.

Table 3.5: Characteristics of ATD3 monoliths. (*) marked values are estimated.

Characteristic	TWC Monolith	TWC Monolith
Length [mm]	60	88
Diameter [mm]	95	132.5
Monolith volume [l]	0.249747	0.748269
Cell size* [mm]	1.037	1.270
Channel size* [mm]	0.927	1.105
Wall thickness [μm]	110	165
Cell density [cpsi]	600	400
Number of channels* [#]	6320	8500
Catalytic area [m^2]	1.207	2.978

ATD4: Straight disposition DOC-DPF device

Figure 3.9: Straight disposition DOC-DPF device.

The device shown in Fig. 3.9 is an ATD for diesel vehicles, with two monoliths: a DOC and a DPF sharing the same canning. Their information is presented in Table. 3.6. The expansion elements at both ends are rounded, the inlet pipe section is a flexible element that connects to the inlet expansion volume with an angle, and the outlet pipe section has a slight curvature. It was classified in the "intermediate geometry" group.

Table 3.6: Characteristics of ATD4 monoliths. (*) marked values are estimated or assumed.

Characteristic	DOC Monolith	DPF Monolith
Length [mm]	135	165
Diameter [mm]	145	145
Monolith volume [l]	1.537	2.185
Cell size* [mm]	1.27	1.358
Channel size* [mm]	1.16	1.078
Wall thickness [μm]	110	280
Cell density [cpsi]	400	350
Number of channels* [#]	10070	8810
Porosity [%]	-	50
Catalytic area [m^2]	5.789	-
Filtration area [m^2]	-	3.135

ATD5: SCR SCR-CUC Underfloor device

Figure 3.10: SCR SCR-CUC Underfloor device.

The ATD shown in Fig. 3.10 is a SCR system. In the inlet side, it has a flexible section and a rigid pipe section, then an expansion leads to a volume where a mixer, an injection port and some sensor ports are located. In this case, the mixer is a perforated tunnel type, whose CAD representation can be seen in Fig. 3.11. Downstream, two SCR monoliths, of which the second one is a SCR-CUC, are placed in a single canning with a separator between them (see the CAD representation in Fig. 3.12); details of both monoliths are shown in Table 3.7. Then, the outlet side has a concentric tapered element followed by a straight round pipe section with some additional sensor ports. This ATD was classified in the "complex geometry" group.

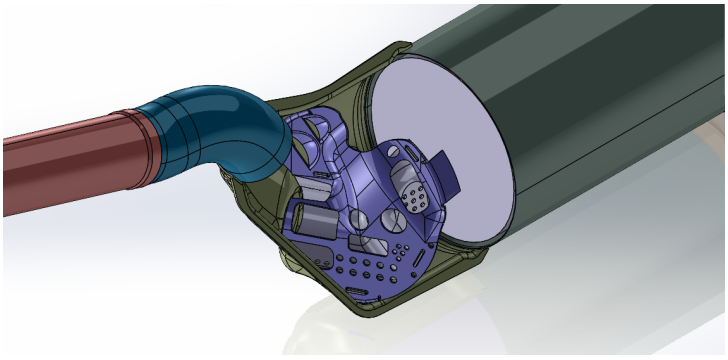

Figure 3.11: CAD file view of the mixer in ATD5.

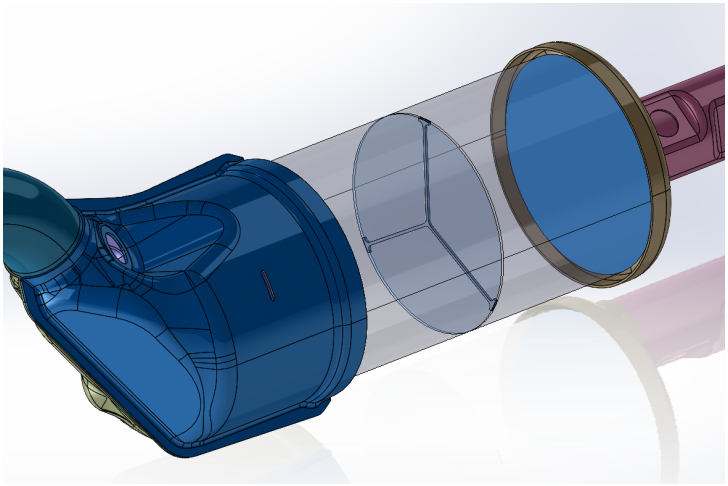

Figure 3.12: CAD file view of the monolith separator in ATD5.

Table 3.7: Characteristics of ATD5 monoliths. (*) marked values are estimated.

Characteristic	SCR Monolith	SCR-CUC Monolith
Length [mm]	120	120
Diameter [mm]	145	145
Monolith volume [l]	1.305	1.135
Cell size* [mm]	1.27	1.27
Channel size* [mm]	1.16	1.16
Wall thickness [μm]	110	110
Washcoat layer thickness [μm]	65	100
Cell density [cpsi]	400	400
Number of channels* [#]	10070	10070
Catalytic area [m^2]	5.065	4.725

ATD6: DOC SCRf SCR-CUC Close Coupled device

Figure 3.13: DOC SCRf SCR-CUC Close Coupled device.

The ATD shown in Fig. 3.13 is a combination of a DOC and a SCR system. As the ATD has several layers of thermal protection and additional elements an auxiliary CAD view is shown in Fig. 3.14. The ATD consists of two close-coupled cannings: the one in the inlet side is smaller and contains a DOC monolith; the union between cannings has a DEF injection port and a perforated plate mixer, shown in Fig. 3.15; the canning downstream is bigger and contains two SCR coated elements, the first is a filtering element, SCRf or SCR coated DPF, and the second is a SCR-CUC. Detailed information on the monoliths is presented in Table 3.8. Downstream of the monoliths there is a contraction volume with two outlets, and thus for characterization purposes the larger one was closed with a purpose-made lid keeping only the curved pipe section outlet. This ATD was classified in the “complex geometry” group.

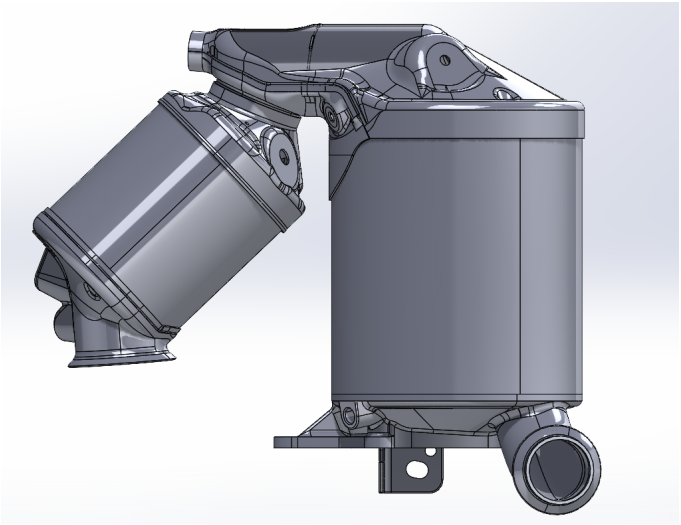

Figure 3.14: Auxiliary CAD file view of ATD6 without thermal protection or fixating elements.

Table 3.8: Characteristics of ATD6 monoliths. (*) marked values are estimated or assumed.

Characteristic	DOC Mon.	SCRf Mon.	SCR-CUC Mon.
Length [mm]	120	105	70
Diameter [mm]	145	173	173
Monolith volume [l]	1.181	1.515	1.338
Cell size* [mm]	1.27	1.358	1.27
Channel size* [mm]	1.16	1.078	1.16
Wall thickness [μm]	110	280	110
Cell density [cpsi]	400	350	400
Number of channels* [#]	10070	8810	10070
Porosity [%]	-	50	-
Catalytic area [m^2]	4.075	-	4.609
Filtration area [m^2]	-	2.808	-

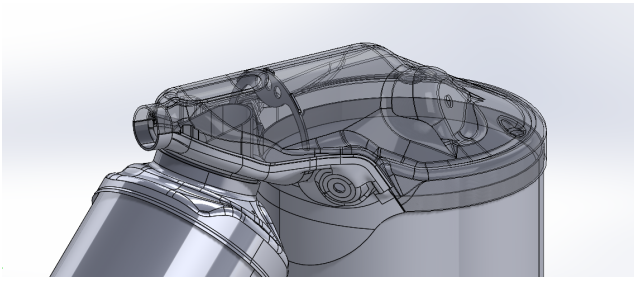

Figure 3.15: CAD file view of the mixer in ATD6.

3.1.2 Preparations required

All the devices presented required preparations in order to be characterized in the experimental facilities to be presented in the following section. As different topics are to be addressed with each device, some preparations were common and some were specific.

- **Common preparations**
  - Sensor and injector ports were sealed.
  - OEM supplied the devices with monoliths still sealed and seals had to be removed.
  - Adapters to fit each ATD to the test rigs were prepared.
- **Specific preparations**
  - ATS1 was a complete ATS instead of a single ATD and it required to be split into ATDs; each of the resulting ATDs required adapters, but specifically clamps in order to allow for their recombination.
  - As mentioned above, ATD6 had two outlets and a lid was prepared to seal the larger one.
  - ATD3 was used to check for the influence of having a sensor mounted in a sensor port, as it is an obstacle for the flow. This specific sensor port was sealed with a threaded element with the possibility to mount it as just a seal or as an obstacle.

3.2 Experimental Test Facilities and their usage

This section is focused on presenting the experimental test facilities, their functioning principles, measuring procedures and complementary details, such as specific preparations or the post-processing applied. Three main facilities were used: the cold flow test bench (CFTB) used to address the PD, the impulse test rig (ITR) to measure the TL and determine the elements of the scattering matrix, and the unsteady flow gas stand (UFGS) to obtain benchmark measurements in engine-like conditions, i.e, high temperature and pulsating flow. Also, the two approaches used to characterize the acoustic dissipation and the arrangement used to soot-load PF devices are presented, and finally a brief summary of the measurement plan is given.

3.2.1 Pressure Drop Measurement: Cold Flow Test Bench

The pressure drop characterization of all studied devices was performed in the CFTB. General information on the experimental setup itself and on the assessment procedure is presented bellow; further details of the procedure can be found in [93].

The facility includes a roots compressor that provides the required mass flow, a settling tank of large volume which suppresses any residual pulsations from the compressor and homogenizes the flow to avoid disturbances in the PD measurement. The outlet pipe section of the settling tank is flanged, which allows for interchangeable adapters and pipes of various diameters to be fitted in order to match the rig to the needs of each measurement. Aside of the device to be characterized, two straight pipe sections are also mounted for the test, one that is attached to the flanged outlet of the tank, referred to here as inlet duct since it corresponds to the inlet side of the device, and the other (the outlet duct) downstream of the device. These ducts are selected with a minimum length of ten times their respective diameter in order to guarantee fully developed flow. Each device was assembled to the inlet and outlet ducts with purpose-made adapters.

The compressor is regulated by a PID controller in which the target mass flow and the direction, either impulsion or suction, can be set; PD

measurements were made in impulsion condition. The maximum mass flow rate for most devices was in the range $800 - 850$ kg/h depending on the PD induced by the device installed. The tank is instrumented to provide the stagnation pressure and temperature of the fluid, which is necessary to compute the gas density. All the tests were performed close to room conditions.

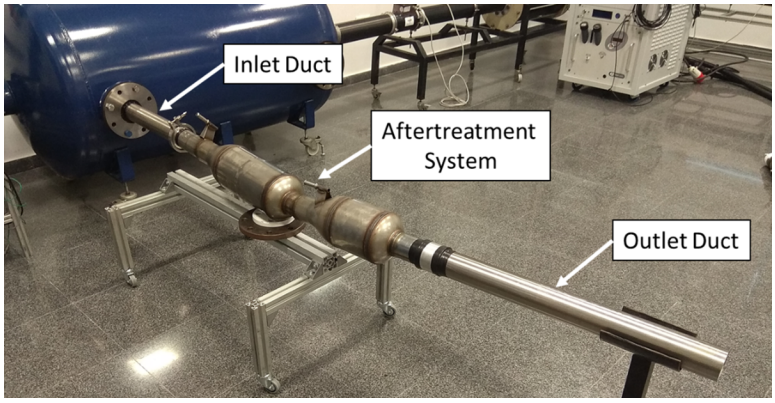

Figure 3.16: Experimental setup for the pressure drop measurement of an after-treatment device or system

The experimental setup of one of the measurements is shown in Fig. 3.16; ATS1 is being measured in this example. The difference between the stagnation pressure in the tank and the atmospheric pressure measured in the laboratory provides the stagnation PD of the assembly, which includes the PD due to the device, but also that taking place in the inlet and outlet ducts. In order to account for the PD in the inlet and outlet ducts and to estimate that of the device alone the following test procedure is applied:

1. Step 1: Do a first PD measurement with the complete assembly (ATD and ducts) in the test bench.

2. Step 2: Do a second PD measurement of the inlet duct alone.

3. Step 3: Compute the results of the previous steps to obtain an estimation of the PD to due the device alone.

A pressure drop coefficient K, also known as K factor, is used to characterize the stagnation (total) PD of the device. This coefficient correlates with the Reynolds number, Re, at the after-treatment inlet, and relates the stagnation PD with the kinetic energy ($\rho u_{in}^2/2$) of the flow. K is calculated for a given inlet duct diameter. Next how to change the K value for different inlet diameters will be explained. This is important for comparison purposes with other devices or for different packaging or coupling solutions.

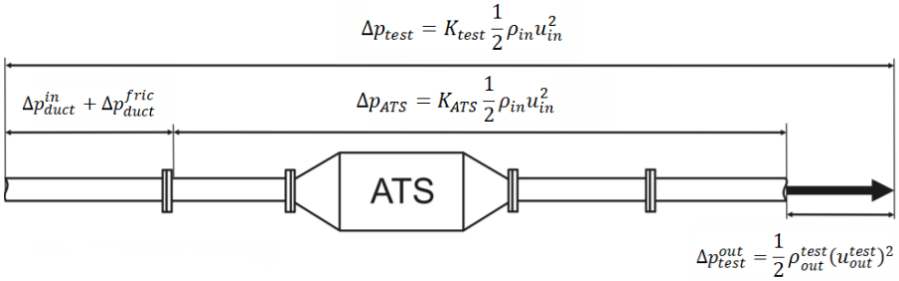

Figure 3.17: Scheme of what the configuration measures as pressure drop.

The measurement corresponding to step 1 is presented schematically in Fig. 3.17; this also corresponds to the calculated K_{test} coefficient which includes the following PD contributions:

- **Inlet duct:** Inlet PD due to the discharge from the tank and the friction at the duct itself.
- **After-treatment system:** Inertial contribution (inlet and outlet volumes and inlet and outlet monoliths) and the local friction contribution.
- **Outlet duct:** Friction PD and PD due to the discharge to the atmosphere; since the flow is fully developed, this coincides with the loss of the kinetic energy.

In the second step, the inlet duct is measured alone. In this test the K_{duct} coefficient is obtained, which accounts for the inlet PD, the local

friction contribution and the PD due to the discharge to the atmosphere, i.e. loss of the kinetic energy. Fig. 3.18 presents it schematically.

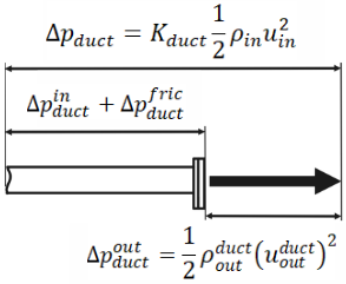

Figure 3.18: Scheme of what inlet duct measures as pressure drop.

In order to properly isolate the stagnation (total) PD caused by the ATS (Δp_{ATS}) it would be necessary to remove the contribution to the stagnation PD caused by the inlet duct, friction and inlet, and the contribution of the outlet duct. By considering the different PD contributions included in K_{test} and K_{duct} it is possible to account for the PD due to the characterized ATS almost independently, as only the PD caused by friction in the outlet duct cannot be subtracted, but this is considered negligible in comparison with the remaining contributions.

To do this calculation (Δp_{ATS}), the measured inlet duct PD (Δp_{duct}) is subtracted from the PD of the complete assembly (Δp_{test}). In order to account for the PD due to the discharge of the flow to the atmosphere it is necessary to include additional terms. On one hand, Δp_{test}^{out} is subtracted, and in this way this contribution is removed. Notice that this contribution is calculated accounting for the gas density and velocity in the inlet duct, so that any possible difference in diameter between the inlet and outlet ducts is considered in this term. On the other hand, Δp_{duct} takes into account the PD due to the flow discharge to the atmosphere when the inlet duct is tested (Δp_{duct}^{out}). Since in the test of the complete system this PD does not exist it must be subtracted to calculate the actual PD due to the characterized ATS.

Presenting this as equations, the stagnation PD across the ATS is given by

$$\Delta p_{ATS} = (\Delta p_{test} - \Delta p_{test}^{out}) - (\Delta p_{duct} - \Delta p_{duct}^{out}) \tag{3.1}$$

where the first bracket represents the stagnation PD in the whole assembly, and the second bracket the stagnation PD attributable to the ducts (except friction in the outlet duct). Reordering terms, one has

$$\Delta p_{ATS} = (\Delta p_{test} - \Delta p_{duct}) - (\Delta p_{test}^{out} - \Delta p_{duct}^{out}) \tag{3.2}$$

Now, as indicated in Figs. 3.17 and 3.18, one has

$$\Delta p_{test}^{out} = \frac{1}{2}\rho_{test}^{out}(u_{test}^{out})^2; \quad \Delta p_{duct}^{out} = \frac{1}{2}\rho_{duct}^{out}(u_{duct}^{out})^2 \tag{3.3}$$

In the case of the duct, assuming incompressible flow (constant density), and since the diameter is the same as that of the inlet (as it was the case for several of the devices characterized), one has

$$\rho_{duct}^{out} = \rho_{in} \quad \rightarrow \quad u_{duct}^{out} = u_{in} \quad \Rightarrow \quad \Delta p_{duct}^{out} = \frac{1}{2}\rho_{in}u_{in}^2 \tag{3.4}$$

In the case of the device, one assumes again incompressible flow, but in this case one needs to consider the eventual change in the diameters, so that the constancy of the mass flow now gives

$$\rho_{test}^{out} = \rho_{in} \quad \rightarrow \quad D_{out}^2 u_{test}^{out} = D_{in}^2 u_{in} \tag{3.5}$$

and the corresponding PD is

$$\Delta p_{test}^{out} = \frac{1}{2}\rho_{test}^{out}(u_{test}^{out})^2 = \frac{1}{2}\rho_{in}\left(\frac{D_{in}^4}{D_{out}^4}\right)u_{in}^2 \tag{3.6}$$

Now, just subtracting the expressions obtained

$$\begin{aligned}(\Delta p_{test}^{out} - \Delta p_{duct}^{out}) &= \frac{1}{2}\rho_{in}\left(\frac{D_{in}^4}{D_{out}^4}\right)u_{in}^2 - \frac{1}{2}\rho_{in}u_{in}^2 \\ &= \frac{1}{2}\rho_{in}u_{in}^2\left[\left(\frac{D_{in}^4}{D_{out}^4}\right) - 1\right]\end{aligned} \tag{3.7}$$

Finally, expressing the ATS stagnation PD in terms of the kinetic energy in the inlet duct

$$\Delta p_{ATS} = K_{ATS}\frac{1}{2}\rho_{in}u_{in}^2 \tag{3.8}$$

it is possible to calculate the corresponding PD coefficient K_{ATS}, as:

$$K_{ATS} = K_{test} - K_{duct} - \left(\frac{D_{in}^4}{D_{out}^4} - 1\right) \tag{3.9}$$

The key point in all this processing is ensuring that PD coefficients correspond to the same Reynolds number. As the values of the Reynolds numbers in the two tests are similar but not exactly equal, values of K_{duct} are interpolated at the Reynolds numbers at which K_{test} is available. All this development is based on the assumption that the flow is incompressible, i.e., the density is regarded as a constant, and the value used for reference was that obtained from the pressure and the temperature measured in the settling tank (this is, the stagnation density). As this density is only used to compute the incoming kinetic energy, and this last magnitude vanishes in the final result, it follows that as long as it is used consistently in the two tests the PD results will not be affected.

However, the density is also used to compute the velocity (from the mass flow and the cross-sectional area) and, jointly with the velocity, also the Reynolds number. As this is the dimensionless quantity that

allows for putting together the results from the two tests, it might be worthwhile to estimate which is the difference between the stagnation density and the actual density in the upstream duct.

For such an estimation, consider the expression of the stagnation density ρ_0 of a perfect gas (assuming compressible flow):

$$\rho_0 = \rho \left[1 + \frac{\gamma - 1}{2} M^2\right]^{\frac{1}{\gamma - 1}} \tag{3.10}$$

where γ is the ratio of specific heats and M is the Mach number. In the incompressible limit, $M^2 << 1$ and one can approximate this with the first term of the Taylor expansion:

$$\rho_0 \approx \rho \left[1 + \frac{1}{\gamma - 1} \frac{\gamma - 1}{2} M^2\right] = \rho \left[1 + \frac{1}{2} M^2\right] \tag{3.11}$$

and, considering a safe upper bound for the Mach number in these tests (say, $M = 0.25$) this gives $\rho_0 = 1.03\rho$, i.e. the density is overestimated by 3%, which seems acceptable.

The experimental information produced for each device derived from the CFTB measurements comprises:

- The $\mathrm{Re} - M$ trend between the Reynolds and the Mach numbers, in order to ensure that the measurements correspond to a fully developed turbulent and incompressible flow.
- The representation of K_{test}, K_{duct} and K_{ATS} as a function of the Reynolds number.
- The representation of Δp_{test}, Δp_{duct} and Δp_{ATS} as a function of the mass flow rate.

3.2.2 Acoustic Characterization: Impulse Test Rig

The evaluation of the acoustical performance of devices, usually mufflers which are also part of exhaust lines and are directly devoted to noise abatement, is performed using insertion loss (IL), transmission loss (TL), and noise reduction (NR) as metrics [37]. Among these metrics, TL is found to be the more convenient for the acoustic characterization intended, as it represents the inherent capability of the device to attenuate sound if both the source and termination are assumed to be anechoic, and with the additional advantages that it can be reliably computed from measurements and numerically simulated without any information about the engine [37]. In this research the TL, and the scattering matrix were calculated from the measurements of the acoustic response of the element to be characterized when excited by a controlled pulse; such measurement is performed in the Impulse Test Rig (ITR).

Facility

Figure 3.19: View of the Impulse Test Rig with no device mounted.

The ITR is prepared to perform the measurements required to calculate the TL and to determine the elements of the scattering matrix of the mounted element. For reliable results several measurements are required both with and without the element (replaced by a straight duct). The facility is also prepared to perform these measurements with and without superimposed mean flow. It is shown in Fig. 3.19, and a schematic representation and illustration of the measurement principle is depicted in Fig. 3.20. The facility is composed of several systems explained below:

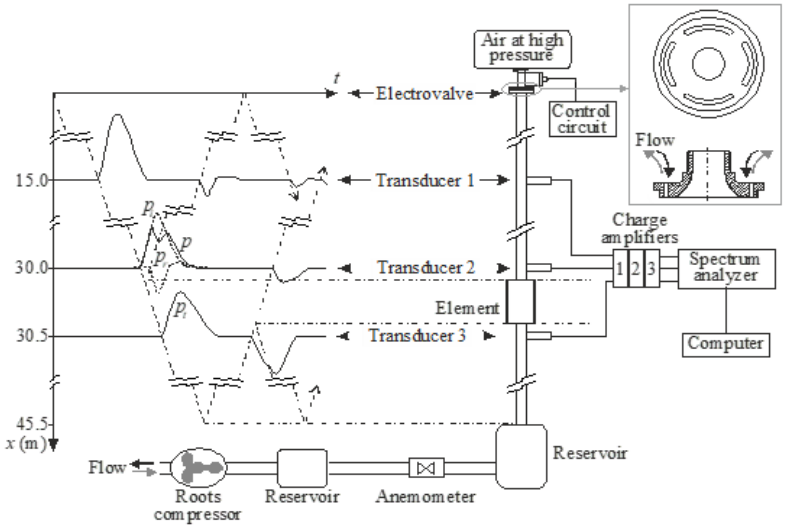

Figure 3.20: Scheme on the Impulse Test Rig operation for transmission loss measurements.

The **superimposed mean flow system**, only used when required, supplies a steady air mass flow and consists of a Roots compressor driven by an electrical motor connected to the voltage source through a frequency converter, allowing for the automatic control of the mass flow through the element studied. A 30 litre expansion chamber is located downstream of the compressor in order to reduce the pressure fluctuations generated by the blower. The stabilized mass flow is conveyed through a 110 mm diameter pipe up to a hot film anemometer, where

the mass flow rate is measured. A 200 litre volume is placed six diameters downstream of the anemometer in order to ensure stagnation conditions downstream of the flow meter; the volume outlet provides the last reflecting boundary to the pulse propagation within the ducting.

The **pulse generation system** generates the pressure pulse used to excite the element. This is done by means of a high-speed electro-valve that controls the discharge from a high-pressure tank. The amplitude of the generated pulse depends on the tank pressure, whereas the duration of the pulse can be controlled by modifying the opening time of the valve. Both are adjusted in a way such that a substantially flat spectrum is achieved, thus ensuring a proper excitation at all the frequencies of interest. The detail in the Fig. 3.20 shows the four ports drilled in the flange connecting the electro-valve to the propagation duct, which were designed considering the PD generated, which should not be excessive for the blower, and the room available for different diameters of the propagation duct. When tests are performed with superimposed mass flow there may be some limitations in the amplitude of generated pulses.

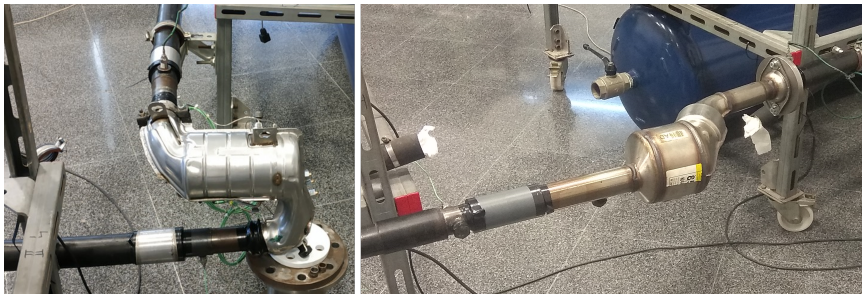

Figure 3.21: Examples of the rig with devices mounted.

The **propagation system** consists of the ducting for pulse propagation. Two pipe sections are used at a time, one upstream and one downstream of the device. The duct lengths between the valve and the first transducer and between the third transducer and the last reflecting boundary were chosen to be sufficiently long so as to guarantee the isolation of the pressure pulses in the time domain. Three pipe diameters are available at each side to make it easier to adapt to any requirement. Inlet and outlet side diameters can be different if needed, and the ele-

ments are mounted in a mobile frame structure, allowing to rearrange the positions and adapt the rig to the geometrical disposition of the inlet and outlet of any device. For instance, in Fig. 3.21 the mounting of two devices with different inlet/outlet configuration is shown.

The **measurement system** consists of the elements used in order to sense and record the instantaneous pressure at three different points distributed along the propagation system. These are Kistler 7001 piezo-electric pressure sensors mounted on Kistler 7501 adapters, and connected to Kistler 5015 charge amplifiers by means of Kistler 1631C2 connecting cable. Output is acquired with a Brüel & Kjær 3050-A-060 acquisition system controlled with the Pulse v.8 software. The acquisition is triggered by the incident pulse, and 8192 samples along a time window of 0.25 s are simultaneously recorded at the three transducers, so that the sampling frequency is 32768 Hz. The choice of this arrangement with Kistler 7001 piezoelectric transducers, which are not acceleration-compensated, is made on the basis that they have a low background noise and thus the signal-to-noise ratio is adequate for this application.

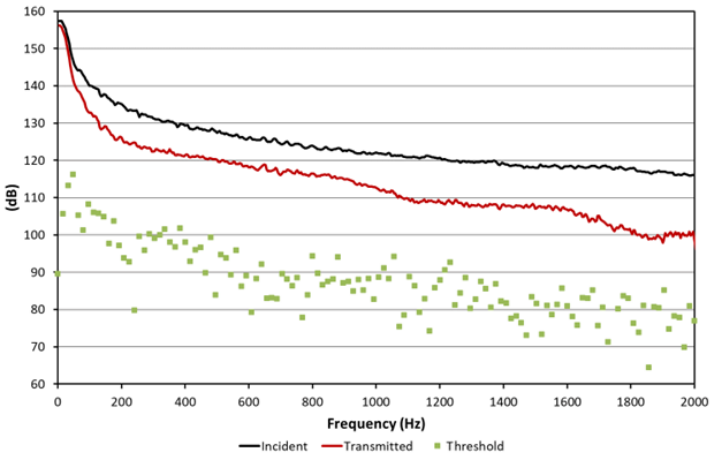

Figure 3.22: Background noise in the location where pressure is measured.

As an example, Fig. 3.22 shows the spectrum of an incident pulse,

a transmitted pulse and the background noise signal, referred to as "threshold" for a given measurements. It is apparent that the incident spectrum is essentially flat and smooth, as it should be, and that the spectrum of the transmitted wave is well below that of the incident wave. On the other hand, it can be observed that the background noise is certainly low, in general more than 20 dB below the transmitted signal.

Processing of signals

In order to explain the processing of the registered signals to obtain the TL and the scattering matrix elements, further detail on the location and what each transducer measures, following the nomenclature presented in Fig. 3.20, is given below:

- Transducer 1, midway between the electro-valve and the ATS.
  - With and without the device registers the generated pulse (p_{gen}).
- Transducer 2, just upstream of the ATS.
  - With the device registers the superposition of incident and reflected pulse, denoted as the composed pulse (p_{comp}).
  - Without the device registers the incident pulse, (p_{inc}).
- Transducer 3, right downstream of the ATS.
  - With the device registers the transmitted pulse (p_{tran}).

Then the isolated pulse reflected by the ATD (p_{ref}) is estimated following the procedure described in [94]:

1. The ATS is tested with multiple generated pressure pulses with the same amplitude and duration (repeatability within a prescribed uncertainty below 5%). These tests provide the profiles of the generated pressure pulse (transducer 1), the superposition of the incident and reflected pulses (transducer 2) and the transmitted pressure pulse (transducer 3).

2. The ATS is replaced with a straight duct and the test is repeated using generated pressure pulses similar to those used in step 1. In this way, the pressure pulse recorded in transducer 2 is similar to the incident pulse that excites the ATS in step 1. These tests provide the profiles of the generated and incident pressure pulses.

3. The best matching pair of step 1 and step 2 tests are identified based on the comparison of the generated pressure pulses recorded by transducer 1, using the statistical procedure described in [39].

4. Once the matching tests are selected, the incident pressure pulse in the ATS test (step 1) is considered equal to that measured by transducer 2 in the straight duct test (step 2). This incident pressure pulse is combined with the measurement of transducer 2 in the ATS test to determine the reflected pressure pulse applying Equation (3.12) [95],

$$\left(\frac{p_{ref}}{p_0}\right)^{\xi} = \left(\frac{p_{comp}}{p_0}\right)^{\xi} - \left(\frac{p_{inc}}{p_0}\right)^{\xi} + 1, \tag{3.12}$$

where $\xi = ((\gamma - 1))/((2\gamma))$, γ is the ratio of specific heats and p_0 represents the pressure of the unperturbed medium.

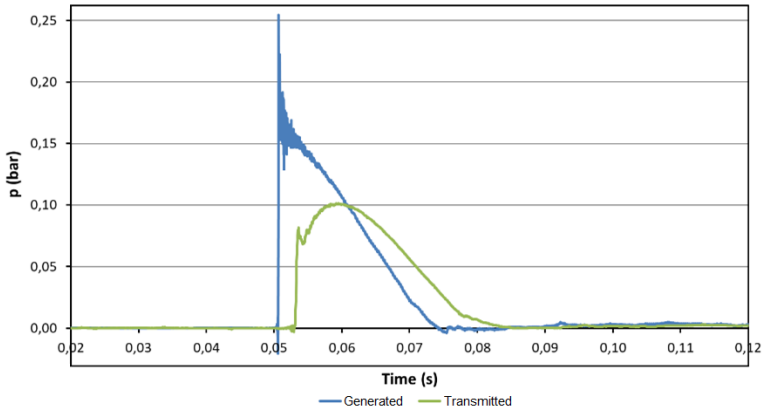

Figure 3.23: Example of generated and transmitted pulses in the time domain, from a step 1 measurement.

Fig. 3.23 shows an example of the recorded generated and transmitted pulses from transducers 1 and 3 in the time domain as in step 1. It is apparent that the registered pulses are directly isolated without the need for any additional windowing or any other processing. Then Fig. 3.24 shows an example of incident pulse, the superimposed incident and reflected pulses as from transducer 2 in step 1, and the resulting estimation of reflected pulse from the application of Equation 3.12.

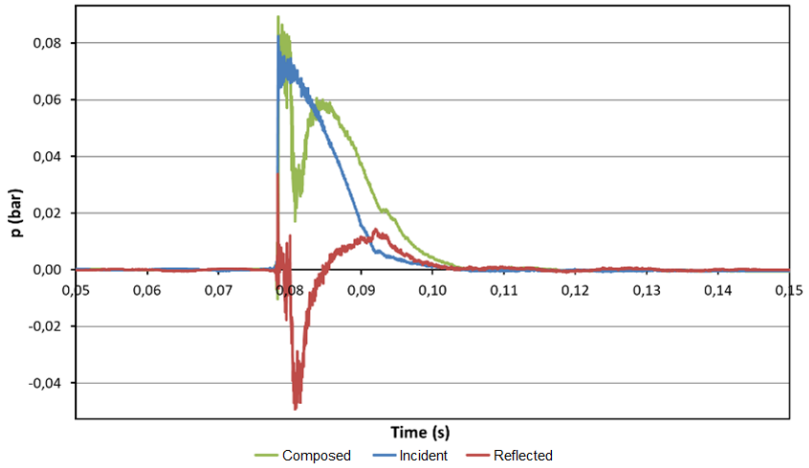

Figure 3.24: Example of composed (transducer 2), incident and reflected (computed) pulses in the time domain as produced with application of the procedure.

Figure 3.25: Nomenclature of pulses when an ATS is subject to an upstream excitation and with a non-reflecting downstream termination.

As all the information required has been obtained up to this point,

and in order to establish a consistent nomenclature for the pulses and their spectrum, the following is set as shown in Fig. 3.25:

- Incident pulse p_{ref} is denoted as p_1^+ and its spectrum P_1^+.
- Transmitted pulse p_{tran} is denoted as p_2^+ and its spectrum P_2^+.
- Reflected pulse p_{ref} is denoted as p_1^- and its spectrum P_1^-.

Determining the Scattering Matrix elements

The scattering matrix is a square matrix relating the incident and scattered sound waves in terms of their amplitude and phase. The number of rows and columns in the matrix correspond to the number of incident and scattered waves. As applied in this assessment, assuming linear propagation across the device, it is used to calculate the reflection (r_1, r_2) and transmission coefficients (t_{12} , t_{21}) from the following formulation:

$$\begin{pmatrix} P_2^+ \\ P_1^- \end{pmatrix} = \begin{pmatrix} t_{12} & r_2 \\ r_1 & t_{21} \end{pmatrix} \begin{pmatrix} P_1^+ \\ P_2^- \end{pmatrix} \tag{3.13}$$

The ITR procedure presented makes it possible to obtain the coefficients of the ATS scattering matrix in the excitation direction measured; therefore, for the complete acoustic characterization of the ATS it is necessary to determine the response in both possible propagation directions: inlet-to-outlet, as it is designed to be installed in the engine, and outlet-to-inlet. This can be done experimentally when the ATS is in clean condition by performing two tests on each device:

- In the direct test (inlet-to-outlet) the inlet reflection coefficient r_1 and the inlet-to-outlet transmission coefficient t_{12} can be determined.
- In the reverse test (outlet-to-inlet) the reflection coefficient at the outlet r_2 and the transmission coefficient from the outlet to the inlet t_{21} can be evaluated.

Since the direction of propagation of the pulse cannot be changed, the change from direct test to reverse is done by reversing the ATS

position in the ITR. There is a limitation to this approach when the ATS to characterize is in soot load condition, as carrying out the reverse test would cause the detachment of the soot layer. For this reason, the methodology described in [40], which allows to estimate the inverse response of the system based on the reciprocity properties and the dissipation of the ATS, was used.

Calculation of Transmission Loss

Transmission loss refers to the reduction in sound or acoustic power as it travels from one point to another. It is typically measured in decibels (dB) and represents the difference in sound pressure level between the source and the receiver. The TL can be obtained from the ratio of the incident spectrum to the transmitted spectrum, both as functions of the frequency f, with an additional term accounting for eventual area differences between the upstream and the downstream ducts:

$$TL(f) = 20\log_{10}\left|\frac{P_1^+(f)}{P_2^+(f)}\right| + 10\log_{10}\frac{D_1}{D_2} + 20\log_{10}\frac{1+M_1}{1+M_2} \tag{3.14}$$

where D_1 and D_2 are the diameters, and M_1 and M_2 the Mach numbers, subscript 1 referring to the section where the incident pulse is recorded, and subscript 2 to the section where the transmitted pulse is recorded.

Fig. 3.26 presents the complete signals of TL calculated for the no-flow condition with standard amplitude pulse in blue, and that for 300 kg/h and large amplitude pulse in orange. These signals serve as an example of how noisy / oscillatory the TL determined from raw measurements can be.

Experimental measurements were recorded up to 12796 Hz, but in most cases during modelling the benchmarking considered data up to 2500 Hz, and most results are presented up to 1000 Hz. Fig. 3.27 presents the TL calculated from the measurements obtained for ATD4 in the ITR, direct position up to 1000 Hz as example.

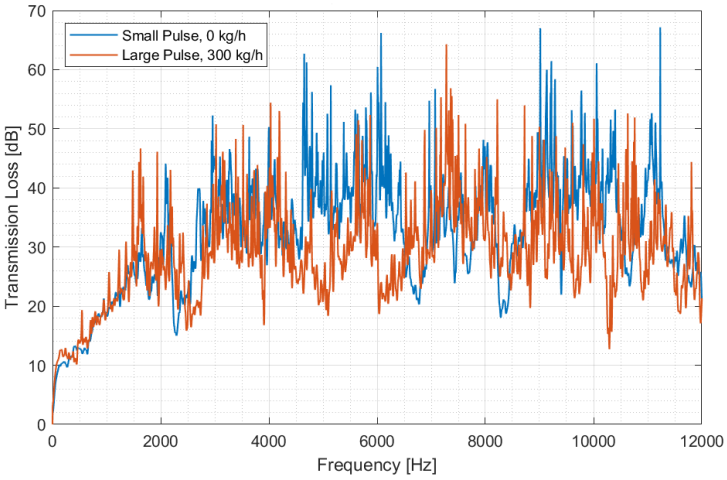

Figure 3.26: Example of raw TL calculated for two conditions, with and without superimposed mean flow.

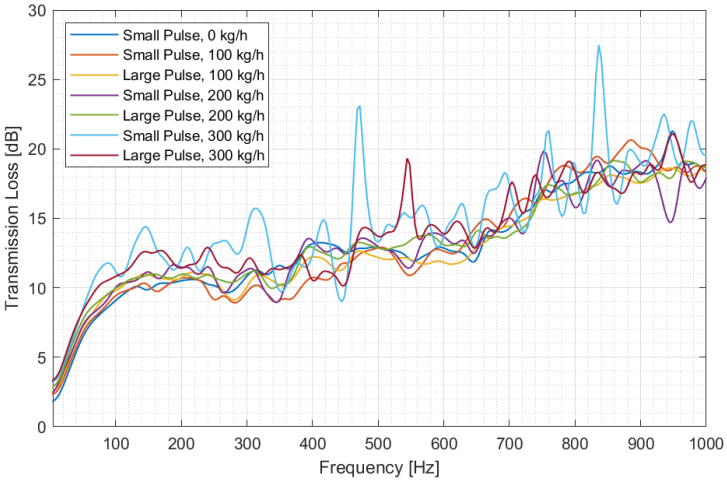

Figure 3.27: Example of TL from measurements at different pulse and flow conditions, of ATD4 in direct position, up to 1000Hz.

Smoothing

In view of the level of noisiness of the raw measurements, it was decided that a smoothing of the data would be pertinent. Smoothing of acoustic measurements, and in general of experimental measurements, is often done to remove or reduce the excess in fluctuations, what makes it easier to interpret and analyze the data and to identify relevant trends or patterns, often blurred by the fluctuations. Another benefit of smoothing is to help reducing the impact of outliers or random fluctuations that may be present in the data, leading to a more accurate representation of the underlying signal. Therefore, smoothing is an important processing step that adds value to the acoustic data obtained as it can improve the accuracy and reliability of both the signal and the analysis.

There are several methods available in the literature, as well as implemented in computational tools. In particular, for the smoothing of acoustic measurements a few common choices include simple moving average, weighted moving average, Gaussian smoothing and Savitzky-Golay. The choice of method depends on the type of data being smoothed and the desired outcome, as each method has its own strengths and weaknesses. Here, the Savitzky-Golay filter was chosen on the basis that it is highlighted in the literature for being more effective than other methods when the data varies rapidly.

Fig. 3.28 compares the raw and smoothed signals for the small amplitude pulse with 300 kg/h up to 2500 Hz, and shows how this approach allows to keep relevant information of the signal while sorting out unwanted oscillations. Complementarily Fig. 3.29 presents the results of the smoothing process of the data shown in Fig. 3.27. Both figures were obtained using a window of 40.

3.2.3 Analysis of reflective and dissipative effects

An interesting analysis approach to deepen the understanding of how each device participates in the noise abatement, therefore shedding additional light on the phenomena occurring internally, is to account for the relative importance of reflective (reactive) and dissipative (resistive) effects. In this research several approaches were used to perform such analysis.

In this section, S represents the cross-sectional area, ρ the density,

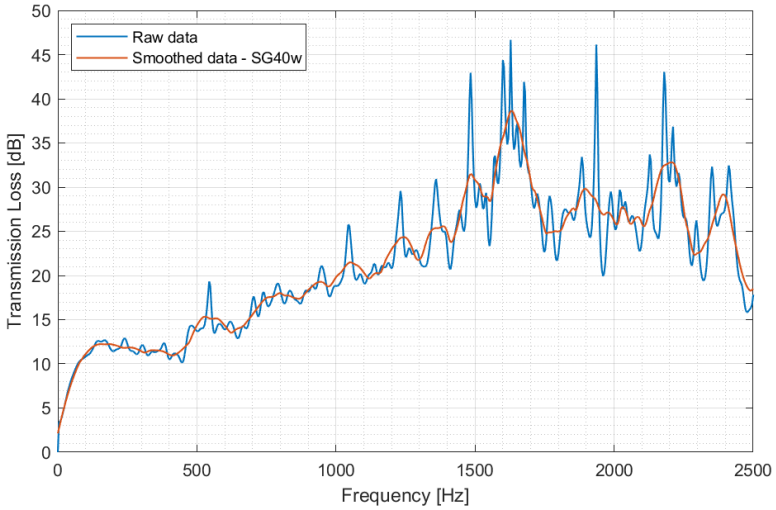

Figure 3.28: Influence of smoothing on a TL signal up to 2500Hz.

c the speed of sound and M the Mach number. Subscripts 1 and 2 correspond to upstream and downstream respectively.

Logarithmic approach:

This analysis is based on the useful decomposition of the TL into reflective and dissipative parts, proposed in [96]. Having an ATS subject to an upstream excitation and with an anechoic termination at the downstream side so that $P_2^- = 0$, which corresponds with the setup of the ITR, then the power balance may be expressed by stating that the difference between the acoustic power upstream and downstream is the power dissipated at the device. According to Morfey [97] this can be expressed as:

$$\frac{S_1}{\rho c}\left[\left|P_1^+\right|^2(1+M_1)^2 - \left|P_1^-\right|^2(1-M_1)^2\right] = \frac{S_2}{\rho c}\left|P_2^{+2}\right|(1+M_2)^2 + W_d \tag{3.15}$$

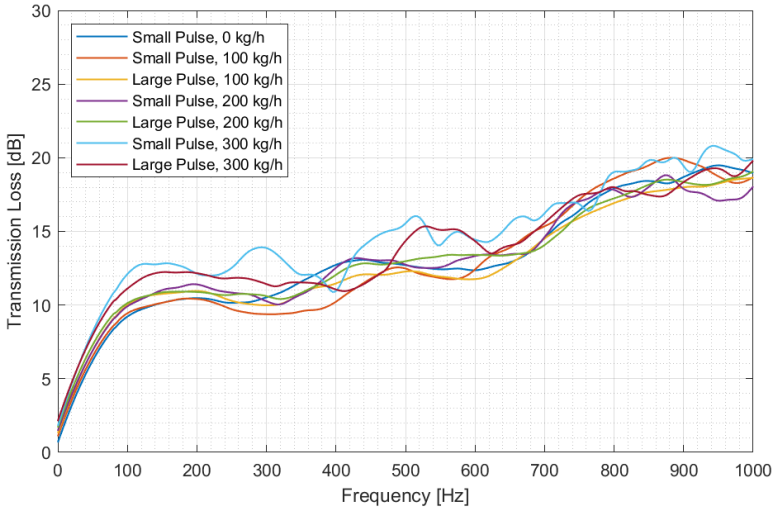

Figure 3.29: Example of smoothed TL at different pulse and flow conditions, for ATD4 in direct position, up to 1000Hz.

where W_d is the power dissipated. Now, identifying the incident, the reflected and the transmitted power as

$$W_i = \frac{S_1}{\rho\ c}|P_1^+|^2(1+M_1)^2 \tag{3.16}$$

$$W_r = \frac{S_1}{\rho\ c}|P_1^-|^2(1-M_1)^2 \tag{3.17}$$

$$W_t = \frac{S_2}{\rho\ c}|P_2^+|^2(1+M_2)^2 \tag{3.18}$$

the balance equation can be written as:

$$1 = \frac{W_r}{W_i} + \frac{W_t}{W_i} + \frac{W_d}{W_i} \tag{3.19}$$

However, in order to characterize the dissipative behaviour of the device it may be preferable to compare the actual power transmitted

by the system to the power transmitted in the absence of dissipation. In that case, setting $W_{dis} = 0$ gives for the power transmitted with no dissipation W_t^{ND}:

$$\frac{W_t^{ND}}{W_t} = 1 - \frac{W_r}{W_i} \tag{3.20}$$

and the aforementioned ratio would thus be

$$\frac{W_t^{ND}}{W_t} = \frac{W_i}{W_t}\left(1 - \frac{W_r}{W_i}\right) \tag{3.21}$$

Substituting the expression of the incident and the reflected powers, introducing the reflection coefficient r_1, and taking the logarithm one gets

$$10\log_{10}\frac{W_t^{ND}}{W_{tra}} = 10\log_{10}\frac{W_i}{W_t} + 10\log_{10}\left[1 - |r_1|^2\,\frac{(1-M_1)^2}{(1+M_1)^2}\right] \tag{3.22}$$

Now, denoting the left-hand side as the dissipative contribution to transmission loss, TL_d, and noticing that the first term in the right-hand side is precisely the transmission loss, one can write:

$$TL_d = TL + 10\log_{10}\left[1 - |r_1|^2\,\frac{(1-M_1)^2}{(1+M_1)^2}\right] \tag{3.23}$$

Interpretation of the previous equation in the light of the overall power balance suggests that the second term in the right-hand side should be related to the reflective contribution to transmission loss, TL_r, so that this could be defined as:

$$TL_r = -10\log_{10}\left[1 - |r_1|^2\,\frac{(1-M_1)^2}{(1+M_1)^2}\right] \tag{3.24}$$

and therefore

$$TL = TL_r + TL_d \tag{3.25}$$

The expression of the dissipative contribution can be written explicitly in terms of the transmission and reflection coefficients making use of the expression of TL given by Eq. 3.14:

$$TL_d = 10\log_{10}\left[\frac{S_1}{S_2(1+M_2)^2}\frac{1}{|t_{12}|^2}\left((1+M_1)^2 - |r_1|^2(1-M_1)^2\right)\right] \tag{3.26}$$

that, in the case of equal diameters upstream and downstream of the device, assuming again incompressible mean flow so that $M_1 = M_2 = M$, reduces to the expression found in [96]:

$$TL_d = 10log_{10}\left[\frac{1}{|t_{12}|^2}\left(1 - |r_1|^2\frac{(1-M)^2}{(1+M)^2}\right)\right] \tag{3.27}$$

Linear approach:

This linear approach addresses the decomposition in terms of acoustic power rather than TL. Consider again the power balance as given by equation (3.19):

$$W_i = W_r + W_t + W_d \tag{3.28}$$

Of course, the value of W_d is actually obtained from Eq. 3.28, whereas the expressions for the other terms have been shown above.

In order to identify the contributions of reactive and dissipative effects, one may consider that any reflection from the device is substantially determined by reactive effects, and therefore these can be characterized by the reflected power ratio W_r/W_i. From equations 3.16 and 3.17, one obtains that the reflected power ratio is

$$\frac{W_r}{W_i} = \frac{|P_1^-|^2}{|P_1^+|^2}\frac{(1-M_1)^2}{(1+M_1)^2} = \frac{(1-M_1)^2}{(1+M_1)^2}|r_1|^2 \tag{3.29}$$

Then, the power that is not reflected back is either dissipated or transmitted, and thus the proper way to characterize dissipation appears to be the ratio of the power dissipated to the power not reflected, that is $W_d/(W_i - W_r)$, that will be referred to as dissipated power ratio. From equations 3.28 to 3.18 one gets

$$\frac{W_d}{W_i - W_r} = 1 - \frac{S_2}{S_1}\frac{|P_2^+|^2(1+M_1)^2}{|P_1^+|^2(1+M_1)^2 - |P_1^-|^2(1-M_1)^2} \tag{3.30}$$

and introducing the transmission coefficient of the system one finally has

$$\frac{W_d}{W_i - W_r} = 1 - \frac{S_2}{S_1}\frac{|t_{12}|^2(1+M_1)^2}{(1+M_1)^2 - |r_1|^2(1+M_1)^2} \tag{3.31}$$

These two power ratios, that can be determined if the transmission and reflection coefficients are obtained from ITR test, form the basis of several of the analyses performed.

3.2.4 Engine-like Condition Validation: Unsteady flow gas stand

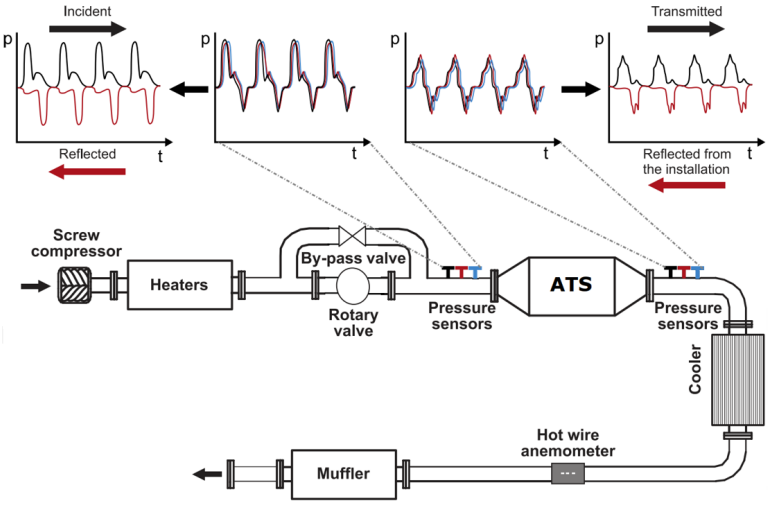

Figure 3.30: General Scheme of the unsteady flow gas stand.

The unsteady flow gas stand (UFGS), allows to carry out tests with engine-like, unsteady periodic flow under controlled temperature and mass flow conditions. The schematic configuration of the facility and an example of the information produced are shown in Fig 3.30.

Installation

The main components, instrumentation and their functions are:

Components

- A screw compressor that supplies the mass flow by pumping air, the rotational speed of the compressor controls the flow rate.
- A set of electric heaters located downstream of the compressor that heat the flow with a total power of 72 kW .
- A rotary valve with a bypass system to generate the pulses.

  - The amplitude is controlled by the opening of the by-pass valve.
  - The frequency is controlled by the speed of the rotary valve.

- Downstream is the spot where the ATS to be studied can be mounted.
- A heat exchanger (cooler) allows to cool down the flow before it is discharged.
- A muffler is placed before the discharge to the atmosphere to abate the noise generated during measurements.

Instrumentation

- Four K-type thermocouples located in cross sections at 0.9 m from the inlet and outlet of the ATS measure the flow temperature.
- An ABB SensyflowIG FMT081-A3E1A3 hot-film anemometer downstream of the cooler registers the mass flow.
- Kistler 4045A5 cooled piezo-resistive sensors installed upstream and downstream of the ATS measure the absolute mean pressure.
- Six Kistler 7061B cooled piezo-electric sensors, distributed in two groups of three transducers, measure instantaneous pressure.
- Kistler 5011B charge amplifiers modulate the signals from the sensors.

The six sensors for instantaneous pressure are key for the successful application of the measurement procedure, as they provide a high sensitivity, which allows for the detection of pressure fluctuations below 200 Pa. Each group of three is placed six diameters upstream and downstream of the inlet and the outlet of the ATS, respectively, at equally spaced axial positions. This particular disposition is key for the proper estimation of wave components through the beam-forming post-processing described below.

Data acquisition

- DL716 model 701830 Yokogawa system for the instantaneous pressures, recorded at a sampling frequency of 100 kHz.
- Mean temperatures were registered with an Agilent 3497OA data logger.
- The signal of a tachometer was also acquired in order to properly identify the periodicity of the pressure signals.

An example of the raw results obtained is shown in Fig. 3.31. It is apparent, in view of the small differences existing between the signal recorded by the three transducers in the array, that a careful calibration is imperative, both in amplitude and phase. The details of the calibration procedure can be found in [98].

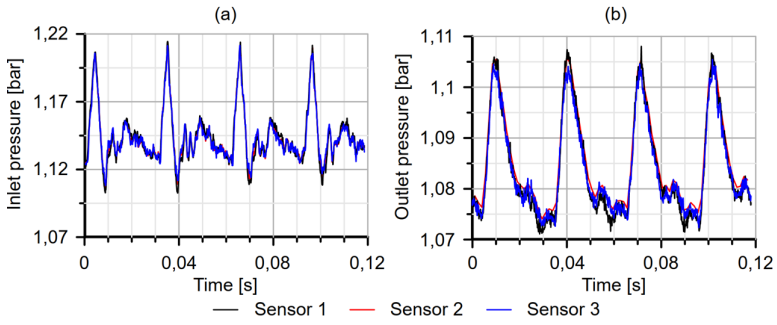

Figure 3.31: Example of raw measurements in the unsteady flow gas stand (a) upstream; (b) downstream. Sensor numbers as specified in Fig. 3.30.

Processing of signals: Beam-forming

Beam-forming is a signal processing technique that acts as a spatial filter, thus allowing to enhance and focus on the signal coming in a specific direction. A beam-former usually involves an array of sensors placed carefully, and a series of weighting factors which multiply the output from those sensors, to allow for the energy coming from a certain direction to be preferentially received by the array, whereas the energy

reaching the array from any other direction is suppressed or significantly attenuated.

The application of a beam-forming technique [98] allows to estimate the forward and backward wave components both upstream and downstream of the ATS from the raw measurements of the instantaneous pressure mentioned above. In this particular application, each group of three instant pressure transducers acts as the sensor arrays which, alongside with weighting factors chosen accordingly with the only two propagation directions in the duct, forward and backward, form the upstream and downstream beam-formers. This approach assumes that the pulse propagation between sensors is linear, which is acceptable when the separation between the sensors of each group is small when compared to the wavelength.

With this setup, the output of the beam-former is the wave component propagating either forward or backwards, thus behaving in a similar way as the conventional two-microphone method [71], which is basically the same with an array of two sensors. However, adding a third transducer to the array offers significant advantages in terms of robustness under noisy signals, due to the enhanced filtering action of the array.

In this way, it is possible to evaluate the sound pressure level reflected and transmitted by the ATS. As indicated in the scheme of Fig. 3.30 the beam-former upstream of the ATS accounts for the incident and reflected waves, meanwhile the downstream beam-former accounts for the transmitted wave and that reflected from the downstream ducting. An example of the results of the upstream beam-former is shown in Fig. 3.32.

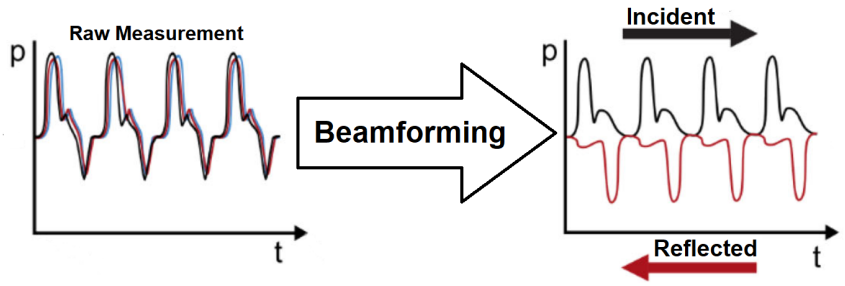

Figure 3.32: Example of how the beam-forming turns the raw signal into directional pulses.

3.2.5 Soot loading of devices

Two different devices containing WF PFs were soot-loaded in order to assess for different aspects. Some details on each soot loading process is presented bellow:

- The DPF monolith of ATD0 was soot-loaded until it reached 13 g/l of soot by mounting the device into an engine test bench with a commercial high-speed, direct-injection CI engine. The associated assessment is presented in Chapter 4.
- The GPFc monolith of ATD1 was not intended to keep an specific soot load but to be representative of the equivalent first few kilometers and hours of use. Therefore, the device was placed in a test bench with the native engine of the system and run for 10 WLTP cycles, equivalent to 232.5 km of road distance or 5 h of driving time, with the specific gear shifts configured for a Sport Utility Vehicle. The test bench was instrumented so additional information of changes during the process were registered. Such information and the assessment of changes due to the first few load-regeneration cycles is presented in Chapter 6, Section 6.5.

3.3 Modelling and Computational Tools and Approaches

This section is focused in presenting the software and computational tools used to complement the characterization of the studied devices. Some were use to handle the data obtained from the measurements, the CAD files and to process or post-process them, serving as input and benchmark for the modelling; others were used to simulate the devices and attempt to replicate the measurement results. Accordingly to the second objective stated in Section 1.3, different modelling options suitable for engineering practice have been explored, and approaches with different levels of complexity were applied, including 1D, 3D and even for particular applications 1D-3D coupling. The approach most notably used was the one-dimensional modelling, in which the concept of virtual or digital twinning for both the experimental facilities and the devices was key.

The common practice is to evaluate results from 1D models in regards to those from previously developed 3D models, however, direct comparison of 1D models to experimental measurements was also considered here, since an important part of the motivation specific to the computational modelling assessment was to evaluate the potential of 1D models developed in the commercial gas dynamic code GT-Suite to replicate as accurately as possible the characteristics of the devices, as well as the logic and methodology of the experimental study, validating in case of success the possibility of using the simplest level of modelling with a high level of confidence as sources of information and convenient tools to be incorporated into the design and optimization process of complete exhaust lines, exploiting the usual benefits of simulation to its most: reduce costs of prototypes, reduce time spent with more complex approaches and overall allowing for a better understanding of the acoustics and fluid-dynamics.

All the simulations prepared were based on the Virtual Twinning concept. Virtual or digital twins, at least within industrial, R&D and engineering fields, are virtual representations of physical objects or systems, such as machines or buildings. The twins are computer generated models designed to imitate the behaviour of the real-world object or system they represent; most common applications include the possibility

to simulate, analyze and predict how their real-world counterpart could perform under different conditions, study potential modifications, troubleshoot problems and deepen understanding of their operation, thus being a useful tool for engineers, designers and researchers. Digital twins are becoming increasingly popular in engineering, due to their benefits in reduction of cost and time associated with physical testing and prototyping. They can also provide valuable insight into how objects and systems behave in real-world situations, which can help to improve their design and performance.

Digital twins are typically created using data gathered from sensors and other sources. Here the idea was to prepare virtual twins of both the devices and the experimental facilities, aiming at accurately replicate the results by simulating the tests with the same working principles, sensors, processing and even the ambient conditions. The three different approaches used, the 3D, 1D, and 1D-3D co-simulation, were assessed following such approach. Measurements of the actual parts, CAD files and complementary information on the monoliths supplied by the OEM allowed to prepare the virtual twins of the devices for both the 3D and 1D approaches. The 3D approach did not require for the virtual twinning of the experimental facilities, as flow and all other conditions can be imposed at the boundaries, and for the 1D approach the precise virtual twins of the experimental test facilities were attempted but found not suitable; however, templates mimicking the working principles of the tests were achieved.

3.3.1 Programs and tools used

A brief description of the software and tools used and their application within this research is presented:

Microsoft Excel was used to import and organize data from the experiments in predefined templates prepared to make part of the calculations in order to produce the results of interest, and later exported for post-processing if needed. Also to organize and format the modelling results, and then visualization options were very useful for the comparison assessments; several plots were made with this program.

The templates filled with data from experimental measurements also

included relevant complementary information, such as the dates in order to have a complete register, and ambient conditions which are then taken into account for the modelling.

MATLAB short for Matrix Laboratory, is a numerical computing software developed by MathWorks. It provides a programming environment that enables to write and run code to solve complex mathematical problems. It also includes lots of pre-built functions and toolboxes that make it very useful for data analysis, numerical calculations, signal processing and visualization. The software supports a wide range of data types, including matrices, vectors, and arrays, which makes it particularly well-suited for working with large datasets.

For the acoustic characterization in the ITR, the comparison and selection of the best matching pairs of Step 1 and Step 2 measurements from the processing of signals described in Subsection 3.2.2, is automatized thanks to a MATLAB script. Then TL calculated from experimental data is imported and the smoothing process applied through pre-built functions, also most of the production of plots were made with MATLAB.

GT-Suite is a system simulation software developed by Gamma Technologies, LLC and widely used in automotive industries and the engine community, and the one chosen here for the 1D approach. The software supports a wide range of simulation techniques, including steady-state, transient, and dynamic simulations. It is also compatible for co-simulation with other software tools specialized in FEA or CFD. It can also be described as a comprehensive set of simulation tools as it is subdivided in several modules that can be used independently; in this research the following three modules were used:

- GT-Ise, which is the main modelling environment, extensively used here for 1D simulation although it includes some other options. This tool works on a modular modelling approach, and offers a wide variety of pre-built elements classified into convenient libraries that make both the selection and configuration of individual elements easier. It contains certain pre-set applications, being GT-Power the one used, which pre-loads the libraries for Engine

Performance and Acoustics. It also includes useful features for sensitivity analysis, DOE, manual and integrated optimization, also extensively used in the early steps to define the 1D modelling methodology.

- GT-Post, which is the tool to access the results, including several complementary options for analysis, plotting, comparing and exporting results.

- GEM3D, which serves as a translator to import CAD files and turn them into equivalent 1D models that can then be used in GT-Ise. It offers assistance and advice for the user to choose, rather than forcing a direct translation; however, the CAD file to be supplied still has to be preprocessed elsewhere. This CAD-to-1D translation option helped to account for volumes with very intricate geometrical disposition and to learn the logic of the discretization internal to the software which in turn allowed to developed a proprietary discretization process.

Regarding the preparation of CAD files needed before the use of GEM3D, GT-Suite also has a module to create, modify and import CAD files, GT-SpaceClaim, which was tested but in the end the use of SolidWorks was preferred. Also during the development of the work several versions of the software were used, updating models and procedures to the latest available, as internal software improvements fixed limitations found in early stages.

SolidWorks by Dassault Systèmes. Is a popular, user-friendly 3D CAD software commonly used in mechanical engineering and product design. It is used to create and modify 3D models of parts and assemblies with a parametric modelling approach. It also has tools to perform simulations and analysis, and to generate engineering drawings. Here it was used for the preparation of received CAD files, to make them suitable for either the 3D or the 1D approach; this could be done by suppressing elements that do not interact with the fluid, to create alternative simplified CAD or to extract the fluid domain for CFD.

Simcenter STAR-CCM+ is a computational fluid dynamics (CFD) software tool developed by Siemens Digital Industries Software. It was chosen as the main program for the 3D approach on pressure drop and in general to have an idea of the flow pattern and several other characteristics. The key points for this decision, besides the availability of the license, include:

- Capability to import CAD files easily.
- Automated meshing features that help create high-quality meshes for complex geometries reducing the time and effort required.
- Compatibility with GT-Suite, for 1D-3D coupled simulation.

COMSOL Multiphysics is a powerful simulation software tool that enables to simulate and analyze complex physics-based systems. It is a widely used software in many different industries, including the automotive. Some of the key features of COMSOL include; the simultaneous multi-physics simulations, capacity to work with imported CAD files, capacity for FEA, BEM and FVM simulations, and tools to prepare 2D and 3D visualization easily.

3.3.2 Previous Steps for Modelling

Similar to the preparations required by the devices in order to test them in the experimental facilities, there are also preparation needed in order to properly perform the computational modelling using the 3D and 1D approaches intended. This includes the preparation of templates or virtual twins of test facilities to perform the simulations in the 1D approach, the discretization of devices into parts for 3D or elements for 1D, and the selection of parameters, models or the like to be applied in the configuration of each case prior to run the simulations.

In this sense, the 3D approach needs relatively less preparations as there is no need for a virtual twin of the test facilities, focusing the preparations on the proper discretization of the components into parts, the extraction of the fluid domain (explained in Section 3.3.3 and the selection of meshing, parameters and models which were decided on the basis of literature, experts advice and the trial and error of the first

few modelling attempts for each device. The final selections on these options are shown in Section 3.3.4.

On the other hand, 1D modelling does require the preparation of templates that represent, even if not as accurately as a virtual twin, the working principles of the experimental facilities and thus allow to produce information equivalent to those coming from experimental measurements. This approach also requires the proper discretization and selection of elements representing each component, and the parameters to configure the 1D virtual twins.

Bellow are presented the preparation of PD and TL testing templates, a set of guidelines for the discretization of devices into components, and how to configure them into 1D and 3D models, and finally a summary of DOEs and sensitivity studies.

Preparations of PD and TL Testing Templates

It was initially intended to have detailed and precise virtual twins of the experimental facilities, to use them along the virtual twins of the devices to reproduce experimental results even in terms of measurement procedure. As such attempts failed, the approach was changed; Figs. 3.33 and 3.34 show the templates for PD and TL measurement simulation respectively. Even though it is not a precise virtual twin of the CFTB facility, the working principle, procedure, adapters and sensor positions are kept in the case of PD template, producing information equivalent to that of PD experimental results. On the other hand, the TL template includes minor modifications of a built-in non-linear TL template native of the software, in order to mimic the experimental measurements particularly between the second and the third transducers of the ITR facility, this is, also considering adapters and pipe section between the transducers, thus producing results comparable to those from the experiments, at least after smoothing post-processing.

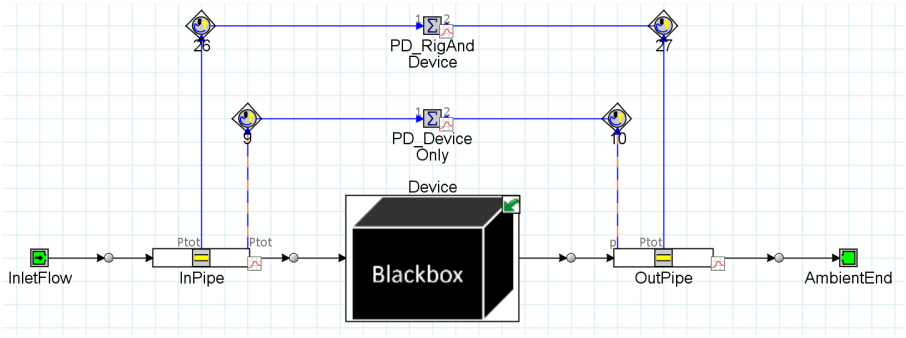

Figure 3.33: Pressure drop testing template, based on the Cold Flow Bench and its procedure.

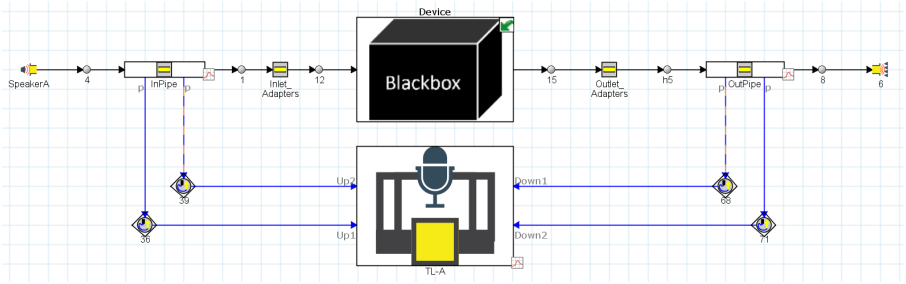

Figure 3.34: Transmission loss testing template, adapted from built-in software template.

Figs. 3.35 and 3.36 show examples of results obtained using these templates compared to equivalent results from experiments. The importance of the inclusion of adapters, particularly to obtain satisfactory results for the TL, could be evidenced in the first attempts; Fig. 3.36 also shows the difference of including them or not in regards to experimental post-processed TL results.

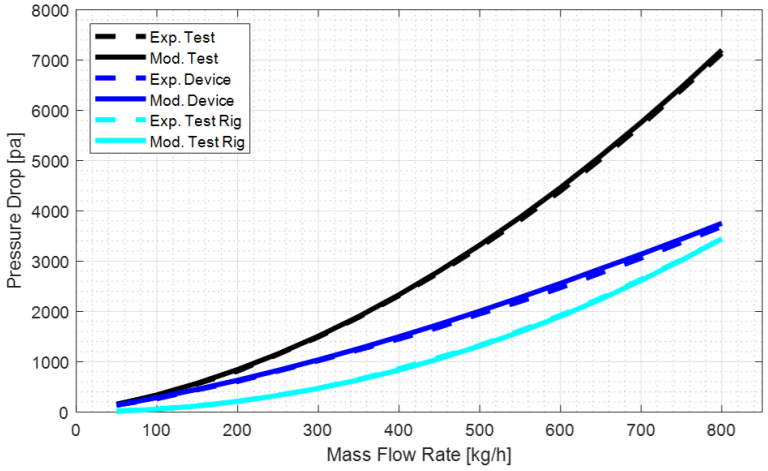

Figure 3.35: Example of pressure drop results obtained with the template compared to experimental equivalent, in this case for ATS1-D2 in the 50 to 800 kg/h range.

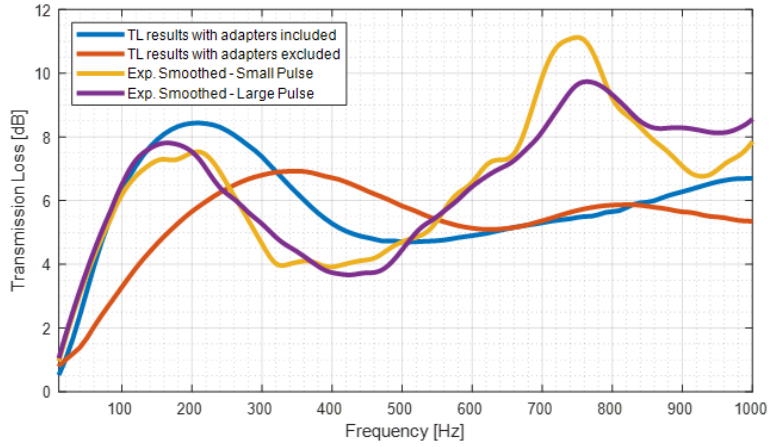

Figure 3.36: Example of transmission loss results obtained with the template compared to experimental post-processed equivalent, effects of considering the adapters shown. Modelled results for ATS1-D2 with a mass flow rate of 100 kg/h.

As an additional validation of the modelling results produced with the PD testing template being representative of experimental results, the direct comparison of the $Re - Ma$ trend, K_{test}, K_{duct} and K_{ATS} factors were compared for each final model. Fig. 3.37 shows the example for ATS1-D1.

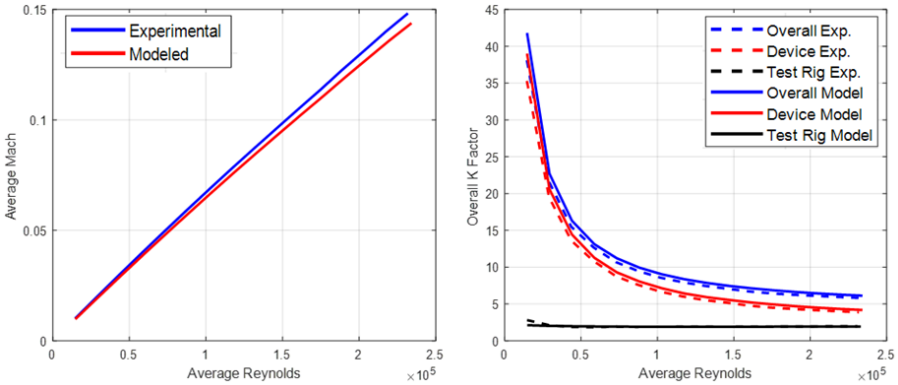

Figure 3.37: Experimental vs Modelled validation; Re-Ma trend (left side), K_{test}, K_{duct} and K_{ATS} factors (right side). Results for ATS1-D1.

Additionally, another predefined template from GT-suite libraries, the "TMatrixGenerator" shown in Fig. 3.38, allows to obtain the coefficients of the acoustic transfer matrix for the virtual twins of devices by placing two copies, one configured in the direct and the other one in the inverse flow direction. This template also produces another TL measurement with an internal calculation different from that of the TL template. With these coefficients it is possible to account for the dissipative and reactive components and thus to compare with the results of the decomposition analysis applied.

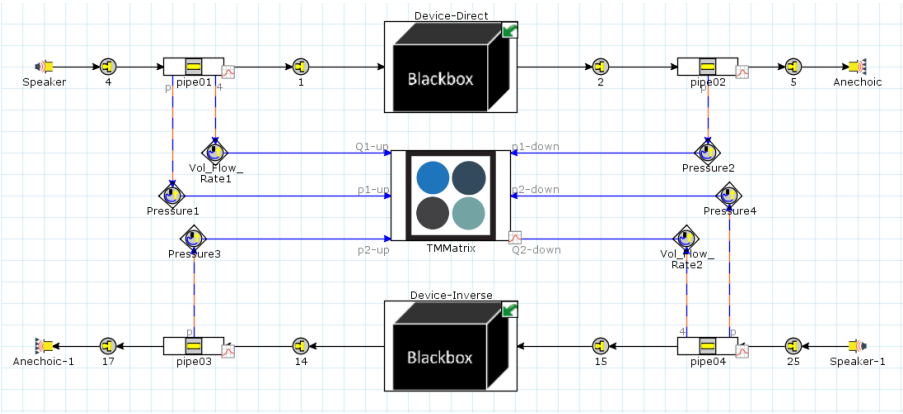

Figure 3.38: Acoustic Transfer Matrix template, built-in software template used directly

Discretization Guidelines and Recommended Elements

Discretization Guidelines:

Starting with the *Discretization Guidelines*, to properly represent the devices in their 1D and 3D counterparts, it is important to identify and distinguish the relevant parts to be represented in the model and any other elements that can be either neglected or combined into a single one. As this is intended to apply for ATDs and it has been previously stated that a complete ATS is an array of devices, these guidelines are to be applied to each individual composing device within the system; for intermediate pipe sections it can easily be considered that each half of the section belongs to the device it is connected to.

CAD files, in particular cleaned up CAD as explained below in Section 3.3.3, are very convenient for this step as it is easier to recognize the shape of elements, and several components to be neglected such as thermal protection, fixation elements and ports have already been suppressed.

Devices with monoliths:
The following elements may be considered:

- The first and easiest to identify are the monoliths; each monolith must be considered as a unique element in the models, with slightly different considerations between flow-through (FT) and wall-flow (WF) monoliths that are explained in the paragraph on recommended elements per component.

- The gap between monoliths is the second element to be identified when a device has more than one monolith. Even if this gap is very short, it has noticeable effects, and neglecting it can even produce computational errors if the total number of channels is not equal for consecutive monoliths.

- Empty sections of cannings upstream and downstream of the monoliths can either be considered as an element or as part of the volume they are connected with.

- Pipe sections, expansions and contractions (tapered elements) are to be modelled as independent elements in 1D but can be part of a single integrated volume in 3D. Pipes with diameter changes can be divided into different elements or treated as a single one depending on the element used in the modelling.

Of course, external elements that are not in contact with the flow are not of interest and should not be included in the models regardless of the approach.

Devices without monoliths:

There are cases where a device does not contain any monolith; in such cases, separating components by physical/geometrical or functional criteria is the key.

- Any element that constitutes an obstacle to the flow can be considered as an element, such as the case of mixer inducers, sensors, injectors, baffles, among others.

- Special volumes that are connected to pipe sections, or are pipe sections themselves, but comply an specific function in the device should be considered apart as well. These include mixing pipes or lateral cavities for sensor or injection ports.

- The same guidelines apply for pipe sections, tapered and external elements.

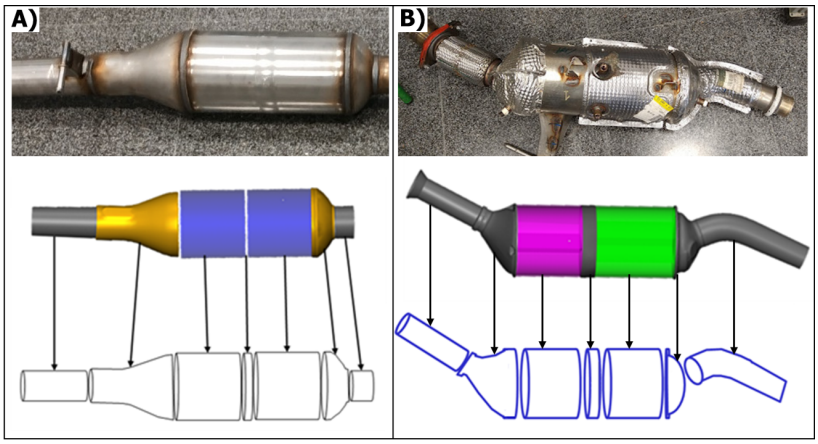

Figure 3.39: Example of application of discretization guidelines in devices with monoliths; A) on low complexity device ATS1-D1, B) on intermediate complexity device ATD4.

Fig. 3.39 shows and example of what is obtained from the application of the suggested discretization guidelines in two devices with monoliths classified in different geometrical complexity categories; ATS1-D1 and ATD4. In both cases, besides their geometrical disposition differences, the discretization produces equivalent arrays of seven pieces with two monoliths, intermediate gap between monoliths, inlet and outlet pipe sections, an expansion and a contraction. Even so, the selection of element and components as advised in Table 3.9 should produce different results in 1D and 3D.

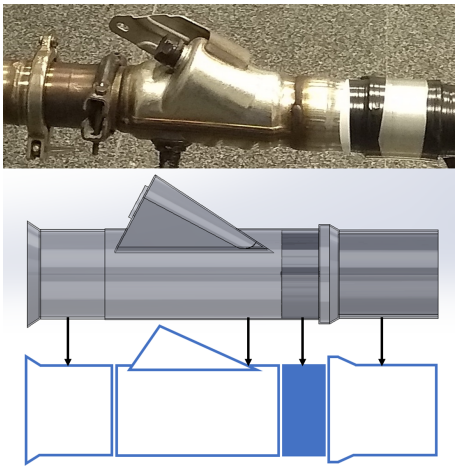

Figure 3.40: Example of application of discretization guidelines in devices without monoliths, low complexity device ATS1-A.

Then Fig. 3.40 illustrates what is obtained from the application of the suggested discretization guidelines to a device without monoliths. In this case, four pieces are distinguished: the inlet and outlet pipes, the mixer –as it is an obstacle and also complies a specific function–, and the DEF injection port volume, together with the pipe it is connected to, form a single element.

Recommended representations of components in models

Once the discretization of the devices is clear, the next step is to choose the elements that will be used to configure the model in the 1D approach, and the portions of the fluid domain to be treated as different parts (volumes) and assigned to different regions in the 3D approach.

As the order of increasing complexity was chosen to assess the modelling of the ATDs, special characteristics were assessed one at a time, for example starting with ATS1-D2, which has straight inlet and outlet pipes, straight tapers and a FT monolith, and then ATS1-D1 that has the same characteristics plus a second monolith placed in the same canning, with an empty gap between the monoliths. This allowed the first few iterations of 1D modelling to be focused on testing different

options and combinations of elements to represent each component. It was also evidenced that translation to 1D assisted by GEM3D, while very useful for irregular volumes, is not as effective with monoliths, which are best configured manually, and probably not as worth to use with pipes, specially if the pipes are straight. A series of recommended elements to represent each usual component of ATDs was defined with the experience of the modelling workfront.

Another finding of these modelling iterations was that overall volume, lengths and changes in diameter are the most important factors to be correctly represented in order to obtain adequate simulated results, which means that curvatures, bends and several other small details (small when compared to the volume of the component, or the selected discretization length) can be neglected, this making the 1D modelling significantly easier. This also supports the use of simplified equivalent CADs used as described in step 6 of Section 3.3.3.

Similarly, the first attempts on 3D modelling, while still assessing the selection of models and configurations, allowed to define some good practices in order to represent the fluid domain portions as different individual or integrated parts, and assign them into regions. The advice for both modelling approaches is summarized in Table 3.9.

Table 3.9: Recommended model representations per component.

Component	**Recommended 1D Representation**	**Recommended 3D Representation**
Flow-Through Monoliths	CatalystBrick	Individual part Porous Region
Wall-Flow Monoliths	ParticulateFilterAcoustic ParticulateFilter (standard)	Individual part Porous Region
Empty Gap between monoliths	PipeRound FlowSplitGeneral	Individual Part Fluid Region
Empty Sections of Canning upstream or downstream of monoliths	PipeRound Consider the volume part of adjacent non-monolith part	Integrated Part Fluid Region
Pipe Sections	PipeRound PipeTable	Integrated Part Fluid Region
Expansions and Contractions	PipeRound FlowSplitGeneral	Integrated Part Fluid Region
Enlarged Cavities	PipeRound FlowSplitGeneral	Integrated Part Fluid Region
Flow Restrictions	PipeRound	Individual Part Fluid Region

From Table 3.9 it is evident that for non-monolithic elements PipeRound is the preferred element, followed by FlowSplitGeneral (probably GEM3D aided) to account for irregular volumes. Some additional remarks on the selection of the representations are listed bellow:

Clarifications:

- Expansions and contractions include any shape that may have the volumes before and after the monolith, usually conical or slightly rounded, but devices such as ATD1 and ATD2 have more intricate shapes in such volumes.
- Enlarged cavities refer to any volume that does not correspond to the expansion/contraction group, for example the volume between monoliths in ATD3 and the DEF injection port volume of ATS1-A, or skewed junctions, among others.
- Flow restrictions refer to any other element that constitutes an obstacle to the flow, such as partitions, plenums, mixers, sensors or injectors in contact with the flow, etc.

On 1D representations:

- In the case of the WF monolith, element ParticulateFilterAcoustic, specially when converted into a compound, produces by far the best TL results, but has some incompatibilities with the approach used to simulate PD. In such cases, ParticulateFilter (standard) could be used, thus having two Virtual Twin models for devices with WF monoliths, one for TL and one for PD.
- Empty gaps between monoliths can be represented by either PipeRound or FlowSplitGeneral, being the first preferred, but if the length of the gap is lower than half of the discretization length, the FlowSplitGeneral option should be used. There is an alternative FlowSplitNode supposed to be suitable for very small volumes to be considered as a point, but its use is not advised (not even by the software support information).
- The decision between PipeRound and PipeTable to account for pipe sections is purely aesthetic; if properly configured a PipeTable summarizes up to five PipeRounds, but the computational treatment is identical. In the models developed for this research individual PipeRounds were preferred.
- In the case of expansions and contractions, straight aligned tapers or rounded volumes can be represented by PipeRounds taking care

of volume correspondence; intricate volumes or eccentric tapers may be better represented by FlowSplitGeneral.

- For flow restrictions it was found that PipeRounds, but with a modified equivalent diameter calculated to match the area left open by the obstacle, are the best way to account for the restrictive effect.

On 3D representations:

- In the case of monoliths, regardless of their kind (FT or WF) each monolith has to be considered as an individual part, but they can be assigned to a shared Porous Region if the properties of the monolith (apart from the length of the brick) are identical; for example in ATS1 (complete) the three monoliths are identical, so that each one has to be represented by an individual part, but the three parts can be then assigned to the same Porous Region.

- For components suggested as an Integrated part, this means that the fluid domain partition can be a single one with adjacent non-monolith components. This could simplify the configuration of the model, but if preferred for any reason each one can also be represented by an individual part.

  - For example, in ATS1-D2 all the upstream components can be treated as a single part, and the same applies downstream. Therefore, its 3D representation has 3 parts (upstream side, monolith and downstream side) and two regions (a porous region for the monolith and a fluid region for the upstream and downstream sides.)

- Regardless of non-monolith components being treated as individual or integrated parts, all they should be assigned to a single Fluid Region.

DOE and Sensitivity studios

Another preparation required was to define which parameters were going to be considered for model adjustment, and the importance of the precision with which characteristic dimensions should be represented in the model, i.e., the geometrical characteristics of the actual elements. For such end, several DOE and sensitivity studies were prepared and executed.

Tested parameters included some model-specific parameters: forward loss (discharge) coefficient, friction multiplier, discretization length and surface roughness. Some parameters related to ambient conditions: relative humidity, ambient pressure, ambient temperature, imposed wall temperature. Regarding characteristic dimensions, the precision of volumes, lengths, diameters and curvature were assessed.

The following is a summary of findings:

- Ambient-related parameters showed very weak effect on both PD and TL results, but if the information is available a proper configuration of the data is still advised.
- Model-specific parameters showed strong and noticeable effects on PD results (forward loss coefficient and friction multiplier) and computation time (discretization length), but almost negligible effects on TL, basically small shifts ups and down with the curve shape unchanged.
  - The forward loss coefficient and the friction multiplier were chosen as tuning parameters for the models developed, as they showed sufficiently strong effects, are easy to set and change, and are available in most of the software elements.
  - Using the Direct Optimizer tool of GT-suite, and setting FM and FLC as the values to be handled by the program, the results suggested that PD is about three times more sensitive to FLC than to FM; this information should be taken into account when fine-tuning the model.
- The effect of the discretization length on PD results was found to be almost negligible, its importance being directly related to computation time.

  - Differences may be significant if a system very long compared with the discretization length set is modelled.
  - Even though the PD result barely changes, the computation time spent on each case does. When modelling just a few cases and rather simple devices, this might not seem as a big issue, but the difference was noticeable even for the simple case of the DOE prepared.

- The precision in the characteristics dimensions, except for the curvature, has a noticeable effect on both PD and TL, but TL effects are far more evident.

  - Regarding the effect on TL, it was found that there is a hierarchy in the order of importance: volume, diameter (cross sectional area) changes and length must be accounted for in that order. Therefore, it is preferable a near 100% volume correspondence, even if this requires a small error in the diameters or the length.
  - Having a CAD file to collect data for characteristics dimensions is preferable, but any other measurement to obtain the required data can be used with an increased probability to induce errors.

- The surface finish can be defined in three ways: set as smooth, choosing a material from a list, or entering the value manually. The overall effect found was noticeable shifts up and down on both PD and TL.

- Some tips on the selection of discretization length and surface roughness values are presented below.

- Parameters are therefore highly important for PD, and TL is essentially determined by characteristic dimensions; this trade-off is to be carefully tuned as models with good correlation in both aspects are desired.

Finally, the Flow Loss model, which defines the solver and equations used by the software, was also tested. In particular, the difference between Explicit, which is recommended for acoustics and wave dynamics,

and Quasi-Steady, which is recommended for after-treatment devices, both thus covering the topics assessed in this research. The default maximum simulation time when using the explicit solver was found to be optimizable, and therefore two scenarios of explicit flow loss model were considered (default and optimized time).

A test with three copies of PD testing for ATS1-D2 were ran with all other configurations besides the flow loss model unchanged: Explicit (Default Time), Explicit (Optimized Time) and one with Quasi-Steady. The duration registered also depends on the characteristics of the computer, but the difference is very indicative. Table 3.10 shows the results of the test.

Table 3.10: Comparison of computation time and mean error to experimental reference from the use of different flow loss models.

Flow Loss Model	**Last Case Computation Time**	**Complete Simulation Computation Time**	**Mean Error Compared To Experimental Results**
QuasiSteady	5 seconds	1 min 25 sec	1.35
Explicit	15 min 20 sec	4 hours 10 min	1.27
Explicit (Reduced Time)	8 min 15 sec	2 hours 20 min	1.27

During this DOE and assessment of the sensitivity of models to different parameters, a series of recommended seed values were determined, which were then revised and updated with the progress of software versions and modelling iterations. Table 3.11 summarizes most of them. These seed values were found to be a very good starting point from which little fine tuning is expected; in this sense, these could be used in the early stages of design for a new ATD or exhaust line as they should produce indicative results.

Table 3.11: Recommended parameters to configure 1D models.

Parameter	**Value**	**Remarks**
Friction Multiplier	0.7	In fact a range from 0.55 to 0.85
Forward Loss Coefficient	-CG = 0.05 -IG = 0.1 -SG = 0.2 -NM = 0.15	-CG Complex Geom. -IG Intermediate Geom. -SG Simple Geom. -NM No Monolith
Discretization Length	-General=15 to 25 mm[a] -Test rigs=20 mm -Mon.=10 mm -No Mon.=5 to 10mm[b]	-Mon. stands for Monolith -Specific values suggested worsen computation time but produce better TL results
Surface Roughness	Steel (0.046 mm)	If material is known use the proper one, if not Steel is better than default (smooth or drawn metal)
Ambient Related	-Match registers from measurements -ISO conditions	-First if reproducing a measurement -Second if designing or no experimental data available
Flow Loss Model	-QuasiSteady[c] -Explicit[d]	-QuasiSteady for PD DOE and similar -Explicit for definitive results

Additional Remarks:

- [a] From the sensitivity analysis on the discretization length, the range between 15 and 25 mm was found to have a local optimum in terms of the accuracy of results vs. computation time trade-off per case; therefore it can serve as a general good starting point, yet it might be too long in regards to some gaps, perforated plate mixers and some other elements.

- [b] Thumb Rule: 5 mm was found to be the limit were computation time starts to increase significantly without much change in results; if after discretization guidelines are applied there is any element smaller than 5mm, two option arise: set the overall discretization length as twice the length of the smallest component, or set an exclusive value on the element representing it. The latter would be equivalent to the use of an special meshing in a small component in 3D approaches.

- [c] and [d] The sensitivity analysis on which flow loss model to choose led to the following findings:

  - QuasiSteady is not compatible with TL and TM templates, but as models are first prepared, tested and tuned for PD, there is a huge difference in the computation time between using QuasiSteady or Explicit model with an accuracy downgrade lower than 5% when using QuasiSteady, and therefore DOEs to test any changes, sensitivity analysis on PD or attempts on new designs are recommended with such model; then, when the model is considered ready one can move to Explicit.
  - The Explicit model was used, and it is recommended, for PD run on definitive models, and it is required for any acoustic assessment (TL and TM testing) and for the integration of these virtual twins into larger simulations with engines.
  - For the use of the explicit flow loss model within this research, the simulation time reduction approach mentioned before was used several times.

3.3.3 CAD Handling

The OEM supplied highly detailed CAD files for each of the studied parts, which served as a valuable source of information on the inner volumes and shapes of the devices, and provided an easy way to get the geometrical information needed for the modelling. These supplied CADs included heat protection elements, fixating structures, gaskets and ports for injectors and sensors. All of these elements are out of the interest of the modelling approaches, as most of them do not interact with the flow, or at least not in the experimental setup being reproduced. Therefore Fig. 3.41 shows the processing applied to such files in order to use them in the 3D and 1D modelling approaches.

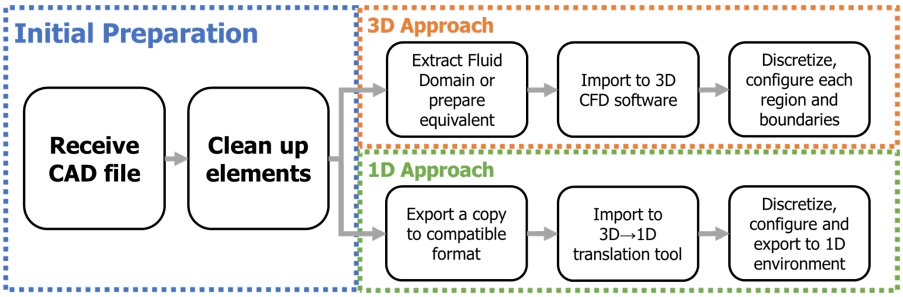

Figure 3.41: Flowchart of the use of CAD Files.

Following is the step by step description of the process:

1. Received CAD files were imported to SolidWorks.
2. Perform the “clean up” of elements.
    - Suppress elements that do not interact with the flow: heat protection elements, fixating structures, sensor and injector ports.
    - Suppress elements that may interact with the flow but are not relevant to the simulation intended: gaskets, cloth layers around monoliths.
    - Patch holes and gaps, fix any overlapping.

3. Once the cleaned up file is ready, two copies are created, one for each approach.

4. The *copy for 1D approach* is saved and exported to STEP format (.stp), compatible with GEM3D.

5. The *copy for 3D approach* still needs more steps as the 3D approach needs the fluid domain, i.e the volume occupied by the flow, rather than the walls of the device itself.

    - Include lids to the assembly of the device, in order to create an enclosed volume inside.
    - Save the assembly as a part.
    - Prepare a prismatic volume, larger than the assembly.
    - A new assembly with the prismatic volume and the device is composed, a "cavity" operation subtracts the device volume from the prismatic volume creating two separated volumes, one internal and one external in regards to the device. The internal one coincides with the fluid domain, which is the one of interest.
    - The external volume is deleted, so that the prismatic volume becomes the fluid domain and it is saved and exported to either Parasolid (.x_t) or STEP (.stp) formats.

6. In some cases the CAD file received was not compatible to be fixed or patched as described above. In such circumstance, a new *equivalent simplified CAD* was prepared, and then steps from 3 to 5 were repeated. The simplified CADs were prepared with the following characteristics:

    - Monolith and cylindrical volumes are kept intact in diameter and length.
    - Pipe sections are represented keeping the volume, length and diameter but neglecting any curvature.
    - Irregular volumes are represented mostly with truncated cones, keeping the volume and the diameters connecting with other elements.

7. For the 1D approach, once the cleaned CAD or simplified CAD are the imported into GEM3D, the software opens an assistant that guides and suggests options for the translation of different sections into 1D model elements. Finally, the result can be used within the GT-Ise environment.

8. For the 3D approach, the imported fluid domain stills needs to be configured:

   - Monoliths have to be converted into porous regions.
   - The volumes inside pipe sections, tapers and gaps have to be configured as fluid regions.
   - Surfaces that would be in contact with device walls have to be configured as wall boundaries.
   - The surfaces created by the lids added in step 5 represent flow inlets and outlets, and are to be set to impose all known flow properties and characteristics as boundary conditions.

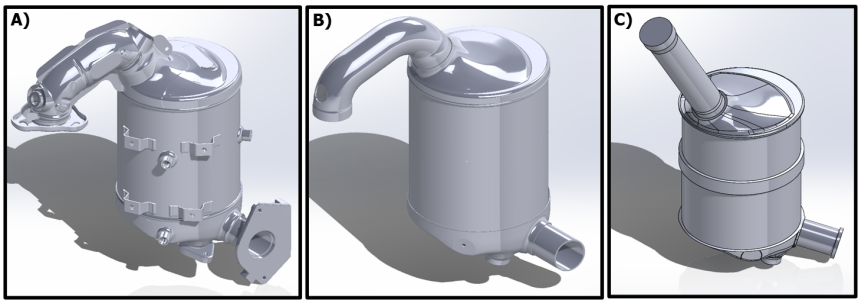

Figure 3.42: Examples of different stages of CAD processing, for ATD0; A shows CAD as received, B shows the same file after the clean up process, C shows the extracted fluid domain from an equivalent simplified CAD

Fig. 3.42 shows as and example the different stages of the processing for the CAD file corresponding to device ATD0. Fig. 3.42(A) shows the CAD as it was received; in this case thermal protection, ports and fixating elements cover the device all around, even the precise shape and

size of the inlet and outlet pipes is barely noticeable. Fig. 3.42(B) shows how the CAD ends after the clean-up; a copy of this stage is transferred to GEM3D and translated into 1D model. Finally Fig. 3.42(C) shows the extracted fluid domain from a simplified equivalent CAD ready to be exported for the 3D CFD software (STAR-CCM+).

3.3.4 3D Approach

3D CFD simulations in STAR-CCM+ were used to assess the pressure and velocity across the devices, including pressure distribution, velocity distribution, flow patterns and the pressure drop from inlet to outlet boundaries. The simulations are started when the fluid starts to flow and are carried out until the steady state is reached. The starting point of these simulations is the fluid domain extracted from either the cleaned-up or the simplified CAD; the initial setup corresponds to that described above in the eight step of CAD handling. Boundary conditions are configured according to the information registered in the results from experimental measurements.

Similar to the inlet and outlet ducts used in the CFTB to guarantee a developed flow, the surfaces corresponding to the inlet and outlet are extended 10 times their diameter. Several copies are created to run a copy for each mass flow rate condition tested in the experiments.

Fig. 3.43(A) shows the extracted fluid domain of ATD3 with the extended inlet and outlet pipe sections already configured into corresponding regions, Fig. 3.43(B) shows the result of the meshing applied, and Fig. 3.43(C) and Fig. 3.43(D) present the detail of the surface and the inner appearance of the meshing in a section including the complex volume between monoliths, the second monolith, the outlet eccentric taper and the outlet pipe.

As usual with modelling assessments, the process was iterative, and the first few iterations allowed to choose between the various options available which could be best fitted for the interest pursued. This was done also with the assistance and advice of CFD experts and advisors from PWT Engineering Srl within the activities of the remote research placement. The following is the procedure followed.

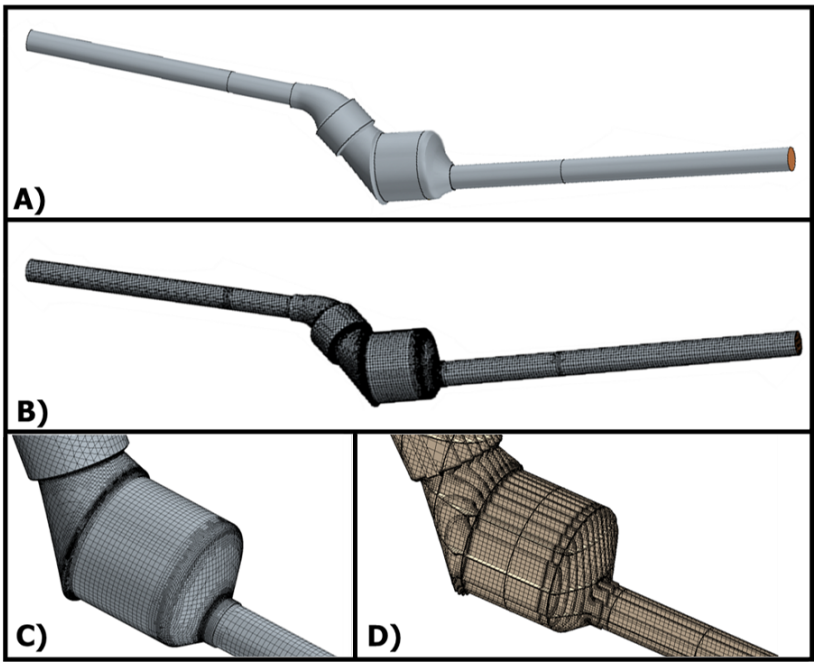

Figure 3.43: Example of preparations and meshing in 3D approach, for ATD3; A the fluid domain plus extended pipe sections already divided into parts, B the device with trimmed meshing applied, C and D auxiliary detailed views of the trimmed meshing result in the surface and inside.

Procedure for 3D modelling in STAR-CCM+

1. Import the fluid domain (extracted from clean-up or simplified CAD) as surface mesh from a parasolid or step file using either the "high" or "very high" tessellation option; as the CAD file is already composed by parts this creates an assembly of parts with individual curves and surfaces.

2. Prepare the file to properly define regions and boundaries according to the discretization intended; during the import process automatically recognized curves and surfaces are usually excessive, and thus the following is done with each part:

- Expand each part in the navigation tree.
- In the curve folder of each, run the "Split Non-contiguous" option.
- Remove any curve that is not meaningful for the desired sub-component splitting.
- Once the remaining curves divide each part surface into inlet, outlet and walls, move to the surfaces folder and execute "Split by part curves" option.
- Rename each surface, set inlet and outlet as upstream and downstream flow boundaries and the remaining as wall boundary.
- Renaming is advised, especially the overall Flow Inlet and Flow Outlet boundaries.

3. Create the inlet and outlet pipe extension.

4. Proceed to define the Regions:

   - Use the assign parts to region in the right-click drop-down menu.
   - Assign all pipe section, tapers, and any empty space or cavity between monoliths to a fluid region.
   - Assign monoliths to porous regions as follows:
     - If there is only one monolith it should have a region for itself.
     - If there are two or more monoliths, any monoliths with the same type and geometrical configuration can share region but each has its own boundaries; different kinds of monoliths require separated regions.
   - Check if all interfaces needed between parts were properly recognized by the automated process. If any interface is missing, it can be manually defined as follows:
     - Expand region boundaries, use multi-selection to highlight the two faces in contact of the missing the interface, and use the "Set Interface" option.

5. Prepare the meshing with the Geometry → Parts → Operations → New → Mesh → Automated Mesh option.

6. Two main meshing strategies were used: the "Poly-Tetra" and "Trimmed" options, the selection of meshers were done as shown in Table 3.12.

    - In the "Poly-Tetra" option, the Polyhedral mesher is applied to pipe sections, monoliths and straight shaped empty volumes such as gaps between monoliths, or canning sections upstream and downstream of monoliths, whereas the Tetrahedral mesher is applied to complex shaped volumes, usually the tapered elements. Different parts with the same mesher can be configured in a single operation.
    - In the "Trimmed" option, the Trimmed Cell Mesher is applied to every part, but due to a limitation in the automated mesher each part needs to be meshed in an individual operation.

7. Define Continua by choosing the models to be applied; the selection is shown in Table 3.13.

8. After the continua and meshing are properly set and check, the following can be done:

    - Assign the material as Air and configure its dynamic viscosity to the value of $1.86E^{-5}$ Pa-s.
    - Configure the imposed mass flow rate in the Fluid Region → Boundaries → Flow Inlet Boundary → Physics Value → Mass Flow Rate as needed for each copy; also set the Flow Outlet Boundary as Pressure outlet.
    - Configure the Porous Regions as follows:
        - In Physics Conditions look for the Turbulence Specification, and set Method as Intensity + Length Scale.
        - Porosity value has to be set depending on the kind of monolith represented: 0.85 for any FT monolith, 0.74 for WF DPF monoliths and 0.66 for WF GPF monoliths.

  - Set the Porous Inertial Resistance and Porous Viscous Resistance definition as Orthotropic Tensor, the values of the orthotropic tensors depend on how the monolith is aligned in regards to X, Y and Z axis.

9. Set the stopping criteria to a certain number of iterations; after several trials the $1000 - 1500$ iterations range was found to be adequate as the simulation has reached a steady result with a reasonable computational cost.

10. Finally, in order to have access to both numerical and visual results the section planes, scenes and reports of interest have to be defined:

    - Create as many section planes as required, this can be defined in the Derived parts $\rightarrow$ Section planes, taking into account the following tips.
      - Section planes coinciding with the inlet and outlet of the device.
      - Section planes coinciding with the inlet and outlet of extended pipes.
      - At least three section planes parallel to the XY, XZ, and YZ planes of the complete system.
      - At least one section plane in the middle of any cylindrical section (monoliths, gaps, pipes).
      - Complementary sections planes when required in complex geometry volumes.
    - Define scenes; this creates the tabs to have access to different visualizations as needed.
      - Two volume scenes, one for the complete system volume and one for the group of derived sections.
      - Two mesh scenes: one for the complete system volume and one for the group of derived sections.
      - Two scalar scenes: one for Pressure(Total) and one Velocity(Magnitude) on the group of derived sections.
      - One vector scene: for Velocity(Vector) on the group of derived sections.

- Define in Reports – New Reports the information to be stored and displayed; also, set up the ways in which the information is to be visualized (derived plots, scenes, monitors, annotations).
  - Flow / Energy: Pressure Drop
  - Metrics: Surface Average - Velocity
  - System: Total Solver CPU Time, Total Solver Elapsed Time.

11. Run Simulation.

Table 3.12: Settings for Meshing.

Option	**"Poly-Tetra" Option**	**"Trimmed" Option**
Surface Mesher	Surface Remesher	Surface Remesher
Optional Surface Repair	Automatic Surface Repair	Automatic Surface Repair
Core Volume Meshers	Tetrahedral or Polyhedral (Hexahedral) Mesher	Trimmed Cell Mesher
Optional Volume Meshers	Generalized Cylinder Mesher	None
Optional Boundary Layer Meshers	Prism Layer Mesher	Prism Layer Mesher

Table 3.13: Selection of models to define Continua.

Option	**Selection**
Space	Three dimensional
Material	Gas
Flow	Segregated flow
Equation of state	Ideal gas
Energy	Segregated fluid temperature
Time	Steady
Viscous Regime	Turbulent
Reynolds Averaged Turbulence)	$k-\epsilon$ Turbulence
Complement to prior	Wall distance
$k-\epsilon$ Turbulence Models	Standard $k-\epsilon$
Complement to prior	High $Y+$ Wall Treatment

Fig. 3.44 shows the pressure related results of the simulation run of ATD3 with 300 kg/h of mass flow rate, following the procedure described.

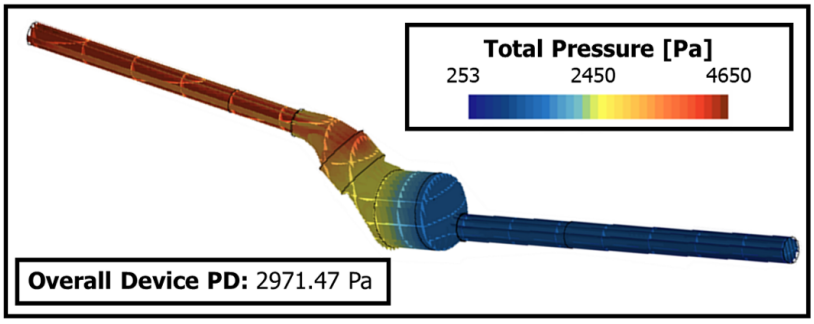

Figure 3.44: Example of pressure related results from 3D approach, ATD3 at 300 kg/h

Acoustic Properties in COMSOL

The modelling of acoustics were extensively assessed with the 1D approach; however, for the case of the static swirl mixer, as the flow was expected to be considerably affected by the mixer, it was decided to use COMSOL multiphysics to account for the acoustic properties of the device and possible interactions of the mean flow with the acoustic field by solving the linearized Euler equations. For this, the extracted fluid domain CAD was loaded and turned into mesh, and then the mean flow was mapped by interpolating the data obtained from its corresponding CFD simulations, similarly as performed in [99, 100]. Further details of this application and the results obtained are presented in Section 5.3.

3.3.5 1D Approach

Most of the focus of the modelling work was put on the 1D modelling in GT-suite, as the most convenient outcome would be to define a methodology and guidelines to produce virtual twin models capable of providing useful information in regard to experimental results without the cost of CFD, or at least able o produce results sufficiently satisfactory to allow using 1D modelling most of the time.

Fig. 3.45 shows the flowchart of the overall methodology followed within 1D simulations. First and second steps in the light blue boxes correspond to several cycles of iteration in the modelling of each device, with many options tested for each element. Fig. 3.46 shows how each of the aforementioned steps was conducted.

1D Modelling Methodology

The 1D modelling methodology consisted of preparing virtual twins of the devices in 1D and test them in the templates prepared in Section 3.3.2. The 1D virtual twins of the devices were prepared through iterative attempts, from which a procedure was formulated and revised several times during the development of the research. The following is the resulting formulation for ATD.

Procedure to prepare 1D virtual twins of devices

1. Fetch the part to be modelled –it can be either the actual piece

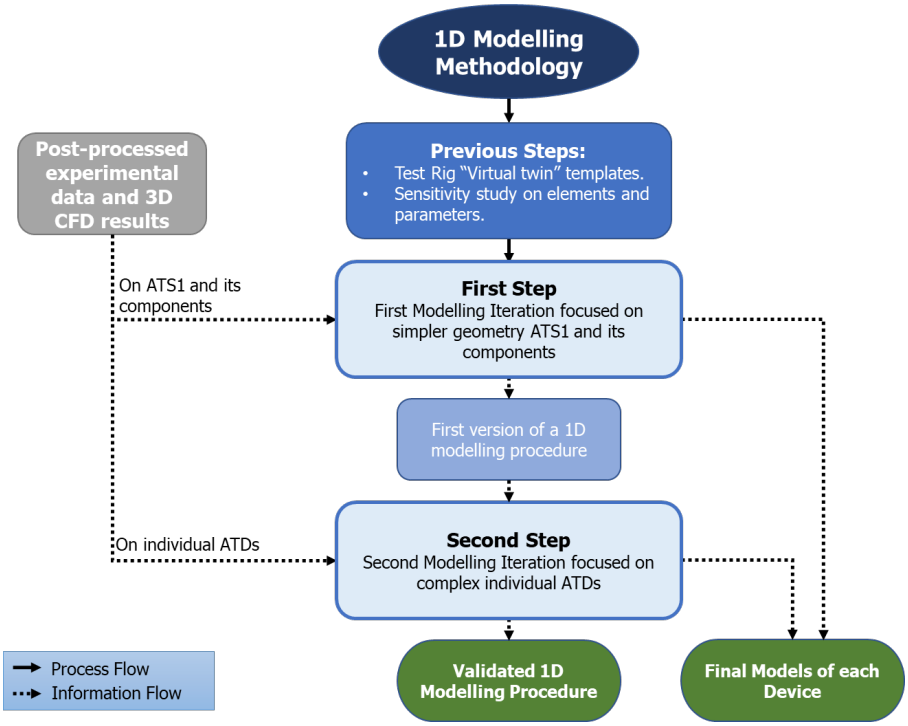

Figure 3.45: Flowchart of the Modelling Methodology in the 1D approach.

or the prepared CAD file (cleaned-up or simplified)–, and complementary information.

2. Check if it fulfils the device definition as stated in the scope (Section 1.3); inlet and outlet pipe sections with a functional component in-between, or a system (array of devices). If it is a device, proceed to apply the discretization guidelines; if it is a system, apply the discretization guidelines to each composing device on its own.

3. With the initial discretization obtained, proceed to prepare the 1D model, with one element per component with the geometrical information. For this step three paths can be followed:

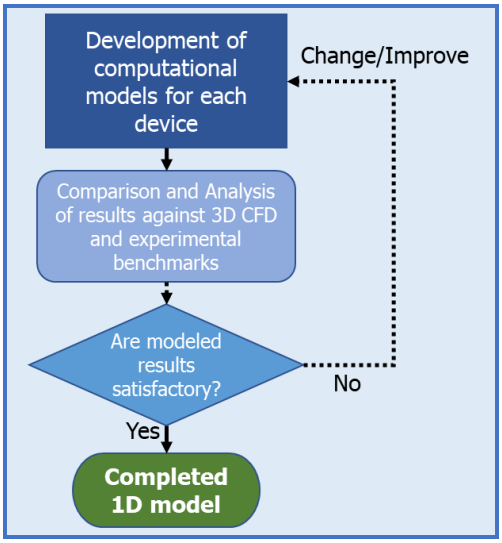

Figure 3.46: Detail on how each modelling iteration works.

- *Purely Manual:* Prepare a 1D model in GT-Ise from scratch using recommended elements to represent each component (see Table 3.9), using the part or CAD to obtain geometrical data and complementary information to set up the elements.
- *GEM3D:* Upload the CAD to GEM3D, and use it to translate each component from CAD to a 1D model, preferably choosing elements following the list of recommended elements, and once moved into GT-Ise check if anything is missing in each element configuration.
- *GEM3D Assisted:* Recommended when some volume or volumes are too complex to be simplified manually; this helps obtaining a proper FlowSplit representation.

4. Set up the rest of the parameters, using for the first iteration seed values recommended in Table 3.11.

5. Set up ambient conditions.

6. Save the virtual twin model as a GT external assembly, or alter-

natively save it as a model where the device is a sub-assembly to then copy-paste.

Execute the measurement simulations

1. Start with the PD simulation.
    - Use the template for pressure drop testing. Adapters, if any, must be included.
    - Compare the results obtained with the benchmarks (3D and experimental, giving priority to experimental).
    - If the results are satisfactory, proceed to the next step; otherwise, the troubleshooting may start by checking the volumes and, if needed, adjust the tuning parameters of the virtual twin model.
2. Once the PD results are satisfactory, proceed to the TL simulation. From the experience acquired, the better the PD results, the more likely the TL results will be satisfactory and trustworthy.
    - Use the template for transmission loss testing. Adapters, if any, must be included.
    - Compare the results obtained with the benchmarks, 3D CFD and experimental results.
    - If the results are satisfactory, proceed to next step; otherwise, the troubleshooting may by limited to geometry checks, as at this point changes in parameters are not very effective.
3. Use the template for Transfer Matrix to obtain real and imaginary coefficients, which can be used to determine the scattering matrix of the virtual twin models, which can be post-processed to compare with the results from the decomposition analysis performed.

Results produced up to this point are ready to be analyzed and compared to their benchmarks. Example results are shown in Figs. 3.35 and 3.36. Details on the models and results for each devices are presented in Chapters 5 and 6. In this thesis the TL benchmark was mostly the post-processed experimental results.

3.3.6 1D-3D Coupled Simulation Approach

In some cases, it was considered interesting to evaluate the convenience of using the co-simulation capabilities of integrating 1D modelling and 3D CFD. Co-simulation involves coupling two or more simulation tools together to analyze a system that cannot be accurately modelled using just one software; it can also help to improve the accuracy of results by combining the strengths of different codes while compensating for their respective drawbacks. For instance, a complete 3D CFD approach is significantly more time consuming and implies a higher computational effort, but is far more competent in assessing three-dimensional flow effects and producing detailed information about fluid and flow properties. Meanwhile, a 1D approach produces important information at system levels in a considerably faster and less computationally expensive manner, but is not capable of assessing the effects of complex local 3D features of the flow.

Co-simulation is specially advisable in cases where it is suspected that 3D effects might have considerable importance, using the 1D as the master simulation and letting the 3D to account for specific elements where, due to their geometry, considerable 3D flow effects could be expected. This leads to a more optimal use of computational power, focusing the 3D simulation only where it is really needed.

In this research the coupling of GT-suite and STAR-CCM+ was used. Among the options available, the CFDInterface method was selected for its convenience and relative simplicity.

Preparation and coupling

When using the CFDInterface method, a few adaptations are needed in both the 1D and 3D models. The 1D model is rather a modified copy of the original, as it needs to run as a normal 1D model for a certain number of cycles, reach a steady point and then turn into the coupled mode to feed the 3D software with a starting point close to the one desired to be simulated. For the 3D, only the fluid domain of the region to be 3D simulated has to be loaded and configured, and therefore a model different from that considered the 3D virtual twin has to be prepared.

- In the 1D model three elements have to be included: CFDInterface, CFDFlowConn and CFDComponent.
  - CFDInterface acts like a switch that marks the places were the connections to 3D CFD software take place –two per each 3D connection–; once the coupled cycles start, the elements of the 1D model between two consecutive CFDInterface will be turned off and replaced by the CFD.
  - CFDFlowConn allows to configure what information is going to be exchanged between the programs; two per component represented in the 3D CFD software are required: one that sets the information sent from 1D to 3D and one that controls the information read back.
  - CFDComponent is used to tell the software which 3D CFD file it has to connect with and execute.
- The load and set up of the 3D region to be executed by the coupled simulation has to be previously made. Also the co-simulation model has to be loaded and the kind of connection and name of the 1D file specified.
- It is strongly recommended that the inlet and outlet of the volume to be 3D simulated correspond to straight sections. To accomplish that, in some cases what was considered as a unique straight pipe in the 1D and 3D virtual twins had to be split into two, in order to place the CFDInterface in a straight section.
- The fluid properties translation between both codes has to be defined from GT-suite side using CFDSpecies, CFDSpeciesMap and CFDDefinedSpeciesMap; manuals include some guidelines on how to simplify multicomponent and multiphased flows for the 3D.

The following figures show examples of the difference between standard and prepared for coupling files of both 1D and 3D; further details and results and shown in Chapter 6.

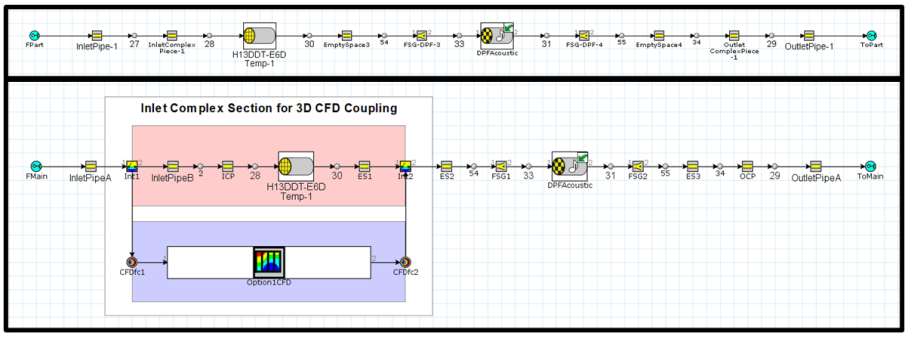

Figure 3.47: Comparison of a standard 1D model (upper side) and a copy prepared for 1D-3D coupling (lower side), example for ATD1.

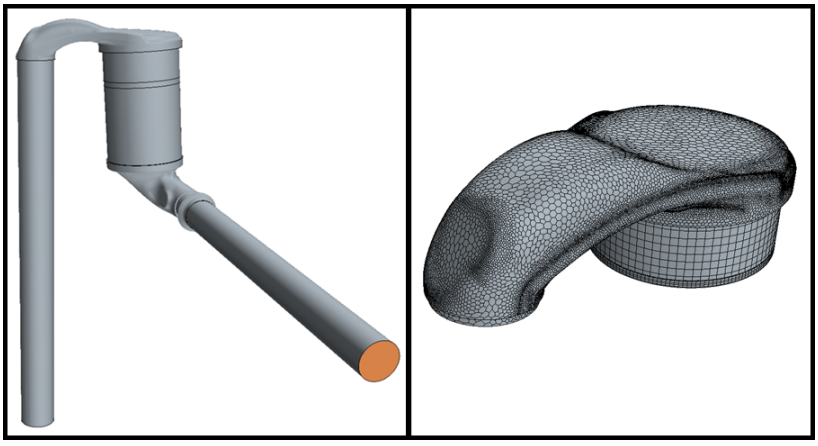

Figure 3.48: Comparison of the fluid domain for standard 3D (left side) and integrated 1D-3D coupling (right side), example for ATD1.

Chapter 4

Significance of Cold Condition Measurements to actual in-engine conditions

Part of the information presented in this chapter can also be found in the paper *On the Applicability of Cold Acoustic Measurements to High-Amplitude Hot Pulsating Flows* [3], which is a JCR publication derived from this part of the research. Also, some of the elements here presented can be tracked down to preceding publications by the supervisor of this work, in particular *Phenomenological methodology for assessing the influence of flow conditions on the acoustic response of exhaust after-treatment systems* [39] and *Assessment of acoustic reciprocity and conservativeness in exhaust after-treatment systems* [40] as such pieces of work served as background to this assessment.

4.1 Introduction

As this research aims at the experimental and computational characterization of after-treatment systems in terms of their fluid-dynamic and acoustic behaviour, the latter accounts for a significant part of the work. Most existing procedures used to obtain an experimental characterization of the acoustic behaviour of after-treatment systems, or any other exhaust line elements, resort to ambient or cold condition mea-

surements, in order to get rid of any potential difficulties for a proper temperature control or uncertainties related to the effects of temperature on the measurement. Such is the case of the procedure used with the Impulse Test Rig that has been presented in Section 3.2.2, and which is the experimental measurement procedure used in this research to characterize the acoustic behaviour of all the studied devices.

There is a considerable confidence on how indicative these cold condition measurements results can be for the cold end of the exhaust line (the placement for silencing elements), where the temperature and amplitude of pressure waves have already been weakened by dissipative and reflective effects upstream. However, the after-treatment systems which are the focus of this research are usually located in the hot end of the exhaust line, where both the temperature and amplitude of pressure oscillations are close to their maximum values, what casts important doubts on how representative the results of the experiments can be.

In this context, a direct assessment was attempted to tackle doubts on the significance of cold conditions measurement results to represent the actual behaviour of ATS in a hot and pulsating, closer to actual in-engine flow, conditions. The details of such assessment are presented in this chapter.

The chapter is organized as follows:

- Some relevant precedents, concepts, and considerations are presented in the *Background* section.
- Further detail on the device chosen, its preparation, the measurement set-ups, the measurements themselves and the post-processing are reviewed and discussed in the *Assessment Procedure* section.
- Key results and their analysis are summarized in the *Results and Discussion* section.

4.2 Background

A variety of measuring techniques are available for acoustical characterization [69]. Some use with external sound level meters as in [70], whereas other use multiple in-duct sensors [71], commonly condenser microphones. In regards to the use of in-duct sensors there are also various levels of complexity, from those with two sensors, one per side of the device tested [72], to those that use multiple sensors on each side which grant greater details on structural and flow conditions [69].

As controlling the temperature would involve additional difficulties during the measurements, usually all the aforementioned experimental characterization techniques are applied at room temperature, and are naturally valid as benchmarks for models that also consider room conditions. This is considered sufficient for assessing mufflers, as they are in the cold end of the exhaust line, with moderately high temperatures and pressure amplitudes, which can be considered close enough to measurement conditions. The ATDs, usually placed in the other end of the exhaust line, operate at considerably higher temperatures and pressure amplitudes, what may raise doubts on the adequacy of cold condition results to represent them.

In fact, in a preceding work it was proven that in ATS the PD does not fully follow the expected similarity as a function of the Reynolds number, and the differences could not be explained on the single basis of compressibility effects [101]. However, until the article derived from this part of the research was published, no other assessment could be found of the adequacy of extrapolating acoustic measurements results obtained in ambient conditions to hot and high-amplitude pulsating flow conditions. Thus this chapter (alongside the article) are the first to provide such an assessment by combining well established techniques into a novel methodology allowing for the direct evaluation of such extrapolation.

Other relevant and direct precedents of this assessment come from [39] were a phenomenological methodology which allows to correct a baseline experimental acoustic characterization in order to account for the effects of pressure perturbations and flow conditions, and [40] were the compliance of acoustic reciprocity and conservativeness properties in ATS systems were checked, and their implications on the definition of

the scattering matrix elements was discussed alongside with dissipation.

In [39] the panorama of computational models often failing to account properly for wave transmission across ATS, specially in the presence of intricate geometrical features, thus leading to the necessity of experimental measurements, was presented. However, the latter cannot cover all the diversity of flow conditions under which these devices operate. This limitation was thus tackled with a hybrid approach, a phenomenological methodology that allows for the sound extrapolation of experimental results to flow conditions different from those used in the measurements, coming the information from computational, gas dynamic models, developed in parallel with the desired conditions. The methodology draws on the integration of the base transfer matrix obtained from experimental tests, particularly the impulse rig, for different excitation amplitudes and mean flows, and then fitting the experimental coefficients to Fourier series whose characteristic periods change due to the influence of the flow conditions. This can also be used for predictions when the Fourier series approach is coupled to a gas dynamic model able to account for the sensitivity of propagation velocity to variations in those flow conditions.

Later on, in [40] an assessment of compliance and implications of the following properties of the ATS was presented:

- **Reciprocity** [102, 103] involves that the response at a given location to a disturbance applied at another point is identical to the response that would be obtained if the positions were exchanged [104].

- **Conservativeness** means that the energy of the waves transmitted and reflected by a system is the same as the energy of the waves incident to the system.

For such purpose, various experiments in the impulse test rig were contrasted to others performed in real operating conditions. The influence of different excitation amplitudes and superimposed mean flows was also considered. Then, using the transfer matrix enables the mathematical definition of reciprocity and conservativeness [105]. These properties have been relevant for practical applications in complex systems, as in the case presented by Easwaran et al. for multipole systems [106].

Once the compliance with the properties was validated, the dissipative effects were also taken into account, providing simple expressions allowing to predict the response of ATS from outlet to inlet based on the transmission and reflection properties obtained with the measurement from inlet to outlet.

When properly combined, the procedures and the properties validated in those articles establish the basis for the assessment presented here. It allowed to reduce the overall number of measurements (tests) and gas dynamic models required to do the acoustic characterization of ATS using the combination of experimental and computational tools, and to envision the possibility to make the most of cold condition measurements to predict or estimate the behaviour under other conditions.

4.3 Assessment Procedure

On the basis of the background presented, one of the devices considered in Section 3.1 was chosen to develop the intended validation, and two of the experimental facilities described in Section 3.2 were used to collect the experimental information required:

- The device labelled as ATD0 was the one used. This consisted of a DOC and a DPF in a single canning, and its main characteristics are listed in Table 3.1.
- The first facility, the impulse test rig, allows for cold condition tests to be carried out using an isolated pressure pulse either with or without superimposed mean flow, producing results to be then convoluted with excitations estimated via computational models.
- The second facility, the unsteady flow gas stand, was used to carry out tests with engine-like, unsteady periodic flow under controlled temperature and mass flow conditions.

As the ATD has a WF monolith, a DPF, it was tested in both clean and soot-loaded conditions in order to include in the assessment the influence of the soot load on the acoustic behaviour. The loading process was carried using a commercial high-speed, direct-injection CI engine, until the PF monolith reached 13 g/l of soot.

Making use of wave decomposition techniques, the measured characterization was convoluted with the hot-flow excitation and the device responses were directly compared.

Impulse Test Rig

Using the methodology described in Section 3.2 the test protocol listed in Table 4.1 was completed for clean condition, and then the measurement with 150 mbar and 14 ms was repeated with the soot loaded condition.

Table 4.1: Amplitude and duration of the incident pulse generated in the impulse test rig and values of the superimposed mean flow.

		Duration[ms]	
		11	14
Amplitude [mbar]	80	w/o mean flow	-
	150	-	w/o mean flow
	150	-	mean flow 170 kg/h

The raw results in the time domain are presented in Fig. 4.1, and first observations are fully consistent with what was expected:

- The pulses with higher amplitude have a higher propagation velocity and therefore reach each sensing point earlier.
- The superimposed mean flow also induces a shift as the whole medium is moving as the pulse is propagating reaching the sensor even earlier.

Similarly, the results in the frequency domain are shown in Fig. 4.2, where it can be highlighted that the pulses applied were able to excite all the frequencies of interest, but a certain ripple can be noticed; this will be further commented when discussing the determination of the scattering matrix elements.

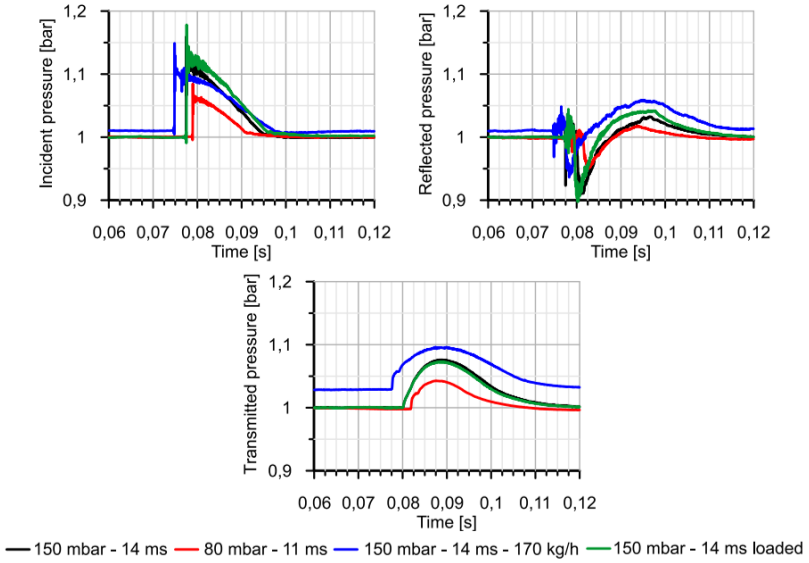

Figure 4.1: Impulse rig: raw results in time domain.

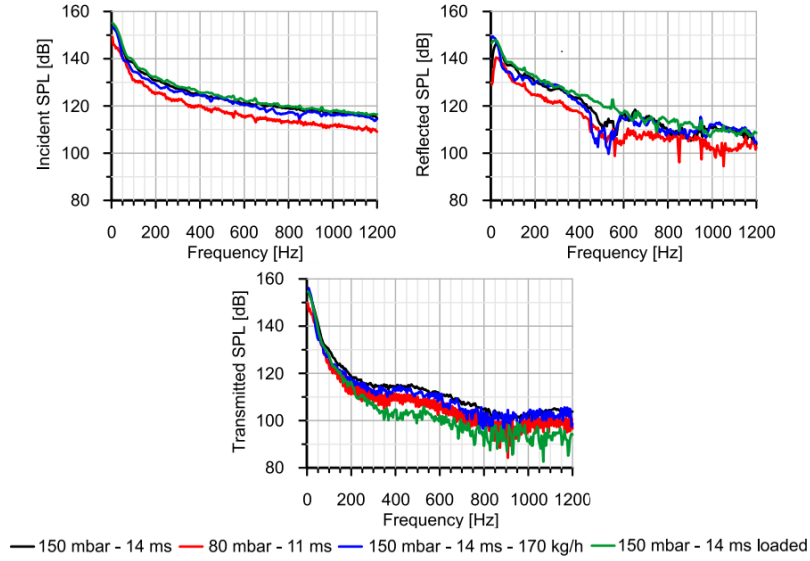

Figure 4.2: Impulse rig: raw results in frequency domain.

Unsteady flow gas stand

An extensive experimental plan was carried out, but for direct comparative assessment and to streamline the analysis, six cases were chosen. A baseline case scenario defined by the five key parameters: mass flow rate, flow temperature, pressure amplitude and frequency, and soot loading; then in each of the other five cases a single variable was modified. Table 4.2 summarizes the operating conditions of these six cases, being the first row the baseline and the subsequent rows having their parameter differing from the baseline highlighted in bold style. The operating conditions were carefully selected to relate them with actual engine operation; for instance, the case with altered frequency has the baseline frequency increased to 100 Hz which is equivalent to the operation of a four-cylinder engine running at 3000 rpm. Soot loaded case was tested at 200°C to prevent regeneration in the presence of O_2 to take place [107].

Table 4.2: Operating points: frequency, mass flow rate, temperature, pulse amplitude and loading.

Freq. [Hz]	Mass flow [kg/h]	Temp. [°C]	Amplitude [bar]	Loading
33	300	200	0.25	no
33	300	200	**0.10**	no
100	300	200	0.25	no
33	300	200	0.25	**yes**
33	300	**500**	0.25	no
33	**500**	200	0.25	no

An example of the raw results obtained for one of this cases is shown in Fig. 4.3.

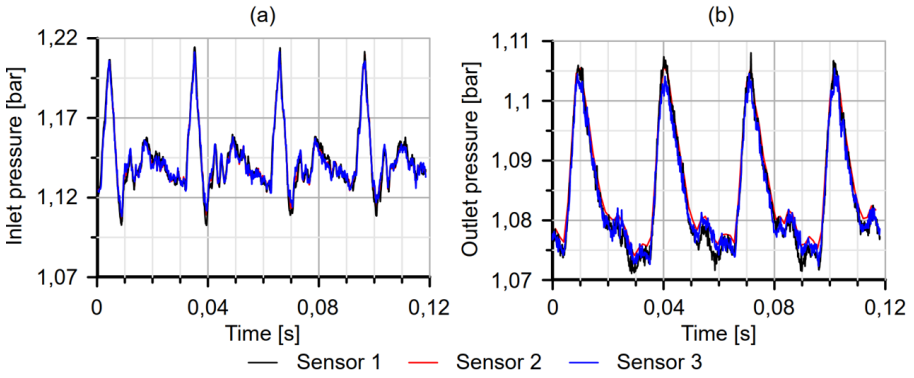

Figure 4.3: Example of raw measurements in the unsteady flow gas stand ($f = 33$ Hz, $\dot{m} = 300$ kg/h, $T = 200°$C, $\Delta p = 0.1$ bar, clean): (a) upstream; (b) downstream. Sensor numbers as specified in Fig. 3.30.

Procedure Application

The procedure followed can be summarized as an experimental implementation of the time-frequency computational method described in [108]. Fig. 4.4 presents the nomenclature used for the pressure components upstream and downstream of the ATS in this assessment.

Figure 4.4: Nomenclature for pressure components.

As shown with the aid of the arrows, p_1^+ and p_2^- are the pressure components travelling towards the ATS, or the exciting components, whereas p_1^- and p_2^+ are the pressure components travelling away from the system, or response components. Assuming linear propagation across the device, these pressure components upstream and downstream will be related by the scattering matrix, as follows:

$$\begin{pmatrix} p_2^+ \\ p_1^- \end{pmatrix} = \begin{pmatrix} t_{12} & r_2 \\ r_1 & t_{21} \end{pmatrix} \begin{pmatrix} p_1^+ \\ p_2^- \end{pmatrix} \tag{4.1}$$

Equation 4.1 also describes the relationship between elements that enables to extrapolate the characterization given by the scattering matrix to any other flow conditions different from those originally used in the measurements. In order to perform the extrapolation, the input pressure components, p_1^+ and p_2^-, and the response components p_1^- and p_2^+, corresponding to the hot and pulsating flow are to be obtained from the application of the beam-forming decomposition outlined in Section 3.2 to the unsteady gas stand measurements. The input components will be used in the extrapolation, whereas the response components will be the benchmark for the scattering matrix extrapolation to be compared with.

The elements of the scattering matrix t_{12}, r_2, r_1 and t_{21} are obtained from the ambient condition measurements in the Impulse Test Rig, as presented in Section 3.2, but still these need be corrected for the flow and the temperature existing in the hot gas stand.

As briefly summarized in the background section, in [39] the influence of flow conditions at room temperature was analysed in detail. The outcome was the formulation of Eq. 4.2 to define the elements of the transfer matrix in terms of two Fourier series. If $\psi_b(f)$ is used to represent the real or imaginary part of any of the elements of the experimentally obtained scattering matrix for the baseline operation point, denoted as b, then it can be expressed as the following sum:

$$\psi_b\left(f\right) = \varphi_b\left(f\right) + \varepsilon_b\left(f\right) \tag{4.2}$$

Here, the first term, $\varphi_b(f)$ corresponds to the Fourier series fitted for the baseline operating point, defined as follows:

$$\varphi_b\left(f\right) = \sum_{k=0}^{n} \left[a_k \cos\left(k\tau_{b,exp} f\right) + b_k \sin\left(k\tau_{b,exp} f\right)\right], \tag{4.3}$$

being a_k and b_k the Fourier series constants, and $\tau_{b,exp}$ the characteristic period.

Meanwhile, the second term $\varepsilon_b(f)$ corresponds to the Fourier series fitted to the difference between the result of applying Eq. 4.3) and the actual experimental data:

$$\varepsilon_b(f) = \sum_{k=0}^{n} \left[a'_k \cos\left(k\tau'_{b,exp} f\right) + b'_k \sin\left(k\tau'_{b,exp} f\right) \right], \tag{4.4}$$

This approach was found to be very robust to reproduce the shift experimented by the elements of the scattering matrix when the propagation velocity varies. Key findings to highlight are:

- Function $\varepsilon_b(f)$ is the same for any device and any element of the scattering matrix.
- Function $\varphi_b(f)$ condenses the effects of geometrical features of the system and response to excitation in the following manner:
  - The constants of the Fourier series are directly related to the geometry.
  - The characteristic period is sensitive to any kind of excitation variation that produces a change in propagation velocity.

In light of this, The characteristic period is the only parameter that has to be modified in order to capture the shift in the elements of the scattering matrix. This in turn enables the use of the scattering matrix measured for a certain baseline flow condition to extrapolate it to any other flow condition if one is capable to determine the value of the characteristic period, τ_b, of the target condition.

Within the same study it was found that the required change in τ_b can be estimated as that required in order to reproduce the change experienced by the elements of the scattering matrix of a simple straight duct when temperature and mean mass flow are modified, as these elements are explicit functions of the two dimensionless quantities characterizing the physics of wave propagation: the Helmholtz number, $\mathrm{He} = kl$, where k is the wave number and l is the duct length, and the Mach number, Ma. In fact, they can be easily obtained from linear acoustic modelling.

An additional advantage of this procedure is that any small inconsistencies in the experimental results, usually related to the need of combining the results of direct and inverse tests, are smoothed out. This is convenient as it provides a representation suitable for a sound interpolation of the data at frequencies different from those directly available in

the measurements. As an example of this, the resulting modulus of the elements of the scattering matrix can be seen in Figs. 4.5 and 4.6, being apparent that the procedure provides conveniently smoothed, suitable for interpolation, results while, in contrast, the raw spectra of measurements shown in Fig. 4.2 exhibited a much more oscillating behaviour.

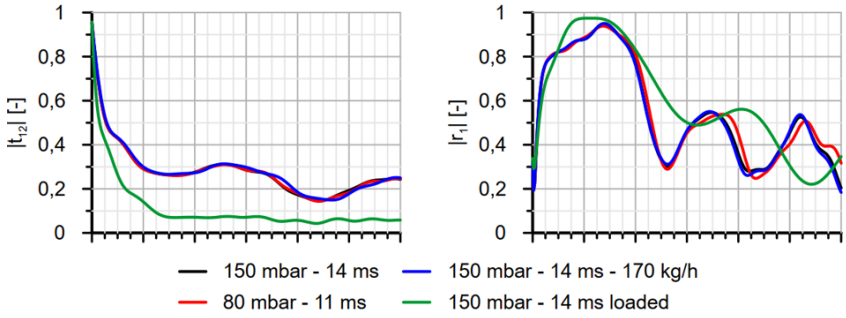

Figure 4.5: Impulse rig: transmission and reflection coefficients from the direct pulse.

Additionally, from Figs 4.5 and 4.6 a first insight on the actual effect of each variable can be drawn:

- Mean flow and pulse amplitude do not have strong influence on the acoustics of the device within the tested range; this matches what was expected.
- Soot load has a significant impact on both the transmission and reflection coefficients, being the effect less pronounced in the reflection side.
- For assessing the temperature effect, the complete extrapolation procedure was needed as changes of this variable affect the coefficients also through the Helmholtz and Mach numbers.

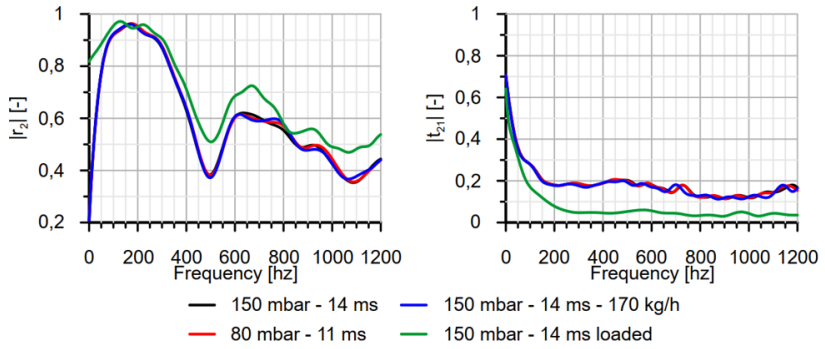

Figure 4.6: Impulse rig: transmission and reflection coefficients from the inverse pulse.

Another relevant source of information is the application of the wave decomposition procedure to the raw measurements from the Unsteady Gas Stand (those shown in Fig. 4.3). This would produce the values of p_1^+ and p_2^- to be used as input to equation 4.1, and the output would serve as the benchmark to be compared with the results of the scattering matrix extrapolation. The results of this decomposition are shown in Fig. 4.7; as the mean values are not provided by the decomposition procedure, these have been assigned arbitrarily to provide the best view of the time domain curves, Fig. 4.7(a). Sound pressure levels plotted in Fig. 4.7(b) have been computed relative to $20\mu Pa$, and it can be observed that the values obtained are in the right order of magnitude when compared to the amplitudes existing in real exhaust lines, and that the wave components upstream of the ATS exhibit larger amplitudes than the downstream components, which also coincides with what could be expected.

The overall assessment procedure is summarized in the flowchart presented in Fig. 4.8; this schematic representation helps to clarify the information supplied and the role played by each of the procedures used and how they interact. The most critical issue is the transformation of the scattering matrix coefficients from the flow conditions in the impulse test rig to those occurring in the unsteady gas stand, since the ability of the period ratio to capture the dependence on the Helmholtz number was not checked in the initial formulation of the method [39].

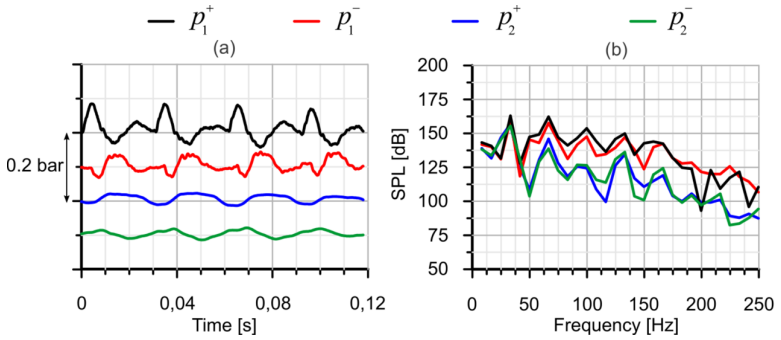

Figure 4.7: Example of wave decomposition results ($f = 33$ Hz, $\dot{m} = 300$ kg/h, $T = 200°$C, $\Delta p = 0.1$ bar, clean): (a) time domain; (b) frequency domain.

4.4 Results and Discussion

The direct comparison of the procedure, as indicated with the grey doted line in Eq. 4.8, is made between the two key sets of results, which are labelled "scattering matrix" and "wave decomposition". The "scattering matrix" set corresponds to the results obtained from the application of Fig. 4.1, this is, the extrapolation using the corrected scattering matrix coefficients and the input components from the wave decomposition of the test in the unsteady gas stand. The "wave decomposition" set is the output components p_1^- and p_2^+ identified by the wave decomposition procedure, this is considered as the experimental benchmark as it comes from measurements within a shorter post-processing procedure.

This direct comparison is graphically presented in Figs. 4.9 and 4.10 for the first eight engine orders (H2 to H16) of the equivalent four-cylinder, four-stroke engine. This is well beyond the usual range of interest in exhaust applications, where the relevant range rarely exceeds the fourth engine order [109].

From the comparison of the two sets of results for the upstream backward components presented in Fig. 4.9, it can be stated that, in general terms, there is an acceptable agreement between the levels estimated through the extrapolated scattering matrix and those directly obtained from wave decomposition. Each case is commented individually bellow.

In the baseline scenario, Fig. 4.9(a), it is apparent that the tendency

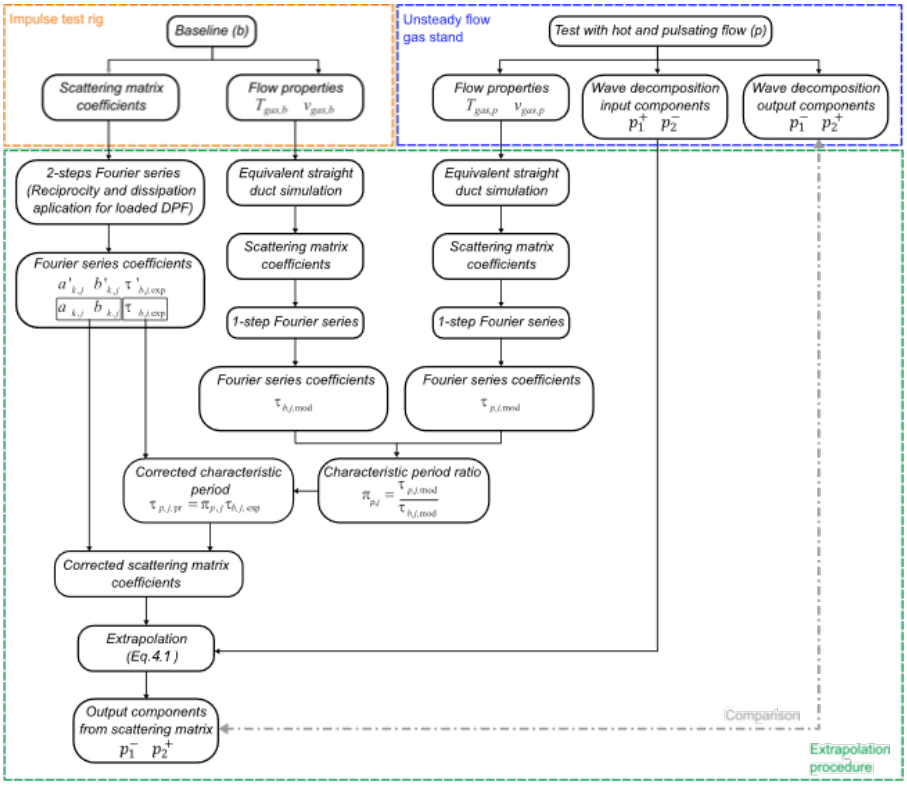

Figure 4.8: Overall flowchart of the assessment procedure.

of the sound pressure level and the dependence on the engine order are perfectly reproduced. The values provided by the scattering matrix lie above those obtained from wave decomposition, with the exception of the first engine order, being all the differences small. In all the engine orders, the discrepancies in the actual level are within 5 dB, which is considered as acceptable for model validation in industrial practice.

In case (b), the pressure amplitude was decreased from 0.25 bar to 0.1 bar, see Fig. 4.9(b); the results still follow the general evolution, but the behaviour is more erratic. It is reasonable to link this to the noise-to-signal ratio as the decreased amplitude worsens that ratio and this poses serious challenges to the use of the wave decomposition procedure, even if a robust algorithm is used.

Case (c) assesses the change in frequency, with an increase from 33 Hz to 100 Hz. The results can be observed in Fig. 4.9(c); this change does not induce any remarkable difference to the results of the baseline case: deviations are in the same order of magnitude and the matching between trends in both datasets is slightly better than for those conditions.

Case (d) corresponds to the soot loaded condition, with 13 g/l of soot; the results are shown in Fig. 4.9(d) and, similarly to case (c), the maximum deviation is comparable to that of the baseline case, and the trend with the engine order is fairly captured.

For case (e) the temperature is increased up to $T = 500°\text{C}$, and the results are shown in Fig. 4.9(e). In comparison with the baseline case, the results are of a similar quality, except in the sixth order, in which the highest deviation for any of the conditions tested is observed. Besides this discrepancy, the overall dependency with the order number is well captured.

Finally, in case (f) the effect of increasing the mass flow rate up to $\dot{m} = 500$ kg/h is assessed, and one may observe in Fig. 4.9(f) that the results are of a similar quality when compared with the baseline case: the dependency with the order number is again well reproduced, and the particular deviations remain within the aforementioned acceptable margin.

These results indicate that the extrapolated scattering matrix approach is able to provide a sufficiently representative picture of the effects of the ATS on the flow upstream of the device.

The corresponding comparison for the downstream forward components is shown in Fig. 4.10 where, again, it can be seen that the extrapolated scattering matrix approach offers an overall fair reproduction of the results provided by the wave decomposition, although the quality of the results is slightly worse than for the upstream backward components. Accordingly with previous comments, this might be expectable, since the ATS produces a significant decrease in amplitude and thus any negative repercussions of the noise-to-signal ratio on the performance of the wave decomposition method should be even more apparent.

The baseline case scenario is presented in Fig. 4.10(a) and, as for the upstream backward components, all deviations lie within the acceptable margin with the exception of the twelfth engine order; something similar

will be evidenced in some of the following cases as well, but always in engine orders above the tenth, which are associated with relatively low amplitudes and out of the usual range of interest. The overall trend reproduction is satisfactory.

Cases (b) and (c), which results are presented in Fig. 4.10(b) and Fig. 4.10(c), also capture the overall trends properly, but deviations are more evident, in particular in the fourteenth engine order for the decreased pressure case and the twelfth engine order for the increased frequency case, both above the usual range of interest.

The soot loaded case (d) and the increased temperature case (e) showed very good agreement between datasets. As one can observe in Fig. 4.10(d), the results are those closest to the baseline scenario, whereas in Fig. 4.10(e) the only remarkable deviation occurs in the sixteenth engine order and the trend is clearly captured with the exception of that engine order.

Finally, case (f), the one with the increased mass flow operating condition (500 kg/h), can be seen as the outsider of the study. In Fig. 4.10(f). it is evident that the agreement between datasets, the trend replication and the deviations are not comparable to those of previous cases. A reasonable explanation would come, again, from the consideration of the noise-to-signal ratio of the measurements: the higher velocities occurring in this operating condition should give rise to strong turbulent fluctuations that, in the upstream side, can be overcome by the relatively high amplitude of the deterministic signal but, in the downstream side, this may be an insurmountable difficulty for the wave decomposition algorithm.

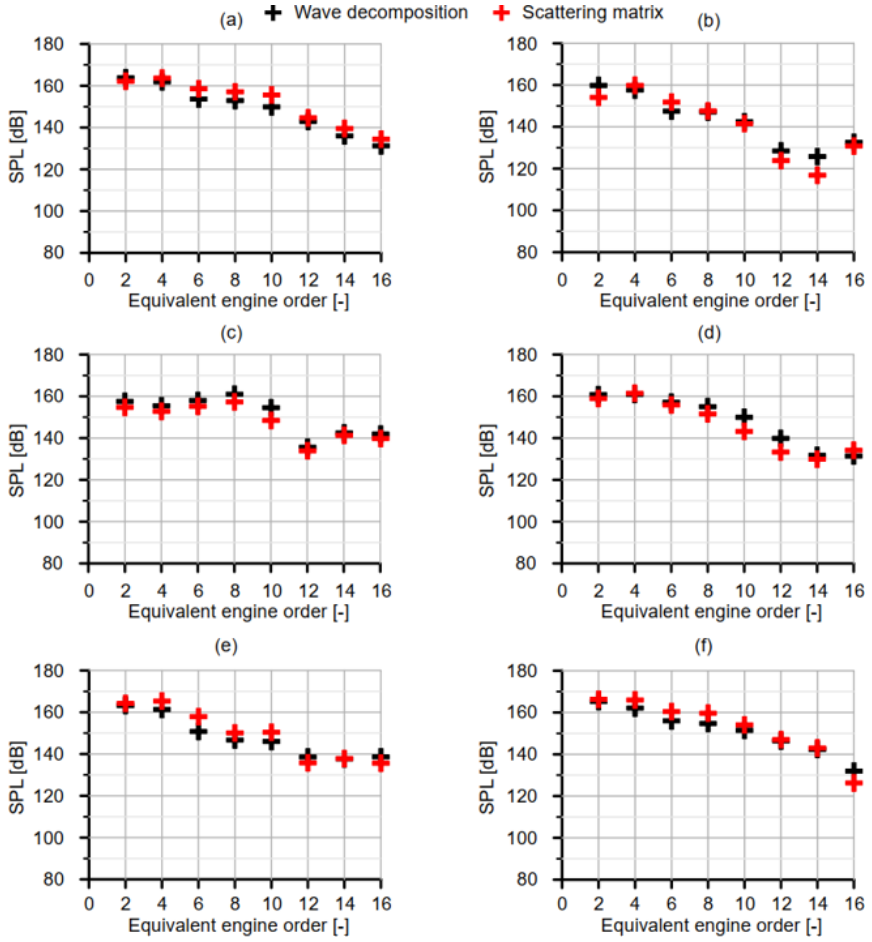

Figure 4.9: Comparison of measured and estimated backward components upstream of the ATS, p_1^-: **a** baseline ($f = 33$ Hz, $\dot{m} = 300$ kg/h, $T = 200$°C, $\Delta p = 0.25$ bar, clean) **b** $\Delta p = 0.1$ bar **c** $f = 100$ Hz **d** loaded **e** $T = 500$°C **f** $\dot{m} = 500$ kg/h.

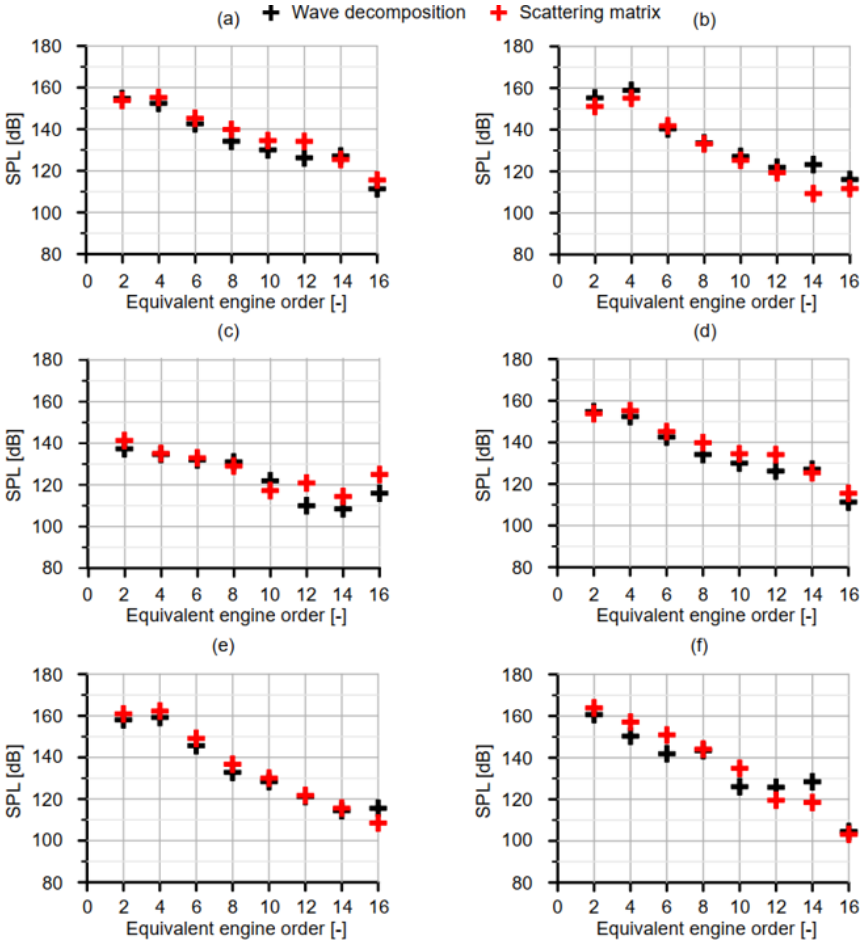

Figure 4.10: Comparison of measured and estimated forward components upstream of the ATS, p_2^+: **a** baseline ($f = 33$ Hz, $\dot{m} = 300$ kg/h, $T = 200$°C, $\Delta p = 0.25$ bar, clean) **b** $\Delta p = 0.1$ bar **c** $f = 100$ Hz **d** loaded **e** $T = 500$°C **f** $\dot{m} = 500$ kg/h.

Chapter 5

Case study on a complete SCR exhaust line with static swirl mixer

Part of the approach, results and analysis presented in this chapter, in particular in the section *The overlooked effect of auxiliary devices* can also be found in the paper *Assessment of the fluid-dynamic and acoustic behaviour of a swirl static mixer for after-treatment systems* [1], which is a JCR publication derived from this part of the research. Also some of the insights related to the discussion of decomposition analysis results might be similar to those presented in the other thesis-related publications enumerated in the *Publications* section.

5.1 Introduction & Background

The extensive use of diesel engines and their intrinsic NOx emission issues have consolidated Selective Catalytic Reduction (SCR) systems as one of the more common [110] and effective solutions to apply [111]. The historical development of this after-treatment technology started in industrial stationary equipment to be then transferred into marine propulsion systems, and at last around 2005 to automotive applications, with the corresponding challenges to adapt its design, function and integration to automotive powertrains [112].

Selective Catalytic Reduction technology can be found as either Flow-Through monoliths, which is the standard application and is commonly referred as slow SCR or simply SCR, or applied as catalyst coating on some DPF applications, often called catalyzed DPF (DPFc), SCR-F or SDPF in the literature [113, 114, 115, 116]. The functioning principles of SCR systems involve several chemical reactions; for such end, diesel exhaust fluid (DEF, also known as urea-water solution, UWS) is injected to the exhaust fluid upstream of the monolith [20].

The two key aspects to check for proper and efficient SCR operation are the DEF injection and the mixing [111]: injecting the right amount at any given operating conditions is key to avoid insufficient NOx reduction due to lack of, or unacceptably high, ammonia slip due to excess. On the other hand, uniform flow distribution and mixing of the reductant with exhaust gases must be ensured to achieve the desired high NOx conversion. Maldistribution can also induce poor NOx conversion and ammonia slip in specific channels, even simultaneously [117]. Designing and tuning the trade-off between NOx conversion efficiency and ammonia slip is challenging [110], and the use of mixers (mixing inducers) or considering a sufficient mixing pipe length upstream of the SCR catalyst are the most common solutions [20, 111].

Regarding the mixer there are several embodiments, term that accounts for their specific shape and interaction with the flow; some of them are: Swirl inducing mixers [118, 119, 120], lateral line tabs and baffles [121, 122, 123], perforated plate and tunnel type [124], wire-mesh-like wall structure [125], spiral passages [20] and even sometimes combinations have been used [126, 127, 128]. Some of these embodiments are illustrated in Fig. 5.1.

There is a relatively abundant literature on the mixing efficiency and the pressure drop (PD), as well as on the use of numerical modelling, specially CFD, to approach these devices. Related studies involving both experimental measurements alongside with numerical simulation date back to Seo et al. in 2008, who studied the effects of blade characteristics of a swirl mixer on the fluid mixing [131], and are still an active field, as shown by the recent contributions of Zhang et al. [132], Blinov et al. [133] and Zhao et al. [134]. In contrast, no research regarding nor mentioning the acoustic influence or the transmission loss (TL) of the mixer element has been found, and thus it is presumed that due to

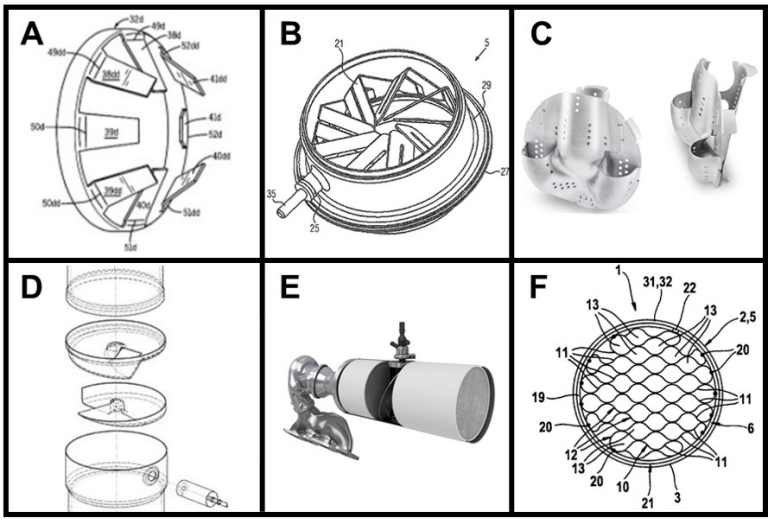

Figure 5.1: Examples of several types of static mixer embodiments; A: Axial tabs Type [121], B: Swirl or Fan Type [119], C: Perforated Plate/Tunnel Type [129], D: Septum type [130], E: Intermediate Baffle Type [128], F: Directional Mesh Type [125].

the rather small size of these elements in comparison to the whole ATS system it is directly assumed that their influence should be negligible and considered out of interest for acoustic research.

Against this backdrop, this chapter is dedicated to the thorough characterization of a complete exhaust system labelled as ATS1 which is a SCR system, representative of current commercial application, that has a DEF injection port, a static swirl mixer inducer, a considerable pipe length to reach homogeneity and two cans containing standard FT SCR monoliths, two in the first can, and one in the second. The opportunity to study a device with a straight-forward geometrical configuration, which has components that can be studied either isolated or assembled, allowed to assess aspects such as the effect of having one or two monoliths, the interactions between components (additivity of PD and TL) and the acoustic importance of the auxiliary device, in particular its mixer element, as well as to explore the ability of different modelling approaches to reproduce the experimentally measured

behaviour.

The acoustic and fluid dynamic characterization of all devices in this chapter and the following (Chapter 6) were performed considering two flow configurations: steady flow and impulsive flow. The steady flow condition can be easily related to the real exhaust flow for vehicles when the engine operates at high speeds, as the mean component dominates over all fluctuations related with engine operation; this was explored in depth in [135]. On the other hand, the impulsive flow condition is representative of low to medium engine speeds.

Steady flow is reached for each mass flow rate imposed in the CFTB, and only then the total PD across the device is measured as exposed in section 3.2.1. On the other hand, the tests for acoustic response characterization in the ITR with superimposed mean flow, following the procedure described in 3.2.2, account for the unsteady behaviour. Despite the differences in temperature and impulsiveness of the actual flows in an exhaust line, the work done in the previous chapter (Chapter 4), and presented in [3], demonstrates that the acoustic response measured with the ITR is representative on actual engine conditions. And for the PD measured with the CFTB, it was shown in [101], that the results may be safely extrapolated to those conditions.

5.2 Assessment of individual devices containing monoliths

Assessment Procedure

The assessment procedure involves both experimental and computational workfronts. ATS1 is by itself the subject of study of this chapter alongside its composing devices and their partial assemblies. This first section is devoted to the two composing devices that contain monoliths, ATS1-D1 and ATS1-D2. In order to characterize each device isolated –interactions and results of combining them are assessed in Sections 5.4 and 5.5– it was necessary to split apart the system as indicated in Fig. 5.2. Clamp adapters were prepared in order to fit the ATDs into the experimental installations and to combine them back together for further tests. As this systems has a quite straightforward geometry the clamps needed were relatively small, which in turn helped to keep modifications

at a minimum.

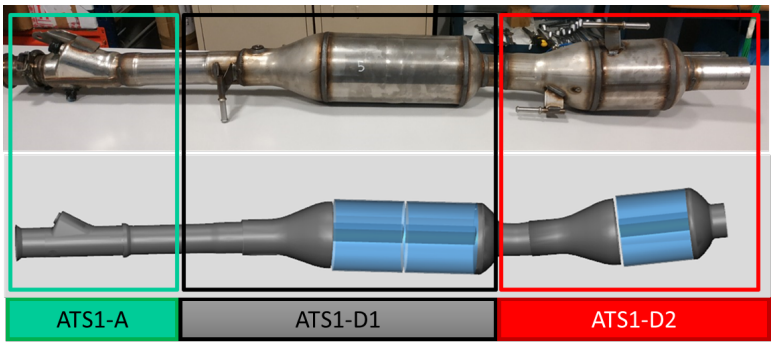

Figure 5.2: ATS1 (before split) and its composing ATDs

Pre and Post Split Validation

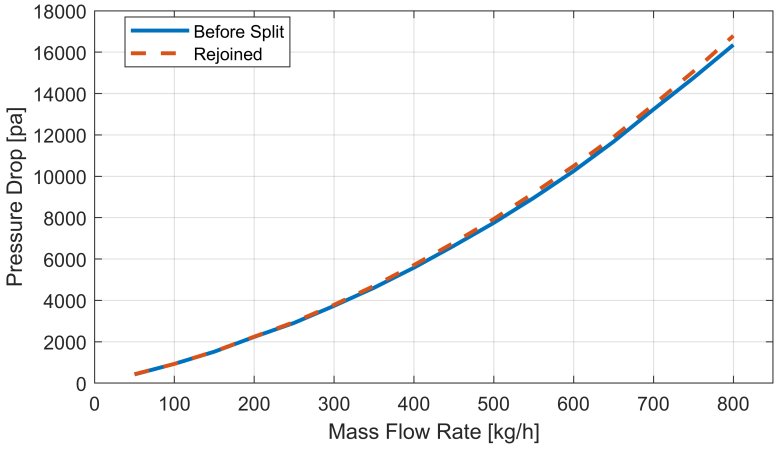

Figure 5.3: Validation of changes induced in PD due ATS1 split preparation

The differences induced by the splitting were revised experimentally, comparing the results from measurements taken before and after the

split, more precisely, after all other measurements required for the characterization of isolated and combined devices that will be presented in this chapter were finished.

Figs 5.3 and 5.4 show the results of that comparison for the PD, Re-Ma trend and K factors. It can be seen that the Reynolds-Mach number trend changed slightly but this can be attributed to the addition of clamp adapters for reassembling. On the other hand, the K factors K_{test} (installation + ATS) and K_{ATS} are virtually unaffected, which is consistent with PD results being barely changed.

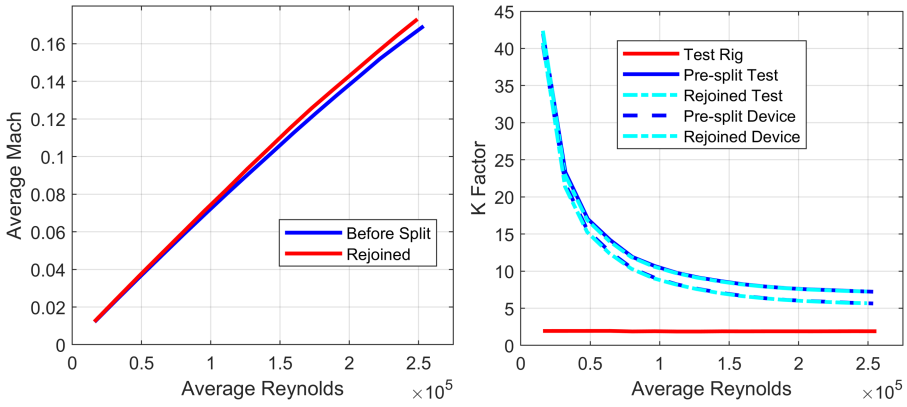

Figure 5.4: Validation of changes induced due to ATS1 split preparation on; Re-Ma trend (left side), K_{test}, K_{duct} and K_{ATS} factors (right side).

Regarding TL, comparison of results with 100 and 300 kg/h of superimposed mean flow are presented in Figs. 5.5 and 5.6 respectively. For the first case, minor differences were found up to the 1200-1300 Hz range, keeping essentially the same trend. The discrepancies observed might even fall within the range of acceptable variation for an unaltered device given the complexity of the test procedure. On the other hand, for the 300 kg/h the resemblance between results is less evident due to a considerably more oscillating behaviour, but the main trends are also preserved.

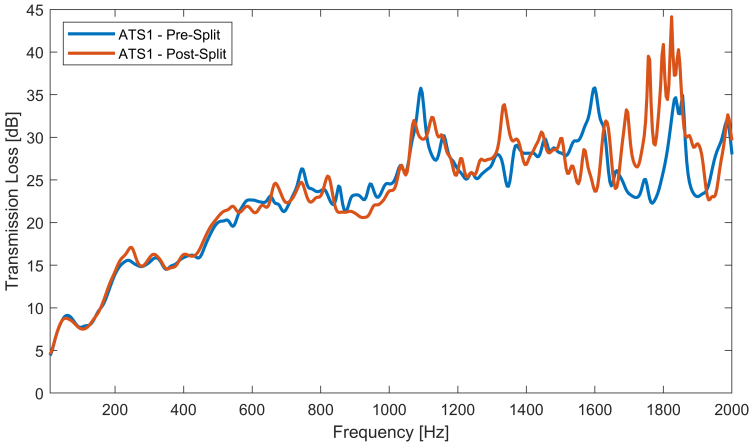

Figure 5.5: Validation of changes induced in TL due to ATS1 split preparation with a 100 kg/h of superimposed MFR

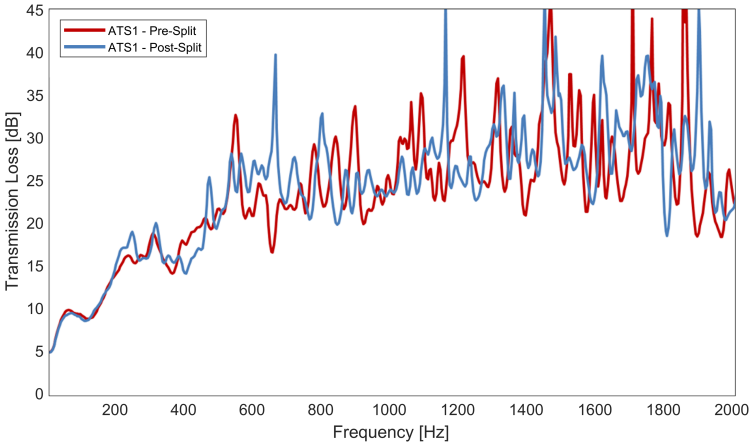

Figure 5.6: Validation of changes induced in TL due to ATS1 split preparation with a 300 kg/h of superimposed MFR

These observations lead to conclude that, at least for the two characteristics of interest, the back-pressure and the sound attenuation, neither the splitting process nor the tests performed on the composing

devices have affected the behaviour of the different composing devices. In consequence, the results of the characterization performed before the splitting are to be the ones used as reference in all comparison with individual devices and their partial combinations.

Experimental assessment

Table 5.1 summarizes the measurements taken for ATS1-D1 and ATS1-D2.

Table 5.1: Information on the experimental measurements taken for devices ATS1-D1 and ATS1-D2.

Characterization		**ATD**	
Test Facility	*Condition*	*ATS1-D1*	*ATS1-D2*
Pressure drop testing on CFTB	Min. MFR	50 kg/h	50 kg/h
	Max. MFR	800 kg/h	800 kg/h
	Increase steps	50 kg/h	50 kg/h
Transmission loss testing on ITR	Orientation	Dir. & Inv.	Dir. & Inv.
	Flowless	1 pulse amp.	1 pulse amp.
	MFR 100 kg/h	2 pulse amp.	2 pulse amp.
	MFR 200 kg/h	2 pulse amp.	2 pulse amp.
	MFR 300 kg/h	2 pulse amp.	2 pulse amp.

Preparation of modelling assessment

ATS1-D2: Single Monolith Device

Regardless of it being originally placed downstream of ATS1-D1 and being labelled with the number 2, this is the less complex of all the devices with monoliths, and was therefore chosen to start the modelling assessment. Fig. 5.7 shows the CAD file equivalent to the part, with colours to highlight differences between components after the discretization. It was also the first in which the iterative process allowed to account for differences produced by the ways to represent components in the modelling. Fig. 5.8 shows three of the alternatives considered for this device, being Option 3 the one selected, and finally Fig. 5.9 shows the 1D model prepared accordingly.

Figure 5.7: CAD file of ATS1-D2 showing the different components after the discretization process.

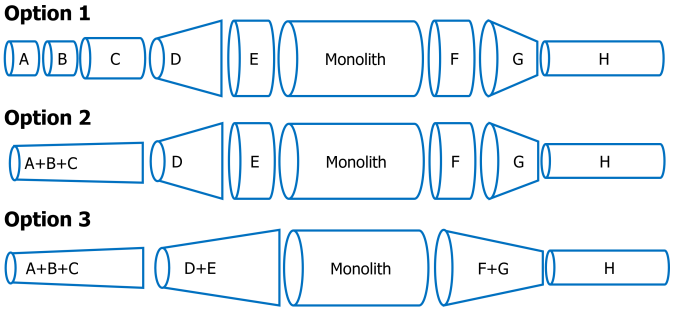

Figure 5.8: Considered options to represent ATS1-D2 components in the 1D modelling approach.

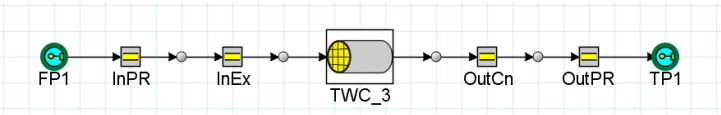

Figure 5.9: 1D Model representing ATS1-D2.

ATS1-D1: Double Monolith Device

The second device to be assessed was ATS1-D1, continuing with the philosophy of increasing the complexity one step at a time. This device is almost identical to the previous one but with the inclusion of a second monolith, both monoliths identical, and an empty gap between them. An early schematic of the potential discretization of this device was shown in Fig. 3.39; now, taking as starting point the discretization and modelling of ATS1-D2, Fig. 5.10 shows the definitive discretization and how it was translated into the 1D model.

Several options were considered to account for the gap between monoliths, preparing DOEs from which the preference of PipeRound and FlowSplitGeneral over neglecting or representing it with FlowSplitNode was deducted. It should be highlighted that neglecting the gap induces errors in the software if the consecutive monoliths do not have identical number of channels, and even if the simulation runs, it fails to produce satisfactory results. Fig. 5.11 shows the final 1D model produced.

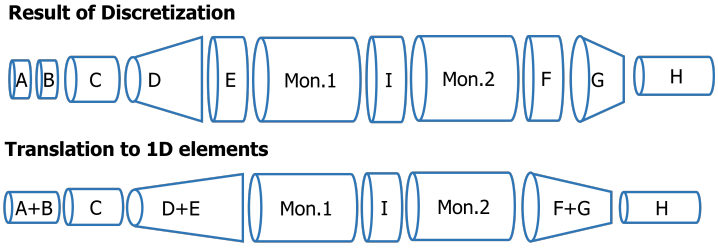

Figure 5.10: Discretization and translation into 1D modelling of ATS1-D1.

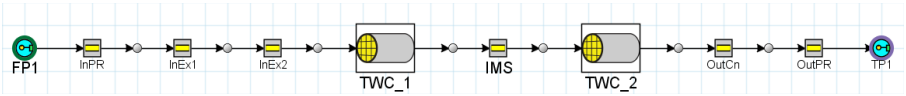

Figure 5.11: 1D Model representing ATS1-D1.

Results and Discussion

ATS1-D2: Single Monolith Device

Moving to the results and their analysis, Figs. 5.12 and 5.13 show the pressure related results derived from CFTB. The PD exhibits a quasi-quadratic behaviour as a function of increasing mass flow rate, as expected; however, the presence of a FT monolith induces a linear term related to the laminar flow effects occurring within the monolith channels, which in this case are strong given the proportion of volume occupied by the monolith in the complete device. Additionally, the pressure drop coefficient exhibits the right asymptotic behaviour within the measurement uncertainties, and it appears that stable fully-developed flow conditions have been reached at high Reynolds numbers. For both cases the device contribution to the test is larger than that of the duct.

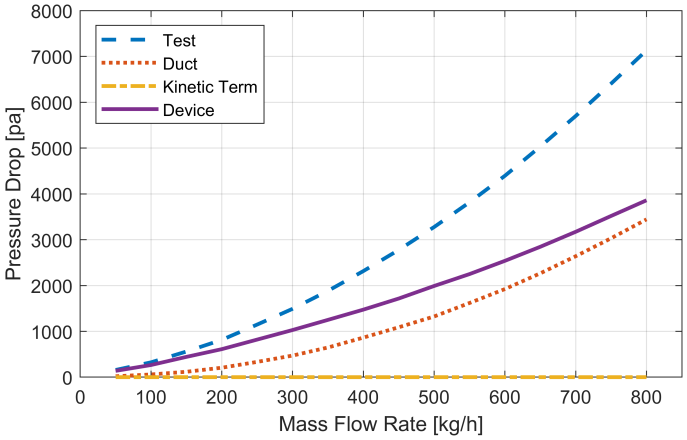

Figure 5.12: Experimental PD results from ATS1-D2 characterization.

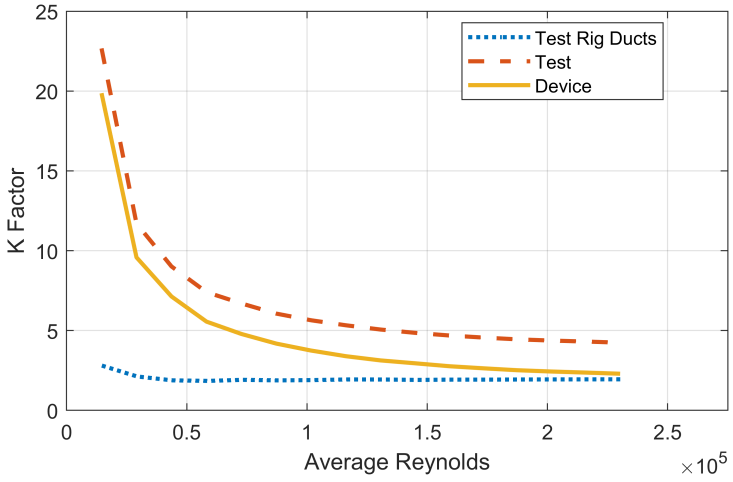

Figure 5.13: Pressure drop coefficient, K factor, from experimental assessment of ATS1-D2.

Fig. 5.14 shows the results obtained when using the prepared virtual twin of the device in the PD testing template prepared; both experimental and modelled PD results for the test, the device and the ducts of the rig are shown. The agreement obtained for this device is excellent, which confirms that the tuning of parameters is adequate and can be considered as a starting point as, even being the less complex of all the devices, it already contains the core components of most of them (the exception is the auxiliary device), this is: inlet and outlet pipes, some expansion and contraction volumes and the presence of a monolith in between, even though all other monolithic devices have at least two monoliths.

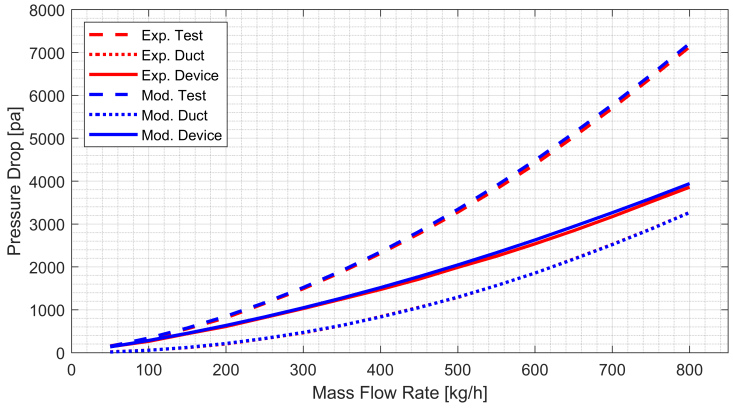

Figure 5.14: Comparison of Exp. and 1D Mod. results for ATS1-D2.

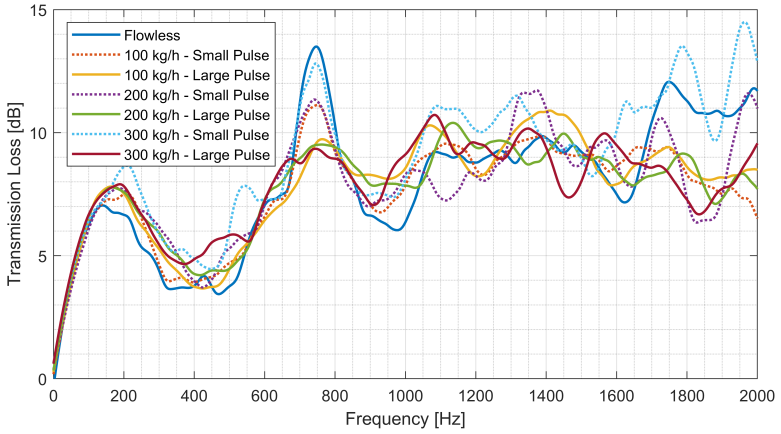

Figure 5.15: Complete set of exp. smoothed TL results for ATS1-D2.

Fig. 5.15 presents the complete set of smoothed TL results available for this device, i.e. the results for the flowless measurement, and two results for each mass flow condition, one per pulse amplitude. From these results, the effect of flow seems to be that expected: an increase in the attenuation associated with dissipative flow-related effects, but otherwise keeping the trends unchanged, except in the vicinity of 730 Hz

where an unexpected resonant spike appeared. This spike is very evident in the flowless case, and appears to be damped, but still noticeable, in the cases with superimposed mean flow. This attenuation is more evident in the cases excited by a large pulse. No explanation coming from the geometrical characteristics was found for the resonant spike, which is certainly strange in such a simple geometry; it is likely that it might be related to some defect, either in the part or in the mounting.

Even though similar sets of results are available for all the devices and systems characterized, both before and after the smoothing process, plots like Fig. 5.15 including modelled results provide an inadequate visualization of the results for comparative analysis, as the amount of lines plotted is excessive. In this respect two decisions were made:

- The use of the smoothed TL is preferred in most situations, in particular to compare with modelled results. Figs. 3.27 and 3.29 already exemplified the convenience of this representation back in Chapter 3.

- Similarly, for results with superimposed mass flow, those from tests with large pulses are preferred over those made with small pulses. It was evidenced that for all the characterizations performed, the results produced with small amplitude pulses tend to be more oscillatory or "noisy", even after smoothing, but keeping the overall behaviour. Therefore, the information provided by having both small and large pulse results together is not significant, just making the visualization of results and their analysis less evident.

Therefore, from this point on, the 1D vs experimental TL results showing the effect of superimposed mass flow rate will be focused on those with large pulse; Fig. 5.16 is thus the first figure with results presented in such a manner.

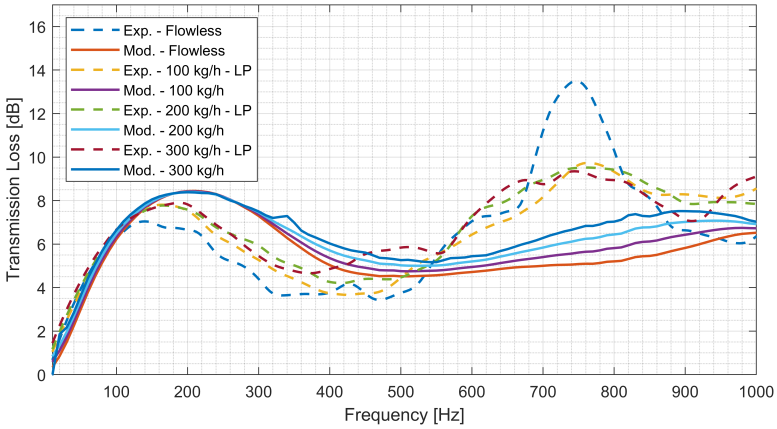

Figure 5.16: Comparison of exp. smoothed and 1D mod. TL results for ATS1-D2.

This first two results show some traits that most of the final 1D models prepared share to some extent:

- The initial ramp, from 0 to 200 Hz approximately, which is known to be strongly related with a precise volume representation, is properly captured.
- Around 500 Hz in this case, and in the $500 - 650$ Hz range, where in this case the modelled and experimental results intersect each other, was found to be a common frequency range where the modelled results start to lose precision.
  Nonetheless, in this case the unexpected and unexplained resonant spike in the experimental measurements explains most of the discrepancies.
- The effect of mass flow is properly reproduced.
- Some points to take into account using this frequency range as reference:
  - The overall shape of the TL curve up is captured.
  - Up to the mentioned range, 500 Hz in this case, all differences are within a 3 dB margin, and beyond the range most are

within a 5 dB range, this is, within the reasonable margin considered as acceptable for model validation in industrial practice.

– The order of magnitude of the peak attenuation up to 500 Hz is adequately reproduced.

– This overall satisfactory results are from a 1D model being directly compared to its experimental benchmark, which supports the idea of this tool being useful and indicative for the design process.

ATS1-D1: Double Monolith Device

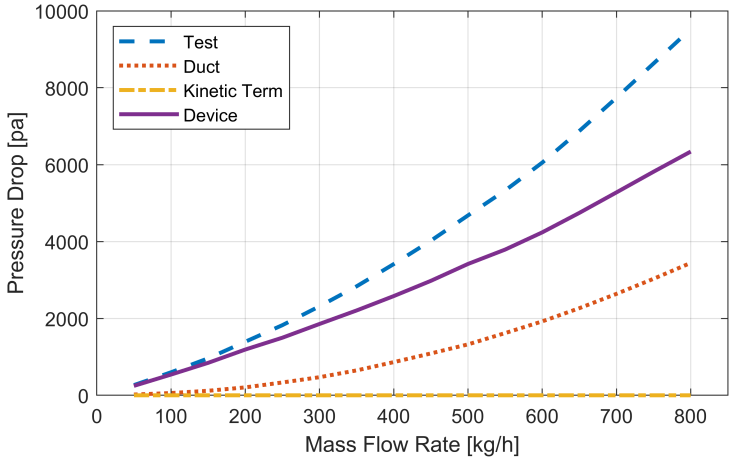

Figure 5.17: Experimental PD results from ATS1-D1 characterization.

Figs. 5.17 and 5.18 show the results from the experimental characterization of ATD1-D1. Its PD exhibits the expected quasi-quadratic behaviour, with the linear term present due to the double monolith; also the K factor exhibits the right asymptotic behaviour within the measurement uncertainties, and it seems to reach stable fully-developed flow conditions at high Reynolds numbers. Even though direct comparison between devices is presented later, the backpressure is almost double than that of ATD1-D2 (1.65 times), which is understandable as the ef-

fect of the monolith is somehow doubled, and the other elements are practically identical. In both cases, the device contribution to the test is larger than that of the duct.

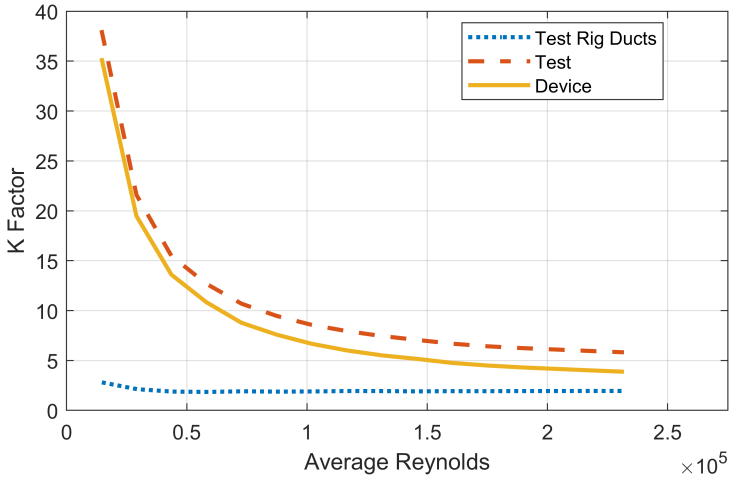

Figure 5.18: Pressure drop coefficient, K factor, from experimental assessment of ATS1-D1.

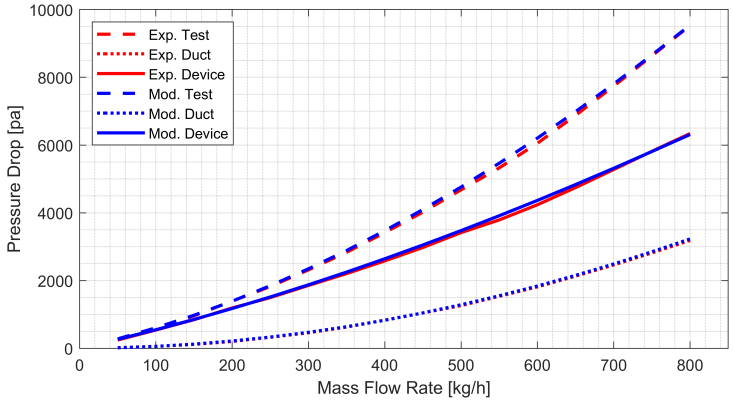

Figure 5.19: Comparison of Exp. 1D and Mod. PD results for ATS1-D1.

Fig. 5.19 shows the comparison of PD results with those from the prepared virtual twin, and once again the agreement is excellent. Therefore, the modelling strategy and the tuning are also adequate for a slightly more complex device, due to the second monolith and the intermediate gap. ATD1-D1 is the first device with two monoliths, a characteristic shared with most other devices, in particular two FT monoliths, as also ATD2 and ATD3 have, being therefore a good reference for comparison and analysis, as presented later in Chapter 6.

Fig. 5.20 shows the experimental TL results. In this case, the increase in attenuation due to flow-related dissipative effects is present but seems to be less significant. The signals are found to be smoother than those of ATS1-D2 (even prior to smoothing), still being the results from small pulse tests more noisy. Also, no resonant spike appears, therefore fully matching what could be expected. Overall, these results may be regarded as the typical behaviour of a two-monolith device: while some of the acoustics of the device are still apparent in the curves, no passbands exist due to the dissipative effects occurring in the monoliths.

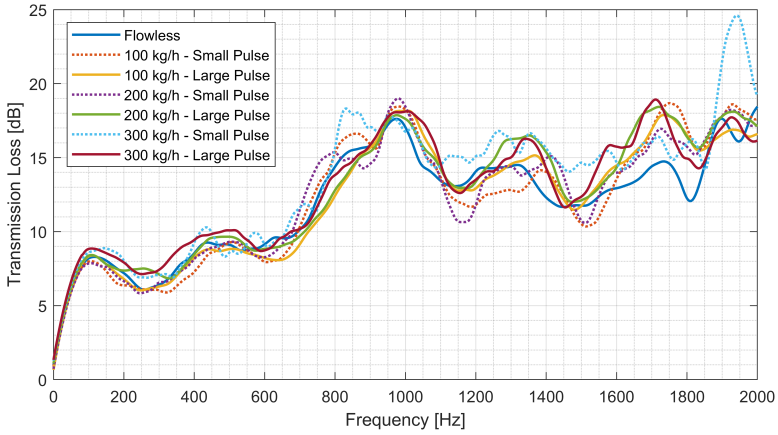

Figure 5.20: Complete set of exp. smoothed TL results for ATS1-D1.

Fig. 5.21 shows the comparison of experimental and modelled results, with the following findings:

- Similar to those of ATS1-D2, the initial ramp is properly captured

suggesting an appropriate volume representation.

- Superimposed mass flow effect is properly represented.
- The overall shape of the TL curve up is also captured.
  - In this case the satisfactory agreement, within a 2dB margin, is kept up to almost 700 Hz.
  - The order of magnitude of the peak attenuation up to 700 Hz is adequately reproduced.
  - Even above 700 Hz the ascending tendency is reproduced, although the precise values are underestimated.
- As there is no resonant spike for this device, it is easier to appreciate the adequacy of the modelled results in these figures.

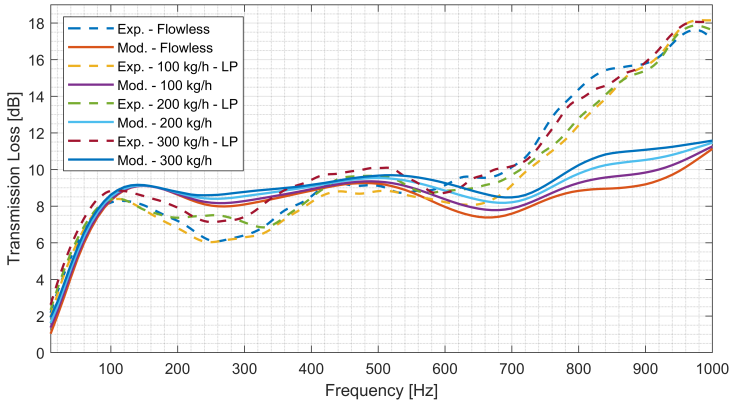

Figure 5.21: Comparison of exp. smoothed and mod. (1D) TL results for ATS1-D1.

5.3 The overlooked effect of auxiliary devices

ATS1, as an SCR system, requires DEF injection for proper functioning; this is supplied by a injector whose port is located in a lateral extended volume (DEF injection port) upstream of the devices with SCR monoliths, and also incorporates a static swirl mixer followed by an straight and reasonably long mixing pipe. Applying the device and system criteria established and the discretization guidelines, the inlet pipe section of the ATS, the DEF injection port, the mixer and about half of the mixing pipe form a functional auxiliary sub-system here classified as a device and studied under the label ATS1-A.

Assessment Procedure

ATS1-A is studied and characterized using the experimental measurement procedures and post-processing described in Chapter 3; all required information was obtained, and then used as the benchmark to assess different modelling options suitable for engineering practice, most notably the 1D modelling approach.

Further details on the static swirl mixer

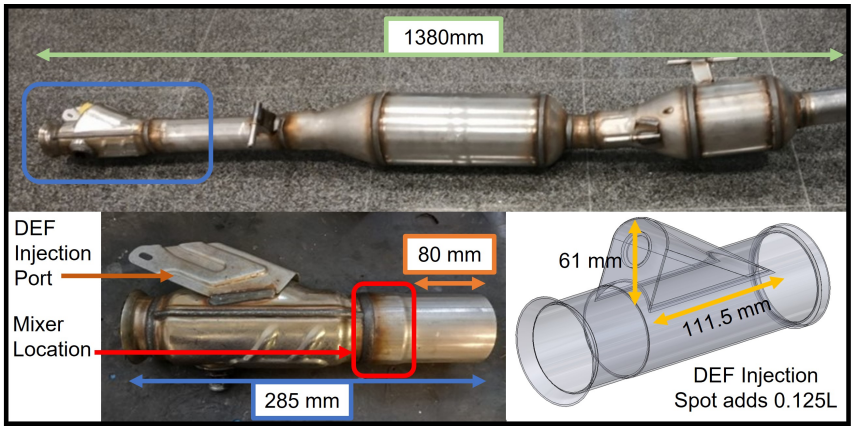

Figure 5.22: ATS1-A and mixer location in ATS1.

ATS1-A has been briefly introduced, but the mixer, which is the core element of this device, has not been properly presented yet. Fig. 5.22 illustrates the geometrical configuration, location and size of ATS1-A in regards of the whole system. The mixer itself can be seen in Fig. 5.23; it has 16 vanes with a certain twist and orientation that divides the flow and forces a spinning motion in the flow, thus rising turbulence and favouring the mixing of injected species. These characteristics place it in the static swirl mixer embodiment, also called fan type but, contrary to the more extended designs of this kind, this mixer lacks of a hole opening in the middle.

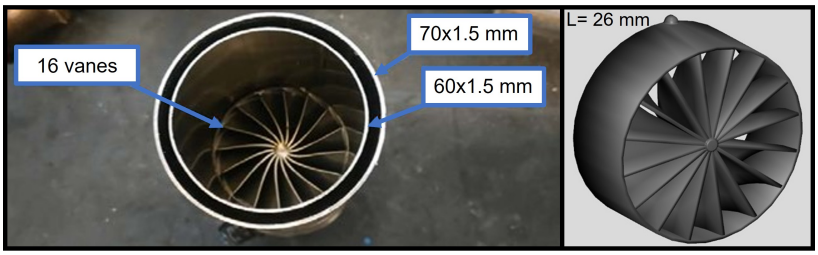

Figure 5.23: Detail of the static swirl mixer of ATS1-A.

Experimental methodology

The measurement campaign for this device is summarized in Table 5.2.

For this device the decomposition and analysis of reactive and dissipative effects was performed with the logarithmic approach as presented in Section 3.2.3.

Computational methodology

In order to get further insight into the behaviour of ATS1-A, and specially the mixer element, 3D and 1D modelling approaches were checked.

Table 5.2: Information on the experimental measurements took for device ATS1-A.

Characterization		**ATD**
Test Facility	*Condition*	*ATS1-A*
Pressure drop	Min. MFR	50 kg/h
testing on	Max. MFR	800 kg/h
CFTB	Increase steps	50 kg/h
	Orientation	Direct and Inverse
Transmission	Flowless	1 pulse amp.
loss testing	MFR 100 kg/h	2 pulse amp.
on ITR	MFR 200 kg/h	2 pulse amp.
	MFR 300 kg/h	2 pulse amp.

1D Approach

For this part, the 1D modelling had two stages: the first was produced by following the same approach as for the devices with monoliths, the 1D virtual twinning methodology on structuration and the guidelines to account for the PD as emulating the measurements in the CFTB, and for the TL up to 1000 Hz (as the software suggests). The results of such stage are those taken into account in the later assessment of additivity. In the second stage, a copy of the model and TL templates were readjusted to account for TL up to 2500 Hz and also to validate the capability of 1D modelling to reproduce certain features identified in the experimental and 3D approaches. The latter stage is presented at the end of the section as it was conceived as a consequence of the results of experimental and 3D approaches still to be presented.

Virtual Twinning

The simplified CAD prepared and the discretization determined for this device, were already presented as an example in Fig. 3.40; the 1D model prepared in concordance to such discretization is presented in Fig. 5.24.

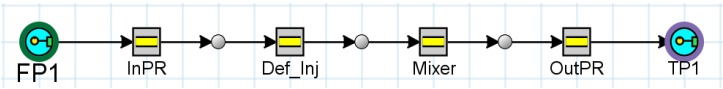

Figure 5.24: 1D Model representing ATS1-A (1st stage).

3D Approach

As an overall reference, full 3D models of ATS1-A were built and are briefly described in the following.

Pressure drop

PD was studied with CFD simulations using the Finite Volume Method (FVM) using STAR-CCM+ for the solution of the Unsteady Reynolds Averaged Navier Stokes (URANS) equations. This simulation was configured as follows:

- The turbulence model chosen was the $k-\omega$ with shear stress transport [136], that was successfully used in cases involving highly detached zones [137] or swirling flows [138].
- The inlet and outlet surfaces were extruded 10 times their respective diameters to avoid undesired effects from the proximity of boundary conditions.
  - Inlet surface was set as a “flow inlet” boundary.
  - Outlet surface was set as a “pressure outlet” boundary with a constant relative pressure of 0 Pa.
    Since the inlet Mach number is lower than 0.3 at any value

of the incoming mass flow the flow can be assumed to be incompressible and, therefore, the results hold valid for different values of the outlet pressure.

- The fluid was assumed to be air, with a constant density of 1.18 kg m^{-3} and a viscosity of $1.86 * 10^{-5}$ Pa s.
- The meshing approach was to use the polyhedral mesh, which usually ensures grid independence with fewer elements than tetrahedral meshes [139], and the following characteristics:
  - The overall maximum size was set to 4.5 mm.
  - In the wall boundaries the mesh size was set to 1.6 mm.
  - The vanes had a special refinement where grid size varied between 0.10 mm at the edges and 0.25 mm at the rest of the blades.
  - Downstream of the blades, the size was 1.1 mm.
    With this configuration a mesh with of approximately $17{\cdot}10^6$ elements was generated.
- A prism layer of thickness 0.80 mm and 14 elements was generated at the walls, ensuring that, for the maximum mass flow, the value of y^+ was kept below 1 for most of the surfaces.
- A grid independence study was conduced with meshes up to $64{\cdot}10^6$ elements, without finding significant discrepancies between the results.

Transmission loss

Assessing the acoustic properties of the device, effects of the mixers, and with interest to account for possible interactions of the mean flow with the acoustic field, the linearized Euler equations were solved using the commercial software COMSOL Multi-physics. The mean flow was mapped onto the mesh by interpolating the data obtained from the CFD simulations, similarly as performed in [99] or [100].

The device was discretized using second order tetrahedral elements, with a maximum size of 10 mm, and refinements to be 1 mm at the

blades and section changes. The resulting mesh generated had approximately $9.7{\cdot}10^5$ elements. The fluid was assumed to be air at $T = 300$ K, with a constant speed of sound (c) of 347 m s^{-1}. A grid independence analysis was performed with meshes of up to $5{\cdot}10^6$ elements, without any relevant differences in the results.

The transfer matrix was obtained by considering two independent boundary conditions at the inlet and at the outlet: first, an acoustic pressure of 1 Pa at the inlet and of 0 Pa at the outlet, and secondly with the same pressure at the inlet but with an anechoic termination at the outlet.

Results and Discussion

The following paragraphs cover the results obtained and their analysis. In order to provide context and to evaluate the influence of the auxiliary device ATS1-A –and in particular the mixer element– several results include also those of the complete ATS1.

Experimental pressure drop results

The complete results (test, duct alone and device) from the CFTB characterization of ATS1-A are shown below. First, Fig. 5.25 shows the PD, which exhibits the expected quasi-quadratic behaviour but, on the contrary to devices with monoliths, it does not surpass the PD of the upstream duct alone; still the results seem to be trustful. Consistently, the pressure drop coefficient results presented in Fig. 5.26 also show the appropriate behaviour, but once again the coefficient of the device is smaller than that of the rig duct; it also seems to have reached fully-developed flow conditions at high Reynolds numbers.

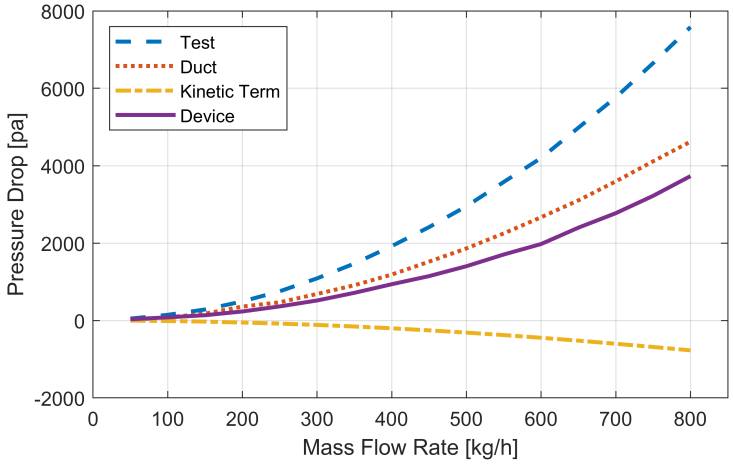

Figure 5.25: Experimental PD results from ATS1-A characterization.

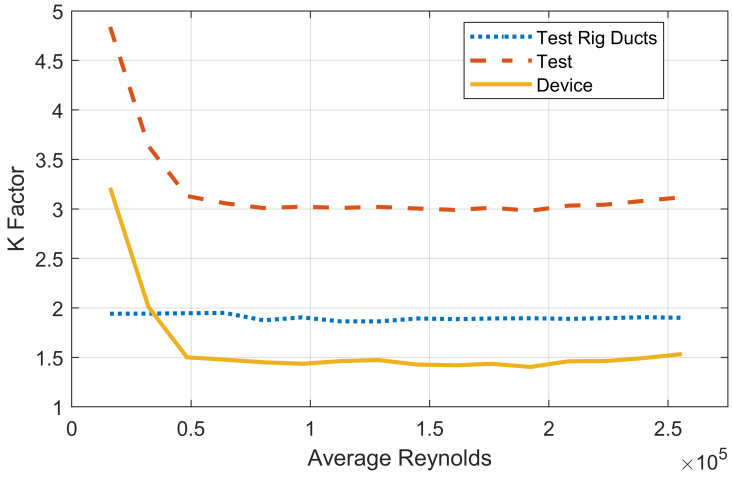

Figure 5.26: Pressure drop coefficient, K factor, from experimental assessment of ATS1-A.

As a way to account for how significant these results for the auxiliary device are in regards to the complete system (ATS1), Figs. 5.27 and 5.28 plot the PD and K factors measured for both ATS1 and ATS1-

A. As observed in Fig. 5.27 the ATS1-A pressure drop in regards to the complete system is not as small as it might initially be expected, bearing in mind that PD is essentially additive, as will be accounted for in Section 5.5. It is apparent that at medium mass flows ATS1-A alone accounts for approximately a 20% of the total PD, reaching almost 30% at the maximum mass flow, thus contributing significantly to the ATS back-pressure. This is a logical consequence of its working principle, as commented in Section 5.1: the mixer induces local turbulence from the vanes that promote the mixing.

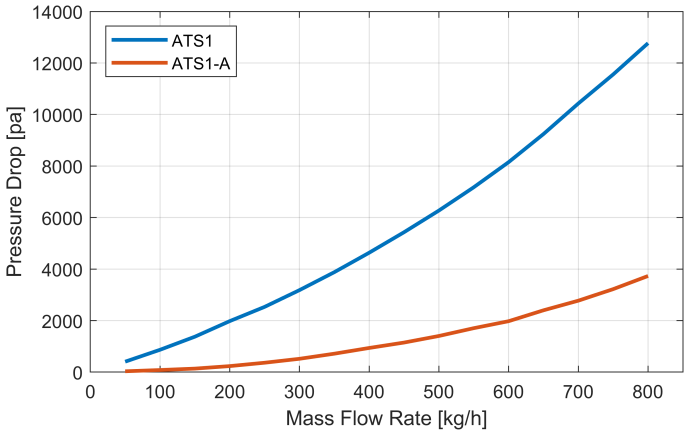

Figure 5.27: Comparison of experimental PD measurements for ATS1-A and the complete ATS1.

Consistently with these results, the pressure drop coefficient plotted in Fig. 5.28 as a function of the Reynolds number, exhibits a substantial decrease in value when compared with that of the complete system. Again, the measurements exhibit the right asymptotic behaviour within the measurement uncertainties, and it appears that stable fully developed flow conditions have been reached at high Reynolds numbers in both cases.

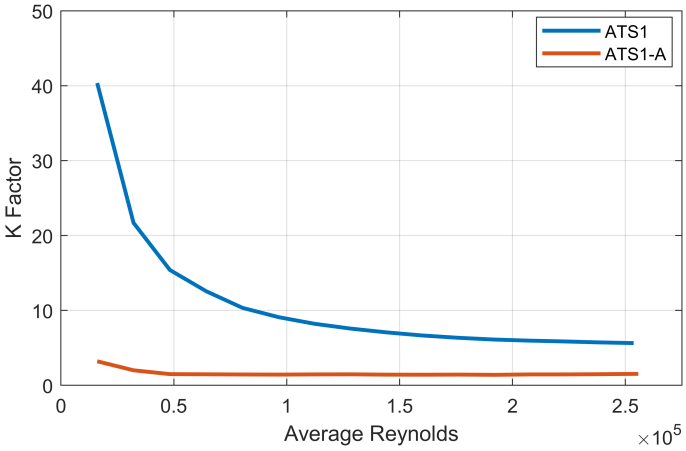

Figure 5.28: Comparison of K factor calculated from the measurements for ATS1-A and ATS1.

Experimental transmission loss results

Fig. 5.29 shows the comparison between the TL of the whole ATS1 and that of the auxiliary system ATS1-A. At a first glance, the TL of ATS1-A is relatively small, specially compared to that of the complete system, which could be misinterpreted at it having a small contribution to the TL; however, since TL is not an additive magnitude, as will be demonstrated in Section 5.5, to properly account for its contribution the TL curve of the system with the auxiliary device removed, which is labelled ATS1-D1D2, and whose detailed characterization is shown in Section 5.4, has to be considered. With this perspective it is apparent that for frequencies below 200 Hz the influence of the presence of ATS1-A is virtually negligible, but it produces a significant increase in attenuation for frequencies between 200 Hz and 700 Hz and between 1400 Hz and 1800 Hz. Therefore, while the attenuation of the auxiliary device alone is certainly small, it seems necessary to characterize it in order to account for any effects occurring when it is coupled to the rest of the ATS.

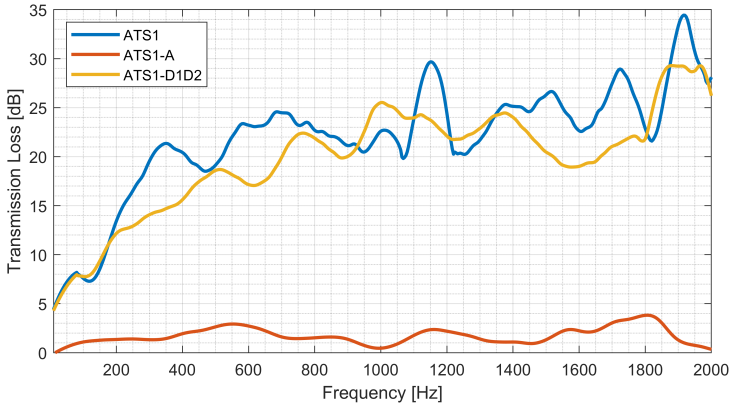

Figure 5.29: Comparison of the TL of ATS1, ATS1-A, and ATS1-D1D2, with no superimposed MFR.

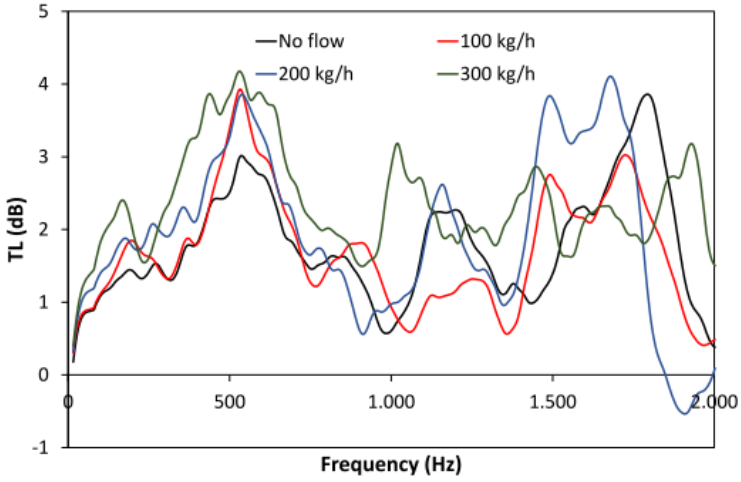

Figure 5.30: Effect of superimposed MFR on the TL of the ATS1-A.

The effect of the flow on the TL of ATS1-A alone is shown in Fig. 5.30. As it could be expected, both convective, with a certain shift in the characteristic frequencies, and dissipative effects, with a noticeable

increase in the attenuation level at low to medium frequencies, are observed. While in all the cases the attenuation remains very low, the apparition of a negative TL in the higher frequencies when there is a superimposed mean flow of 200 kg/h is striking. A negative TL should be interpreted as sound being generated within the device. In fact, the particular geometry of the mixer studied appears to be susceptible of giving rise to turbulent noise generation due to the turbulent mixing in the wake downstream of the device, and the intrinsically unstable character of that wake. The fact that the occurrence of negative TL depends on the value of the mean flow may suggest that this is a vortex-sound effect where shed vorticity can interact with the acoustic waves and dissipate/amplify depending on the Strouhal number [140]. In order to gain insight into this potentially relevant flow-related feature linked to the Strouhal-number, the logarithmic approach of the decomposition methodology was applied to the measurements with 200 and 300 kg/h of superimposed MFR.

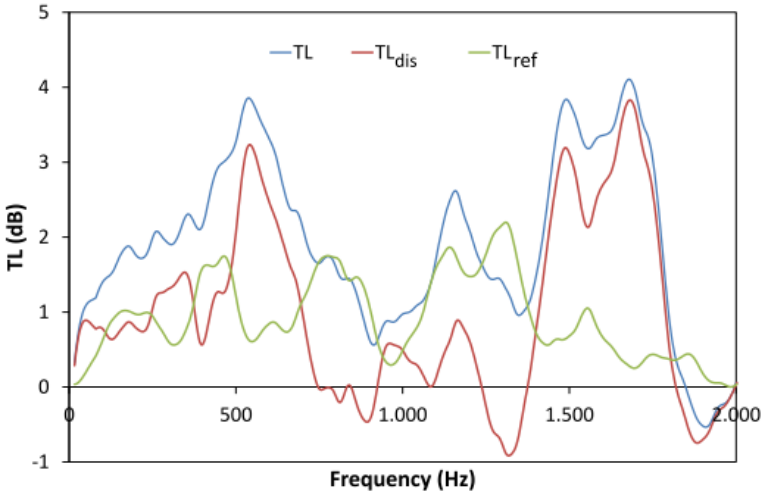

Figure 5.31: Decomposition of the TL results at 200 kg/h.

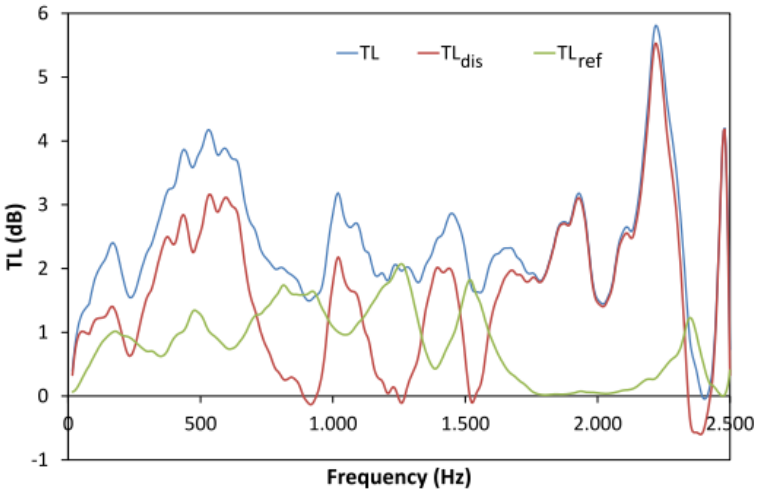

Figure 5.32: Decomposition of the TL results at 300 kg/h.

- *Decomposition of TL measurements with a flow of 200 kg/h*
  - Results up to 2000 Hz are shown in Fig. 5.31.
  - The reflective TL is relatively smooth and remains positive for the complete frequency range.
  - The dissipative TL presents a more oscillating behaviour and becomes also negative at frequencies between 750 and 900 Hz, and around 1300 Hz.
  - The most feasible interpretation is that there could be some flow noise generation at those frequency bands, but the effect is suppressed in the device itself by the reactive effects.
  - As the reactive component tend to decrease starting at 1550 Hz and the dissipative component is negative from 1800 Hz approx. there is a point around 1900 Hz were reactive effects cannot compensate dissipative effects any more and thus the TL becomes negative.
- *Decomposition of TL measurements with a flow of 300 kg/h*
  - Results up to 2500 Hz are shown in Fig. 5.32.

- The frequency at which the dissipative TL becomes negative is shifted to higher values; with the points below 2400 Hz barely surpassing the 0, however, the value obtained (2400 Hz) does not correspond to the same Strouhal number as that observed around 1950 at 200 kg/h.
- It is suspected that the flow noise generation in this device should be strongly dependent on the upstream and downstream reflecting boundaries [141] which, in these measurements, are not those found in the real device operation.
- For this mass flow, the overall TL only reached a slightly negative value, so that results are not conclusive.

When the whole device is considered, the TL, and the dissipative contribution, are both positive at 200 kg/h for all the frequencies; this suggests that either no flow noise is generated or that it is attenuated by the different elements of the complete system.

Computational pressure drop results

The results of the steady flow CFD simulation are presented from Figs. 5.33 to 5.35. First, Fig. 5.33 shows the streamline representation of the flow as it passes through ATS1-A for a mass flow of 540 kg/h (0.150 kg/s); this offers a glimpse of two important features. First, the flow is highly stagnated in the DEF injection cavity and only a small local disturbance is produced in the flow pattern barely upstream of the mixer. Secondly, the complexity of the flow as the mixer induces a rotational swirl motion, which is an unavoidable consequence of its primary function. Then Fig. 5.34 presents the comparison of CFD estimated PD in regards to the experimental measurements. An overall good agreement is observed, with an apparent tendency to underestimate the PD as the mass flow increases.

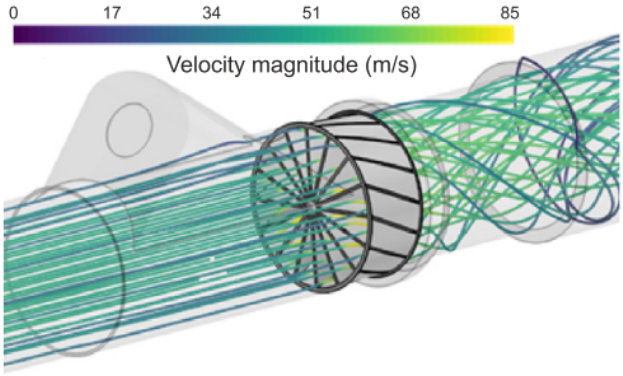

Figure 5.33: Streamline representation of the flow across ATS1-A at 540 kg/h.

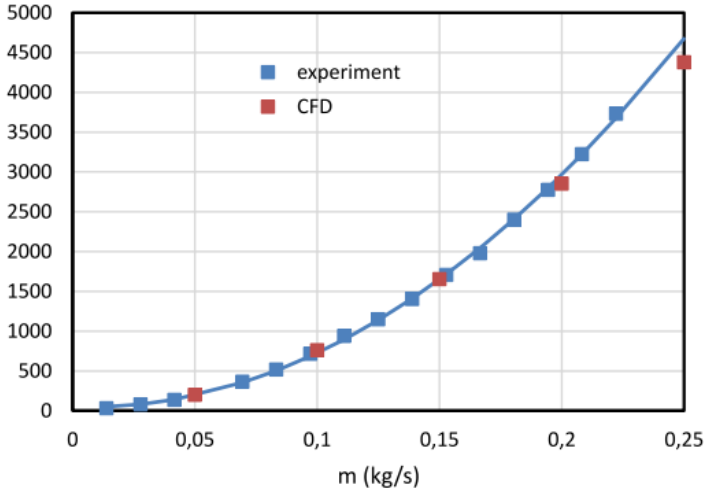

Figure 5.34: Comparison of 3D CFD and experimental PD results of ATS1-A at steady flow condition.

As the PD results are satisfactory, it was considered adequate to analyze the relative influence of the aforementioned features on the resulting PD. The streamline representation suggests that the influence of

the DEF injection cavity should be marginal, whereas the effect of the mixer should be substantial. That is confirmed by the results shown in Fig. 5.35, which presents the total pressure distribution, with an approximately constant total pressure upstream of the mixer and a significant decrease right at the exit of the blades. It is also apparent that losses are higher in the vicinity of the centreline, where the mixing of the wakes is more intense.

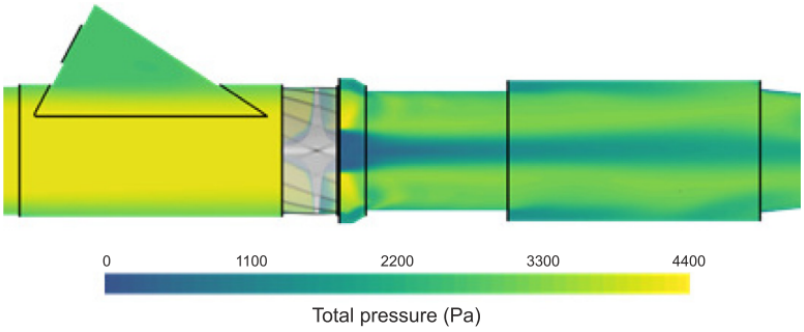

Figure 5.35: Total pressure distribution of ATS1-A at $\dot{m} = 0.150 kg{\cdot}s^{-1}$.

Transmission loss

TL results from the experimental and the 3D approach are shown in Fig. 5.36 for the no superimposed mean flow scenario. The plot also includes the result for the complete ATS in the secondary axis for reference. The results can be considered acceptable, specially considering that the order of magnitude of all values found is quite low. Still the following should be highlighted:

- There are some significant differences in the low frequencies, in which the computation underestimates the measured values.
- The computation captures the resonance spike occurring at about $2300 Hz$ but overstimates its amplitude.

- That spike can only be the attributed to a side resonator effect, and the obvious guess would be the DEF injection port cavity; this was later confirmed in the sound pressure level distribution shown in Fig. 5.37.
  - The figure shows that at the resonance frequency, with no superimposed flow, a complex lateral pattern is established inside the cavity, giving rise to a substantial reduction in the sound pressure level at the inlet of the mixer vanes.
- Thanks to the inclusion of the measurement for the complete ATS it is apparent that the resonant spike transcends to the TL of the whole system, which would indicate an approximately additive behaviour that is consistent with the fact that the attenuation of the rest of the system at those frequencies is essentially dissipative [40].
- The frequency range influenced by the spike is in the limit of what would be considered in industrial practice as the relevant frequency range for exhaust line design, and therefore in some cases it might be necessary to incorporate this issue into the design process in order to achieve a proper description of the exhaust acoustics.
- Looking for a possible explanation of the differences observed in the low frequencies, they are though to be related with the dissipative effects caused by the presence of the vanes, which are not accounted for by the numerical model used. This was verified making use of the logarithmic approach of the decomposition as described in Section 3.2.3.
  - Fig. 5.36 includes the reflective component TL_{ref} extracted from the measurement results, which are quite closer to the 3D CFD results in all the frequency range.
  - Additionally, it may be seen that, as expected, the effect at the resonance frequency is correctly attributed by the TL decomposition to reactive effects, which provides additional confidence in the ability of the method proposed in [96] to identify reactive and dissipative contributions to attenuation.

– The dissipation found in the measurements, even in the absence of a superimposed flow, is a direct consequence of the measurement procedure used: the incident pulse carries with it a transient flow that may excite dissipative structures, even in the fluid is taken back to rest once the pulse has passed [94].

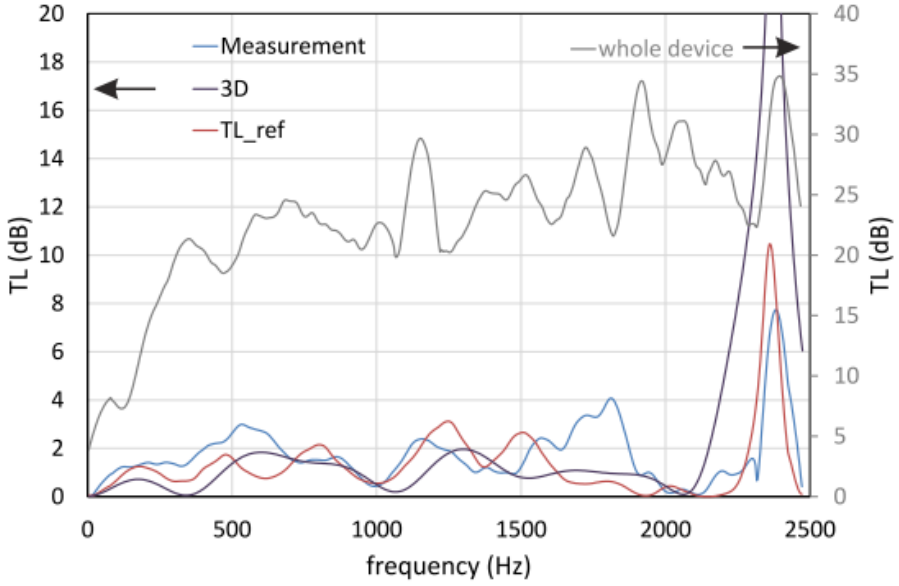

Figure 5.36: Comparison of exp. and 3D CFD TL results without flow for ATS1-A (left axis) and complete ATS1 (right axis).

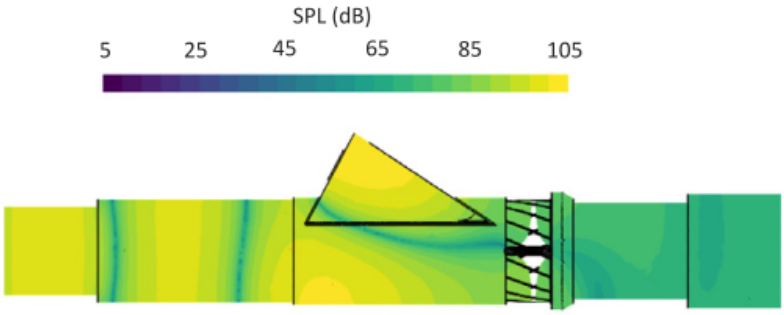

Figure 5.37: SPL distribution in ATS1-A at the resonance frequency with no superimposed mean flow.

Equivalent results are presented for the case with a superimposed mean mass flow rate of 300 kg/h: the TL results in Fig. 5.38, and the SPL distribution at the resonance frequency in Fig. 5.39. It can be observed that for frequencies up to 750 Hz approximately the results are comparable to the measurement, thus indicating that dissipative effects have been accounted for by the computation. Beyond that frequency the attenuation is overestimated, most notably around the resonance spike, but the small shift observed in the frequency has also been reproduced by the computation. Regarding the SPL distribution it is qualitatively similar to that of the no-flow scenario; one can however observe some patterns upstream and downstream of the mixer that should be related with the interaction of the acoustic field with the highly complex mean flow present.

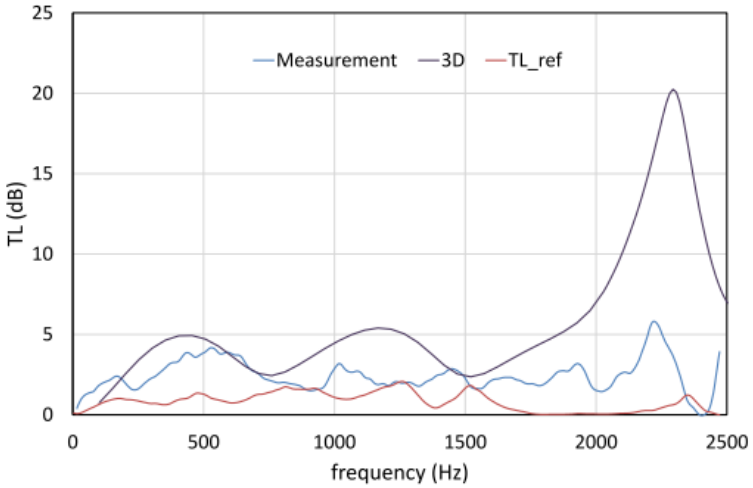

Figure 5.38: Comparison of 3D CFD and measured (total and reflective contribution) TL results for ATS1-A with a 300 kg/h superimposed MFR.

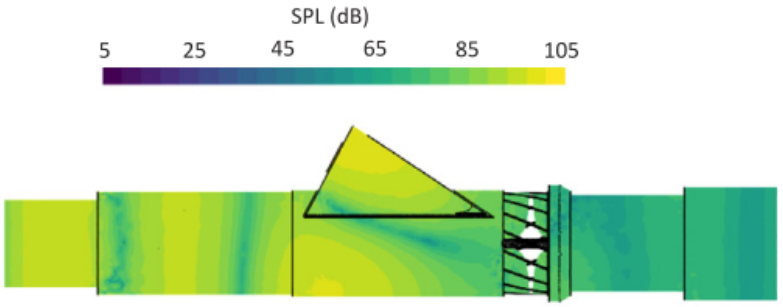

Figure 5.39: SPL distribution in ATS1-A at the resonance frequency with 300kg/h of superimposed MFR.

One-dimensional modelling results

Results from first stage 1D modelling

Fig. 5.19 shows the comparison of experimental PD results against those from the prepared virtual twin; once again the agreement of results is excellent, but as this device does not have any monoliths its tuning took longer and the resulting parameters are the ones that differ more from the seed values. Regardless of further tuning needs, the agreement obtained suggest that the 1D modelling methodology and guidelines established are also adequate for devices without monoliths.

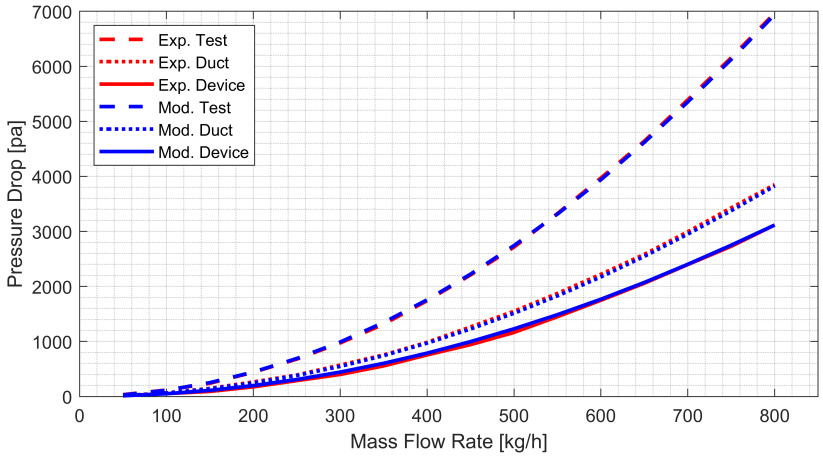

Figure 5.40: Comparison of experimental and 1D modelled PD results for ATS1-A.

Fig. 5.41 shows the experimental smoothed and 1D model (1st stage) for ATS1-A. Similarly to results for devices with monoliths, the initial ramp accounting for volume correspondence is satisfactorily captured. The overall behaviour is also reproduced; the agreement is not so evident due to the scale, but for most of the frequency range plotted the differences are below or close to the 3 dB margin and the effect of mean flow is also properly reproduced.

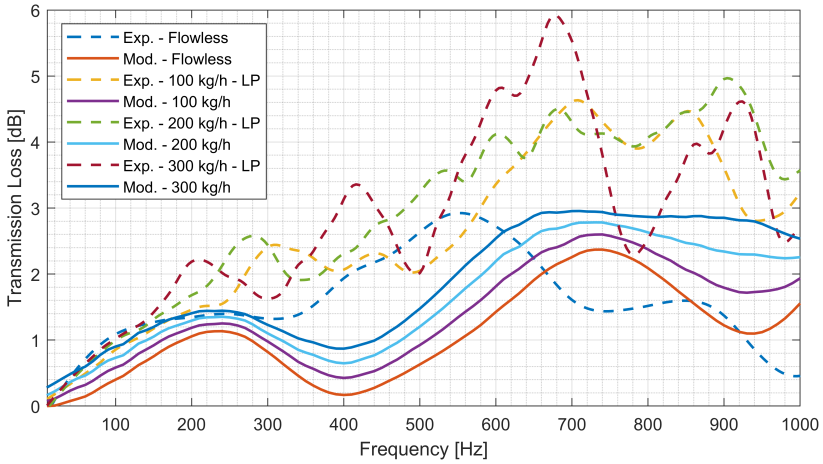

Figure 5.41: Comparison of exp. smoothed and 1D modelled TL results for ATS1-A.

Second stage 1D modelling and its results

From the results discussed above alongside those of the first stage 1D modelling, it appears that the two main ingredients to be incorporated into a simple one-dimensional model for the precise reproduction of ATS1-A behaviour are, on the reactive side, the resonance effect associated with the DEF injection cavity and, on the resistive side, the dissipation produced by the mixing of the wake downstream of the mixer vanes. Any other elements present should be soundly represented by one-dimensional entities (as in the first stage model), with the eventual consideration of length corrections at the sudden area changes, for which the general expression proposed in [142] was used.

Starting from the basis established for 1D models, and having produced a sufficiently satisfactory first stage model for assessing the PD and the TL up to 1000 Hz as for the other devices, the most straightforward solution for reproducing the resonance effect identified implies using a quarter wave resonator with the same resonance frequency to simulate the effect of the DEF injection cavity, while keeping the volume as close as possible to the real one, so that the low frequencies are not severely affected. The length of the resonator was estimated from the

well-known quarter-wave expression, and the corresponding model was built as an alternative virtual twin model also in GT-Ise. The resulting model is presented in Fig. 5.42.

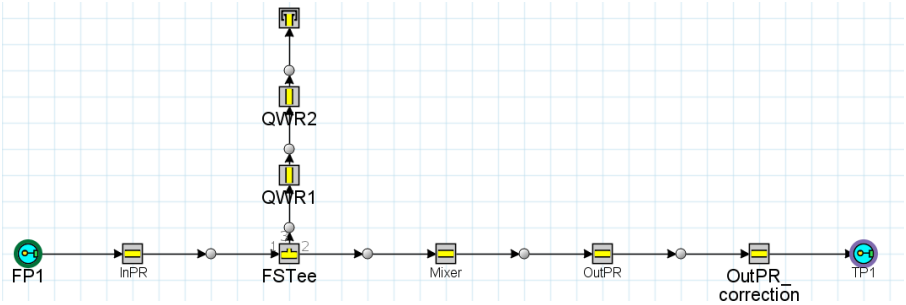

Figure 5.42: 1D model representing ATS1-A (2nd stage).

The no-flow case was chosen in order to allow for direct comparison with the FEM results. Since the real cavity is not a quarter-wave resonator, some trial-and-error tuning of the diameter was required. The final results are shown in Fig. 5.43, where it can be observed that the resonance is adequately reproduced, even so if some excess of attenuation is found right below the spike. For the other frequencies, the results may be regarded as acceptable, considering the extremely low values present.

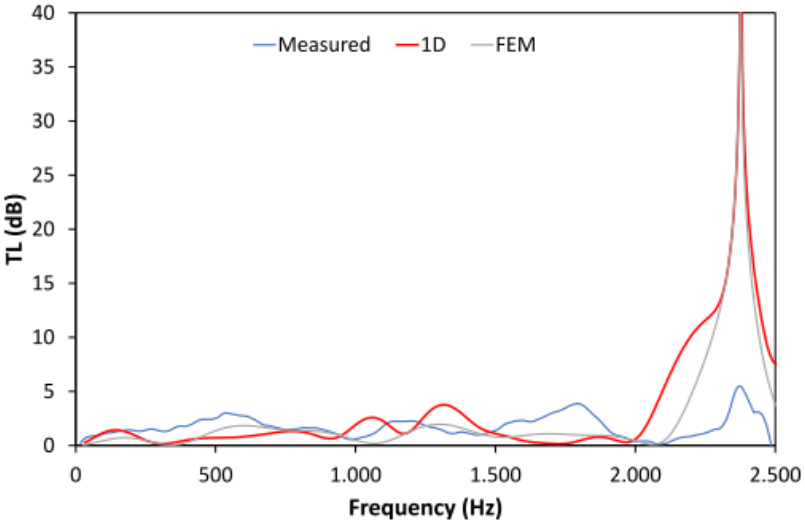

Figure 5.43: Comparison of 3D and 1D results with no flow.

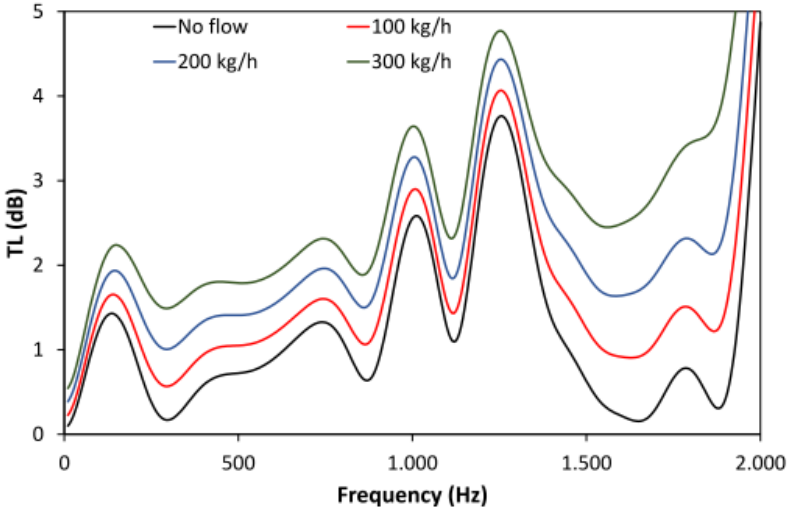

Figure 5.44: Effect of the flow on the 1D results.

With regards to the dissipative effects, the usual way of addressing them is to use a local PD that represents all the losses. Here, advantage was taken of the availability of detailed pressure loss results from the experimentally validated CFD computation. From the total pressure distribution computed, it was possible to estimate an area-averaged pressure drop coefficient across the mixer vanes and the wake. This pressure drop coefficient was later input into the same gas-dynamic code, where such a local PD can be incorporated in a natural fashion.

The results obtained are shown in Fig. 5.44. When comparing with the experimental results shown in Fig. 5.30, it is obvious that, while overall effects such as frequency shifts and an increase in the attenuation with the flow can be observed, the model is not able to reproduce the details in the measured curves. However, and bearing in mind the very low attenuation values present, this should provide a sufficient accountancy for the effect of ATS1-A when considered as integral part of the complete ATS.

5.4 Assessment of combined devices

Assessment Procedure

Now that the isolated devices; ATS1-A, ATS1-D1 and ATS1-D2 have been studied and their 1D virtual twins prepared, the next step is to account for the two partial combinations possible, ATS1-AD1 and ATS1-D1D2, and for the complete system ATS1. All these three options were assessed as it was in the experiments, i.e. assembling the virtual twin models together.

Measurements of the Experimental Assessment

Table 5.3 summarizes the measurements taken for the characterization of these combinations of devices. ATS1 is presented here as, from the modelling point of view and the increasing complexity approach used, it is considered both the combination of the three individual devices and the most complex assembly to be characterized.

The assemblage of devices is possible thanks to the clamp adapters used; also the adapters used to fit them into the test facilities are detachable, therefore no new adapters were needed.

Table 5.3: Information on the experimental measurements taken for devices ATS1-D1 and ATS1-D2.

Characterization		**ATD Combination**		
Test Facility	*Condition*	$AD1$	$D1D2$	$ATS1$-*Rejoined*
Pressure drop	Min. MFR	50 kg/h		
testing on	Max. MFR	800 kg/h		
CFTB	Increase steps	50 kg/h		
	Orientation	Dir. & Inv.		
Transmission	Flowless	1 pulse amp.		
loss testing	MFR 100 kg/h	2 pulse amp.		
on ITR	MFR 200 kg/h	2 pulse amp.		
	MFR 300 kg/h	2 pulse amp.		

Preparation of Modelling Assessment

As virtual twins of the individual devices have been already prepared and tested, the modelling logic for these devices is to also assembly the models, placing and connecting them in the corresponding order, as shown in the following figures that present both the assemblies and their respective virtual twin assemblies.

ATS1-AD1

This corresponds to the union of the auxiliary device and the can with double monolith. Fig. 5.45 shows it placed in one of the experimental facilities for a measurement as well as its 1D modelling counterpart.

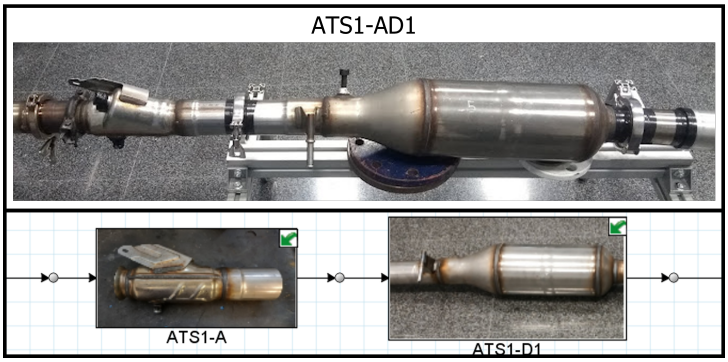

Figure 5.45: Assembly and modelling logic for representing ATS1-AD1.

ATS1-D1D2

This corresponds to what would remain of the system if the auxiliary device was removed; it has been mentioned before in 5.3 as part of the analysis of the contribution of ATS1-A to the complete system acoustic attenuation. Fig. 5.46 shows it mounted in one of the rigs during its experimental characterization (top), and its modelling representation (bottom).

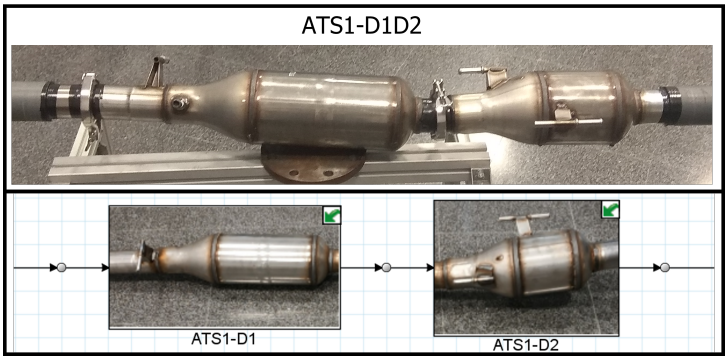

Figure 5.46: Assembly and modelling logic followed to represent ATS1-D1D2.

ATS1

For the complete system, as verified in the "Pre and Post Split Validation" back in Section 5.2, there is no relevant difference between the two states, and from the modelling point of view it is treated and characterized as in the reassembled state. The upper part of Fig. 5.47 shows it mounted in one of the rigs during its experimental characterization and the lower part of the figure shows the assembly of individual models in the modelling environment.

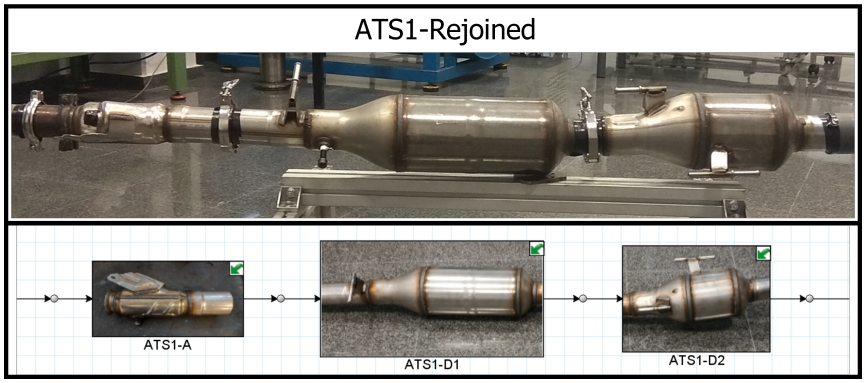

Figure 5.47: Assembly and modelling logic followed to represent ATS1.

Results and Discussion

ATS1-AD1

Figs. 5.48 and 5.49 present the information derived from the characterization of ATS1-AD1 in the CFTB. In both cases, the results match expectations: the PD has the quasi-quadratic behaviour with the linear component linked to the monoliths, and the K factor has the right asymptotic behaviour. Also, as expected due to the presence of ATS1-D1 in the assembly in both cases, the contribution of the assembly to the test results exceeds that of the upstream pipe. The contribution of each device to the result of this assembly will be assessed in Section 5.5.

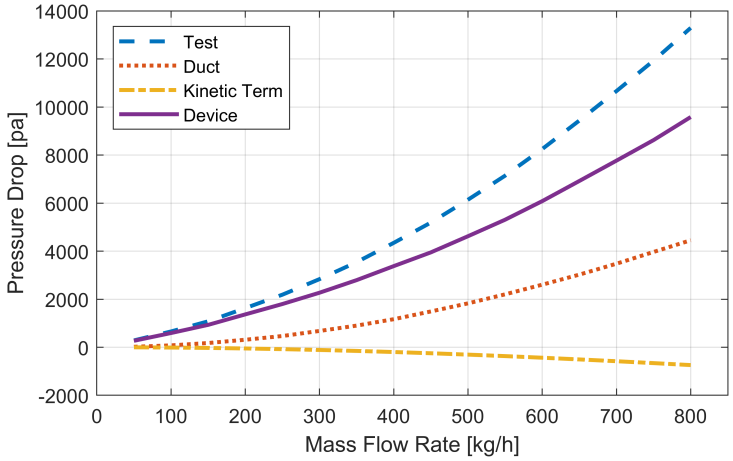

Figure 5.48: Experimental PD results from ATS1-AD1 characterization.

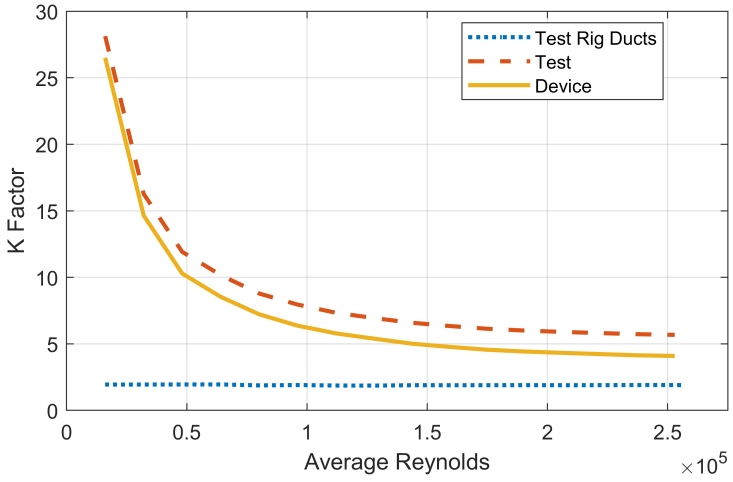

Figure 5.49: Pressure drop coefficient, K factor, from experimental assessment of ATS1-AD1.

Fig. 5.50 present the results of the PD modelling compared with the experimental ones. There is a slight yet noticeable difference that is most likely due to the presence of the model for ATS1-A in the model of the assembly. Still this result can be considered satisfactory taking into account that no further preparation nor tuning of the models except putting them together was done.

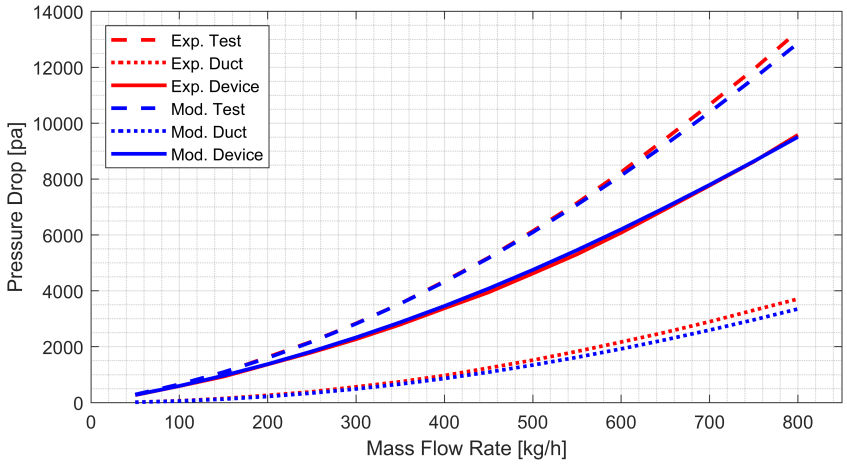

Figure 5.50: Comparison of Exp. smoothed and 1D modelled PD results for ATS1-AD1.

Fig. 5.51 presents the TL results for small and large pulse measurements. As usual, flow dissipative effects produce a certain increase in attenuation regardless of the pulse used; otherwise, the effect of the flow is rather marginal. Additionally, it can be observed that the resonant spike present in the mixer is also apparent here, even though it is wider in this configuration. This suggests a certain additivity in the results (that was not that apparent in ATS1-D1D2), but also the existence of some interaction between the mixer and the can.

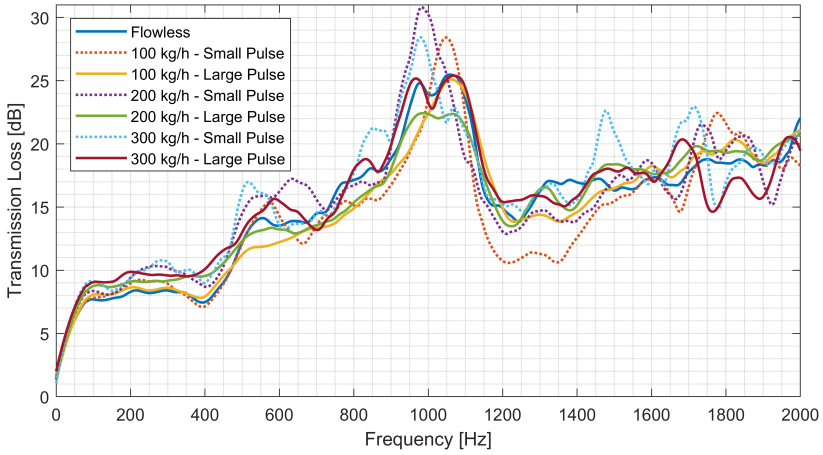

Figure 5.51: Complete set of exp. smoothed TL results for ATS1-AD1.

As little information is provided by considering the experimental results for both small and large pulses, and more details on TL interactions are to be assessed later, only the flowless and large pulse results are plotted in Fig. 5.52 alongside the results from the model. Similarly to the results for the individual devices with monoliths, the initial ramp related to the volume correspondence is satisfactorily represented, and the overall effect of the mass flow is a certain increase but seemingly not as much as shown in the experimental measurements. The overall shape of the curve and the values are reproduced within the acceptable margin up to about 450 Hz; above this point there is still some resemblance but the quality of the reproduction is worsened with the exception of a small frequency range around 700 Hz.

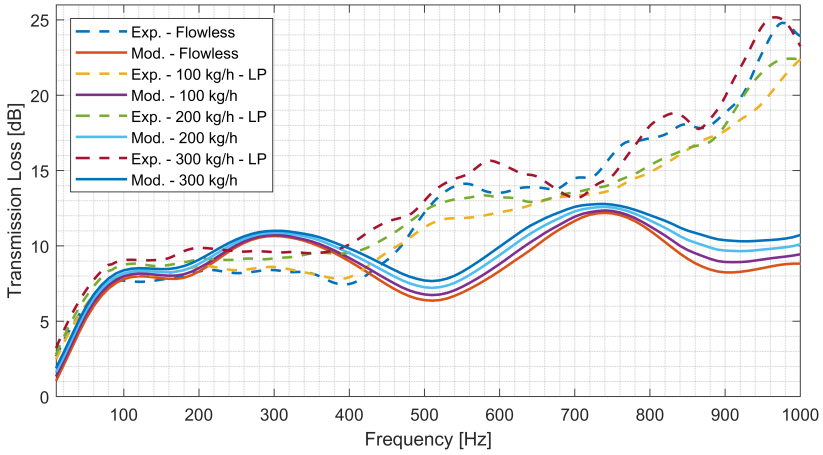

Figure 5.52: Comparison of Exp. smoothed and 1D modelled TL results for ATS1-AD1.

ATS1-D1D2

Figs. 5.53 and 5.54 present the information derived from the characterization of ATS1-D1D2, as both in the isolated cases of both composing elements the PD and pressure drop coefficients exhibited the expected behaviour, and also the contribution of the assembly to the test results greatly surpasses that of the upstream duct. The contribution of each device to the result of this assembly is to be assessed in Section 5.5.

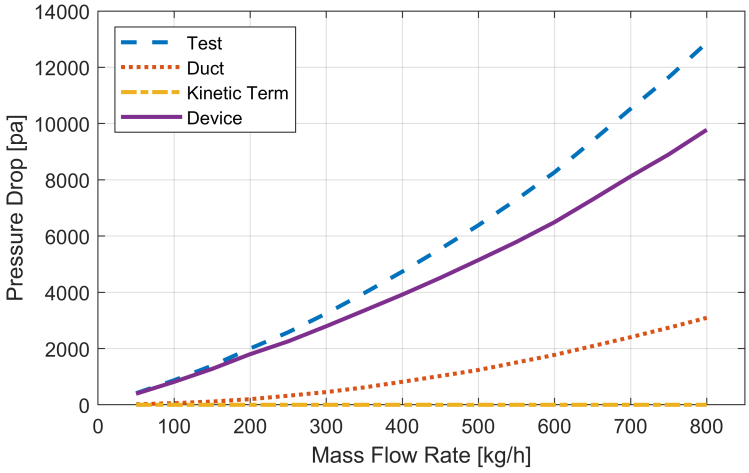

Figure 5.53: Experimental PD results from ATS1-D1D2 characterization.

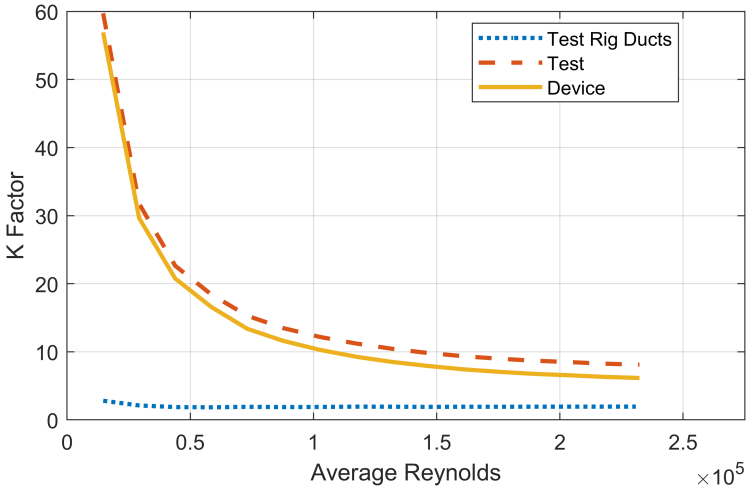

Figure 5.54: Pressure drop coefficient, K factor, from experimental assessment of ATS1-D1D2.

The 1D modelling results for PD are compared with their equivalent measured results in Fig. 5.55 and, similarly to the individual virtual twins that conform this virtual assembly, the results are very accurate at low and high mass flows at the cost of some deviation in the mid mass flows.

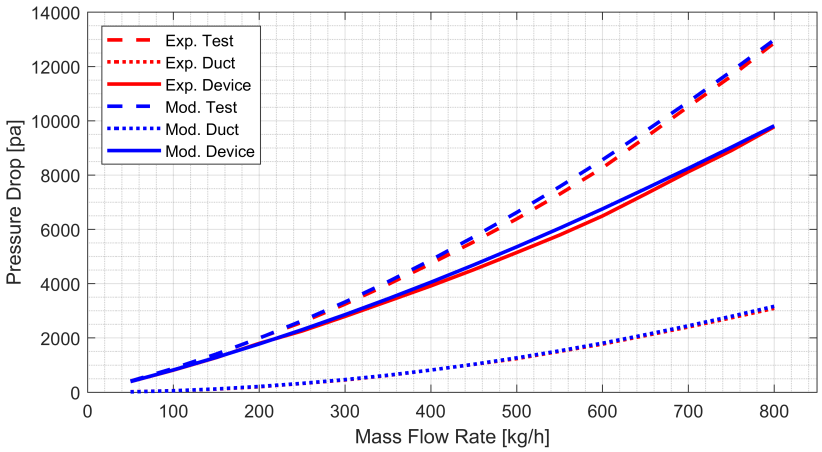

Figure 5.55: Comparison of Exp. Smoothed and 1D modelled PD results for ATS1-D1D2.

The effect of the flow on the TL of ATS1-D1D2 is shown in Fig. 5.56. In general, the usual effect of flow is evidenced for all both small and large pulse measurements; increasing the flow produces a certain increase in the attenuation, but any other change is rather marginal. Additionally, it can be observed that the resonant spike present in ATS1-D2 is not apparent when the two cans are together. This supports the idea that the spike can be an undesired result of the manipulations performed. These results also coincide with previous ones in the sense that small and large pulse results follow essentially the same trend, but small pulse measurements are quite noisier. Up to now, results suggest that the small pulse is too small to stand a mass flow of 300 kg/h.

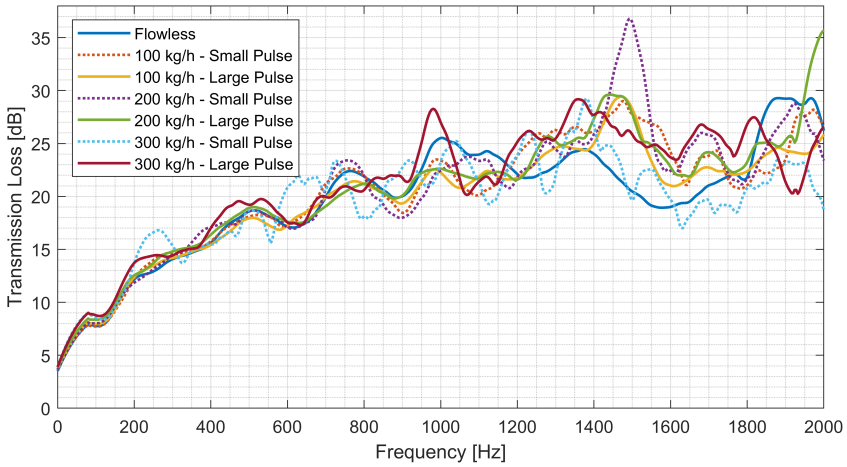

Figure 5.56: Complete set of exp. smoothed TL results for ATS1-D1D2.

Fig. 5.57 shows the comparison of experimental smoothed large pulse results and those from the 1D assembly of virtual twins. As the individual virtual twins for the devices with monoliths showed better agreement than that of ATS1-A, it was to be expected that this assembly might produce better results. The initial volume-related ramp is not captured as properly as it was for the individual devices, but without further tuning the assembly does capture the overall behaviour of the curve and produces indicative values within the acceptable error margin up to 600 Hz.

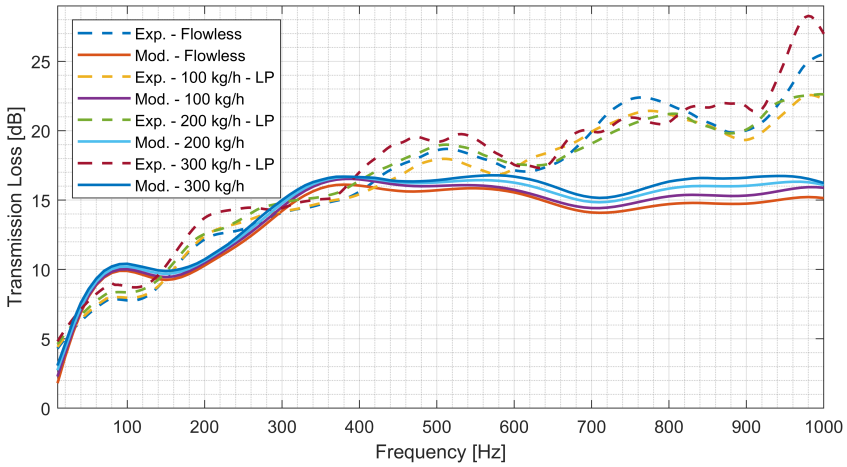

Figure 5.57: Comparison of experimental smoothed and 1D modelled TL results for ATS1-D1D2.

ATS1

Figs. 5.58 and 5.59 show in detail the results from the experimental characterization of the complete system. In the previous analysis in Section 5.3 both the PD and K factor of the device were shown, but having them together with those of the upstream duct alone and the whole test assembly allows to appreciate that the contribution of the system itself to the final result of the test is much larger than that of the duct, which provides sufficient resolution for the results finally attributed to the ATS. These in turn fully matched expectations: the PD has the quasi-quadratic behaviour with the linear component linked to the monoliths, and the K factor has the right asymptotic behaviour, indicating that stable fully-developed flow conditions were reached at high Reynolds numbers.

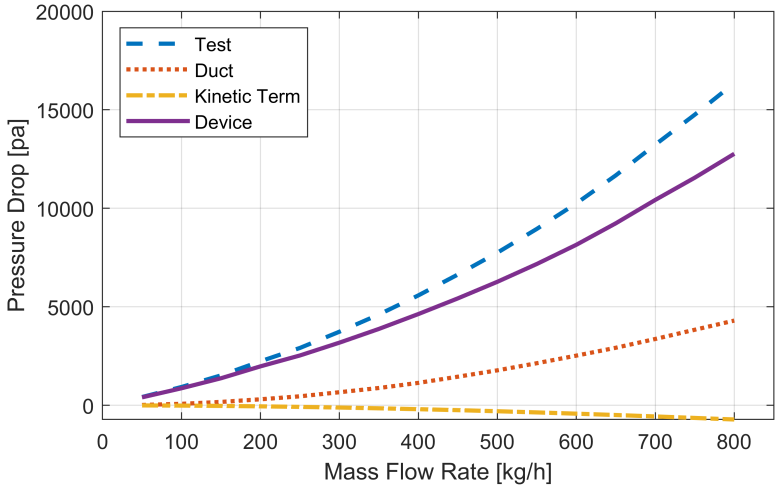

Figure 5.58: Experimental PD results from ATS1 characterization.

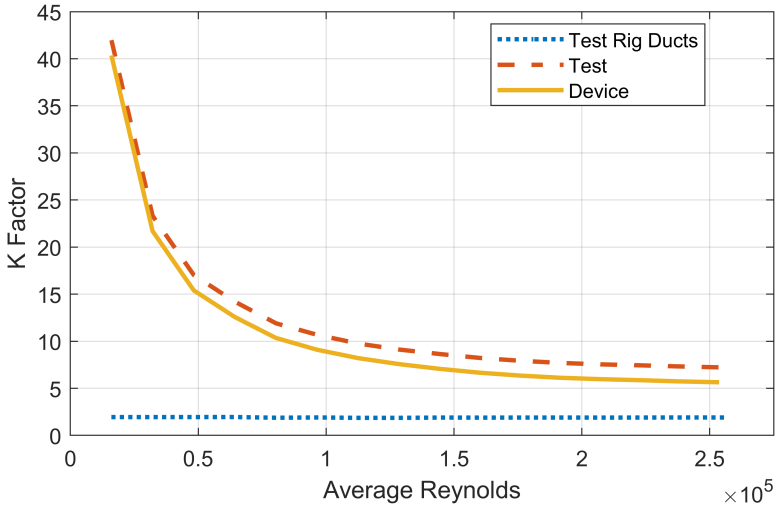

Figure 5.59: Pressure drop coefficient, K factor, from experimental assessment of ATS1.

Fig. 5.60 shows the comparison between experimental and 1D modelled PD results. Considering that the assembly of virtual twins is being applied without further tuning and the limitations of individual models being tuned for the isolated tests, it was to expect that what appeared as small discrepancies in the individual cases are now joined into a more evident difference between measurement and model, but still the results are acceptably close and very indicative.

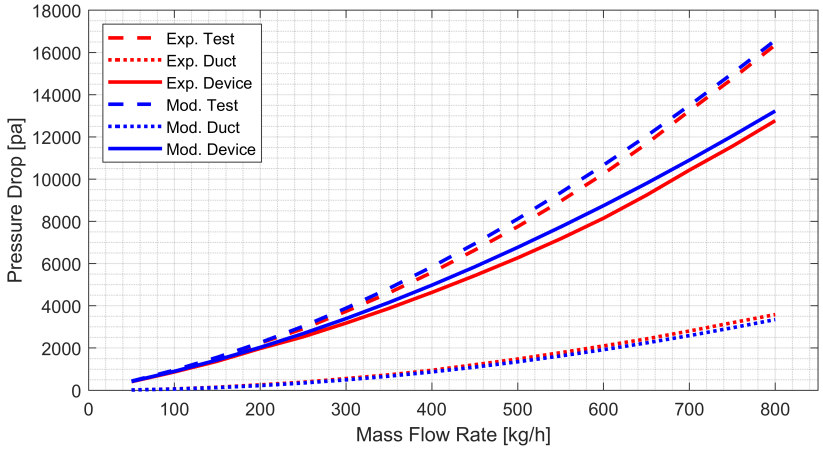

Figure 5.60: Comparison of Exp. Smoothed and 1D modelled PD results for ATS1.

The effect of a superimposed mean flow on the TL results of ATS1 is shown in Fig. 5.61. Flowless and large pulse results are plotted in solid lines, whereas small pulse results are plotted in dotted lines. For the large pulse, the dissipative effects produce a certain increase in attenuation, except just below 400 Hz, where the flow seems to have damped a resonant frequency. At 300 kg/h the signal becomes noisier above 1000 Hz, which is though to be related to the characteristics of the transmitted pulse in these conditions. Regarding the small pulse results, the trends are essentially the same although local spikes start to appear at lower mass flows, which seems to confirm that the noise associated with the flow is somehow contaminating the pulse.

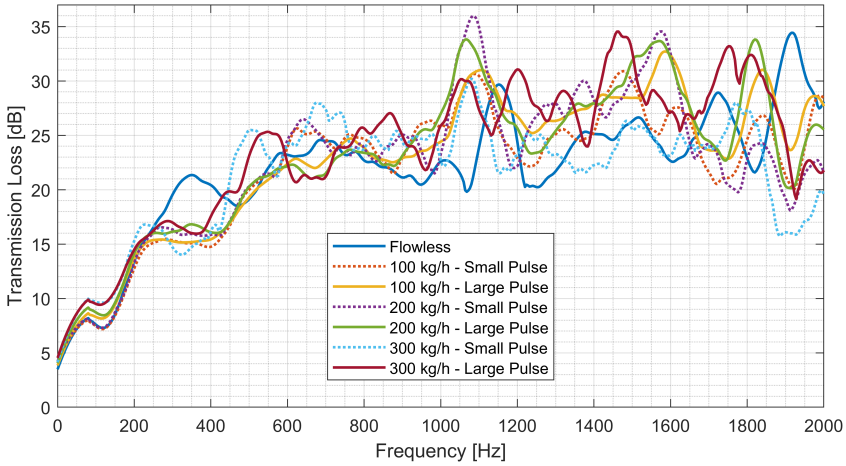

Figure 5.61: Complete set of exp. smoothed TL results for ATS1-D1D2.

Fig. 5.62 shows both the experimental results for flowless and superimposed mean flow excited with large pulse, and the modelled results with all flow conditions. The agreement of results can be once again regarded as acceptable taking into account that no additional tuning was done, and therefore the discrepancies of individual models are brought together with this approach. The initial ramp is almost captured; then up to almost 500 Hz the differences are within the acceptable margin, and above such frequency the differences get larger, but still the overall behaviour is well represented, thus providing some valuable information.

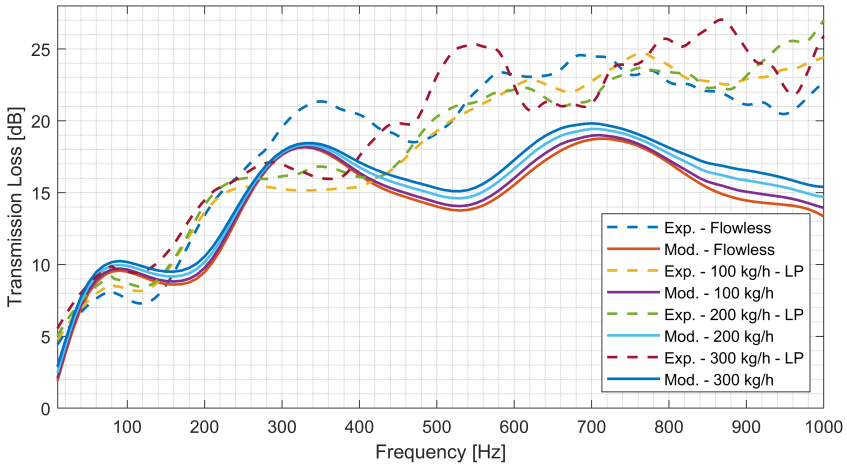

Figure 5.62: Comparison of exp. smoothed and 1D modelled TL results for ATS1.

5.5 Assessment of additivity or interactions

Finally, having the complete set of PD and TL experimental data for all isolated and combined devices, these results were computed, compared and contrasted to account for potential additivity and/or interactions between components. In particular, to validate whether or not the back-pressure and the noise (sound) attenuation associated with each device, represented by their measured PD and TL respectively, have an additive character. The reasoning behind this approach is that only when there is no interaction one should be able to simply add the PD or TL of elements in series.

Assessment Procedure

For both magnitudes the analysis by direct graphical comparison was used, plotting together the results for a combination (ATS1-AD1, ATS1-D1D2 and ATS1), its composing devices and all possible sums of individual devices that would contain the same ones.

Remarks:

- For this purpose raw PD and flowless TL measurements were chosen, in order to avoid any masking due to processing of any interaction or effect.
- This sum corresponds to the direct addition of their isolated results, as presented in preceding sections, without any kind of correction for differences in inlet and outlet diameters.
- As an example, to analyze ATS1, the composing elements are the three isolated devices, and the possible sums include A+D1+D2, AD1+D2 and A+D1D2.

Pressure drop results

Before assessing the additivity, direct comparison of PD results has been barely commented so far; in order to present the complete set of measurements in a plot and analyze them together, such comparison is presented in Fig. 5.63 and commented below.

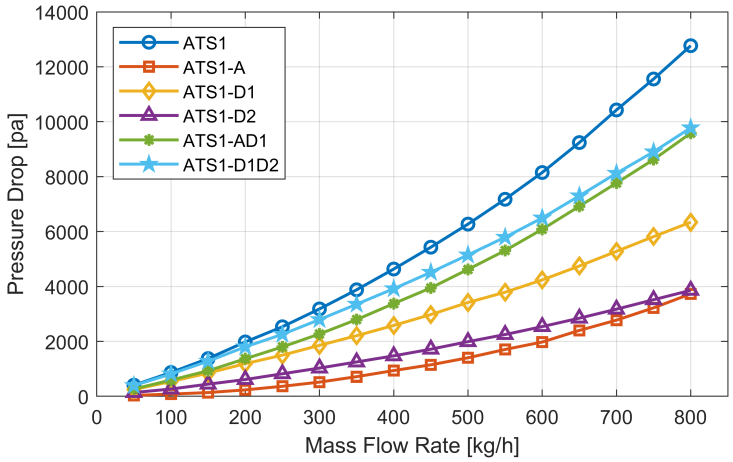

Figure 5.63: Summary of the PD results obtained for ATS1, its composing devices and their partial combinations.

- The PD from ATS1-D1 is the highest of the three isolated devices, almost half of that of the complete system, as could be expected for it being the most complex and large and having two monoliths.

- As stated before, ATS1-D1 generates 1.65 times the back-pressure of ATS1-D2 being practically identical in their geometrical configurations besides the second monolith and the gap in between; the difference can thus be attributed to the latter elements.

- The importance in PD of ATS1-A is larger than one could initially expected from it being almost a straight pipe with an empty lateral cavity and a small (in regards to the device lenght) part, but its PD under a mass flow of 800 kg/h is almost equal to that of ATS1-D2.

- As explained in Section 5.3 most of that PD can be assigned to the static swirl mixer and the turbulence it induces, which means that at high MFR, a 26 mm part rivals in PD a 136 mm long monolith with 15100 cells.

- The effect of the linear term associated with the presence of monoliths is quite clear when one observes the curves ATS1-D2 in regards to that of ATS1-A which have almost equal PD at 800 kg/h.

- The aforementioned is also evidenced between ATS1-D1D2 and ATS1-AD1, where the difference between them is slightly lesser probably due to the presence of two monoliths downstream of the mixer, but still noticeable in comparison with that from a device with three monoliths.

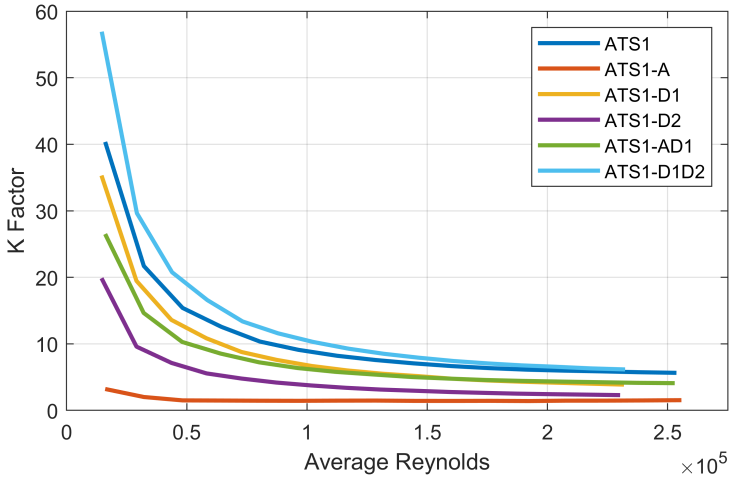

Figure 5.64: Summary of the K factors obtained for ATS1, its composing devices and their partial combinations.

In view of these results, another observation is that regarding the results of ATS1-D1 and ATS1, the PD of the device is noticeably smaller, about 50% of that of the ATS, but regarding the pressure drop coefficients those results are of the same order of magnitude. This is related with the inclusion of the terms for kinetic energies, that account for the difference in the inlet diameters used in the corresponding tests, to compute these pressure drop coefficients. In this sense, it is the PD that allows for a direct comparison between the different contributions, whereas the pressure drop coefficient has the advantage that can be extrapolated to any relevant flow conditions if the value of the diameter used in the characterization is known.

Moving to the additivity assessment, the first case considered is that of ATS1-AD1. Its results are plotted together with those of ATS1-A, ATS1-D1 and the addition of both. It can be observed in Fig. 5.65 that, overall, the sum of isolated measurements produces a very similar result to that of the measurement of the assembly, thus suggesting that there is in fact an additive character in PD, although some expectable differences are observed. These discrepancies are thought to be related with the fact that when assembled, the element placed downstream is

not subject to a fully developed flow as it is guaranteed in the isolated measurements.

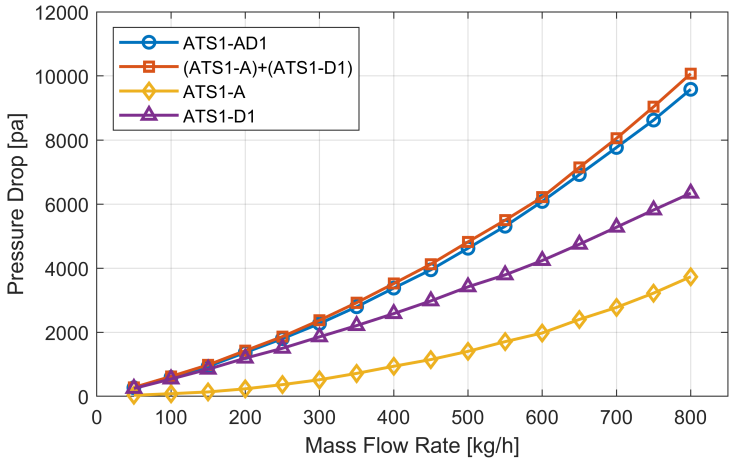

Figure 5.65: PD additivity assessment for ATS1-AD1.

Fig. 5.66 shows the equivalent representation for ATS1-D1D2, where again the similarity of the result for the sum of the isolated devices and the measurement of the assembly is evident, further verifying the additivity of the back-pressure. Once again the small differences are though to be related with the different conditions of flow from isolated to assembled test; if this guess is right, the addition of more isolated devices should obviously cause a larger difference.

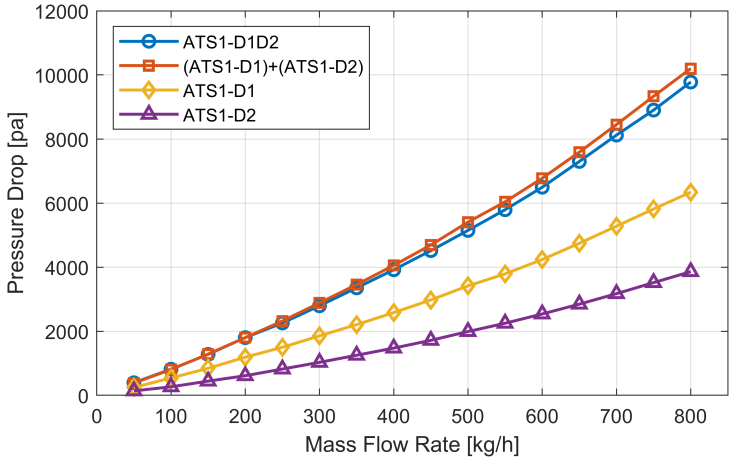

Figure 5.66: PD additivity assessment for ATS1-D1D2.

Conveniently, the additivity check for the complete ATS offers the opportunity to check that there are three combinations of measurements that should produce similar results, apart from the differences found so far; this is shown in Fig. 5.67. As expected, the sum of three measurements shows a slightly larger difference to the complete system than the other two sums, which are the addition of two measurements as in previous cases, and whose results are almost indistinguishable, being the additivity of back-pressure soundly verified.

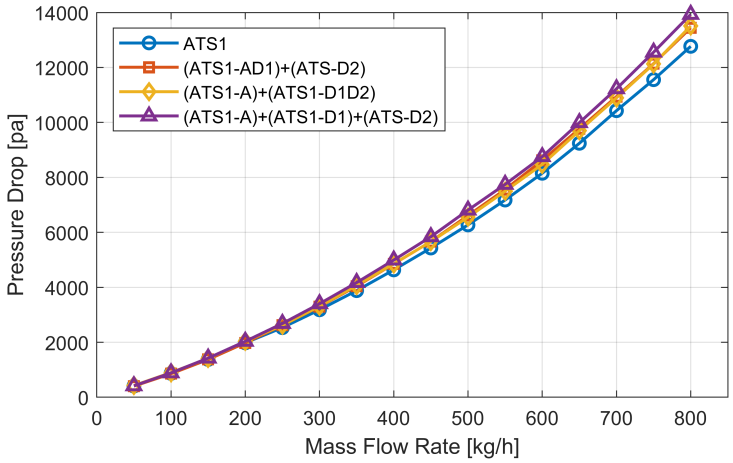

Figure 5.67: PD additivity assessment for ATS1

Some other conclusions to be drawn from these figures now that the additive character of PD has been verified, include:

- Going back to Fig. 5.65, the importance of the contribution of ATS1-A being significant regardless of the size of its mixer is confirmed, as even when coupled with the double monolith device, for the maximum flow measured it contributed about 40% of the PD of the assembly.

- In Fig. 5.66 only results for parts containing monoliths are plotted together, and with the resolution of the plot, the presence of the linear term related precisely to the laminar flow due to the monoliths is very noticeable.

- Now that the PD has been confirmed to be additive, the agreement between results of combinations and sums including ATS1-A confirms that the PD of the device was properly measured regardless of it being smaller than that of the upstream duct.

Considering the small difference between the sum of the three isolated devices and that of the measurement of the complete system, values from the PD isolated measurements can be taken and computed to

estimate what approximate contribution to the total back-pressure can be attributed to each device. Due to their quasi-quadratic behaviour the contribution of each individual device to the complete system varies with the mass flow rate, and therefore two values were checked, the PD at 400 kg/h and 800 kg/h. With these considerations, for instance ATS1-A accounts for about 18.8% at 400 kg/h, and for 27.1% at 800 kg/h, whereas ATS1-D1 and ATS1-D2 move from 29.5% to 28.1% and from 51.7% to 46.1%, respectively. These percentages are consistent with what can be visually appreciated in Fig. 5.63.

Transmission loss results

The logic to assess the additivity check on TL is similar to that of PD, but due to the oscillatory nature of the curves, and to make visual inspection easier, the results for the isolated devices are plotted with dotted lines and the curves of the sums are plotted in red solid lines.

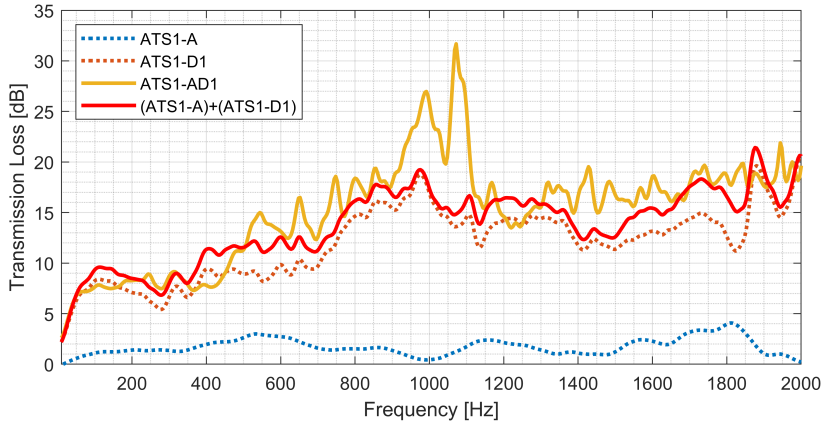

Figure 5.68: Transmission loss additivity assessment for ATS1-AD1.

First, the case for ATS1-AD1 is presented in Fig. 5.68. It can be observed that the low frequency rise is almost identical, consistently with the small volume of the mixer unit. The first significant difference arises in the reactive-driven frequency, approximately between 400 and 500 Hz. Up to this point the sum is either almost identical or sur-

passes the measurement of the assembly, as it could be expected since in the assembly the device placed downstream is not subject to the same excitation as in the isolated test. Above 700 Hz the measurement of the assembly is higher than the sum of individual results except in two frequency bands (approx. $1200 - 1300$ Hz and $1850 - 1900$ Hz), suggesting a considerable interaction, especially in the spikes around 1000 Hz. However, the sum and the measurement of the assembly do keep a considerable resemblance above 1100 Hz, as if there was some additivity. This gives place to the notion that dissipative attenuations can be essentially additive, as only in the vicinity of frequencies where the mixer exhibits some reactive behaviour can one find significant differences between the combination and the sum of the parts.

The same representation is shown for ATS1-D1D2 at flowless condition in Fig. 5.69. In this case several remarks are forthcoming.

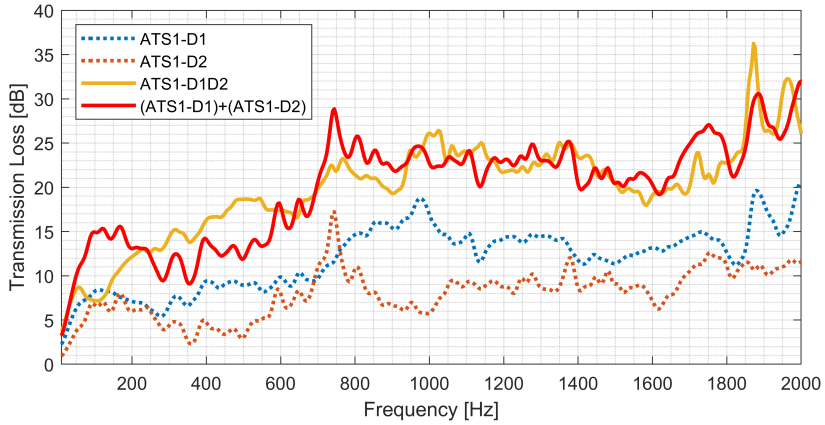

Figure 5.69: Transmission loss additivity assessment for ATS1-D1D2

- On the comparison of ATS1-D1 and ATS1-D2:
  - ATS1-D1 has a larger sound attenuation at all frequencies, except the unexpected spike of ATS1-D2 at around 750 Hz.
  - The difference in the initial ramp, which is known to be related to the volume, is indeed explained by device D1 being larger.

  - For the rest of the frequencies, ignoring the unexpected spike, the presence of the second monolith justifies its more dissipative character.

- On the comparison of ATS1-D1D2 and the sum of the individual devices:

  - Up to 50 Hz the slope of the initial ramp is adequately captured.
  - From 50 to 225 Hz: Some interaction has to be occurring since the result for the assembly is considerably smaller than that of the sum, and even below the TL of the individual ATS1-D1, and similar at around 100 Hz.
  - From 225 to 700 Hz: The assembly surpasses clearly the sum of individual devices.
  - From 700 to 950 Hz: Once again the sum goes beyond the measurement of the assembly, even though the discrepancies are smaller.
  - Above 1000 Hz both results are essentially equal, with most differences falling into the acceptable margin of 3 dB.

Deeper analysis of this observations suggests the following comments:

- The TL seems to be not additive in the range of frequencies known to be dominated by reactive effects, and above approximately 800 Hz, were the attenuation is essentially dominated by dissipative effects, the TL is fairly additive. At such point any potential acoustic coupling between the devices becomes irrelevant.

- The unexpected and unexplained spike identified in ATS1-D2, appears to be somehow present in the measurement of the assembly, at least in terms of shape. Therefore, it is not fully clear if, as stated above, this spike could be an unintended result of the manipulations done when splitting the system into its composing devices.

Finally, in the case of the TL additivity check for the complete ATS, the possible sums to account for the complete device are presented in

separated plots to guarantee appropriate visualization. First Fig. 5.70 compares the results for the complete ATS, with the sum of ATS1-A with the assembly of devices containing monoliths (ATS1-D1D2). Then, Fig. 5.71 compares it with the sum of the assembly ATS1-AD1 and device ATS1-D2. Finally Fig. 5.72 compares the measurement of ATS1 with the sum of the three individual devices.

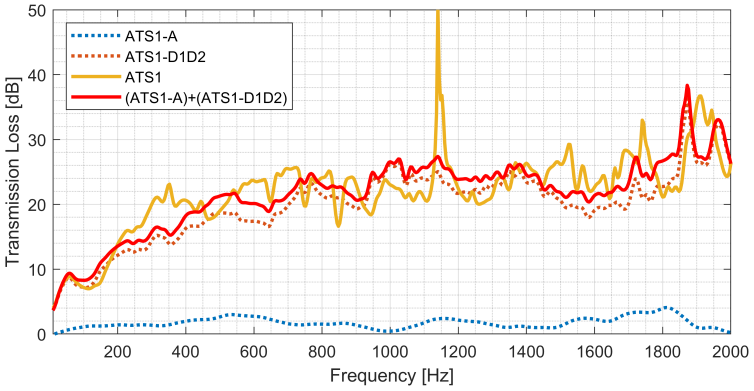

Figure 5.70: TL additivity assessment for ATS1, first approach, compared to ATS1-A + ATS1-D1D2

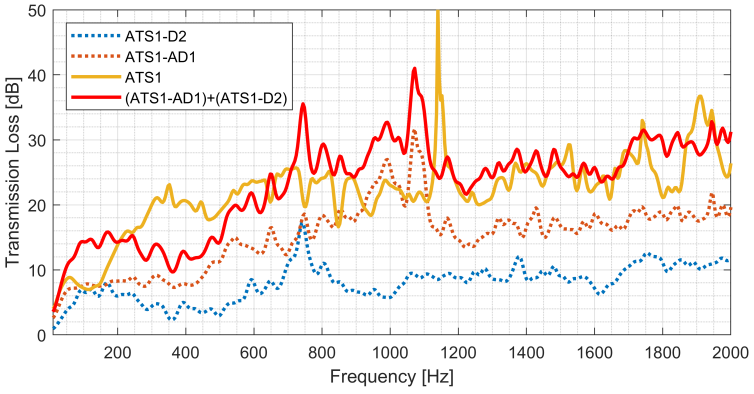

Figure 5.71: TL additivity assessment for ATS1, second approach, compared to ATS1-AD1 + ATS1-D2

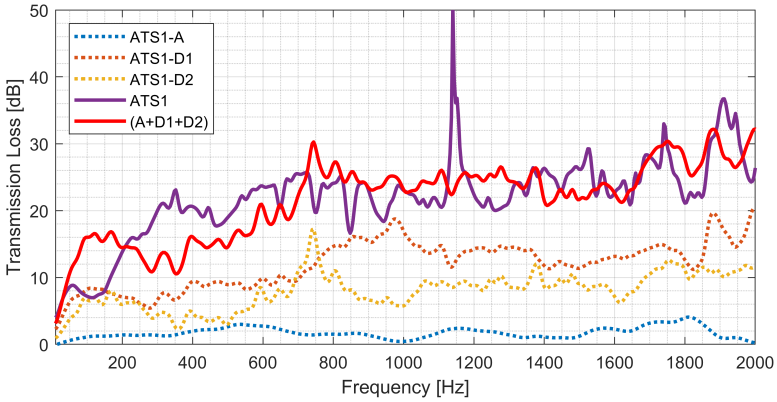

Figure 5.72: TL additivity assessment for ATS1, third approach, compared to ATS1-AD1 + ATS1-D2

- In Fig. 5.70 it is evidenced again that the mixer essentially adds its attenuation to whatever is placed downstream with almost no other significant effects.
- Fig. 5.71 shows a sum that does not match with the system measurement until up to 1200 Hz (after the spike), particularly overestimating with a very oscillatory behaviour between 750 and 1150 Hz.
- Fig. 5.72 shows the sum of the three devices measured independently, and the results are in fact very close to those of the addition of ATS1-AD1 and ATS1-D2.

Finally, in order to make it easier to compare, the result of ATS1 is plotted again alongside with the three sum options in Fig. 5.73.

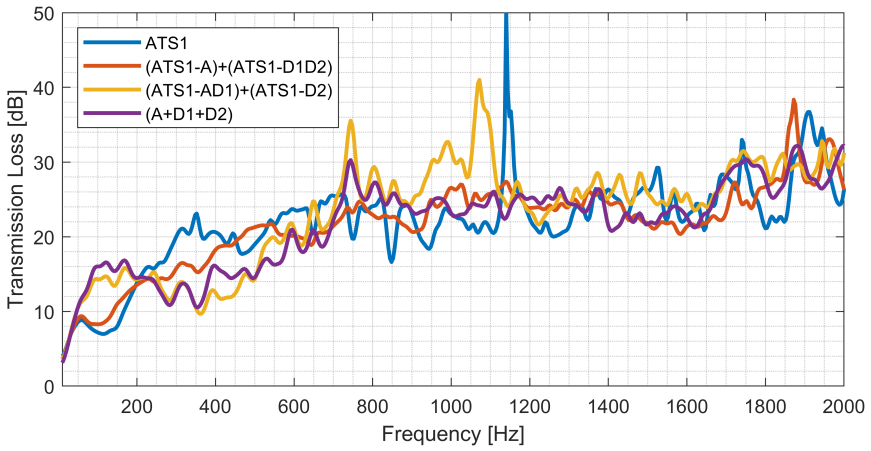

Figure 5.73: TL additivity assessment for ATS1, comparison of sums

None of the results from sums matches properly that of ATS1 measurement; the discrepancies are specially large at low frequencies, whereas around the peak at 1175 Hz, starting at 700 HZ and particularly above 1300 Hz all the sums become quite close one another and to the measurement.

In view of all these results, the preliminary conclusions stated above seem to be confirmed: the high frequencies are essentially additive, indicating that the behaviour is controlled by dissipation, whereas the low to mid frequencies are controlled by reactive mechanisms and the attenuation is not additive due to acoustic interactions between the subparts. Even so, some of the features in the individual subparts can be identified in the whole part but, in any case, with some frequency shift.

Chapter 6

Assessment of Individual After-treatment Devices

Part of the results and analysis presented in this chapter, particularly in the section *The very early life of GPF* can also be found in the paper *A study of the early life of Gasoline Particulate Filters: Reactive and dissipative acoustic effects* [2], which is a JCR publication derived from this part of the research. Also the discussion on reactive and dissipative effects derived from the application of decomposition analysis might share points with those presented in the other thesis-related publications enumerated in the *Publications* section.

6.1 Introduction & background

The previous Chapter was focused on the characterization of a prototype SCR system with a conveniently simple, straightforward and aligned geometrical disposition, but actual after-treatment systems and devices tend to have more intricate geometries as these systems have to fit in the limited and entangled space available for the exhaust line within the engine compartment and the underside of the vehicle. This chapter is focused on the characterization of devices classified in the intermediate and complex geometry categories corresponding to actual parts used in commercial applications. Therefore this varied group of devices comprises a sufficiently wide range of characteristics in terms

of geometry and basic elements so as to be considered representative of any realistic after-treatment device.

Two levels of complexity were added with these devices: first, intricate geometries in the sense of curved, twisted and even flexible pipe sections, contraction and expansion volumes of irregular shape, and secondly the presence of wall-flow filters. The latter were expected to have noticeable effects, mainly in terms of PD. The devices studied included DPF, GPFc and SCRf (DPF with SCR catalyst), three of the most extended particulate filters in use. In that sense and as mentioned several times the characterization of devices was tackled in order of increasing complexity. Following that pattern, this chapter starts with the assessment of devices classified into the intermediate geometry complexity category. First, in Section 6.2 those with curvature and irregular geometries but only FT monoliths, ATD2 and ATD3; then, adding the presence of WF monoliths in ATD4 and ATD1 in Section 6.3, where along the assessment of ATD1 the capabilities and convenience of 1D-3D coupled simulations were also studied. Once the experimental characterization and the modelling, both 3D and 1D, representation of all devices were obtained, comparative analysis was applied between results in order to identify the influence of each element or characteristic on the PD and the TL in Section 6.4.

Then, two special assessments are presented. First the opportunity to fill a knowledge gap relative to the changes that take place during the first few cycles of use of a GPF was seized by cycling ATD1 for the equivalent of 235 km and characterizing it again; this is presented in Section 6.5. Finally, while up to this point the modelling workfront has guided the structuration of the 1D modelling methodology as postulated in Section 3.3.5, the last section (Section 6.6) is dedicated to the characterization of the most complex parts available, ATD5 and ATD6, which are used as test subject to account for the ability of the modelling methodology to produce satisfactory results from scratch, only using CAD geometrical information. The results, that may still be improved by tuning or small adjustments, were found to be quite indicative.

For the sake of presenting more context on the aforementioned knowledge gap, the following background on the topic is provided. Regardles of GPF being a development on the basis and technology transfer from

DPF applied to gasoline direct injection vehicles, and sharing the overall working principles, there are also differences in operation and behaviour, due to differences in the particulate matter and exhaust flow conditions of the different engines they are fitted to. To name a few, compared to DPFs, GPFs are generally exposed to higher exhaust temperatures, lower oxygen concentrations, and finer particles. Regeneration for GPFs is always passive, whereas DPFs can use either passive or active mechanisms. GPFs have higher porosity, which while allows the gas to move more easily across the substrate, also compromises mechanical properties since the substrate is lighter and hence more fragile. The average soot loading capacity of a DPF is around 8 grams per liter (g/l), whereas for a GPF the average capacity is about 1 g/l. The reduced storage capacity of GPFs is not as problematic as it could initially appear to be, as gasoline particulate emissions are about 10 to 30 times smaller, and the frequent regeneration makes it difficult to form and maintain a soot cake layer on the substrate wall [143].

There are some studies in the literature on the early service life of GPFs [143, 144, 18], whose results suggest that at this stage, filtration performance is strongly affected by mass deposition and depends on the microstructure of the substrate: due to their reduced size, GDI particles are capable of entering the porous walls, in a filtration mechanism known as "deep-bed filtration" which modifies the overall substrate structure and therefore the filtration performance; however, those studies are focused mainly on the filtration performance of the devices, disregarding potential acoustic effects.

The effects of all these characteristics on exhaust wave dynamics arise in two different ways: *reactive* effects, mostly associated with wave reflection at the device, and *dissipative* effects associated with flow losses. Such effects determine the wave pattern in the exhaust line downstream of the ATS, and thus set the attenuation required from the silencer. The usual design approach is to consider what would be the worst scenario, that is, the device in never-used condition before any changes in the substrate microstructure due to soot deposition have occurred. However, the fact that this condition may not be found in practice introduces an unnecessary complication in the design of the exhaust line. In fact, the dissipative effects of usage will in general reduce wave transmission across the ATS, thus reducing the actual noise source

at the outlet, whereas the reactive effects will contribute to reduce the negative impact of any resonances associated with the duct connecting the ATS and the muffler. Therefore, with some proper assessment of the influence of usage on the reactive and dissipative behaviour of an ATS including a GPF, design requirements could be relaxed and the development time and costs reduced.

Consequently, the focus of the assessment presented in Section 6.5 has been put on the comparison of "new" and "clean" conditions. The former refers to the never-used state (the devices used were supplied directly from the factory, even with the catalyst bricks sealed), whereas the latter corresponds to the base state acquired by the PF monolith after the device has been used, loaded, and regenerated, but for a short time and distance, in order to avoid that any significant amount of ash may enter the filter. This condition is comparable to that of a vehicle particulate filter at the moment of reaching the customer in a new car. Experimental characterization and 1D modelling results will be discussed and analyzed, with special attention to changes in the reactive and dissipative effects observed in the experiments, and to the ability of modelling to account for such changes.

6.2 Devices with flow-through monoliths, bends and irregular geometries

The next step in the ascending complexity order intended was to assess the individual devices classified as of intermediate complexity, firstly ATD2 and ATD3, as both include peculiar geometrical dispositions but coincide with ATS1-D1 from the simple geometry category in having two FT monolith. ATD2 peculiarities are mostly related to the curvature of the inlet and outlet pipes, along with irregular expansion and contraction volumes, whereas ATD3 keeps straight inlet and outlet pipes, but it has very irregular expansion and contraction volumes and, additionally, a considerably large volume between the monoliths (not in the same canning) and, on the contrary to devices and combinations from the previous chapter, none of the components is aligned with the others.

Assessment procedure

The assessment procedure involves both experimental and computational work-fronts, the experimental one related to the measurements and the computational one with the use of 3D and 1D modelling approaches; as three-dimensional flow effects are naturally expectable due to the intricate geometries, in this chapter the use of 3D CFD tool is more prominent.

Measurements of the experimental assessment

Table 6.1 summarizes the measurements taken for ATD2 and ATD3. ATD3 was measured twice, as it was selected to check for potential differences caused by the presence of a sensor, injector or similar penetrating into the flow path and being in contact with the flow. Also, the back-pressure imposed by this device forced to measure it in both facilities with mass flow rates different from those used for most other devices. ATD2 was also used as the baseline to account for the effect of some cycles of use alongside ATD1 but such assessment is presented in Section 6.5.

Table 6.1: Information on the experimental measurements taken for devices ATD2 and ATD3.

Characterization		**ATD**		
Test Facility	*Condition*	*ATD2*	*ATD3* (Sensor)	*ATD3* (No sensor)
Pressure drop	Min. MFR	50 kg/h		
testing on	Max. MFR	800 kg/h	636 kg/h	
CFTB	Increase steps	50 kg/h	50 kg/h, last 36 kg/h	
	Orientation	Direct & Inverse		
Transmission	Flowless	1 pulse amplitude		
loss testing	1st MFR	100 kg/h, 2 pulse amplitudes		
on ITR	2nd MFR	MFR 200 kg/h, 2 pulse amp.	MFR 150 kg/h, 2 pulse amp.	
	3rd MFR	MFR 300 kg/h, 2 pulse amp.	MFR 220 kg/h, 2 pulse amp.	

Preparation of modelling assessment

ATD2

The CAD file was key to collect geometrical information for a proper 1D modelling as well as to obtain the fluid domain for the 3D CFD modelling. Fig. 6.1 shows the cleaned-up CAD file of ATD2, with colours assigned to differentiate components as decided in the discretization and their treatment; inlet and outlet pipes are highlighted in red, monolith bricks in grey, the irregular shaped volumes in purple and the inter-monolith gap in orange. Then, Fig. 6.2 presents the 1D model prepared

accordingly. From the cleaned CAD presented, along with the addition of lids to close the inlet and outlet pipes, the fluid domain was extracted for 3D CFD modelling.

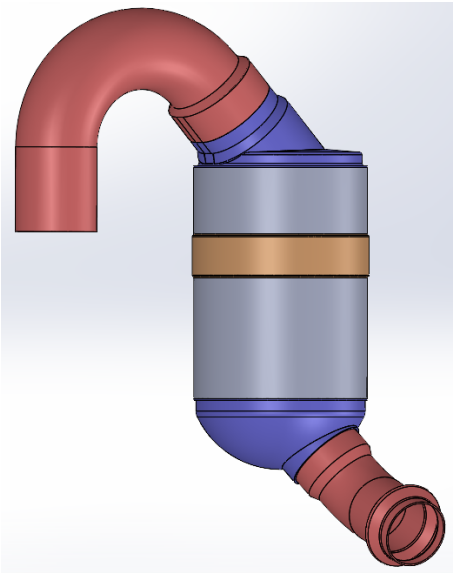

Figure 6.1: Cleaned up CAD of ATD2 coloured to indicate the decided discretization.

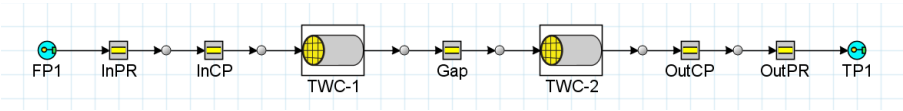

Figure 6.2: 1D model representation of ATD2.

ATD3

Similarly, Fig. 6.3 presents the CAD file for ATD3 after the clean-up processing. The colour code to differentiate the components and their treatment as decided from the discretization is used again, with the

difference that ATD3 does not have a regular gap between the monoliths but a huge irregular volume. Finally, Fig. 6.4 presents the 1D model prepared accordingly; again with the addition of closing lids, the fluid domain for CFD was extracted from this copy of the CAD file.

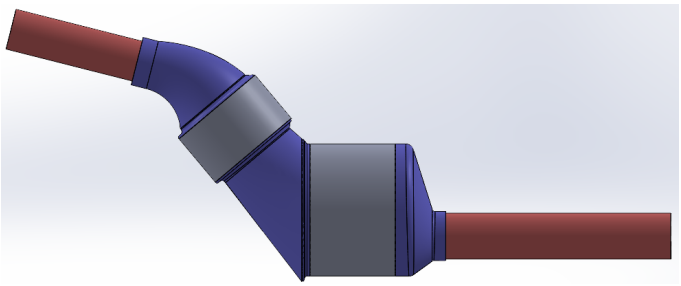

Figure 6.3: Fluid domain for 3D modelling and discretization (colour code) of ATD3.

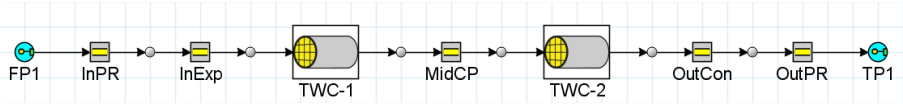

Figure 6.4: 1D model representation of ATD3.

Results and discussion

ATD2

Pressure drop

The PD and K factor results obtained from CTFB measurements are presented in Figs. 6.5 and 6.6, respectively. PD results are fully consistent as the dependence on the mass flow is well represented, being the quadratic and linear terms present, but with a stronger quadratic influence than that found in the results for devices of the simple geometry category. Also the pressure drop coefficient exhibits the appropriate asymptotic behaviour.

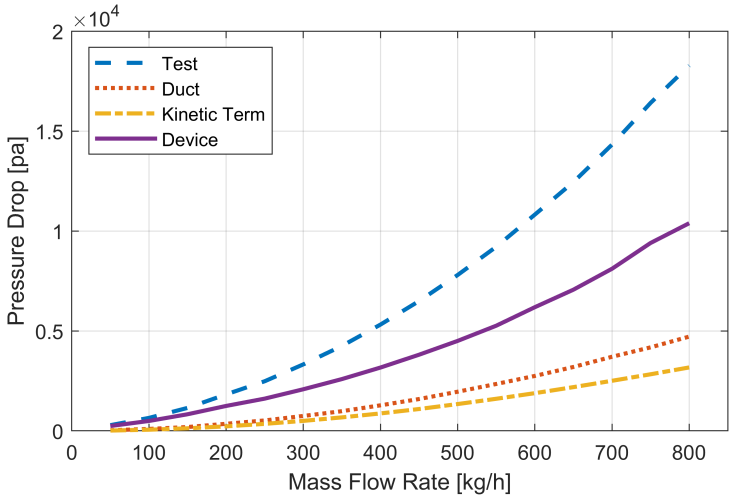

Figure 6.5: Experimental PD results from ATD2 characterization.

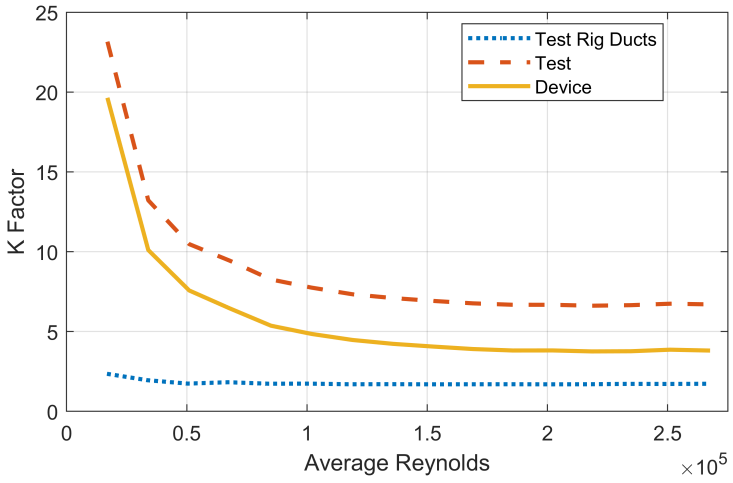

Figure 6.6: Pressure drop coefficient, K factor, from experimental characterization of ATD2.

Fig. 5.14 shows the results from the 1D virtual twin model of the device tested in the PD testing template alongside the experimental results for direct comparison. The agreement obtained for this device is satisfactory: while the precise shape of the curve is not precisely reproduced, the lower and higher values are adequately captured, but at the cost of sacrificing some precision at intermediate MFR conditions.

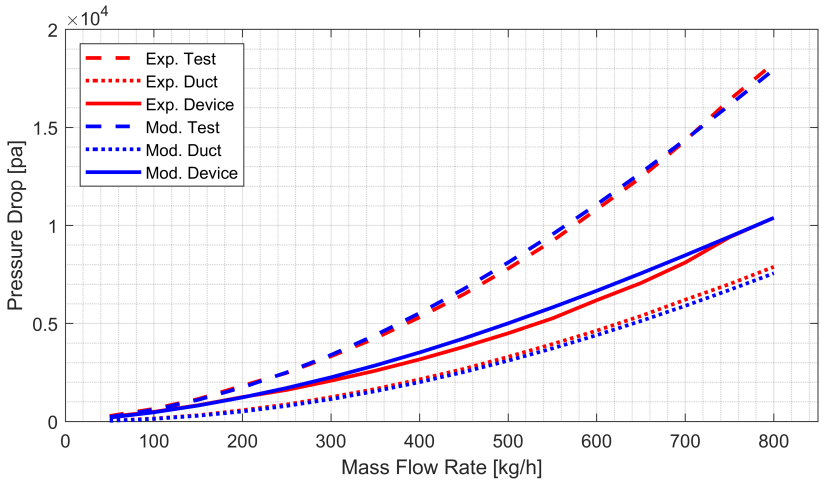

Figure 6.7: Comparison of experimental and 1D modelled PD results for ATD2.

Fig. 6.8 shows the results from the 3D CFD simulation, particularly for the case with a 300 kg/h mass flow rate. Total pressure (right) and velocity vectors (left) were checked, The velocity vector representation gives a clear idea of how the flow is distributed in the volume, and the magnitude of velocity (averaged over the outlet surface) allows to compare the condition of the flow with experimental data and 1D models. Pressure drop, computed as the difference in total pressure between the inlet surface and the outlet surface, is also registered.

In this case, the evolution of total pressure matches what could be expected, with most of the pressure drop occurring in the can containing the monoliths. On the other hand, the velocity vectors offer a clear view of the laminating effect of the monoliths, of the increased velocity in the outlet pipe due to its smaller diameters compared to the inlet

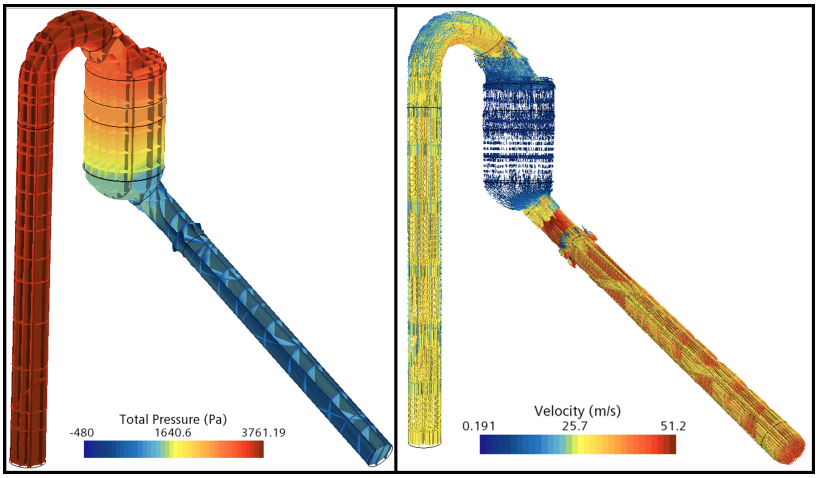

Figure 6.8: Total pressure and velocity vector representation for ATD2 at 300 kg/h.

pipe, and of the particularities of curvature in the inlet side and abrupt diameter change in the pipe at the outlet side. Finally Fig. 6.9 shows the comparison of results of the 1D and 3D modelling approaches alongside the experimental results as a reference.

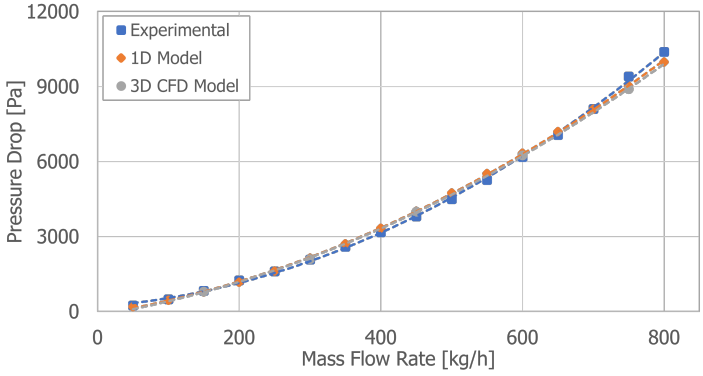

Figure 6.9: Comparison of experimental and modelled PD results for ATD2.

Transmission loss

The complete set of smoothed experimental results for ATD2 are shown in Fig. 6.10. It is evidenced that the overall shape of the curve is the same for the flowless case as for the three cases of superimposed mean flow regardless of the size of the pulse but, as usual, with the results from the small pulse measurements being considerably more oscillatory or noisy, to the point of being not as useful as the large pulse results for further analysis. Additionally, some flow-dependent acoustic features could be detected through their shifting with the flow.

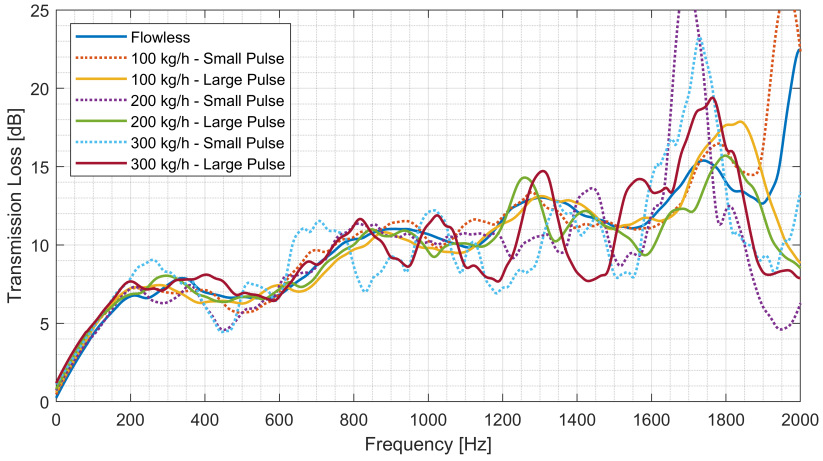

Figure 6.10: Complete set of exp. smoothed TL results for ATD2.

Regarding the effect of a superimposed mean flow, for the large pulse results (solid lines) a small increase can be observed in the attenuation below 1000 Hz. For frequencies above 1000 Hz, a different behaviour is observed at 200 and 300 kg/h with respect to no-flow and 100 kg/h cases, with more marked features subject to the expected frequency shifts. On the other hand, with the small pulse (dotted lines) the trend is essentially the same as for the large pulse, but as usual flow-associated features, such as dissipation and shifts, are more evident here. Overall, as in the previous chapter large pulse is preferred for benchmarking of models, as results for the small pulse become excessively noisy, mainly

at 300 kg/h which can also be noticed in the corresponding large pulse measurements.

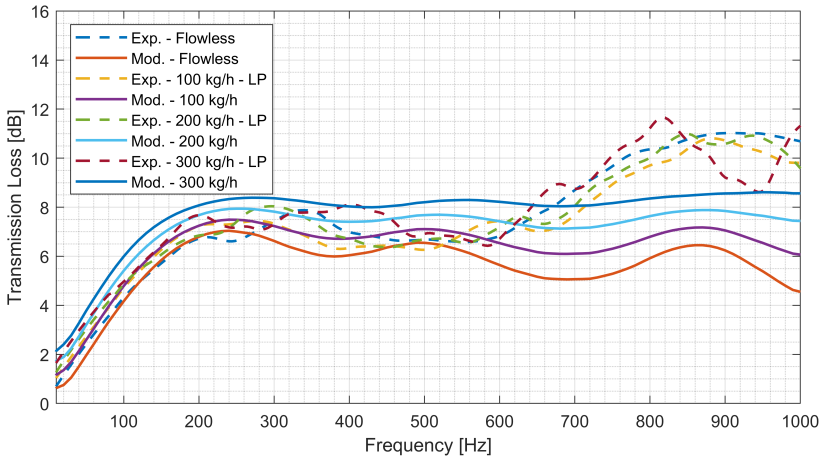

Figure 6.11: Comparison of Exp. Smoothed (large pulse) and 1D modelled TL results for ATD2.

Fig. 6.11 shows the comparison of 1D modelled and experimental smoothed results with large pulse. The overall effect of superimposed flow increasing the attenuation is reproduced, even though slightly overestimated. The initial ramp of the curve is perfectly captured for flowless and 100 kg/h cases, and slightly overestimated, but with the proper slope, for the higher mass flows. Also the shape of the curve and the peak attenuation up to 600 Hz are also captured. Starting at that frequency the attenuation is underestimated, but still the information produced is useful.

Fig. 6.12 shows the results for both small and large pulse at 100 kg/h, where the observations mentioned above can be more easily appreciated.

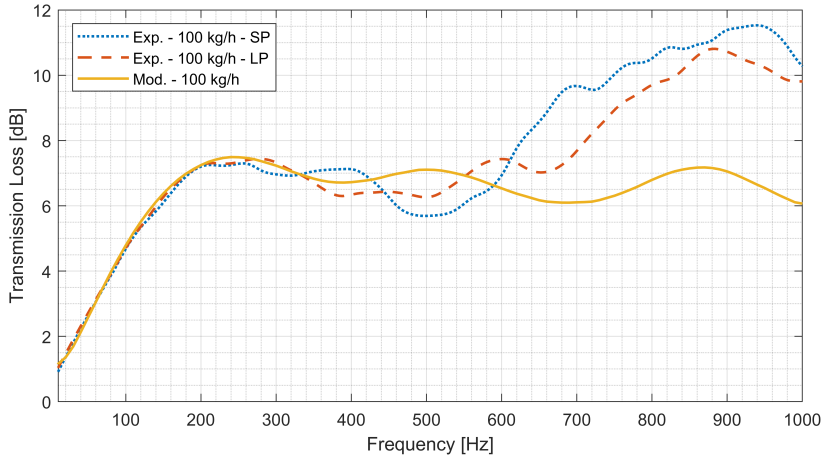

Figure 6.12: Comparison of Exp. Smoothed (both pulses) and $1D$ modelled TL loss results for ATD2 with 100 kg/h of superimposed mean flow.

ATD3

Pressure drop

In the case of ATD3, the device was found to generate a considerably higher back-pressure which made it impossible to reach the 800 kg/h in the CFTB, as in other devices; the maximum MFR reached was 636 kg/h. Considering that the monoliths it contain are of the FT kind, this was considered to be related to its smaller inlet pipe diameter. Aside of this, the results presented in Fig. 6.13 for PD and in Fig. 6.14 for pressure drop coefficients, are fully consistent with the expected behaviour. The PD exhibited the appropriate quasi-quadratic dependence on the mass flow, and the pressure drop coefficient the right asymptotic behaviour at high Reynolds numbers.

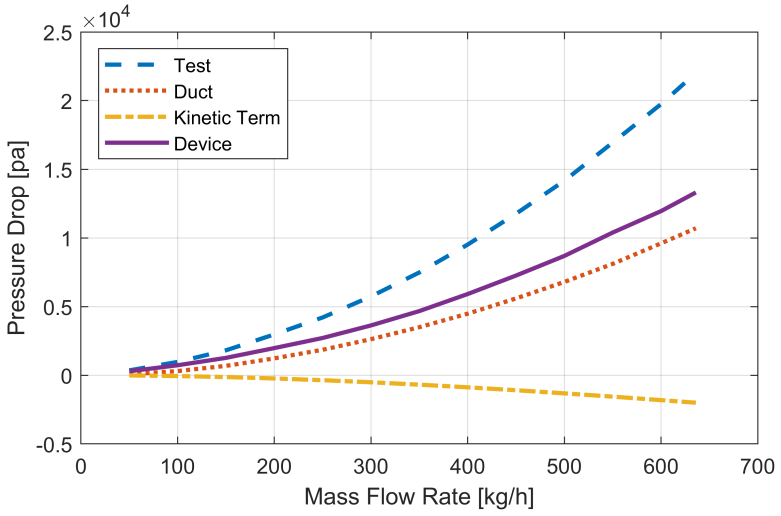

Figure 6.13: Experimental PD results from ATD3 characterization.

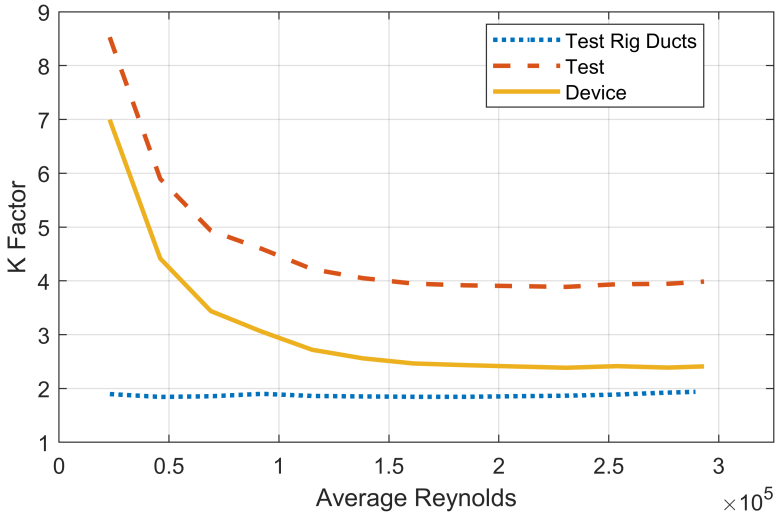

Figure 6.14: Pressure drop coefficient, K factor, from experimental characterization of ATD3.

Fig. 6.15 shows the results from the 1D virtual twin model of the device alongside the measured values for direct comparison. The agreement obtained for this device is excellent, with barely noticeable differences between modelled and experimental curves.

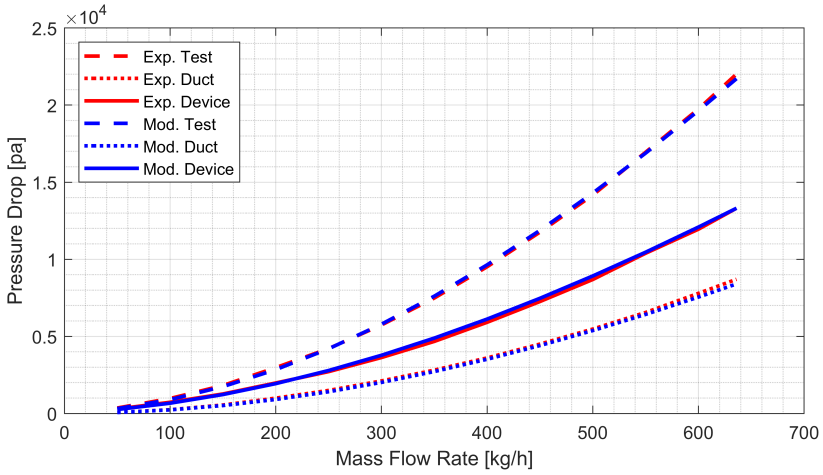

Figure 6.15: Comparison of Exp. and 1D Mod. PD results for ATD3.

Moving to the results of the 3D CFD approach, Fig. 6.16 shows the results for total pressure and velocity vectors for the case with 300 kg/h of mass flow. The overall evolution of the pressure is as expected, with the most relevant pressure drops coinciding with the monoliths; on the other hand, the velocity vectors suggest some abrupt changes in the expansion, intermediate and contraction volumes.

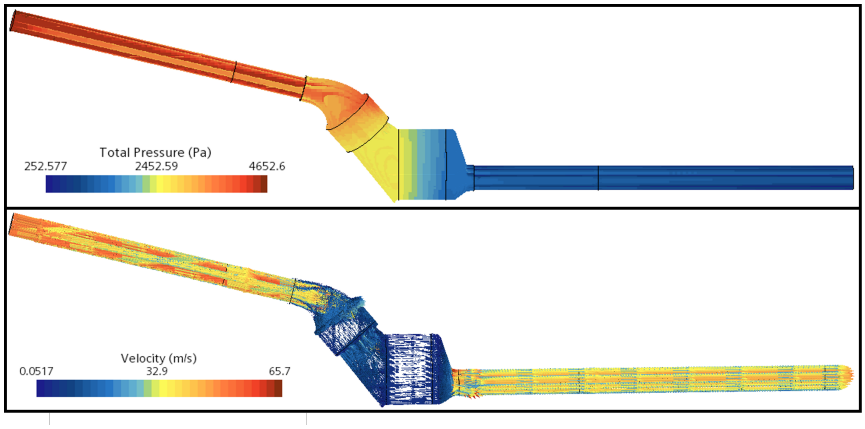

Figure 6.16: Total pressure and velocity vector representation for ATD3 at 300 kg/h.

Finally Fig. 6.17 shows the comparison of results of the 1D and 3D modelling approaches alongside the experimental values as reference. For the sake of comparability with the other devices, experimental results were extrapolated up to 800 kg/h with a second order polynomial fit, adjusted with a coefficient of determination R^2 of 0.9999.

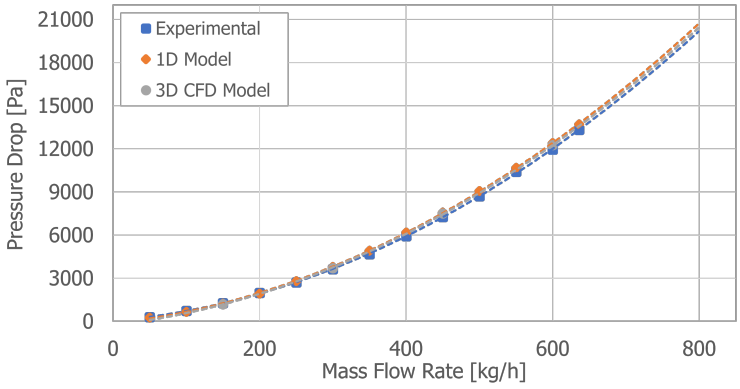

Figure 6.17: Comparison of experimental and modelled PD results for ATD3.

Transmission loss

Similar to the PD characterization, it was not possible to reach the usual mass flow rates during the measurements in the ITR; instead, the measurements were taken with mass flow rates of 100, 150 and 220 kg/h. Additionally, two sets of TL measurements were performed, with and without a probe inserted in a sensor port located in the outlet pipe, to account for the potential effects of a sensor in contact with the flow acting as an obstacle. In both cases, it can be observed that the overall effect of the flow changed sign between the low and the high frequencies, so that increasing flow produced increased attenuation at low to mid frequencies whereas the effect at higher frequencies was a decrease in the attenuation.

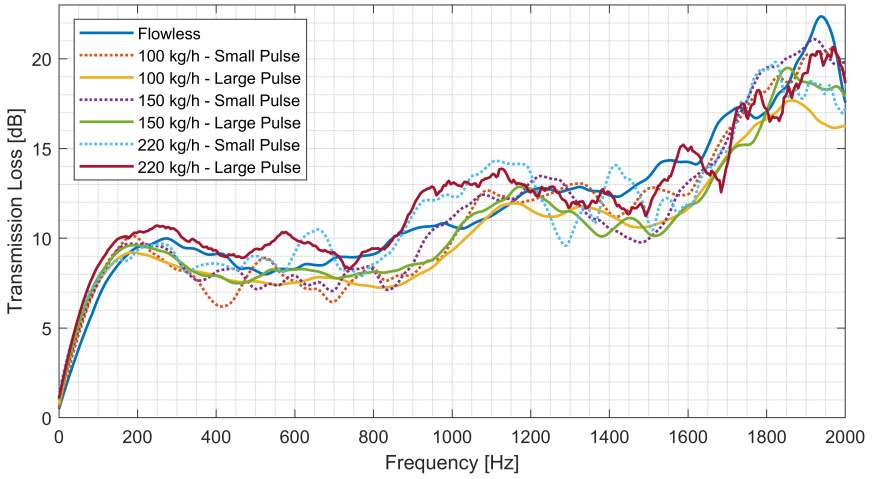

Figure 6.18: Complete set of exp. smoothed TL results for ATD3 with Sensor.

With these preliminary considerations, Fig. 6.18 and Fig. 6.19 show the TL results for the measurements with and without probe, respectively. As usual, the small pulse results tend to be noticeably more oscillatory, but for this device extremely noisy results were obtained for the 220 kg/h mass flow case even with the large pulse, which is not even compensated by the smoothing processing; therefore, those results were

not taken into account. It can be observed that, regardless of the pulse used and of the presence or not of the sensor, flow-related dissipative effects produce a certain increase in attenuation below approximately 800 Hz, whereas above this frequency, there is a certain decrease when increasing the flow.

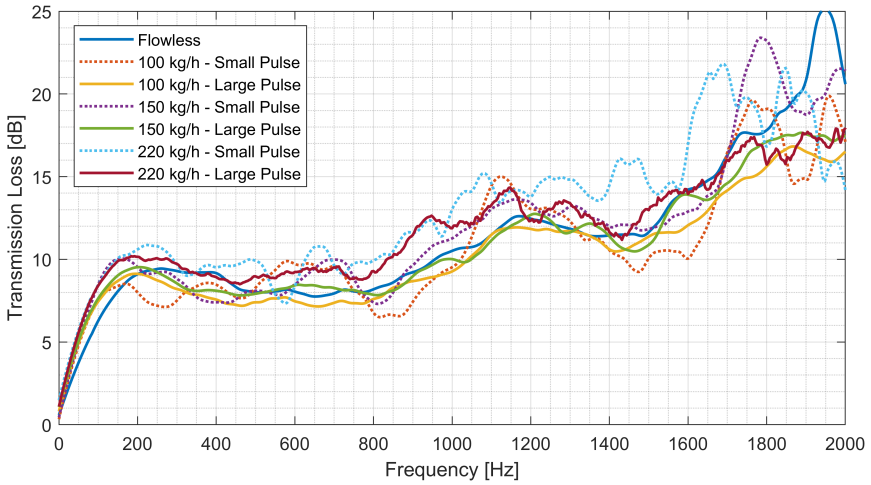

Figure 6.19: Complete set of exp. smoothed TL results for ATD3 without Sensor.

For the thorough analysis of the effect of the probe, the following figures display the comparison of raw TL results with and without the probe at different flow conditions; 220 kg/h results were also neglected in this case. Starting with Fig. 6.20, the flowless results are presented, which are virtually identical below 600 Hz, with some differences within 2 dB at higher frequencies, except for a peak in the case without sensor at about 1900 Hz which punctually overcomes the case with sensor by about 6 dB. In general, it can be said that, in this case and for the range of frequencies considered, the presence of the probe marginally increases the attenuation.

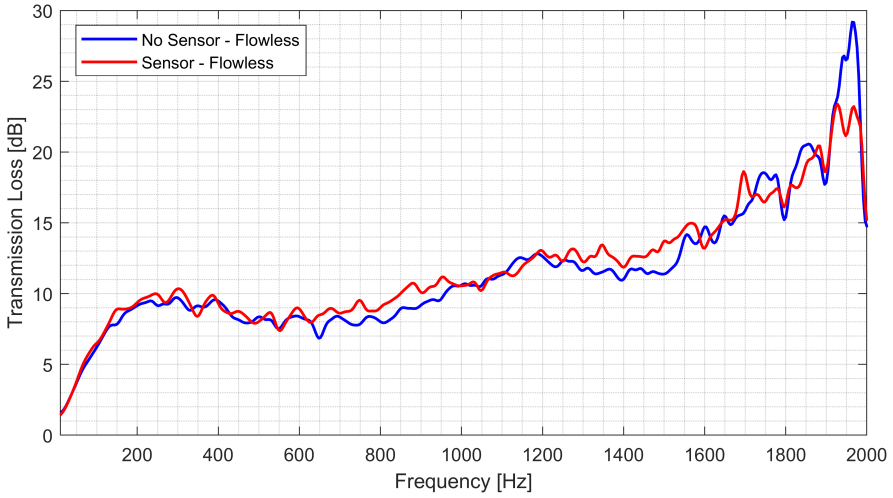

Figure 6.20: Probe effect assessment: Comparison of experimental TL results at flowless condition.

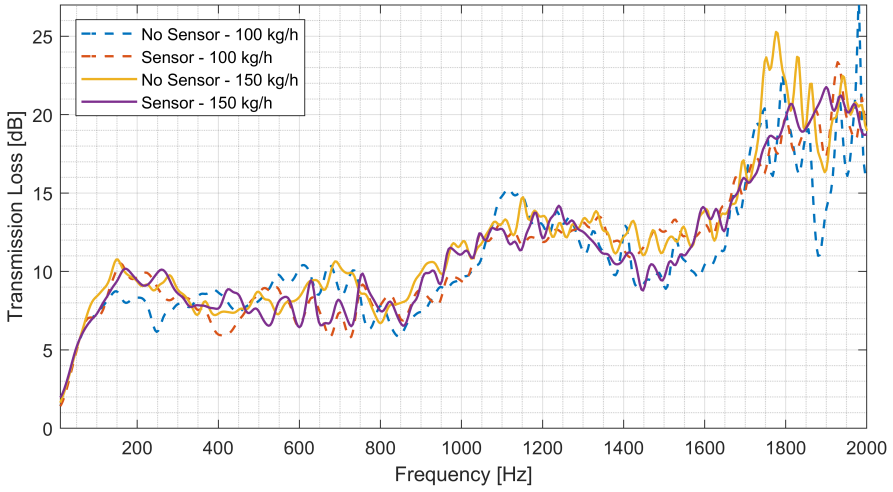

Figure 6.21: Probe effect assessment: Comparison of experimental TL results with small pulse excitement and superimposed flow.

Fig. 6.21 presents the results from measurements with 100 and 150 kg/h of superimposed mean flow and excited by a small pulse. At 100 kg/h some differences arise, so that depending on the frequencies considered the probe produces either an increase or a decrease in the attenuation. However, the influence observed at 150 kg/h is much less remarkable.

Finally in Fig. 6.22 the results from measurements with 100 and 150 kg/h of superimposed mean flow and excited by the large pulse are shown. Overall, a similar behaviour is evidenced: at 100 kg/h the effects are scarcely noticeable, whereas at 150 kg/h no significant differences are apparent below 1000 Hz.

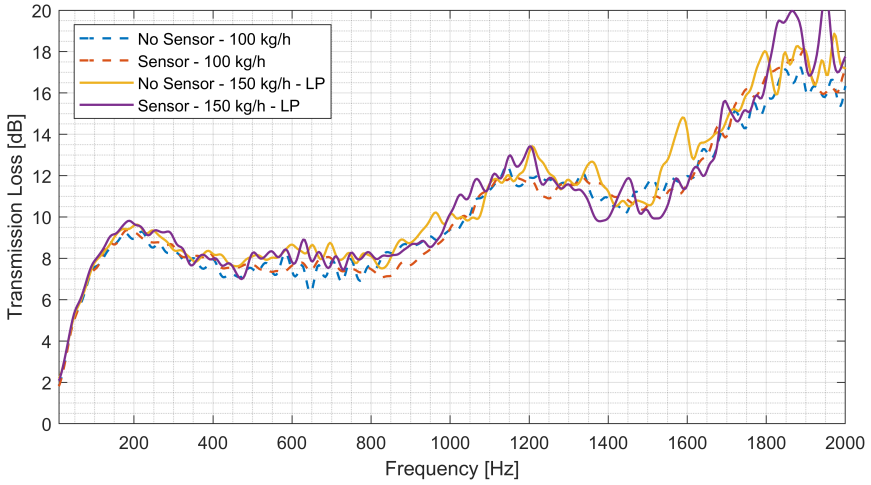

Figure 6.22: Probe effect assessment: Comparison of experimental TL results with large pulse excitement and superimposed flow.

Therefore, in most of the cases analyzed the eventual effect of the probe for the frequency range of interest may be considered as marginal.

Moving to the experimental vs modelling assessment, Fig. 6.23 shows the comparison of 1D modelled and experimental smoothed results of measurements with large pulse. The overall effect of superimposed flow increasing the attenuation is satisfactorily reproduced. The initial ramp of the curves is perfectly captured for the 100 and 200

kg/h cases, and slightly underestimated, but with the proper slope, for the flowless and 300 kg/h cases. Also, the overall shape of the curve is properly captured even beyond the 700 Hz range, with a noticeable overestimation of the peak attenuation values between 150 and 500 Hz, which are still close to the reasonable 3 dB margin.

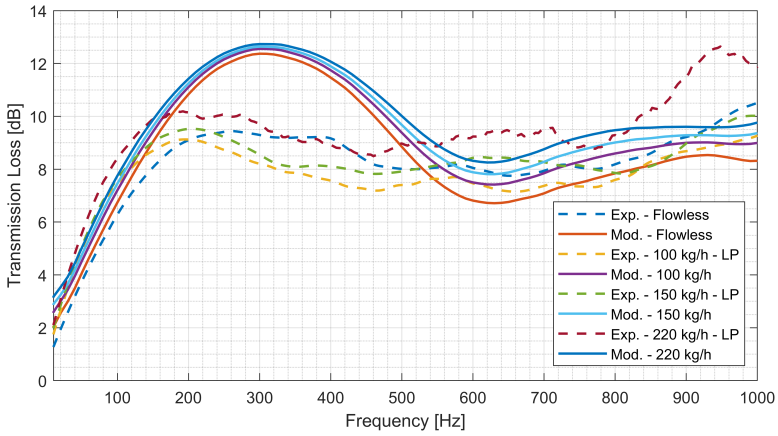

Figure 6.23: Comparison of Exp. Smoothed (No Sensor) and 1D modelled TL results for ATD3.

6.3 Devices with wall-flow monoliths

Moving on, the next devices to be evaluated were those that had realistic geometries, and also a particulate filter elements among the monoliths. ATD4 and ATD1 correspond to this category. The first one is relatively less complex in its geometrical disposition but has a flexible pipe section and a DPF. On the other hand, ATD1 shares its overall geometrical configuration with ATD2, as both were designed for the same family of engines, with some differences mainly in the shape of the inlet side and the substitution of a FT monolith for a GPFc.

Assessment procedure

Similarly to the preceding sections, the assessment procedure involves the measurements in the CFTB and ITR facilities and the computa-

tional modelling, both 1D and 3D. As ATD1 is the most complex within the intermediate category, due to curved pipe sections, irregular volumes at inlet and outlet sides, and a PF monolith, it was chosen to study the capabilities and potential benefits of a 1D-3D coupled simulation.

Measurements of the experimental assessment

Table 6.2 summarizes the measurements taken for ATD4 and ATD1. Similarly to ATD3, it was not possible to measure PD of ATD4 up to 800 kg/h, reaching only 650 kg/h. In contrast, ATD1 was measured twice, in its base condition as with the other parts, and also after a few cycles of use in an engine bench. However, the results for ATD1 after the engine bench are to be presented and discussed later in Section 6.5.

Table 6.2: Information on the experimental measurements taken for devices ATD4 and ATD1.

Characterization		**ATD**		
Test Facility	*Condition*	*ATD4*	*ATD1* (New)	*ATD1* (Clean)
Pressure drop testing on CFTB	Min. MFR	650 kg/h	50 kg/h	
	Max. MFR		800 kg/h	900 kg/h
	Increase steps		50 kg/h	
Transmission loss testing on ITR	Orientation	Direct & Inverse		Direct only
	Flowless	1 pulse amplitude		
	MFR 100 kg/h	2 pulse amplitudes		-
	MFR 200 kg/h	2 pulse amplitudes		-
	MFR 300 kg/h	2 pulse amplitudes		-

Preparation of modelling assessment

ATD4

Fig. 6.24 depicts the fluid domain extracted from the cleaned-up CAD, with the components as decided from the discretization highlighted with the previously used colour code, and the addition of the yellow colour in the inlet side, which is used to indicate a separated pipe section, as the pipe section next to it (highlighted in red) corresponds to a flexible pipe element. The 1D model corresponding to the discretization presented is portrayed in Fig. 6.25.

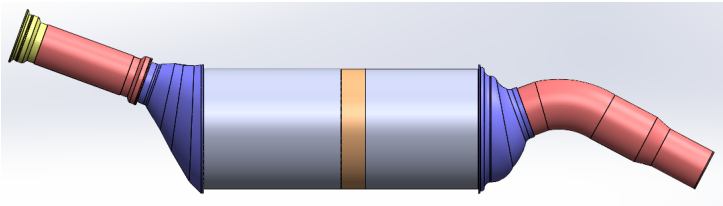

Figure 6.24: Discretization followed in the modelling of ATD4.

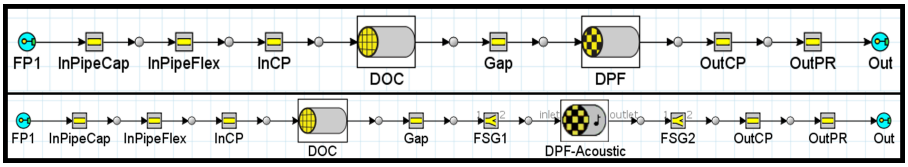

Figure 6.25: 1D models representing ATD4, PD devoted model on Top side, and TL devoted model on bottom side.

ATD1

Fig. 6.26 shows the fluid domain extracted from the cleaned-up CAD of ATD1; once again the colour code is used to indicate the decisions from the discretization. In this case, as there is a regular cylindrical volume at the beginning of the irregular contraction volume, it should

be considered as a short pipe section before that representing the contraction volume corresponding to the element "ES2" in the 1D models presented in Fig. 6.27.

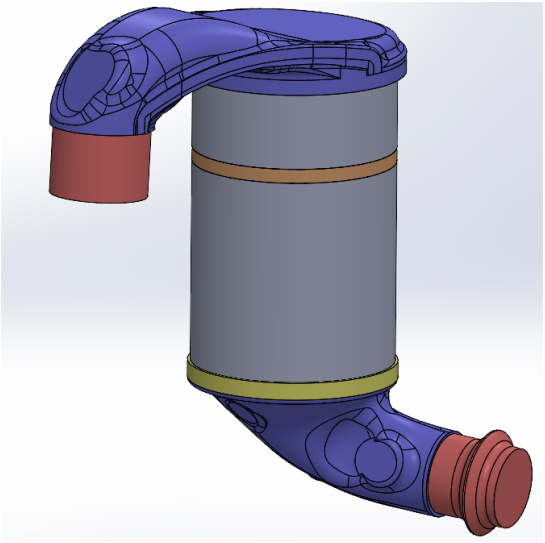

Figure 6.26: Discretization followed in the modelling of ATD1.

Due to the presence of the PF element, and in order to produce the best results, two 1D models were necessary, one for the PD simulation and the other for the TL simulation; both are presented in Fig. 6.27.

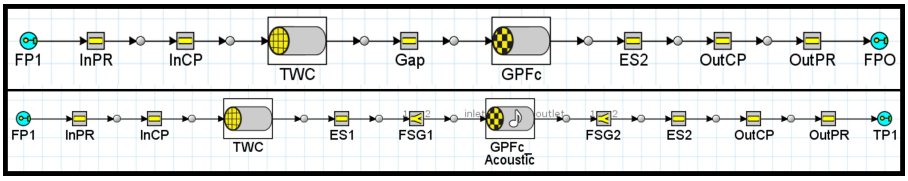

Figure 6.27: 1D models representing ATD1; Top side is the model for PD simulation and bottom side the model for TL simulation.

Results and discussion

ATD4

Pressure drop

The PD and K factor results derived from CTFB measurements are presented in Figs. 6.28 and 6.29 respectively. PD shows the expected quasi-quadratic dependence to the mass flow rate, and the pressure drop coefficients also exhibited an adequate asymptotic behaviour as the Reynolds number increases.

Afterwards Fig. 6.30 shows the results from the 1D virtual twin model of the device alongside the experiments for direct comparison. The agreement obtained for this device is very good, with a small underestimation at low MFR and barely overestimating at high MFR, with an apparent interception at 400 Hz, but apart of this it represented the overall PD curve very well.

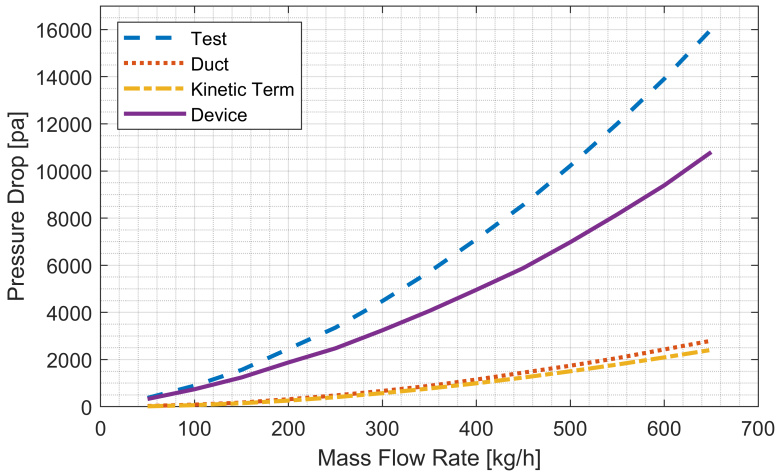

Figure 6.28: Experimental PD results from ATD4 characterization.

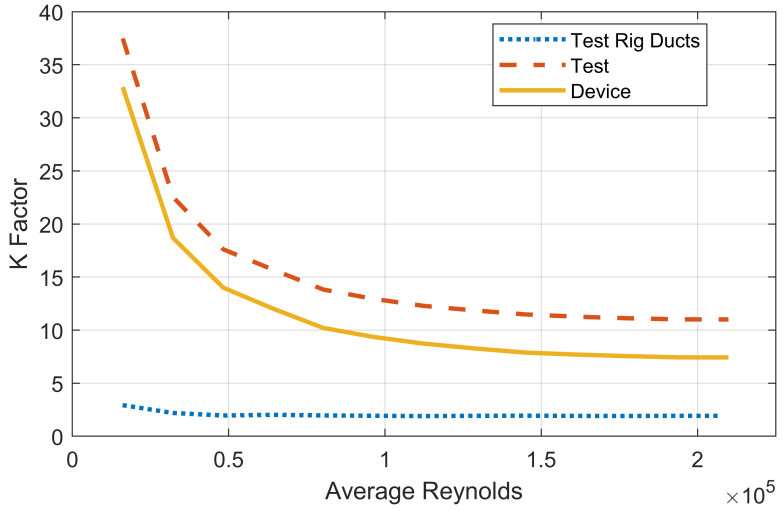

Figure 6.29: K factor, from experimental characterization of ATD4.

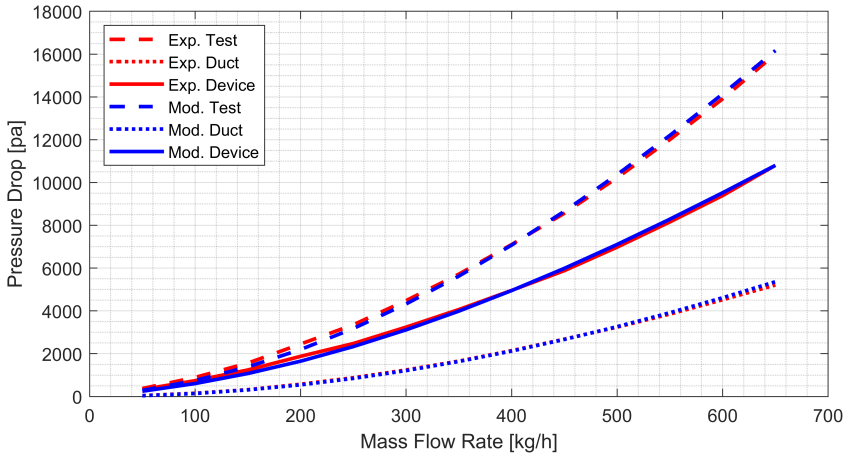

Figure 6.30: Comparison of experimental and 1D modelled PD results for ATD4.

Moving to the results of the 3D CFD approach, Fig. 6.31 shows the results for total pressure and velocity vectors for a simulation run with a mass flow rate of 300 kg/h. The observed diminution of the total pressure in the downstream direction fully matches the expected, even reflecting that the section corresponding to the PF monolith imposed a larger pressure drop. Regarding the velocity vectors, both the organized laminar flow in the channels of the monoliths and the velocity and flow direction changes associated with diameter and cross section changes appears to be correct.

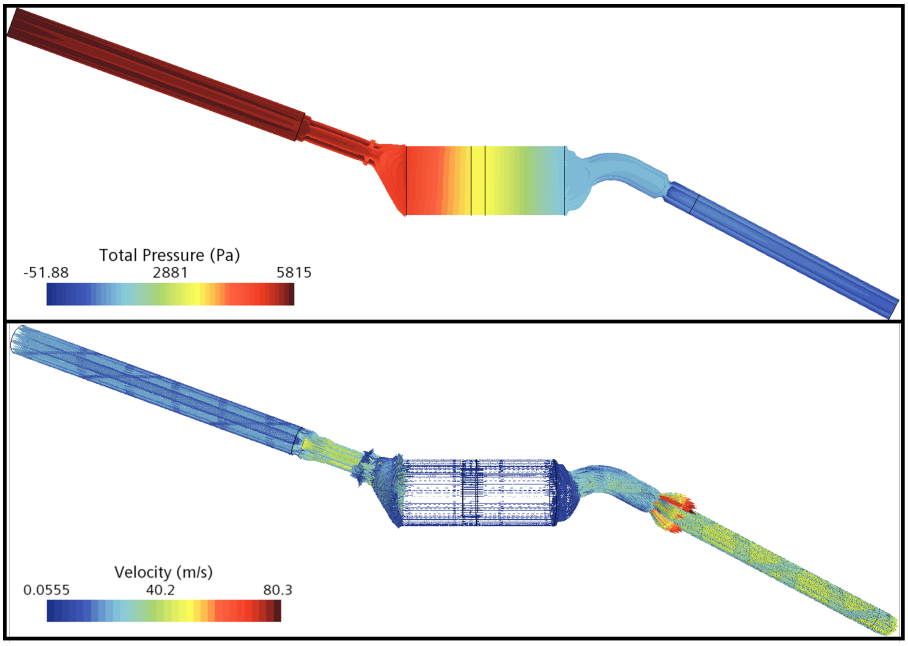

Figure 6.31: Total pressure and velocity vector representation for ATD4 at 300 kg/h.

Finally Fig. 6.32 shows the comparison of results between the 1D and 3D modelling approaches alongside the experimental as reference.

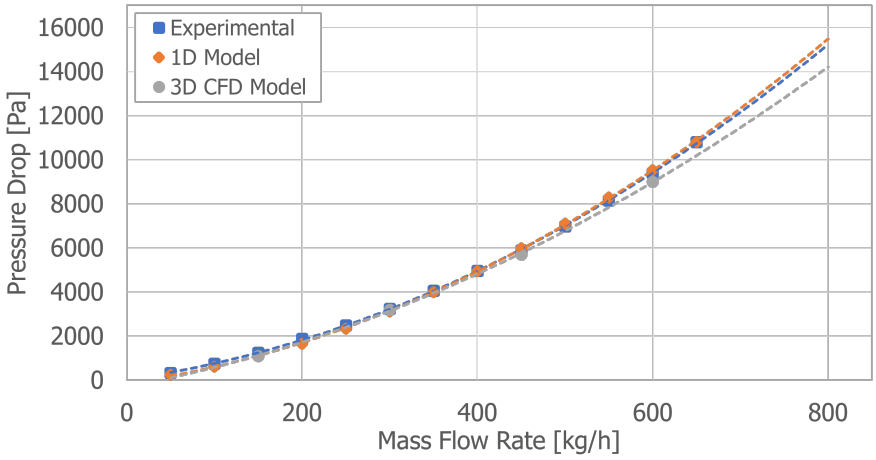

Figure 6.32: Comparison of experimental and modelled PD results for ATD4.

Transmission loss

The experimental TL results of ATD4 are illustrated in Fig. 6.33; neither the flow nor the pulse appear to have a significant effect on the attenuation, apart that the results from measurements with small pulse are considerably more oscillatory. Similarly to ATD3, the higher mass flow case is noticeably oscillatory even for the large pulse after smoothing.

In regards of the 1D modelling results, these are compared to large pulse experimental measurements in Fig. 6.34. In this case, the initial ramps is not completely captured, even if the slope seems to be the adequate one. Also, while not precise, the attenuation values up to 600 Hz are within the margin, and the overall behaviour and tendencies are captured. From experience during the iterative part of the modelling for this device, it was found that the use of FlowSplitGeneral elements for the expansion and contraction volumes could reproduce slightly better

the increase of attenuation beyond 600 Hz, but at the cost of inducing to many differences between PD and TL models, which was not desired.

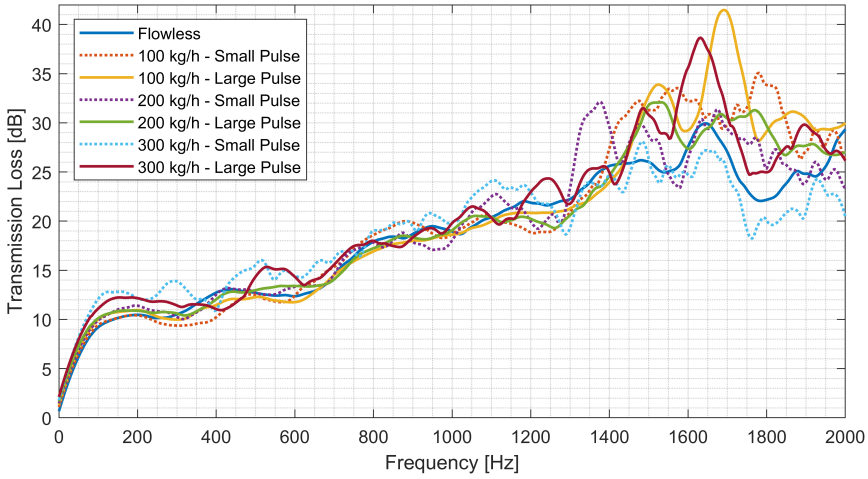

Figure 6.33: Complete set of exp. smoothed TL results for ATD4.

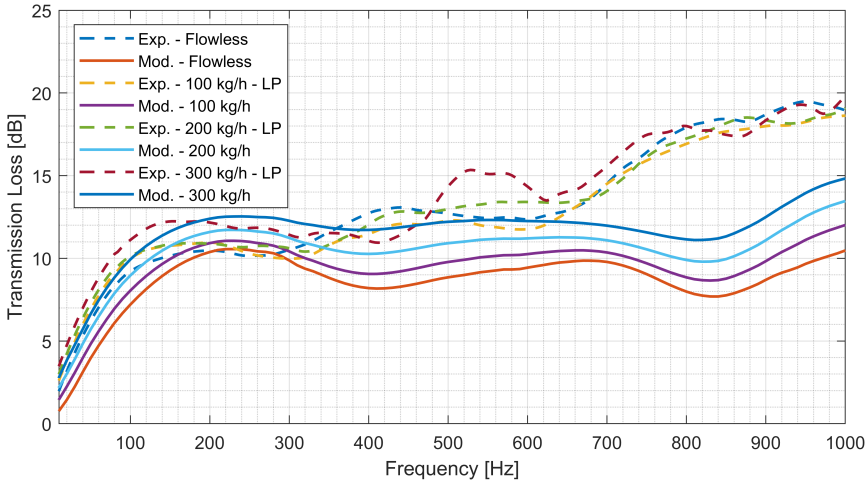

Figure 6.34: Comparison of exp. smoothed and 1D modelled TL results for ATD4.

ATD1

Pressure drop

Moving to results for ATD1 prior to the cycles in the engine bench, Figs. 6.35 and 6.36 present the pressure related results derived from CFTB. It is important to mention that the sudden change in the slope starting at 650 kg/h of mass flow in the test result is associated with an internal change in the test rig that takes place beyond the 17000 Pa range. Then as the value for devices results from a computation of the other curves, it inherits this change in slope. Posterior comparative analyses to models make use of the adjusted second order polynomial trendline. Aside of this, the PD exhibits the expected quasi-quadratic behaviour as a function of increasing mass flow rate. Additionally, the pressure drop coefficient exhibits the right asymptotic behaviour at high Reynolds numbers within the measurement uncertainties and with the change in slope also being subtly present.

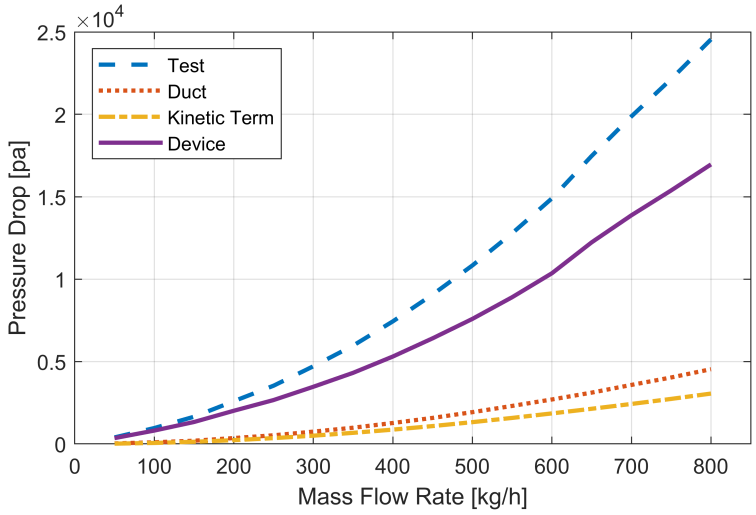

Figure 6.35: Experimental PD results from ATD1 characterization.

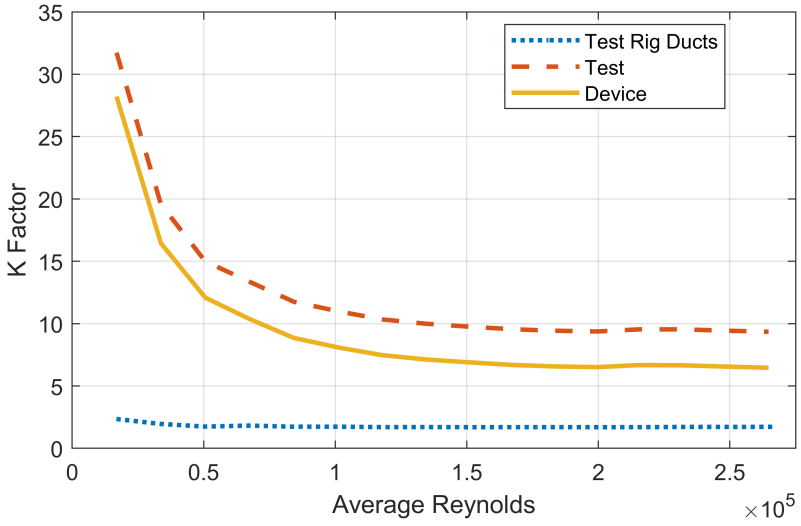

Figure 6.36: Pressure drop coefficient, K factor, from experimental characterization of ATD1.

Fig. 6.37 shows the PD results from the simulation of the PD devoted 1D virtual twin model for ATD1 and from experimental measurements in order to allow for direct comparison. The agreement obtained is good; it somehow overestimates the PD for most mass flow rates, but precisely captures those above the slope change.

Moving to the results of the 3D CFD approach, Fig. 6.38 shows the results for total pressure and velocity vectors for a simulation run with a mass flow rate of 300 kg/h. The observed diminution of the total pressure in the downstream direction fully matches the expected, even reflecting that the section corresponding to the PF monolith imposed a much larger decrease in the pressure. Regarding the velocity vectors, both the organized laminar flow in the channels of the monoliths and the velocity and flow direction changes related to diameter and cross section changes seem correct. There are some particular effects in the inlet side as the bent is not as smooth as that in ATD2.

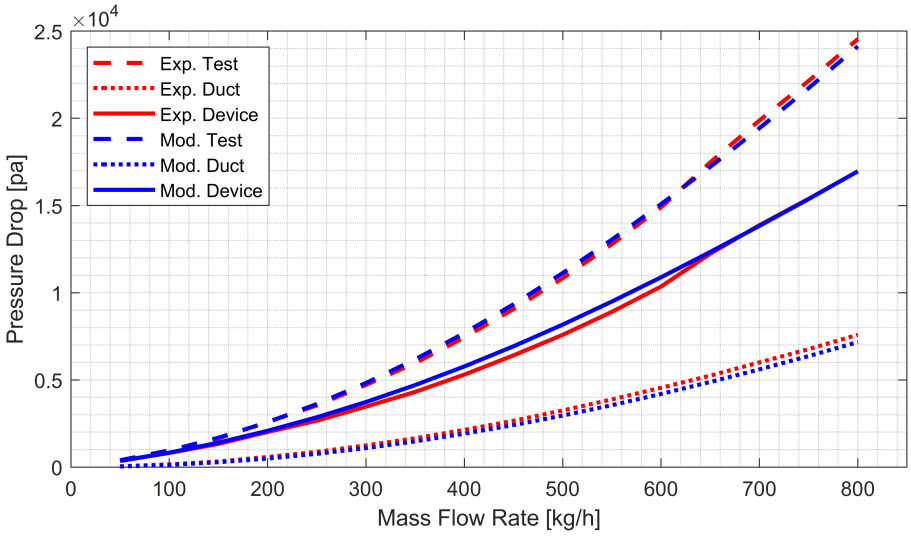

Figure 6.37: Comparison of exp. and 1D mod. PD results for ATD1.

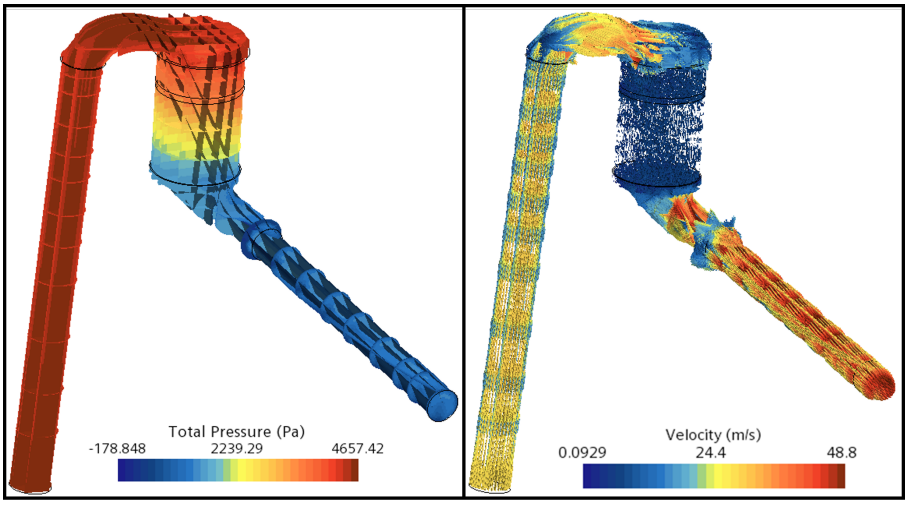

Figure 6.38: Total pressure and velocity vector representation for ATD1 at 300 kg/h.

Finally Fig. 6.39 shows the comparison of results between the 1D and 3D modelling approaches alongside the experiments as reference.

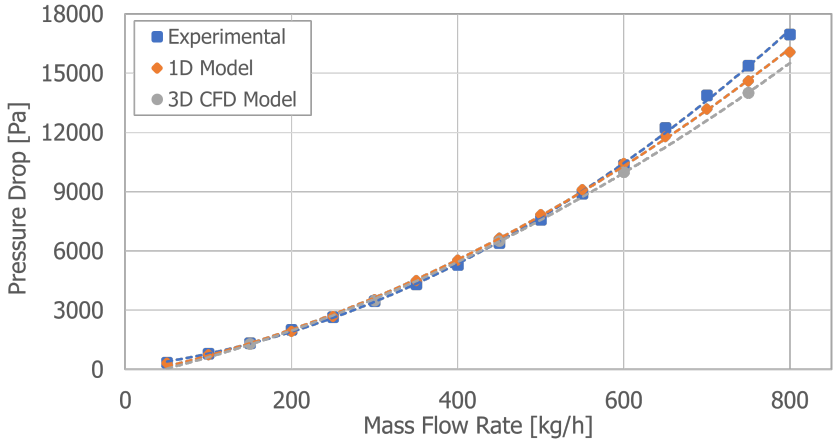

Figure 6.39: Comparison of experimental and modelled PD results for ATD1.

Transmission loss

The smoothed TL results for flowless and superimposed mean flow cases for ATD1, the latter excited with both small and large pulses are plotted together in Fig. 6.40. Here the increase in attenuation with the increasing flow is a little more evident, even if with ATD3 and ATD4 the results are considerably oscillatory even after the smoothing process has been applied. Once again, the effect is stronger for the small pulse but still significant for the large pulse, especially at 300 kg/h.

Afterwards, the comparison between 1D and experimental smoothed results is shown in Fig. 6.41. Even though neither the initial ramp of the curves nor the peak value are completely captured, the overall shape of the results and the effect of mass flow are well represented in the complete range of frequencies, and specific differences are all within the 3 dB margin with the exception of the flowless case above 860 Hz.

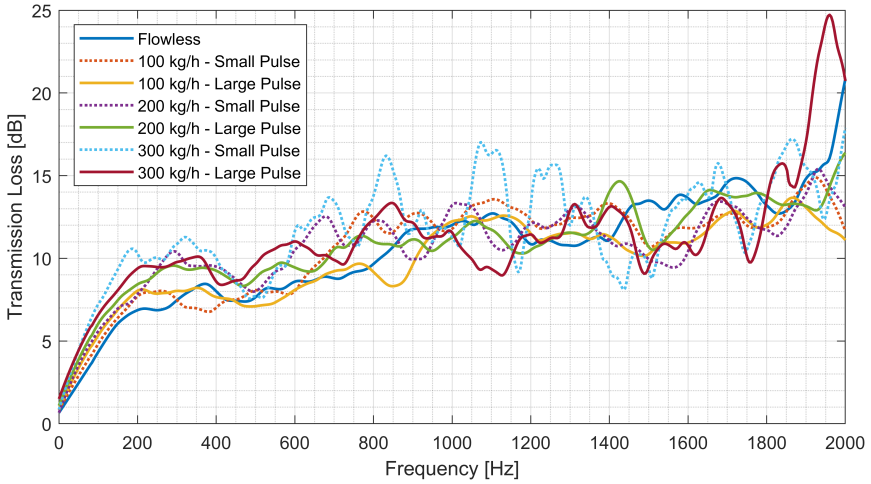

Figure 6.40: Complete set of exp. smoothed TL results for ATD1.

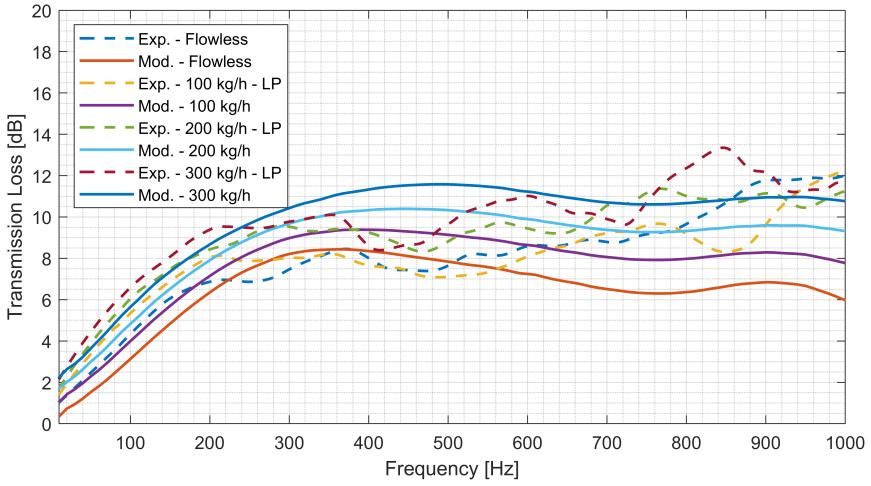

Figure 6.41: Comparison of exp. smoothed and 1D modelled transmission loss results for ATD1.

Testing 1D-3D coupled simulation

Having all the characteristics of interest together in part ATD1, i.e. both FT and WF monoliths, curved sections and irregular volumes, made it the optimal subject to test the benefits of the eventual use of 1D-3D CFD coupled simulation. After choosing the device, and the CFDInterface method as exposed in Section 3.3.6, the next step was to put it to use.

Assessment Procedure

Having tested both 3D and 1D models, their advantages and disadvantages, the convenience and the benefits of using a 1D-3D coupled approach was to be tested. As the comparison of 1D and 3D PD results, given the proper tuning of the 1D models, already produced almost identical results with much less computation time, it was decided to assess the convenience only in terms of acoustic characterization.

Given that pipe sections, monoliths and the gap between (treated as a small pipe section) are clearly well represented by the 1D modelling, and on the other hand the intricate geometries of the irregular expansion and contraction volumes are suspicious of having 3D effects beyond the capacities of the 1D approach in use, it was decided that the most profitable strategy would be to focus the 3D computation capacities on such volumes.

For this, three copies of the 1D virtual twin model were adapted to allow for coupling via CFDInterface method. Back in Section 3.3.6, Fig. 3.48 shows how the 1D models prepared for coupling look like. The three copies were configured for the following:

1. A copy where a fluid domain starting in the last sub-volume of the inlet pipe and ending one sub-volume before the FT monolith is handled by 3D CFD, thus containing the irregular expansion volume.

2. A copy where a fluid domain starting in the last sub-volume of the empty space downstream of the WF monolith, and ending in the first sub-volume of the outlet pipe is handled by 3D CFD, therefore containing the irregular contraction volume.

3. A copy were both previously described fluid domains are handled by 3D CFD simultaneously.

The adapted TL testing template and the built-in TM template were used to evaluate the three adapted models.

Results

One of the key advantages rapidly evidenced was, as expected, that the amount of time consumed is by far less than that of a complete ATD 3D CFD simulation; also, the improvement in the quality of results when compared to 1D was noticeable. Even if it is already decided to use the coupling, the best decision is to use it for as many regions as needed at once, as the computation time vs. improvement of results would be favourable, given that part of the time of handling fluid regions is shared. Therefore the virtual twin model prepared to handle both intricate geometries via CFD was selected.

Additionally, during the iterative tests performed, it was evidenced that tuning the number of uncoupled cycles (completely executed in 1D) to allow for the 1D model to stabilize before moving to the actively coupled phase improves the results in terms of small oscillations, similar to those frequent in raw experimental results which are certainly undesired.

Even though the same model and coupling method was used, some differences were found between using TM and TL templates. First of all, in order to use TM, two copies of the model have to be "placed" in the template, one of them with the elements connected backwards as to account for a measurement in reverse position. When this is used in combination with a 1D-3D coupled approach, it means two copies of each fluid region are to be handled by the CFD software during the coupled phase. Figs. 6.42 and 6.43 show some images from the CFD software when TL and TM templates were used with 1D-3D coupled simulation.

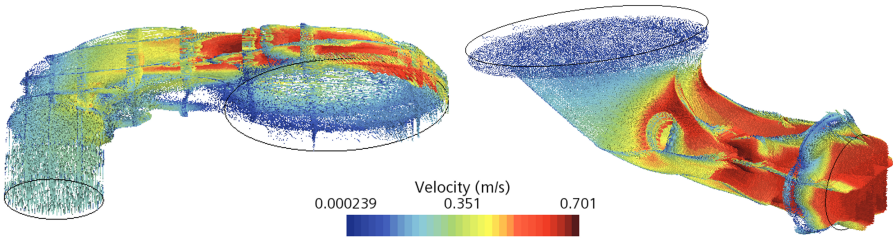

Figure 6.42: Velocity vector representation for inlet and outlet complex volumes of ATD1 being handled by CFD software during a 1D-3D coupled simulation using TL template.

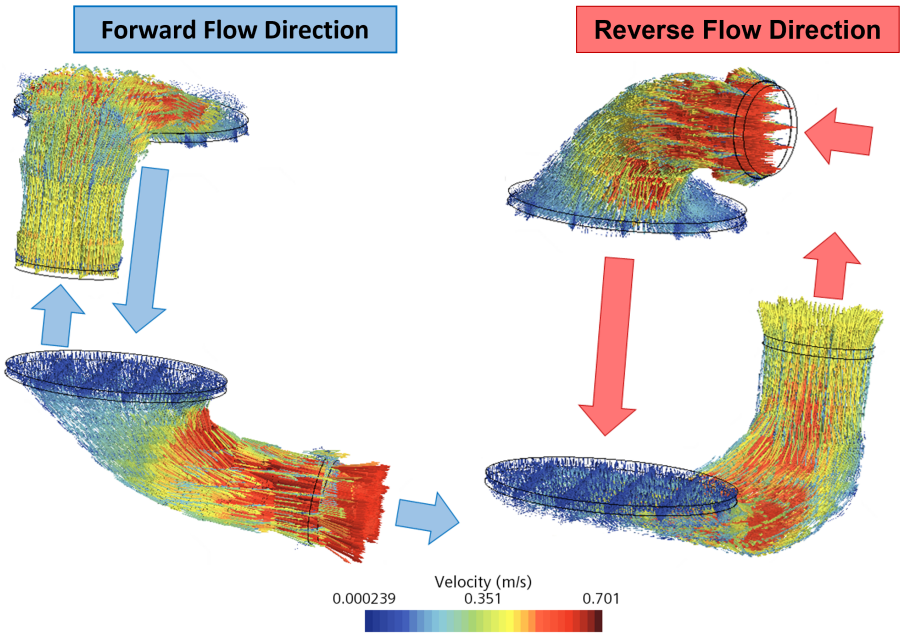

Figure 6.43: Velocity vector representation for inlet and outlet complex volumes of ATD1 being handled by CFD software during a 1D-3D coupled simulation using TM template.

Fig. 6.44 plots together different TL results for the case without superimposed mass flow, in order to compare them, including also the experimental smoothed and the uncoupled 1D results for reference. It is evident that in both cases the results are closer to the experimental benchmark than those from the uncoupled 1D modelling. Nonetheless, TL would be preferred over TM, as the use of that template requires two copies of each fluid region to execute and that naturally translates in longer computation times. However, it could still be useful as it grants access to transfer matrix coefficients providing a complete picture of the acoustics.

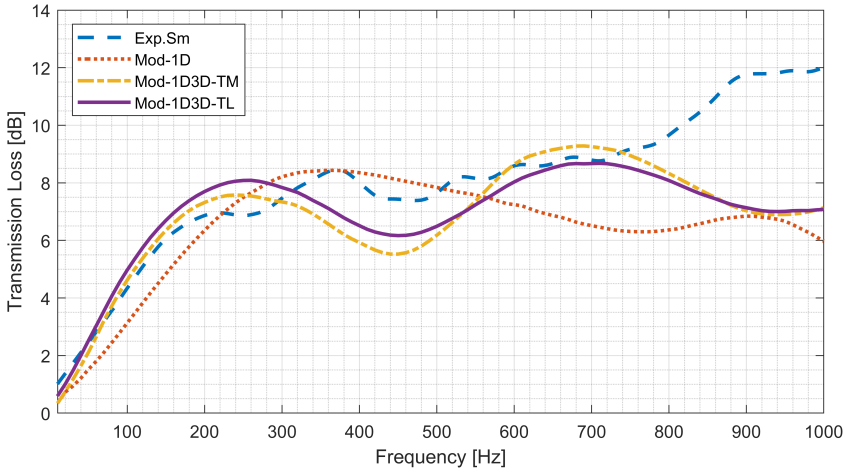

Figure 6.44: Comparison of experimental, uncoupled 1D, and coupled 1D-3D TL results for ATD1 at no flow condition.

As improvements over uncoupled 1D results had been evidenced, the coupled simulation for the cases with superimposed flow were ran. Fig. 6.45 presents the results obtained. This figure can be compared with its uncoupled 1D equivalent, Fig. 6.41.

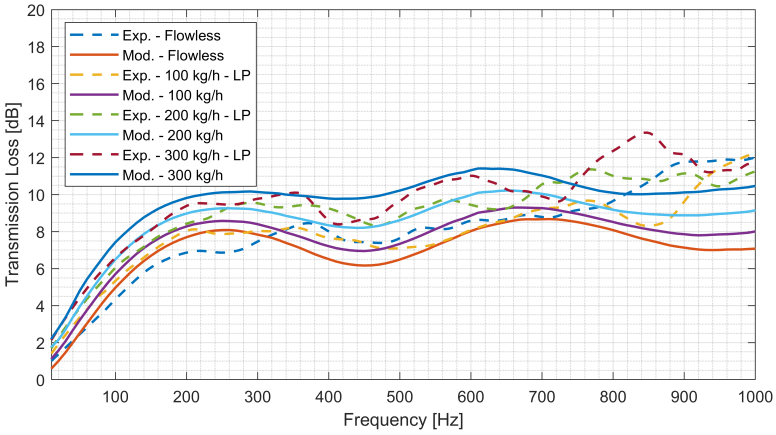

Figure 6.45: Comparison of exp. smoothed and 1D-3D coupled simulation of TL results for ATD1.

Regarding these results the following is to be pointed out:

- Even if still not fully captured, the initial ramps of the curves accounting for volume correspondence are better represented by 1D-3D coupled results.
- The shape of the curves reproduces better the behaviour in the complete frequency range displayed.
- The effect of superimposed mass flow is also reproduced, including the increase of attenuation and the slight shift in the some segments of the curves.
- All discrepancies fall within the 2 dB margin up to 700 Hz, and even above that frequency at some points.

6.4 Comparative analysis of results

Similarly to the comparative analysis presented at the start of Section 5.5, the experimental results of all devices from the intermediate complexity category were compared and analyzed together, in an attempt to outline how each characteristic of the devices might be responsible for the differences in the results.

Assessment procedure

Experimental PD measurements, estimated K factor Vs Reynolds and raw transmission loss results of ATD1, ATD2, ATD3 and ATD4 are plotted together, alongside those of ATS1-D1 as a baseline reference for devices containing only WF monoliths.

Results and discussion

Pressure related results

Fig. 6.46 presents the scatter plot for the PD measurements of intermediate category devices and the aforementioned simple geometry reference. As it was not possible to measure ATD3 and ATD4 beyond 650 kg/h, the corresponding results were again extrapolated with a second order polynomial fit up to 800 kg/h. The coefficient of determination R^2 for all these fits is above 0.9994.

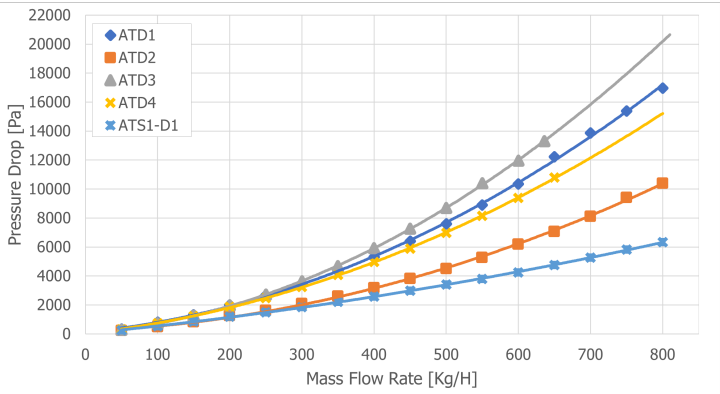

Figure 6.46: Summary of the PD results obtained from the exp. characterization of intermediate geometry complexity, ATS1-D1 added for comparison purposes.

- All intermediate complexity devices have considerably higher PD than ATS1-D1, being ATD2 the closest one; all the other ones have more than double its PD starting at 550 kg/h.

- Even though it has been checked one by one that the behaviour of ATDs is quasi-quadratic with a linear term related to the laminar flow in the channels of monoliths, represented in this way, the preponderance of the quadratic term over the linear one in devices with realistic geometry is far more evident, with ATS1-D1 looking almost as a straight line.
  - Comparing the coefficients of the quadratic term in the equations of the fits, those of intermediate geometry devices are one order of magnitude higher than that of the simple geometry device.
- Aside from the fact that all devices have two monoliths, ATS1-D1 is a convenient reference to compare ATD2 and ATD3 as they all contain FT monoliths only.
- Regarding ATD2:
  - The similitude with ATD2 goes one step further, as both have their two monoliths placed in a unique canning with a simple and straight intermediate gap.
  - The differences observed in PD are likely to be attributable to the complex bent inlet geometry used in ATD2, in contrast with the simple conical geometry of ATS1-D1.
- In relation to ATD3:
  - ATD3, without any WF monolith, yielded the highest value of all measured PD so far, even beyond that of ATD1 which has curved pipes, irregular volumes and a WF monolith.
  - Its PD is significantly higher than those of ATD2 and ATS1-D1, the most similar complex device and its simple counterpart respectively. In particular, at 800kg/h it is twice as much PD as ATD2 and three times that of ATS1-D1. This might indicate that the highly complex geometry of ATD3 is introducing a significant contribution to the PD, other than that of the monoliths.
  - The fact that the gap between the monoliths is rather a complete second expansion volume might allow for some extent

of flow development in comparison with the short gap of other devices, but the flow distribution in such a volume may be highly non-uniform, so that dissipative effects may be present.

- Additionally, this device has the smallest inlet pipe diameter of all the devices tested, which can also contribute to the higher PD observed.

- With respect to ATD1:
  - The obvious device to compare with is ATD2 as both were designed for the same family of engines and to occupy more or less the same space, with small differences in the shape of the inlet side, but broadly speaking the same canning and outlet configurations, being the major difference the presence of a GPF.
  - Any differences observed may be attributed precisely to the WF monolith, which should naturally produce an increase in pressure drop with respect to a through-flow monolith.

- About ATD4:
  - This device can be compared to ATD1, as both have WF monoliths, and also to ATS1-$D1$, as its almost straight-aligned geometrical configuration somehow resembles that of the simple geometry category part.
  - Its PD results are slightly lower than those of its GPF counterpart (ATD1). The difference is suspected to be related with the less complex inlet geometry found here.
  - The results are also significantly higher, more than twice at high mass flow rates, than those of ATS1-D1, with which shares to some extent the complexity of the inlet; this reinforces the importance of the contribution of the presence of WF monoliths to the pressure drop.

The corresponding unified representation of the pressure drop coefficients calculated from experimental results is portrayed in Fig. 6.47. Even though direct comparison of K factor is not as indicative as the

comparison of PD, it can be highlighted that the curves of ATD1 and ATD4, the devices with WF monoliths, are close together, and similarly, but less evidently, those with FT monoliths only are also close one to another. The curve for ATS1-D1 coincides with ATD2 and ATD3 at low Reynolds numbers.

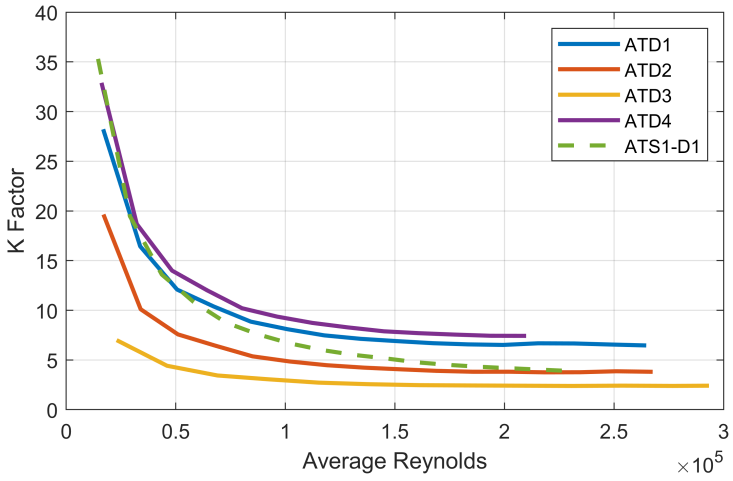

Figure 6.47: Summary of pressure drop coefficients obtained from the experimental characterization of intermediate geometry complexity, ATS1-D1 added for comparison purposes.

Transmission loss results

Moving on to the TL results, Fig. 6.48 brings raw TL measurements for the case excited with a large pulse with a superimposed mass flow rate of 100 kg/h together plotted up to 2000 Hz. The selection of this condition is based on the consideration that in the actual operating condition the devices are subject to flow, but due to the impossibility to measure ATD3 with usual mass flow rates, 100 kg/h is the only superimposed flow condition available for all the devices. The results for the simple geometry ATS1-D1 device are included as a reference again.

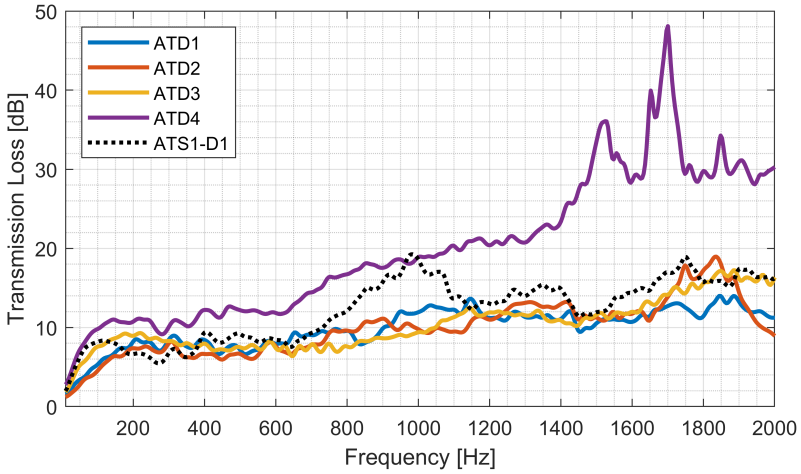

Figure 6.48: Summary of TL measurements with a 100 kg/h of superimposed MFR of ATDs from the intermediate complexity category, ATS1-D1 included for comparison (dotted line).

The following are observations to be highlighted regarding these results:

- The overall shape of the curves of intermediate complexity devices are all very similar, at least up to 1300 Hz.
- ATD4 appears to have the largest effective volume, as it has the highest initial ramp and attenuation up to 200 Hz. This, together with the presence of a WF monolith (DPF), may well be the cause for the significantly higher attenuation achieved by this device.
- ATD1, which also includes a WF monolith, a GPF, follows a similar trend, but with significantly lower attenuation values.
- Now, if one compares ATD2 and ATD1, which as previously commented have essentially identical geometrical disposition and differ in exchanging a FT monolith by a WF one, it is apparent that the differences are not as significant as one may expect given the

differences in PD; in fact, they are close enough as for the attenuation of either ATD to be predominant depending on the frequency range considered.

- Starting around 300 and up to 1800 Hz the attenuation of ATD1, ATD2 and ATD3 is practically identical, considering that all differences fall within the 3 dB margin, the uncertainties of the measurements and the use of non-smoothed curves in this comparison.
- Finally, if one considers the devices with two FT monoliths only: ATD2, ATD3 and ATS1-D1,
  - The simple geometry device has the best attenuation at low frequencies (below 100 Hz), thus indicating that its effective volume is the largest of the three.
  - ATS1-D1 is noticeably more attenuating than its more complex counterparts between 700 and 1400 Hz.
  - Up to 400 Hz, ATD3 exhibits a larger attenuation than ATD2, but above that limit its attenuation is lower.

The key conclusion from this comparative analysis is that the trends in attenuation (TL) do not correspond with the trends in built-up backpressure (PD). Of course, the design of these devices is essentially driven by the efficiency of their pollutant abatement effects.

6.5 The very early life of GPF

The literature review allowed for the identification of a knowledge gap on the effects induced on PF monoliths by the first few load-regeneration cycles, specially in the acoustic aspects. This section aims to help filling such gap in the case of GPF applications. For such end a comparative study between the never-used state, labelled “new”, and the “clean” condition, which refers to the base state acquired by the PF after its first few cycles, was performed. Theoretically speaking, the effects to be expected in both PD and TL should be related to deep-bed filtration of soot filling the pores of the substrate. A TL decomposition analysis was also applied aiming to further understand those effects.

Assessment Procedure

For this assessment, ATD1 was selected as it is a standard production part representative of current practice containing a WF GPFc monolith. The "new" condition of the device corresponds to the results presented in previous section (6.3) and "clean" conditions to that acquired by the ATD after a few cycles of use, in this case in its native engine in a test bench as specified in Section 3.2.5. The measurements that represent the latter state are those indicated in the last column of Table 5.2. Additionally ATD2 was also cycled in order to have a reference on how a similar cycling affects or not an ATD when no PF is present.

PD test were performed as usual, and these results post-processed to obtain the pressure drop coefficient as both magnitudes provide a preliminary assessment of the influence of soot deposition on the dissipative behaviour of the ATS. On the other hand, TL was only measured in the direct position, as the reverse test was not considered convenient to perform even if no soot layer was expected, and thus the inverse response was estimated based on reciprocity properties [40].

The assessment of reactive and dissipative effects applied to both conditions was performed using the linear approach based on acoustic power presented in Section 3.2.3. By applying such decomposition, the reflected power ratio W_r/W_i defined in Eq. 3.29 and the dissipated power ratio $W_d/(W_i - W_r)$ defined in Eq. 3.31 are used to account for the contributions of reactive and dissipative effects, respectively.

On the engine bench cycling

ATD1 was instrumented to obtain the evolution of the pressure differential across the system, in order to evaluate the evolution of GPF loading along the test. The results obtained are shown in Fig. 6.49, where for clarity only the first, the fifth and the last two cycles are represented.

It can be observed that, while the pressure differential increases from cycle 1 to cycle 5, and from cycle 5 to cycle 9, the results for cycle 10 are almost indistinguishable from those of cycle 9, and even a little smaller. This should indicate that, at this point, passive regeneration has taken place but, as commented in the introduction, the system does not retrieve its initial condition but reaches its effective base state related with deep-bed filtration, and after that it oscillates between these

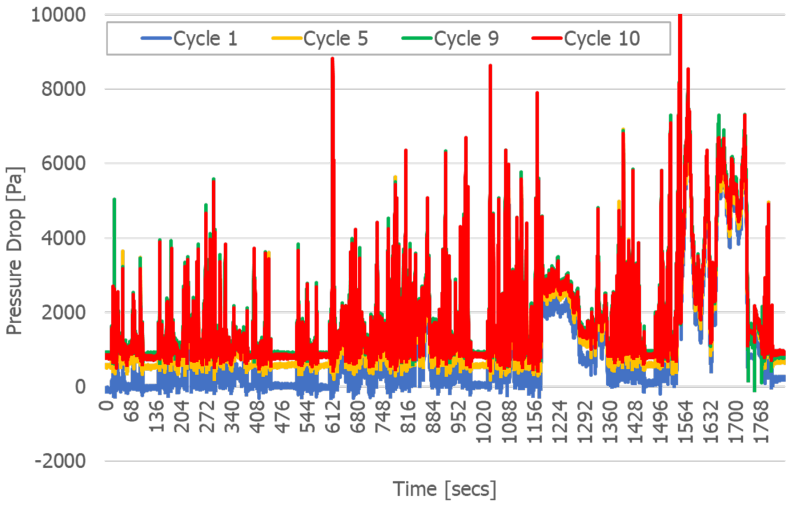

Figure 6.49: Evolution of the pressure differential across the system.

two values of the pressure differential. It was thus concluded that the state achieved by the system is representative of the less dissipative case associated with the "clean" condition, i.e. the actual state of interest for the present work.

Results

Pressure drop

In Fig. 6.50 the effect of the usage on the PD of ATD1 is shown. It is apparent that, as expected, the PD of the device in "clean" state is only slightly higher than that of the "new" condition. In both cases, the dependence of PD on the increasing MFR is quasi-quadratic, but with a most prominent influence of the quadratic term over a non-negligible linear contribution, associated with the existence of laminar flow in the monoliths [101].

The modelling work was centred on the 1D approach; the models presented for ATD1 in the previous section correspond to those of the "new" condition. The basic approach to represent the "clean" condition consisted in taking copies of "new" condition models and readjust

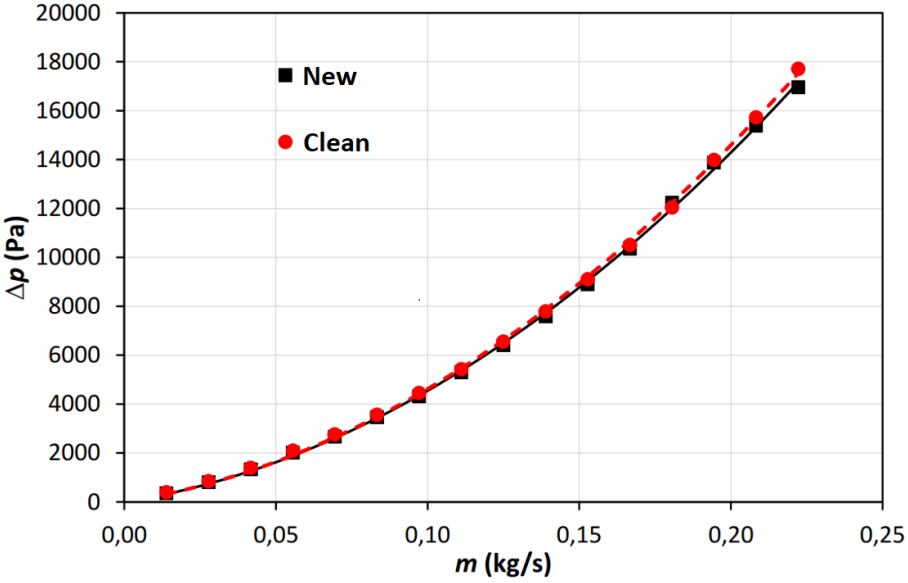

Figure 6.50: Comparison of exp. PD results between "new" and "clean" state of ATD1.

some parameters so that physically meaningful modifications were introduced, therefore reproducing the results for the "clean" conditions by representing the actual changes in the device.

The basic parameters defining the GPF representing element are: the substrate porosity, the substrate pore diameter and the discharge coefficient of the orifices. For the model of the "new" condition, the substrate porosity and the substrate pore diameter were kept at the recommended values of 0.5 and 3 μm respectively, whereas the discharge coefficient of the orifices was set to 0.038 instead of the default value of 0.03. After some iterations, the best parameters for the copy representing the "clean" condition were obtained by changing the substrate pore diameter (to 2.5 μm) and the discharge coefficient of the orifices (to 0.035), both modifications being consistent with the possible influence of soot loading. Another iteration producing similar results was to reduce the substrate porosity. The physical interpretation that justifies any of these changes is to regard them as the consequence of soot parti-

cles filling the pores of the substrate, therefore reducing the mean pore size, the overall porosity or modifying the discharge coefficients.

Additionally, the main tuning parameters are the forward discharge coefficients of the orifice connections upstream and downstream of the particulate filter, in particular, the direct flow value upstream and the reverse flow value downstream; the best results were obtained by setting both to 0.434 instead of the recommended value of 0.5.

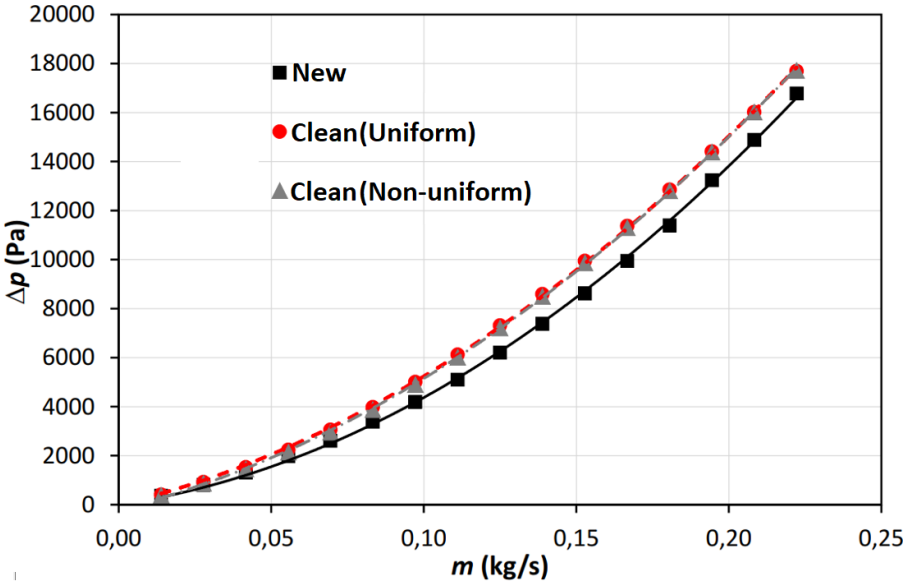

Figure 6.51: Comparison of 1D mod. PD results between "new" and "clean" state of ATD1.

The results are shown in Fig. 6.51, where it is apparent that the experimental trend observed in Fig. 6.50 is qualitatively reproduced, the values at maximum mass flow rate being comparable to the experimental ones in the "clean" condition, and slightly smaller in the "new" condition, so that the influence of usage is more apparent. This is due to the fact that, with the tuning parameters available, it was not possible to reproduce in full the actual dependence of the new device, but only to produce results that exhibited acceptable errors throughout the mass flow range considered, so that the model slightly overestimates the

PD at moderate MFR with a corresponding underestimation at higher MFR. In the case of the clean device, while the agreement at high flow rates is acceptable, the PD at medium mass flows is overestimated, which indicates that the linear term in the PD dependence is too high. One possible explanation could be related with the fact that the soot loading might not be uniform across the WF filter, which might not be negligible, even for an integrated magnitude as the PD.

In order to check this possibility, an effective porosity distribution was considered, based on information available [145], that indicates that the porosity is slightly lower at the inlet and the outlet of the channels, most notably when approaching the closed end at the outlet. This was implemented by changing accordingly the areas of the orifices connecting the inlet and the outlet channels while keeping approximately the same total area. The results are also shown in Fig. 6.51, where it can be observed that a certain reduction in the linear term is achieved. However, the results are extremely sensitive to the degree of non-uniformity: for large non-uniformity it may even produce an increase in the linear contribution, and therefore an explanation based on this can not account by itself for the differences observed.

Transmission loss

Even though the main use of the information generated by the ITR measurements in this special assessment is related to the acoustic power ratio approach, the TL of ATD1 and ATD2 after being subject to identical cycling in the engine test bench, and their logarithmic approach decomposition are presented in Figs. 6.52 and 6.53. ATD2 was tested as a reference and to verify that the effect of usage is not as relevant for devices without WF monoliths. Conveniently, both ATD2 and ATD1 were designed for the same family of engines and an engine test bench with an engine of such family mounted was available to perform the test in their native system.

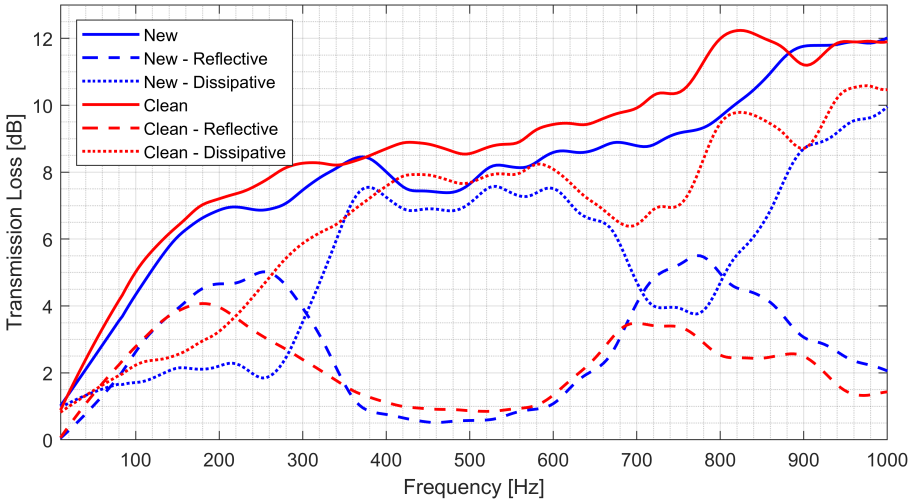

Figure 6.52: Comparison of dissipative and reflective TL components of ATD1, “new” and “clean” conditions, without superimposed mass flow.

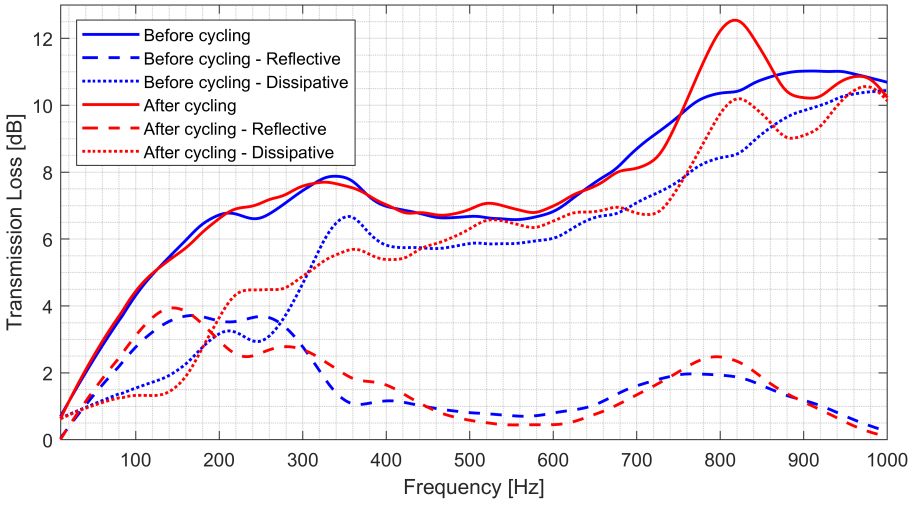

Figure 6.53: Comparison of dissipative and reflective TL components of ATD2, at flowless condition after a few hours of use.

From these results it is evident that the differences between the "new" and the "clean" states of ATD1 are far more notorious than those of ATD2 before and after the same cycling. The changes exhibited in the TL of ATD2 (Fig. 6.53) all fall within the margin that may be easily explained by measurement variability, except the apparition of an unexpected peak around 800 Hz, whereas the changes that can be appreciated in the TL of ATD1, Fig. 6.52, are consistent and cannot be disregarded as measurement variability. Similarly, component wise the reflective and dissipative TL of ATD2 barely changed, whereas those of ATD1 were unequivocally modified. Further analysis and confirmation of the effects on ATD1 are provided below with the acoustic power ratio decomposition analysis.

Acoustic power ratios

Moving to the main part of this assessment, the same 1D virtual twin models for the "new" and the "clean" conditions of ATD1 were used with the transfer matrix template built in GT-ise to reproduce the experimental results as from the decomposition linear approach. This is, no further tuning of the models was performed specifically to reproduce the experimental results. However, the impact of a non-uniform distribution, with the copy of the model that produced the results shown in Fig. 6.51) was investigated.

Specifically, the TM template produced four complex transfer matrix elements, from which the scattering matrix elements were computed and finally the transmission and reflection coefficients, T and R, could be extracted. Therefore having all information needed to produce the reflected and dissipated power ratios, with the same formulations of the analysis of experimental data in order to allow for direct comparison.

The following is the analysis of such results; first, the effect of usage on the reflected power ratio W_r/W_i is shown in Figs. 6.54 and 6.55, for the experimental and modelled results respectively.

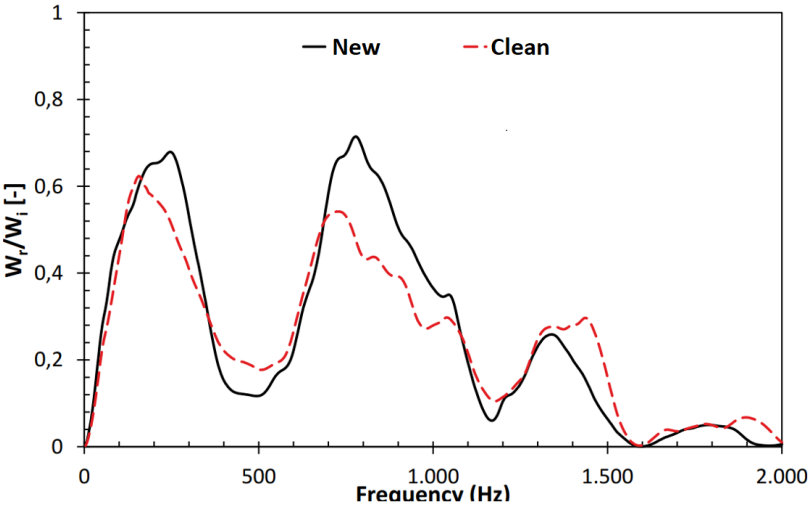

Figure 6.54: Changes on the reflected power ratio due to usage - exp. results.

From the experimental results, it can be observed that there is a noticeable influence of the usage on the reactive behaviour of the system; the following points can be highlighted:

- The overall trends in terms of the frequencies associated with peaks and troughs are not affected
- The "clean" condition curve shows, in general, less pronounced fluctuations, with a single exception between 1100 and 1200 Hz.
- Starting around 1300 Hz and above, the usage seems to increase the reflected power ratio, with the values staying either equal or above those of the "new" condition.
- The effect from the preceding item is thought to be related to the fact that relatively higher frequencies are more affected by geometrical changes at the substrate level.

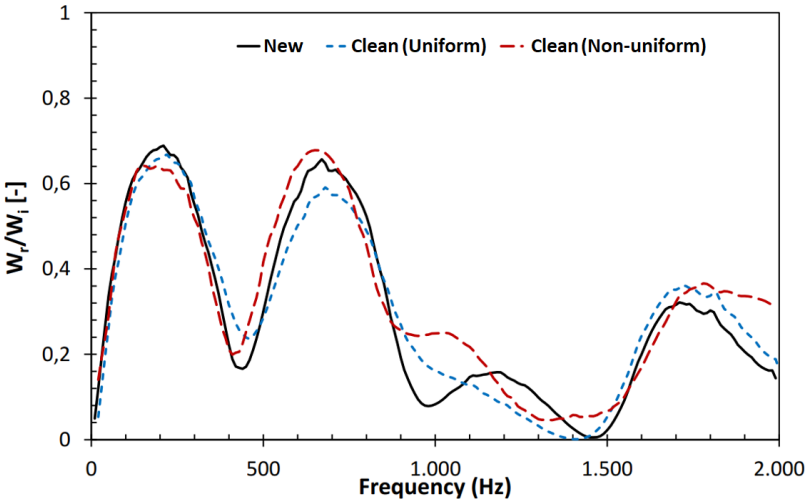

Figure 6.55: Changes on the reflected power ratio due to usage - mod. results.

Regarding the modelling results, some aspects should be commented:

- The overall shape of the frequency dependence of the reflected power ratio is essentially captured for frequencies below 1000 Hz.
  - This is consistent with the claims of the software developer.
  - The values of the two peaks in this frequency range are quite close to those found in the experiments.
  - Even above that frequency, certain aspects are reproduced.
  - However, it is also clear that the model is not able to fully reproduce the precise shape found in the experiments.
- The models are able to reproduce qualitatively the influence of usage, but quantitatively the effect shown is less pronounced than that evidenced in the experimental results.
  - For these results, the model representing the "clean" condition with a non-uniform soot load distribution showed more significant differences with respect to the uniform model than

those found in the pressure drop simulation. However, this only translates into an improvement of results in the low frequencies.

- The frequency distribution of usage effects portrayed by the "clean" results matches quite closely the experimental ones, with the exception of a frequency band from 1000 to 1500 Hz.
- Another trait successfully represented in a qualitative way is the fact that the device in clean condition is more reflective at the highest frequencies displayed.

These results and observations indicate that, even though not completely precise, the 1D models prepared and the modelling approach used are able to provide significant results in regards to reactive mechanisms.

Next, the effect of usage on the dissipated power ratio $W_d/(W_i - W_r)$ is assessed, starting with the experimental results which are shown in Fig. 6.56; then, Fig. 6.57 shows the equivalent results from the modelling approach.

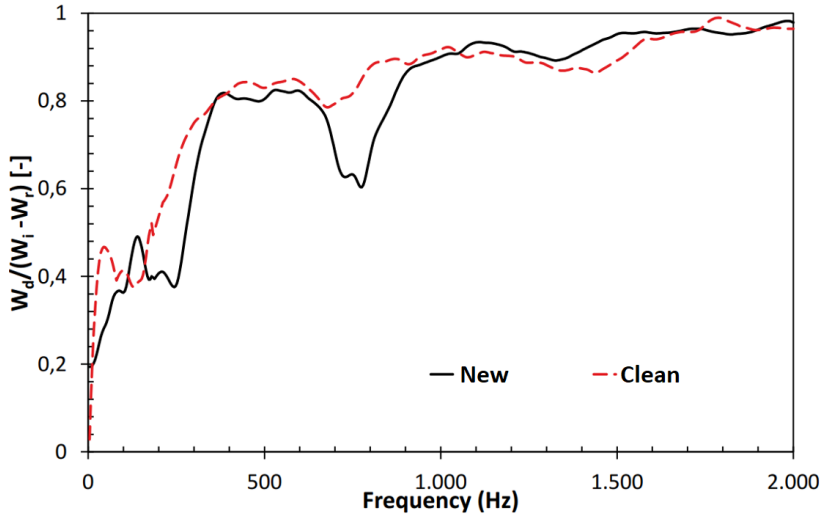

Figure 6.56: Changes on the dissipated power ratio due to usage - exp. results.

Regarding the experimental results:

- It can be observed that for frequencies above 1000 Hz differences are relatively small.
- As expected, and regardless of the condition observed, the attenuation produced by the device is essentially dominated by dissipation, most notably beyond 900 Hz.
- The effect of usage is noticeable precisely below 900 Hz, where the predominance of dissipation is not as forceful.
- The most evident effect of usage is smoothing out the curve, most notably at the two frequencies at which the main spikes of the reflected power ratio occur.
- Overall, as expected, dissipation is higher in "clean" conditions, what can be an advantage when designing the eventual downstream silencer, as pointed out in the introduction.

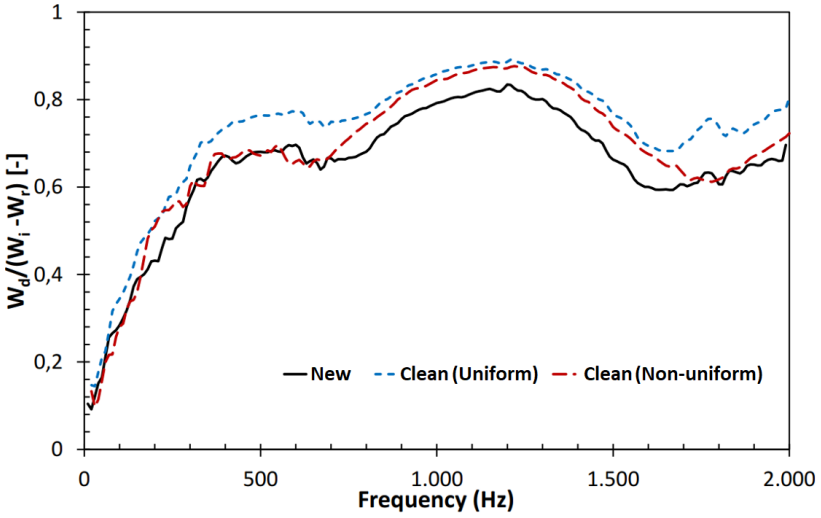

Figure 6.57: Changes on the dissipated power ratio due to usage - exp. results.

When considering the corresponding modelled results, it is apparent that while the model was able to reproduce, at least qualitatively, the trends observed in the reflected power ratio, still the agreement to experimental results is rather poor:

- Results from the model representing the new condition exhibit a far smoother behaviour than that of experiments.
- In the case of the model with uniform load, the effect of usage represented is that of an almost constant increase with respect to the new condition, not presenting any frequency-dependent feature, which the experiments do have.
- The case considering a non-uniform distribution is better in the sense that it at least presents some frequency dependence, yet it does not matches the experimental properly.

These modelling results provide some hints suggesting that considering the non-uniform soot load distribution is the proper way to account for usage effect, and that such consideration is relevant at least from the point of view of acoustic dissipation, even if results were not conclusive in the case of PD.

6.6 Validation of the developed 1D methodology on most complex devices

Up to this point the modelling workfront has guided the structuration of the 1D modelling methodology postulated in Section 3.3.5, as well as its complements. Now, finally the two most complex devices available, ATD5 and ATD6, were used as test subjects to evaluate the capability of the modelling methodology to produce satisfactory results from scratch, only using CAD geometrical information. The results, that may still be improved by tuning or small adjustments, were found to be quite indicative.

Assessment procedure

As mentioned above, this time the experimental data obtained was not used as an input for the iterative modelling, but as a benchmark for

the "final" 1D modelling results from applying the latest formulation of the modelling methodology and its complements to the most complex devices available, so that the validation test might include as many complexities as possible.

Measurements of the experimental assessment

Experimental measurements were taken, the PD testing on CFTB as usual but, on the TL side, only no-flow conditions were tested in the ITR. Details are listed in Table 6.3.

Table 6.3: Information on the experimental measurements taken for devices ATD5 and ATD6.

Characterization		**ATD**	
Test Facility	*Condition*	*ATD5*	*ATD6*
Pressure drop testing on CFTB	Min. MFR	50 kg/h	
	Max. MFR	800 kg/h	
	Increase steps	50 kg/h	
Transmission loss testing on ITR	Orientation	Direct & Inverse	
	Flowless	1 pulse amplitude	

Preparation of modelling assessment

The developed modelling methodology in its final formulation was applied, based solely on the dimensions as obtained from the CAD files and the monolith data supplied, and applying the guidelines for discretization and element selection and using the recommended seed values for the tuning and complementary parameters.

ATD5

This SCR system offers the opportunity to assess a FT only device, but with a flexible pipe element, a DEF injector, a perforated tunnel mixer, curved pipe sections, an expansion volume of irregular shape where additionally the mixer is placed, double SCR monoliths with the presence of a separator in the gap between the monoliths, a relatively short outlet contraction volume and an outlet pipe section with several sensor ports.

Fig. 6.58 shows the cleaned-up CAD file (top) and the simplified CAD (bottom) prepared to extract the diameters and volumes for the 1D model. The colours assigned to the cleaned-up CAD indicate the different elements as identified from the discretization. The mixer was presented back in Chapter 3 in Fig. 3.12 and as it is of the perforated tunnel embodiment; it is represented as a sudden reduced section that will be specified below.

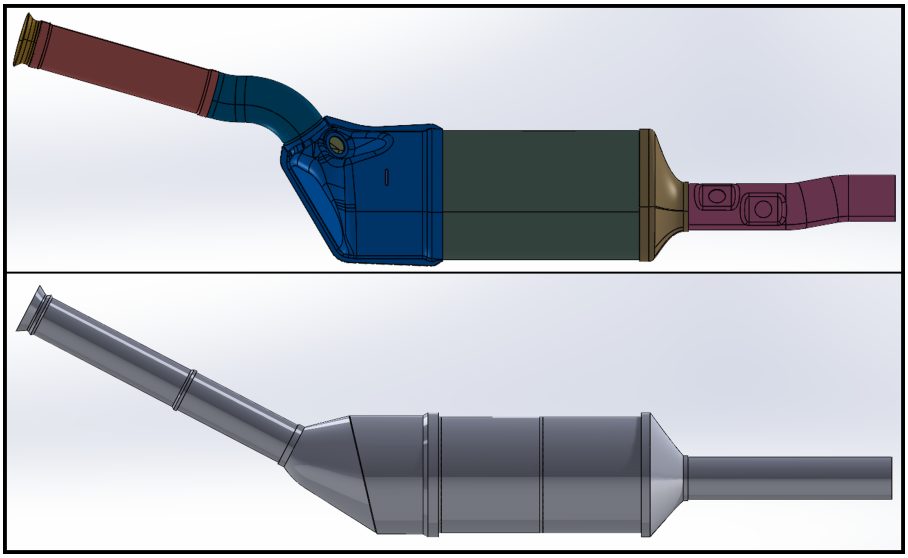

Figure 6.58: CAD files prepared for ATD5 modelling; Cleaned-up CAD (top) and simplified equivalent model (bottom).

Due to the number of section changes and the "high density" of elements to be represented, even though it could fulfil the device definition considered in this work, it is rather represented and treated by sections in the 1D modelling as schematically represented in Fig. 3.12

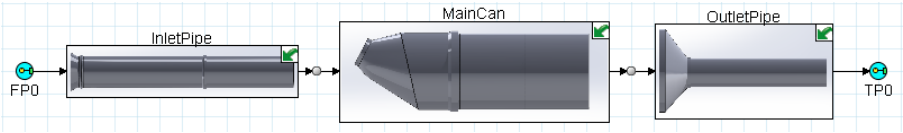

Figure 6.59: 1D modelling approach used for ATD5.

The inlet pipe section was represented in high detail using PipeRound elements only, as shown in Fig. 6.60 as the two longest sections are a flexible pipe and a curved pipe section simplified and the adapters connected to them had several changes in diameter that can act as reflective boundaries.

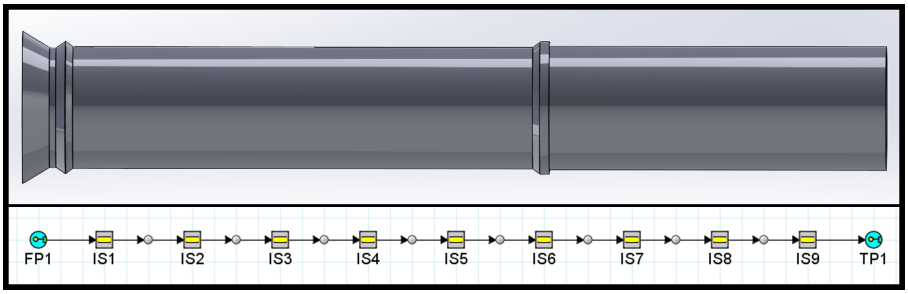

Figure 6.60: Details on the modelling of inlet pipe section of ATD5; Extracted fluid domain (up) and 1D model (below).

Fig. 6.61 shows the modelling representation for the main shell of the device; the orange line represent the separation of two functional groups that were assessed almost as two separate devices: the mixer group and the monoliths group. The presence of the mixer, represented in the simplified CAD by a plate with a circular opening orifice in the middle with an open area equivalent to that of perforation in the actual mixer, is indicated in the figure by the light blue marking. These sections

are represented by PipeRounds. On the other hand the monoliths are represented with the Standard CatalystBrick and the small gaps by PipeRounds; the gap between monoliths is represented by an equivalent area as the presence of the separator previously shown in Fig. 3.12 occupies a certain portion of this empty volume.

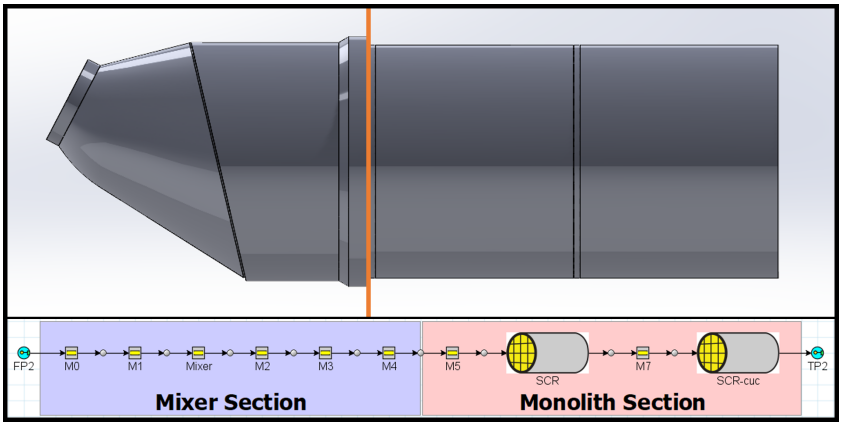

Figure 6.61: Details on the modelling of main can section of ATD5; Extracted fluid domain (up) and 1D model (below).

Finally, the outlet section includes the contraction, a toricone with knuckles at both sides, and the outlet pipes, once again all represented by PipeRounds as presented in Fig. 6.62.

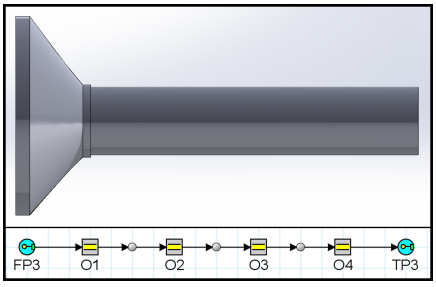

Figure 6.62: Details on the modelling of outlet pipe section of ATD5; Extracted fluid domain (up) and 1D model (below).

ATD6

This ATD is rather an ATS composed of two devices, even three following the criteria established for the modelling. It consist of two cans placed close together, whence its description as "close-coupled". For the sake of the modelling, it is to be considered as depicted in Fig. 6.63, giving an ATD treatment to the first can, the smallest one containing a DOC monolith, whereas the second can includes two monoliths and also a DEF injection port and a perforated plate precisely in the curved and irregular shaped contraction-expansion volume between the two cans. The second can is treated by sections similarly to ATD5, as it can be seen in Fig. 6.65.

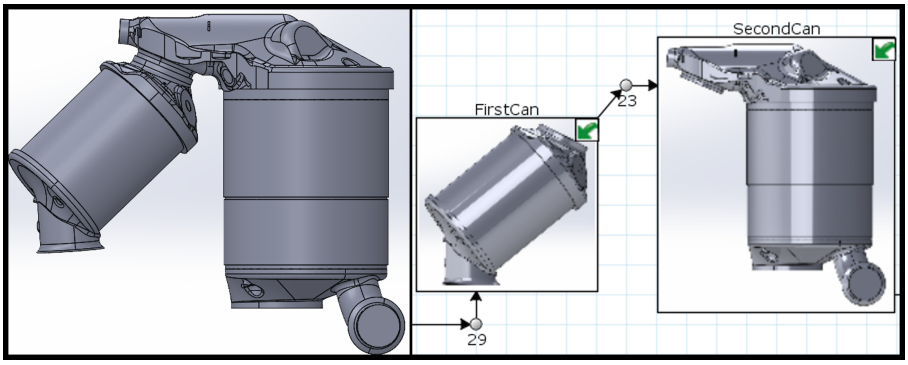

Figure 6.63: CAD file of ATD6 and initial approach for 1D modelling as two independent devices.

The representation of the first can in the 1D modelling environment is presented in Fig. 6.64; PipeRounds were used in order to represent the volumes at both sides of the monolith.

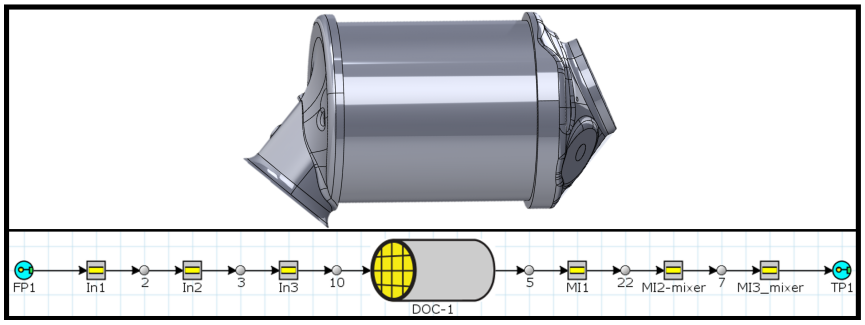

Figure 6.64: Details on the 1D modelling representation for the first device in ATD6.

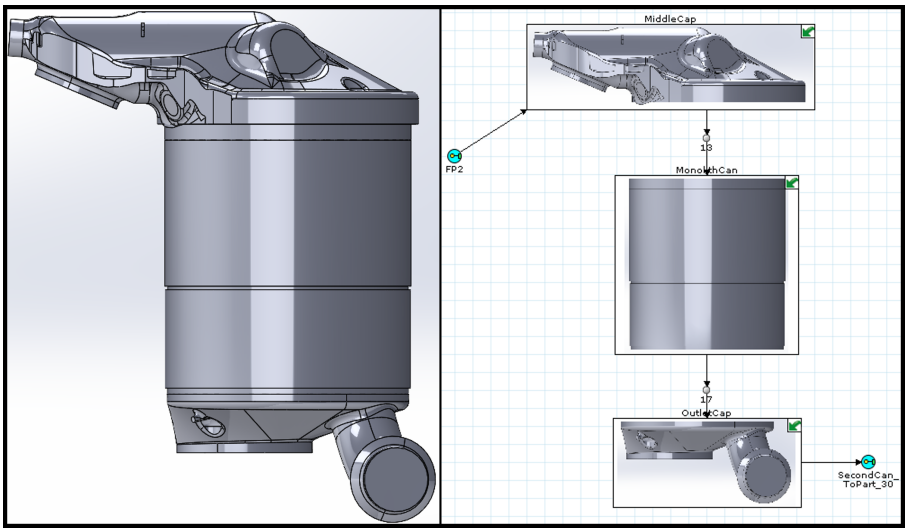

Figure 6.65: 1D modelling approach to represent the second device in ATD6.

What would usually be considered as a FlowSplitGeneral between two PipeRounds, or an array of PipeRounds as a expansion volume of irregular shape, is treated almost a device itself due to the presence of a perforated plate mixer. An auxiliary view of this mixer was presented

on Section 3.1.1, in Fig. 3.15. Now, in Fig. 6.66 the CAD of this section with the location of the plate mixer highlighted by an orange marking is presented alongside its 1D model representation.

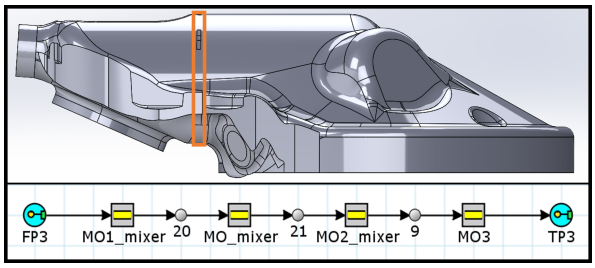

Figure 6.66: Details on the 1D modelling representation for the inlet volume and mixer (highlighted in orange) of the second device in ATD6.

Next, the monoliths and the other empty volumes in this device were represented as portrayed in Fig. 6.67; first the simplified CAD section is shown in the top, then as the first monolith of this device is a SCRf, it was necessary to have two versions, one for PD simulation, shown in the middle, and the other for TL simulation, shown in the bottom.

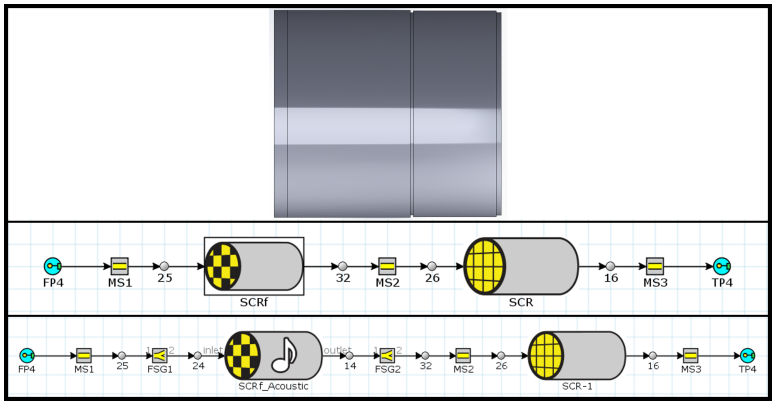

Figure 6.67: Details on the 1D modelling representation for the monolith can of the second device in ATD6; Equivalent CAD (top), model for PD simulation (middle) and model for TL simulation (bottom).

Finally, the remaining elements that constitute the outlet side are represented in the 1D as indicated in Fig. 6.68. It is important to remember that the larger opening was closed with a lid both in the experimental measurements and the CAD representation; therefore, for this characterization it can be regarded as a weird shaped volume.

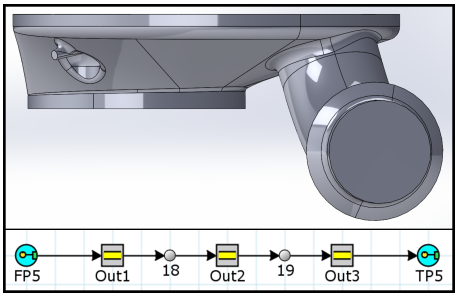

Figure 6.68: Details on the 1D modelling representation for the outlet volume of the second device in ATD6.

Results and discussion: Experimental

The experimental results will be assessed by first presenting the data extracted from the measurements of both devices, and then presenting a comparative analysis with reference to selected information from measurements of simple and intermediate geometry complexity devices.

ATD5

Pressure drop

Figs. 6.69 and 6.70 portray the PD measurements results and pressure drop coefficients calculated from those. The PD exhibits the adequate dependence to the mass flow rate, whereas the K factors present the expected asymptotic behaviour. The level of PD reached rivals those of the highest from the intermediate complexity category.

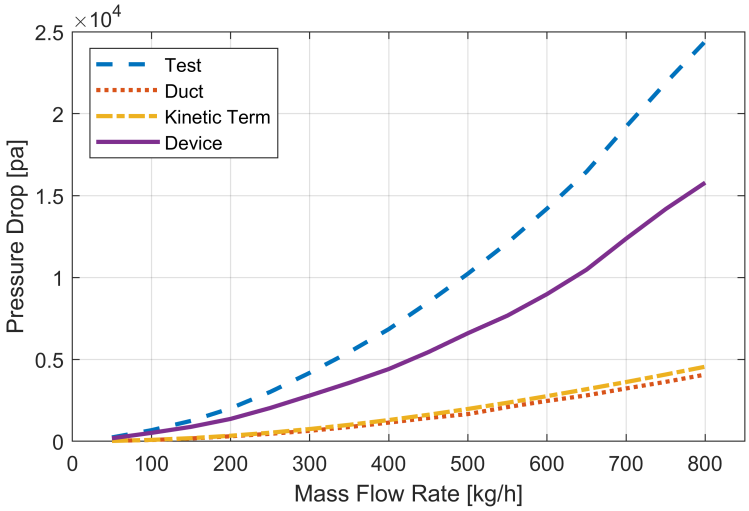

Figure 6.69: Experimental PD results from ATD5 characterization.

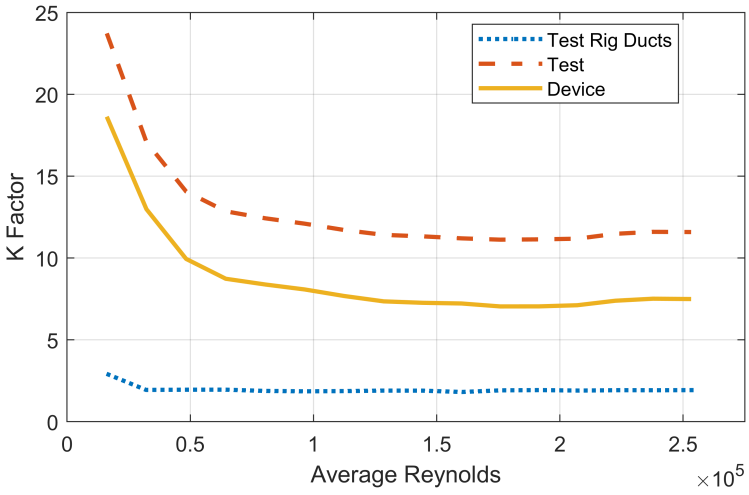

Figure 6.70: Pressure drop coefficients, K factor, from experimental characterization of ATD5.

Transmission loss

Fig. 6.71 presents the raw and smoothed TL curves obtained from ATD5 without superimposed flow up to 2000 Hz. It can be observed that raw results have an oscillatory nature starting as early as 400 Hz, and even with the smoothing processing the behaviour still evidences some oscillations. Apart from the oscillations and from the presence of a punctual spike, probably a resonance, at 1500 Hz, the results present a relatively stable increasing attenuation tendency with the frequency, from an attenuation in the order of 10 dB after the initial ramp and finishing in the 25 to 30 dB range at 2000 Hz. Overall, the attenuation provided can be regarded as relevant to take into account for the design of the silencing element in the complete exhaust line.

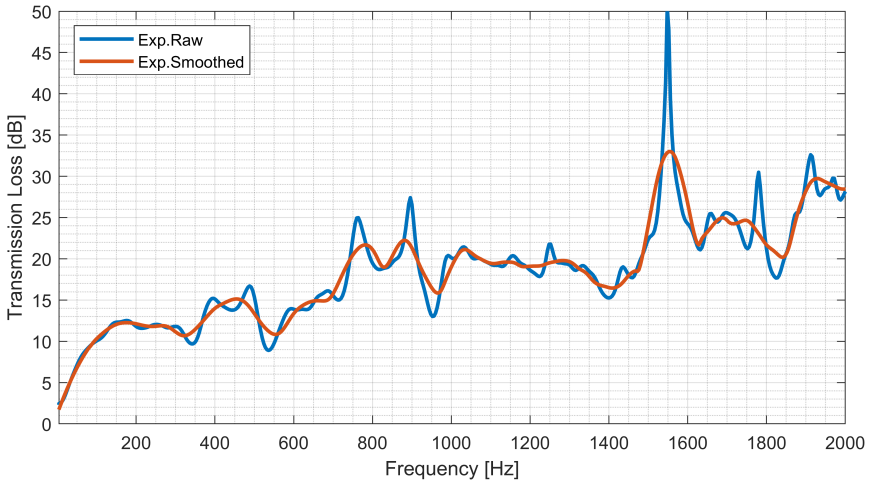

Figure 6.71: Experimental transmission loss results from ATD5 at flowless condition.

ATD6

Pressure drop

Figs. 6.72 and 6.73 portray the PD measurements results and pressure drop coefficients calculated from those. The PD exhibits the adequate dependence to the mass flow rate, and the K factors present the right asymptotic behaviour. Additionally, this is the highest result of PD obtained but, as mentioned in the preparation for the modelling assessment, it can be discussed if it is a single ATD or rather a compact ATS. No separate measurements of its first and second can could be made, but the order of magnitude of its back-pressure is more likely to be found in ATS than in a single ATD.

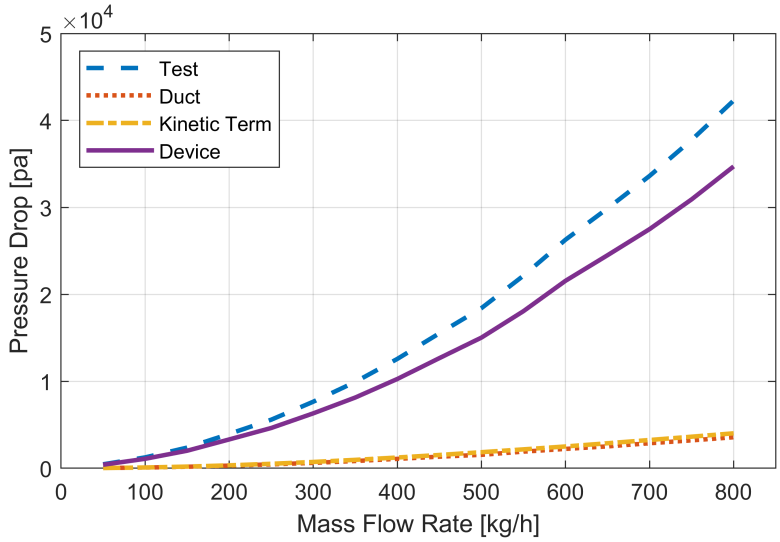

Figure 6.72: Experimental PD results from ATD6 characterization.

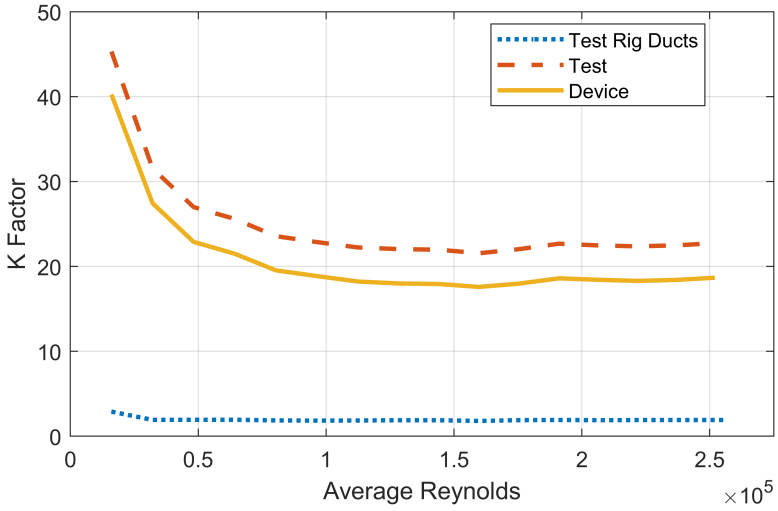

Figure 6.73: Pressure drop coefficients, K factor, from experimental characterization of ATD6.

Transmission loss

Fig. 6.74 shows the sound attenuation results at no flow condition for ATD6; both raw and smoothed results are presented up to 2000 Hz. A few aspects can be commented regarding these results: first, there is a notorious increase in the oscillations with the increasing frequency, which start to be relevant at around 1300 Hz and are prominent beyond 1550 Hz, to the point of not being completely compensated by the smoothing process. Overall, the level of attenuation is quite stable from 400 Hz and on, staying mostly in the order of 20 to 27 dB except in the spikes. Similarly to its category partner, this level of attenuation is relevant as to consider it an important element in the design of an eventual silencing element in the same exhaust line.

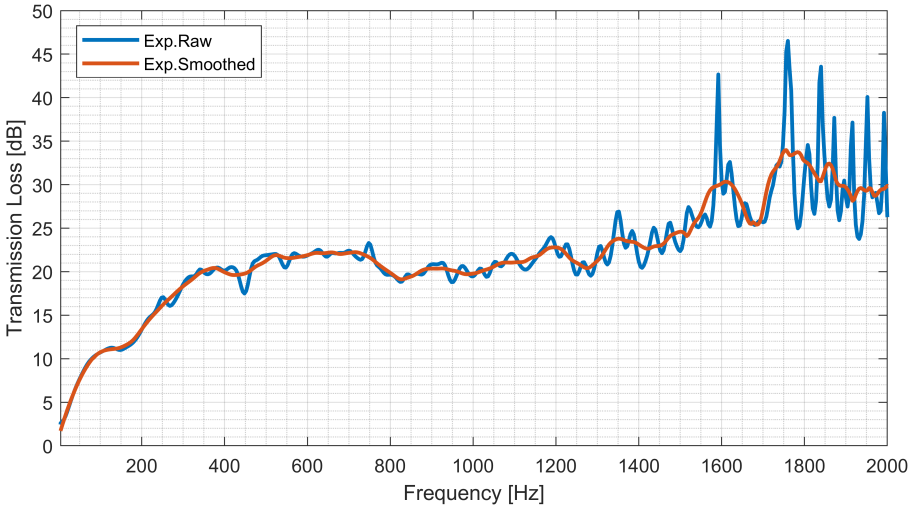

Figure 6.74: Experimental transmission loss results from ATD6 at flowless condition.

Comparative analysis

In order to provide some context for these measurements, a comparative analysis with respect to the most relevant parts in terms of PD, K factor and TL from simple and intermediate complexity categories was made. ATS1 (complete) is the natural choice from the simple geometry group, whereas ATD3 and ATD4 represent the intermediate complexity category in PD and TL, respectively. First, the PD comparison is displayed in Fig. 6.75.

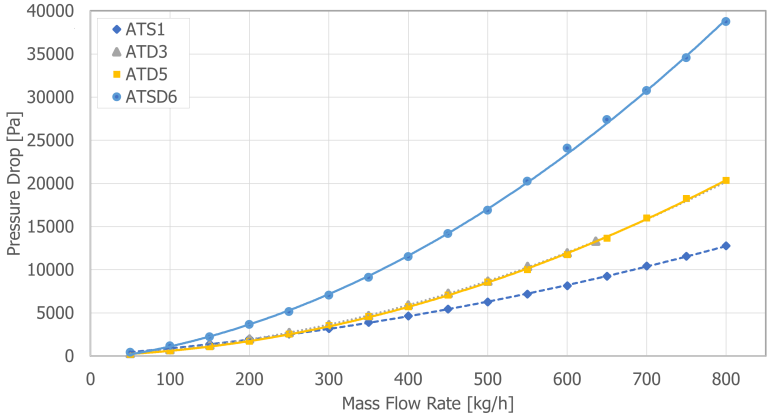

Figure 6.75: Comparison of PD results, complex geometry devices against selected previous measurements.

Regarding the perspective offered by this figure the following points can be highlighted:

- The PD of ATD5 is almost identical to that of ATD3; differences are within experimental uncertainties, including the extrapolated part as it was not possible to measure ATD3 with mass flow rates beyond 636 kg/h. This puts it in pair with the highest PD from intermediate category devices, and its also about 1.6 times higher than the results of ATS1.

- The PD of ATD6 is by far the largest of all the measurements performed; about 1.9 times those of ATD3 and ATD5, and 3 times as much as ATS1. Aside of the presence of three monoliths including a WF SCRf monolith, the intricate and abrupt change in direction in the bent section between the two cans is probably a major contributor to this extremely high value.

- Regardless of having one more monolith than ATD3 and ATD5, and the same amount as ATS1, the behaviour of ATD6 has an evident strong quadratic term over the linear one from monoliths. This reinforces the idea of curvature and geometrical traits being strong contributors to these results.

- As both ATD5 and ATD6 are SCR systems with DEF injection ports and mixer as those characterized in ATS1-A in Section 5.3, even if not of the same embodiment type, it is to expect that their mixers should also induce turbulence, that particular flow pattern also contributing to their high PD.

The pressure drop coefficients computed from the PD results presented in previous figure, are shown in Fig. 6.76.

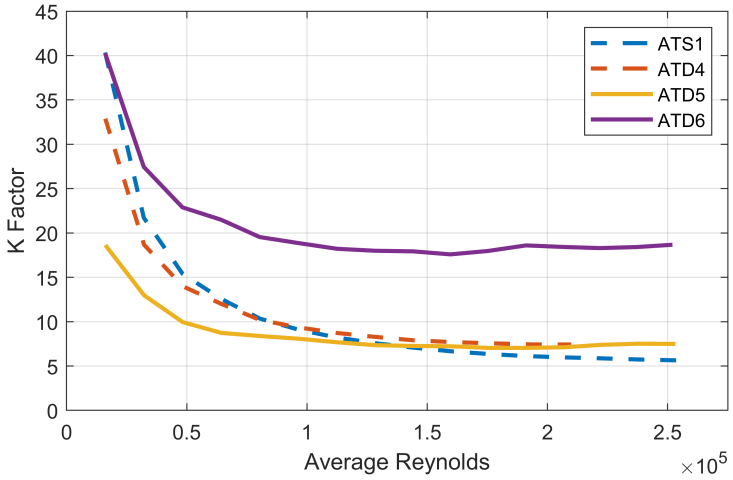

Figure 6.76: Comparison of estimated K factors, complex geometry devices against selected previous measurements.

Finally, the corresponding comparison of no-flow, raw TL results up to 1000 Hz is shown in Fig. 6.77; the decision to keep the comparison below 1000 Hz comes from this being the range assessed in the modelling approach, and the fact that above that range all results are somehow contaminated by resonant spikes or strong oscillations.

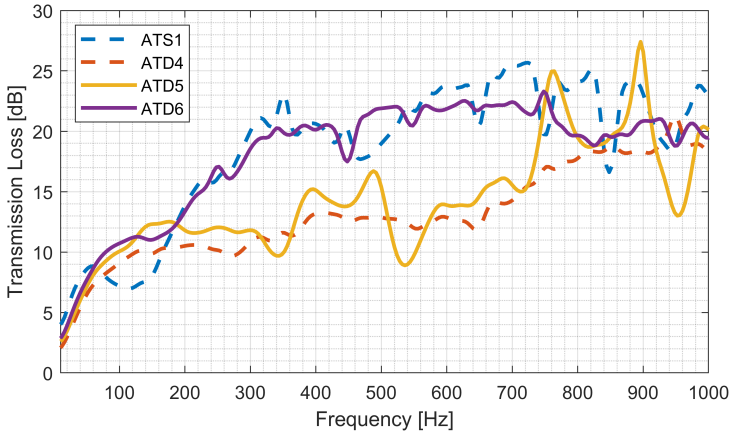

Figure 6.77: Comparison of no-flow TL results, complex geometry devices against selected previous measurements.

From this figure, the following can be observed:

- The TL curves for ATD6 and ATS1 exhibit a rather similar trend, with the exception of the trough that ATS1 results have around 100 Hz. As ATD6 is rather a compact ATS, it could be said that both ATS showed TL results that surpass those of individual ATD.
- On the other hand, ATD5 and ATD4 also exhibit a similar trend with some local differences, mainly attributable precisely to the oscillations of ATD5 results. Once again ATD5 is in pair with the highest result from devices from intermediate complexity category.

These pairs of similar results guide to the fact that, in the case of ATD5 and ATD4 similar PD correlates with –considerably– similar attenuation, whereas in the case of ATD6 and ATS1 a similar attenuation corresponds to the maximal difference in PD.

Results and discussion: Modelling

As the purpose in assessing these two specially complex devices was to test the capabilities of the modelling, the comparison between the results obtained from the models presented above, tuned with recommended seed values and without further improvement were compared to the experimental ones.

ATD5

Figs. 6.78 and 6.79 present the comparison of experimental and modelling results for PD and TL of ATD5 respectively.

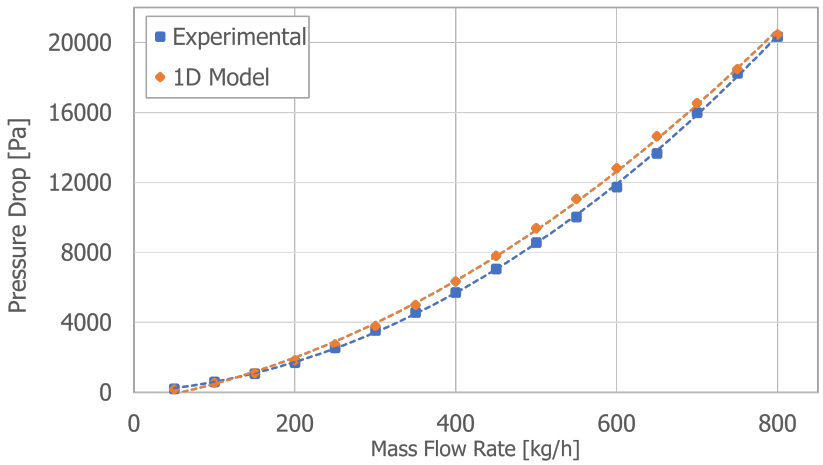

Figure 6.78: Comparison of experimental and 1D modelled PD results for ATD5.

In regards of the PD results:

- Considering that the modelled results are produced using the selected seed values of the parameters in order to test the capabilities of the methodology proposed, the results can be considered satisfactory.
- Indeed if this methodology is used to account for a device for which measurements are available, this would be the base results from

which the iterative adjusting stage would start. If the methodology is being used with information from a CAD or even the concept of a new device in design stages, these results would be very indicative, without the need of measurement, probably as to narrow down concepts or ideas before moving to more advanced 3D simulation or prototyping.

- Overall, the modelling results, while not precise, are close enough so as to represent the device providing an clear idea of the PD at each MFR.

- In particular, PD at the lowest MFR (below 200 kg/h) is slightly underestimated: there is a interception of modelled and experimental results at 200 kg/h and beyond that point the model overestimates the PD to some degree, coming again very close for the 800 kg/h MFR case. This is due to the model presenting a stronger linear term as a consequence of the monoliths, whereas it does not fully capture the quadratic effects related to the rest of the device.

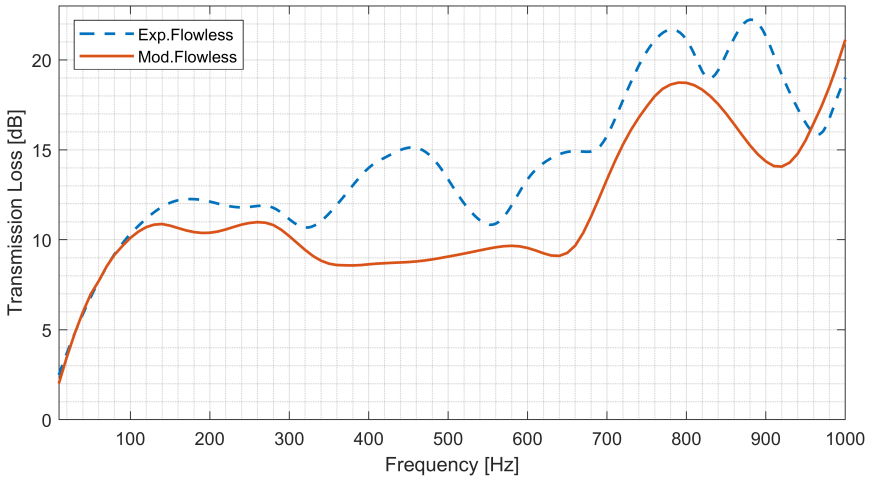

Figure 6.79: Comparison of experimental and 1D modelled TL results for ATD5.

From the comparison of TL results, the following observations arise:

- The initial ramp is almost perfectly captured, which means that at least the overall volume has been properly represented, which in turn means the discretization and simplified representation used for the most intricate portion of the device, that of the expansion volume containing the DEF injection port and the mixer right downstream of a bent, and upstream of the first monolith, was adequately defined.
- The shape and order of magnitude is relatively well represented between 100 and 310 Hz, exhibiting certain shift in the shape alongside discrepancies within the 2 dB margin.
- At mid of the displayed frequency range (320 to 700 Hz) the major differences arise: the model presents an almost flat behaviour, which is with a punctual exception (at 560 Hz) more than 3 dB below the experimental counterpart.
- Then starting at about 700 Hz the model again captures tendencies to some extent, with some values also within the 2 dB margin.

ATD6

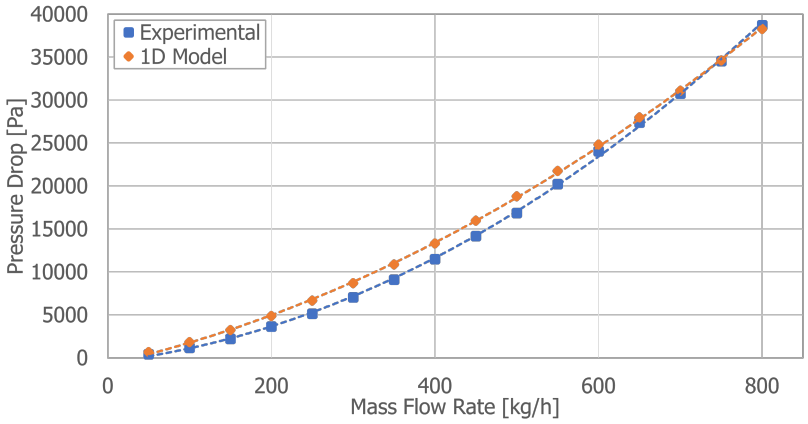

Figure 6.80: Comparison of experimental and 1D modelled PD results for ATD6.

Figs. 6.80 and 6.81 display together the experimental and modelling results for PD and TL of ATD5, respectively, in order to allow for comparison.

From the comparison of PD results, the following can the highlighted:

- Similarly to what was observed in the ATD5 results, the results from the model are satisfactory and can represent those of the device from the point of view of a conceptual design step, and could also be considered a satisfactory starting point for the iterative fine tuning process in regards of experimental data.
- Similarly to what was found with some devices from the intermediate complexity category, the agreement is excellent at the lowest and highest flow rates considered, but the model overestimates the results for all the intermediate mass flow rates.
- Once again the model results are more linear and less quadratic than those of the experiments.

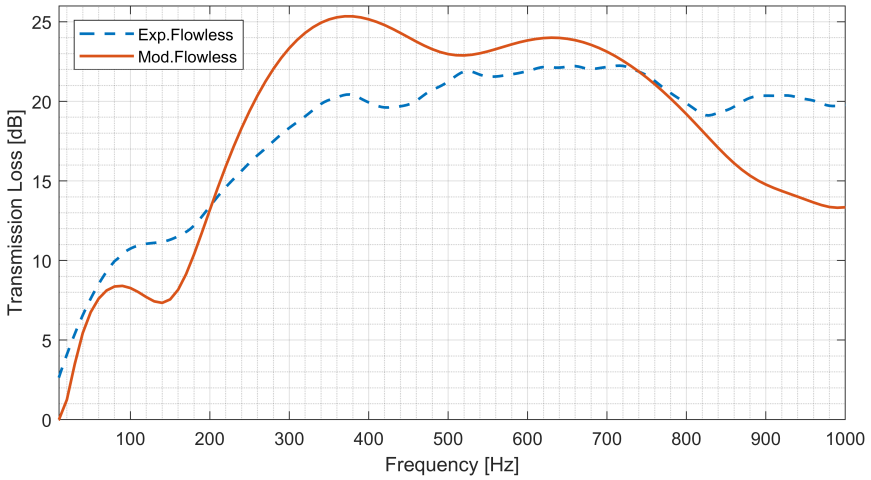

Figure 6.81: Comparison of experimental and 1D modelled TL results for ATD6.

In view of these TL results, it can be observed that:

- For this device the results are far more adequate, and the overall behaviour of the curve is fairly represented.

- The initial ramp, while not fully captured, is almost properly represented; this suggest some minor volume missing, which is understandable considering the several simplifications used, and the difficulties to represent properly the intricate geometry, particularly in the volume connecting the cans, where once again DEF injection port and a mixer are placed, alongside changes in direction and so on.

- The trough evidenced in the modelling results in the vicinity of 150 Hz can be linked to the shape of the experimental curve with a shift.

- From 200 to approx. 750 Hz the model overestimates the attenuation, but the representation of the shape and even the order of the discrepancies in part of that range still can be considered acceptable.

- Above 800 Hz the model again underestimates the attenuation, but this has been observed in previous models prepared, so it is coherent with previously obtained results, even after proper tuning.

Chapter 7

Conclusions and Future Work

7.1 Conclusions

In conclusion, this thesis has provided a comprehensive investigation into the acoustic and fluid-dynamic behaviour of after-treatment systems. A diverse set of after-treatment devices covering most of the components, features and configuration seen in realistic production ATDs have been characterized by experimental measurements and, as a necessary complement, different modelling approaches suitable for engineering practice have been applied to reproduce results and to provide a better understanding of the complex fluid dynamics and acoustic interactions that occur within the systems studied.

The devices available were classified into categories according to the level of complexity in their geometrical disposition and composition, what allowed to assess the modelling work in an order of ascending complexity. As schematized in Fig. 7.1, this order helped in two main ways: first, it allowed to make the most of the iterative process of modelling by structuring a methodology for each modelling approach used and, secondly, it guided the inductive reasoning via direct comparison to associate differences in results with the elements increasing the complexity at each step.

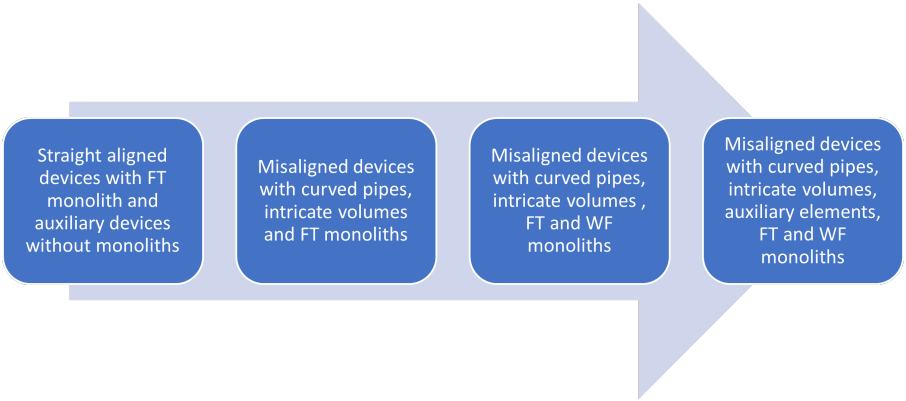

Figure 7.1: Order of ascending complexity followed in the assessment of ATD within this research.

The experimental characterization consisted of experimental measurements, which were developed using well established facilities and techniques available in the hosting research centre. On the other hand, the modelling tasks took advantage of 3D CFD and most extensively 1D modelling, attempting to reproduce the device behaviour and the complete results of experimental measurements based on the concept of virtual twinning for the devices and, as much as possible, the testing installations.

During the research the following aspects were addressed:

- The significance and validity of acoustic characterization made under laboratory conditions when applied to the actual operating condition of the devices.
- The effects of the presence of the following elements or characteristics, both in sound attenuation and back-pressure, of after-treatment systems or devices:
  - Auxiliary elements (mixers, fluid injectors, sensors and probes, adjacent volumes for sensor ports, and separators).
  - Monoliths, either FT or WF.

  - Gaps between monoliths.
  - Irregular volumes.

- The eventual compliance of the additivity property of PD and TL when several ATDs are arranged together as an ATS.

- The effects and implications of deep-bed filtration on the PD and TL of a device containing GPF during its early service life, and the potential benefits of considering such condition in the exhaust line design process.

- The benefits of applying decomposition analysis for TL results, and the deeper understanding of the effects and implications of reflective (reactive) and dissipative effects on sound attenuation produced by such application.

- The capabilities of 1D and 3D CFD modelling approaches to provide additional information for the correct understanding of internal phenomena, fluid dynamic or acoustic interactions.

- The convenience and potential of 1D-3D coupled simulation as a profitable trade-off making the most of the advantages of each individual approach while compensating their weaknesses.

The results of this study are expected to have significant implications for the design, characterization and analysis of either existing or future after-treatment systems and, in the holistic view, the complete exhaust line. Additionally, the methodology proposed, and some procedures and analyses used have the potential to be translated into other applications. To name an example, even if the automotive application of after-treatment systems declines, several systems are shared with marine and industrial applications; also, the case study on the mixer can be an example of how small elements that tend to be neglected can in fact have significant effects. Finally, the way in which the coupled 1D-3D simulation was used could be translated into other applications.

The following sections are dedicated to recapitulate the most important milestones, activities and findings of the main chapters:

Significance of cold condition measurements to actual in-engine conditions

In chapter 4, a new methodology based on the integration of several pre-existing experimental facilities, processing techniques and theoretical concepts was proposed and applied in order to determine the significance of acoustic measurements taken under laboratory conditions (ambient temperature and steady flow) with regards to actual engine operating conditions, or at least engine-like conditions, with high temperature and high-amplitude pressure oscillations. The test benches, Impulse Test Rig and Unsteady Gas Stand, the processing technique (beamforming based wave decomposition) and the theoretical concept of time-frequency coupling were all known to the research institute, but this arrangement constitutes the first ever to allow for the direct evaluation in controlled conditions of the performance of such extrapolation.

Having this methodology to evaluate the validity of cold condition and controlled measurements for acoustic characterizations helps to both fill a gap in the literature and to provide a previously missing basis for current engineering approaches to the problem. The assessment presented in that chapter set the foundation and confirmed the validity of the experimental and computational approaches for ATS and ATD acoustic characterizations developed, presented and used in subsequent chapters.

The proposed methodology was applied to ATD0, an ATD for a commercial diesel engine which contains two monoliths placed in a single shell, a DOC followed by a DPF. The lab-condition measurements were performed in the Impulse Test Rig and provided the information needed to formulate the scattering matrix at room conditions, just aside of additional corrections needed to compensate for the flow and temperature as required.

Additionally, measurements with hot and pulsating flow conducted in the Unsteady Gas Stand alongside the application of the beamforming wave decomposition procedure provided the values of forward and backward components. In this last step it was evidenced that wave components upstream of the ATS had larger amplitudes than downstream components, just as expected.

Later, direct comparison was made between two sets of data, wave decomposition of hot and pulsating measurements against the extrapo-

lation based on the scattering matrix (as presented in Eq. 4.1) obtained from cold condition measurements.

The first insights into the effects of different variables on the acoustic behaviour of the ATD were drawn from the values of transmission and reflection coefficients obtained directly from the impulse test rig measurements:

- Mean flow showed weak influence within the range tested, but its effect was as expected.
- Pulse amplitude had weak influence within the range tested, but its effect was as expected.
- Soot loading showed important influence on both sets of coefficients, especially on the transmission coefficients.
- In the case of temperature, the whole procedure of extrapolation was applied as temperature changes also cause changes in Helmholtz and Mach numbers.

A major difficulty associated with the noise-to-signal ratio of the measurements was evidenced in several cases while applying the wave decomposition technique. This constitutes a challenge for the application of the procedure, even when the algorithm has been thoroughly conditioned.

The baseline case scenario had the following 5 conditions; 300 kg/h of mass flow rate at 200°C of temperature, a frequency of 33 Hz and a pressure amplitude of 0.25 bar with no soot load in the device. Then one change in each condition was applied; the mass flow rate was increased to 500 kg/h, the temperature lifted to 500°C, the frequency to 100 Hz, the pressure amplitude reduced to 0.1 bar, and finally an iteration with soot load of 13 g/l. With these set of experiments carried out, the results were plotted for the first eight engine orders (H2 to H16) of the equivalent four cylinder, four-stroke engine, which is beyond the usual range of interest for exhaust applications. Then the analysis of results was focused on the upstream backward component and the downstream forward component.

From the analysis of comparing results for the upstream backward component as plotted in Fig. 4.9:

- An overall acceptable agreement was found in the direct comparison of results from the wave decomposition analysis of the Unsteady Gas Stand and the scattering matrix extrapolation to all the scenarios. Besides certain deviations, most of them within the 5 dB margin which is considered acceptable for model validation in industrial practice, the tendencies were clearly captured.

- For the baseline scenario, the scattering matrix extrapolation overestimates wave decomposition except in the first order where a slight underestimation could be observed, but for all orders the differences are small.

- The case of decreasing the pressure amplitude from 0.25 bar to 0.1 bar caused the most evident differences between the two sets of data, but even in this case the overall tendency was properly reproduced. The differences can be attributed to the noise-to-signal ratio.

- In the cases were soot loading, mass flow and frequency were increased, the changes did not induce any significant changes in behaviour; the trends were adequately captured, especially in the last case, and deviations remained in the same order of magnitude as for the baseline.

- The case with the temperature increase captured well the trend and dependency with order number, but showed the highest deviation for any of the cases in the sixth order.

Likewise from the results for comparison of the downstream forward component, as shown in Fig. 4.10, the following can be concluded:

- An overall fair reproduction of the results and trends was obtained for all cases, but the level of agreement was slightly worse than for the upstream backward components. This can be explained by the pressure amplitude decrease caused by the passage through the ATS, which in turn worsens the noise-to-signal ratio.

- Most deviations remained within the 5 dB margin, and those that exceeded this range occurred above the tenth order.

- The dependency on the engine orders was also properly reproduced and can be considered satisfactory; the most remarkable discrepancies occurred either by a small margin at the lowest orders or punctual at orders out of the usual range of interest.

- The case where the mass flow rate was increased from 200 kg/h to 500 kg/h, exhibited significant deviations in 5 out of the 8 orders analysed, being the only case were the trend was not properly captured. This was again attributed to the noise-to-signal ratio, as the higher velocities associated with the increased mass flow should cause strong turbulent fluctuations, which can be handled by the algorithm with the higher amplitude of the signal upstream of the ATS but not in the downstream side.

This comparative assessment indicates that the scattering matrix extrapolation approach is capable of producing, at least qualitatively, very indicative and representative information about the effects of ATS on the flow upstream and downstream of the ATS in hot and pulsating flow conditions, the estimations for the upstream side being better.

The theoretically expected effects of modifying each variable were clearly reproduced and identified regardless of the approach (elements of the scattering matrix, components drawn from the wave decomposition or scattering matrix extrapolation), specially the effects of soot loading.

Therefore it can be concluded, within unavoidable uncertainties related with engine-like operation, that cold condition acoustic measurements are fully capable to provide relevant information for the design of the ATS to be placed in the hot-end of the exhaust line.

Case study on a complete SCR exhaust line with static swirl mixer

The most relevant activities and findings from Chapter 5 are recapitulated, first those general to the chapter and then covering the topics addressed in each section.

Generalities

- A prototype SCR after-treatment system, composed of three devices, which were conveniently simple in their geometrical con-

figuration and axially aligned was selected to start the research guided by the simple-to-complex philosophy.

- The assessment of the system involved both the experimental characterization and computational modelling, the latter mostly focused on the 1D approach due to the predominantly simple geometries, but using a 3D approach when required.

- The ATS was characterized and then split into its composing parts, offering the opportunity to characterize a set of devices with simple geometries, as well as their combinations, and therefore account for possible interactions.

- The experimental characterization of the devices, its combinations and the complete system was performed using the CFTB and the ITR facilities presented in Section 3 to account for the PD, pressure drop coefficient and TL.

- The computational work at this stage was centred in structuring a modelling methodology based on the virtual twinning concept capable to reproduce the measurements consistently through 1D models.

- This part of the research, was organized from the modelling point of view to follow an order of increasing complexity; this also helped to organize and analyze the information as consigned in this document.

- Comparative analysis between components, highlighting and accounting for shared and exclusive traits of each one was a very useful tool all along.

Assessment of individual devices containing monoliths

- The chapter started with the assessment of two of the devices extracted from ATS1, those that contain monoliths, ATS1-D1 with two monoliths and ATS1-D2 with one, the three monoliths being the same TWC.

- Regarding the results from CFTB measurements on both devices, the expected behaviour was found:

  - The PD results exhibit a quasi-quadratic dependence on the mass flow, including a quadratic term and a linear term associated with the laminar flow in the channels of the monoliths.
  - The pressure drop coefficient showed an asymptotic trend with the increasing Reynolds number.
  - From the comparative analysis between these two almost identical devices it was found that the PD of ATS1-D1 is almost exactly that of ATS1-D2 multiplied by 1.65 times, a difference that can be attributed almost entirely to the monolith, as the gap is very small.

- Regarding the results from the ITR:
  - The effect of the flow for both devices matched what was expectable: increasing the flow also produces a certain increase in the attenuation, which is associated with dissipative flow-related effects, but without substantial changes in the overall shape of the curve and trends.
  - The attenuation of the double monolith device is larger than that of the single monolith one, as should be expected, with the exception of an unexplained spike in the single monolith device that might be related to either a manufacturing defect or an unintended modification caused during the splitting process.

The overlooked effect of auxiliary devices

- A comprehensive set of PD and TL measurements were performed on ATS1-A, which includes a mixer of the static swirl kind and a side cavity with a port for DEF injection, a very representative auxiliary device for SCR and some other after-treatment systems.
- Aside from the PD and TL measurements, a TL decomposition analysis using the logarithmic approach described in Section 3.2.3 was applied.
- *Remarks on experimental PD results:*

  - Regarding the PD results, they match the expected behaviour, both in terms of the asymptotic trend of the pressure drop coefficient at high Reynolds numbers, and of the dependence of the PD with the mass flow rate.
  - The mixer contribution to the PD of the complete ATS is not negligible, despite of its reduced size; its working principle, which consist of inducing local turbulence to promote mixing, explains this fact.

- *Remarks on experimental TL results:*
  - The occurrence of negative transmission losses, which indicate some flow noise generation in the device, was evidenced when checking for the effect of a superimposed mean flow. While this might be expectable in view of the geometry of the device, it was further analyzed with the aid of the decomposition analysis.
    * Using the logarithmic approach, reflective and a dissipative contribution were identified.
    * This negative transmission loss was found to be associated with negative values of the dissipative term.
    * It was found that the dissipative term also becomes negative even in some cases where the total transmission loss is still positive, suggesting that in those cases the sound generated must be attenuated at the device itself.
  - The occurrence of negative TL may require special care in the mechanical design of the connection to the after-treatment system.
  - A more detailed and dedicated study considering the influence of the actual reflecting boundaries upstream and downstream of the device, such as that presented in [140], would be necessary in order to fully analyze this aspect, but such study is out of the scope of this research.
  - Besides of the negative TL effect, other effects of the flow on the TL of this device exhibited both the convective and dissipative effects expected.

  - It has been observed that, while the attenuation of the auxiliary device itself is indeed small, when coupled to the other components of ATS1 it produces a non-negligible effect, most likely due to the presence of dissipative terms, and therefore its presence should not be neglected in acoustic studies.

- A three-dimensional model was used in order to shed additional light onto the experimental results; findings to highlight include:
  - A resonant effect, similar to that of a side resonator, was identified on the DEF injection port cavity.
  - The overall importance of dissipative effects in the attenuation of the device, even at low frequencies, was evidenced.
  - Interaction in the form of significant coupling between the acoustic field and the mean flow was identified, most notably downstream of the mixer vanes, where the flow is highly rotational.

- Finally, two 1D models were prepared, one following the same steps and considerations as for all other devices, mostly based on the experimental measurements and the geometry characteristics, and a specific one prepared to match the findings of the 3D modelling approach.
  - For the experimentally based one:
    * Similarly to the 1D models prepared for devices containing monoliths in Section 5.2, PD and TL results up to 1000 Hz produce satisfactory and indicative results.
  - For the 3D based one:
    * Information from the acoustic 3D computations was used to adjust an equivalent quarter-wave resonator describing the resonance effects.
    * The detailed results from the steady CFD computation were used to estimate a local pressure drop coefficient for an equivalent restriction downstream of the mixer vanes.
    * The results may be regarded as acceptable, in the sense that at least the dissipative terms and the trends rele-

vant for the ulterior incorporation of such a model into a model of the whole after-treatment are included.

- Overall, both modelling approaches were found to be capable of producing useful information for the design process of auxiliary systems.

Assessment of combined devices and additivity

- The results for ATS1 are fully consistent in terms of the relative importance of the contribution of the different parts: ATS1-D1 (double monolith) has the largest contribution, followed by ATS1-D2 (single monolith) and finally the auxiliary device, ATS1-A.
- Once all measurements for individual and combined devices were available the opportunity to assess the additivity or interaction between the devices both in PD and TL was exploited:
- Regarding the pressure drop:
  - The pressure drop was confirmed to be essentially additive.
  - The small deviations observed are attributed to the experimental uncertainties and the effects due to the flow not being fully developed upstream of some devices in the combinations, which is only guaranteed for the first device in each assembly.
  - This conclusion is also supported by the fact that for the sum options considered for comparison with the complete ATS1, those that added two measurements are practically identical, whereas the one adding three measurements is the one with the most noticeable deviation.
- Regarding the transmission loss:
  - It appears that ATS1-A, particularly due to the mixer element, simply adds up attenuation to whatever is located downstream.
  - For all the other cases, there are acoustic interactions that make the results to be not additive within the low to mid frequency range which is dominated by reactive effects.

  - For higher frequencies, in which the attenuation produced is dominated by dissipative effects, the transmission loss is essentially additive.

In view of these conclusions, the 1D methodology as structured up to the simple geometry category level was found capable of producing models with excellent PD results and satisfactory TL results, fairly accurate for low frequencies (up to the $500-700$ Hz) and at least indicative for higher frequencies. Starting on this ground the characterization of intermediate and complex geometries was assessed in Chapter 6.

Assessment of Individual After-treatment Devices

In this section a summary of the most relevant activities and findings from Chapter 6 is presented, first on the experimental characterization of devices, then moving into the modelling assessment and finally some topic-specific highlights.

On the experimental characterization

- A comprehensive set of PD and TL loss measurements were performed on diverse group of ATDs, from the intermediate and complex geometry categories previously established, all of them representative of realistic production parts.
- Regarding the PD results.
  - All devices were tested on the CFTB installation, trying to measure the PD due to the device in turn under mass flow rates ranging from 50 to 800 kg/h, even though the test had to stop at lower mass flow rate for two devices (ATD3 and ATD4).
  - All devices exhibited the expected behaviour as PD results showed a quasi-quadratic dependence of the PD on the mass flow rate.
  - The quasi-quadratic behaviour has a linear component that is related to the laminar flow that occurs inside the channels on monoliths, either FT or WF, while the quadratic features

are related with the interaction of flow with all other components.

- Pressure drop coefficients (K factors) as a function of the Reynolds number were also calculated from PD measurements.
- All K factor results exhibited, within measurement uncertainties, the appropriate asymptotic trend at high Reynolds numbers.

- Concerning the TL results:
  - All devices were measured without superimposed flow using the ITR installation.
  - Additionally, devices from the intermediate geometry complexity group were also tested with superimposed mean flow at three different mass flow rates, mostly 100, 200 and 300 kg/h, but in the case ATD3 smaller MFR were needed (150 and 220).
  - The measurements with superimposed MFR were taken twice each, using two different pulse amplitudes to excite the devices in order to capture their acoustic response.
  - It was thoroughly checked that small pulses translate into TL curves with notorious oscillatory nature with the increasing frequency, to the point that some measurements are too "noisy" to extract information with confidence.
  - In all cases measured with superimposed MFR, regardless of the pulse amplitude, the effect of the flow was that expected: some dissipative flow-related effects increased the attenuation without substantial changes in the trends (minor shifts, usually).
  - All the measurements were smoothed in the post-processing in order to make them friendlier for posterior comparative analysis with modelling results, although some measurements, mostly excited with small pulses, were still noisy after smoothing.

Comparative analyses between intermediate and complex devices and, for convenient reference, ATS1 and ATS1-D1 from simple geometry category, were made when possible. These comparisons allowed to make the most out of the information produced and the inductive reasoning, as for example, ATD1 and ATD2, are practically identical in terms of geometry, but one of them has a WF monolith where the other has a FT monolith, and therefore their comparison allows to attribute differences to the differentiating elements, in the example the presence of the WF monolith.

The following topics were assessed following the aforementioned analysis approach:

Effects of bends and irregular geometries

Comparison between ATS1-D1, ATD2 and ATD3, that share the double FT monolith arrangement, led to the following conclusions:

- The PD results of ATD3 are the highest of the three, and of the complete intermediate complexity category, significantly higher than those of ATD2 and even further of ATS1-D1.
- Considering ATS1-D1 as the base line for the PD of a device were the linear term due to monoliths is predominant over rather simple pipe and tapered volumes, the differences between it and ATD2 are likely to be attributable to the intricate and curved inlet geometry used in ATD2, in contrast with the simple conical geometry of ATS1-D1.
- Similarly, the comparatively reduced pipe diameters and the highly complex geometry of its expansion, contraction and intermediate volume should be contributing significantly to the PD of ATD3.
- In regards of TL, the best attenuation was provided by ATS1-D1, for frequencies above 400 Hz and below 100 Hz, whereas ATD3 has the larger attenuation between 100 and 400 Hz but out of that interval its attenuation is in general lower than that of ATD2. Therefore, the trends in attenuation do not correspond with those in pressure drop, even for the low frequencies.

Effects of the presence of Wall-flow monoliths

The comparison previously used as example, ATD1 and ATD2, allowed to account for effects attributable to the presence of a WF monolith as both devices share their overall geometrical configuration and even were designed for the same family of engines:

- The differences found in PD, being the back-pressure of ATD1 about 1.6 times larger than that of ATD2 at 800 kg/s, is to be associated mostly with the presence of the WF monolith, even though CFD results also indicate some effects in the entrance to the inlet side irregular bend that could explain partially the difference.
- Regarding the TL results, differences change sign depending on the frequency range considered, and are not as large as one would have expected from the significant difference observed in the PD.

Similarly, comparison between ATD1 and ATD4, allows to look for differences between to devices that have TF-WF monolith combination, but ATD4 having a less complex inlet geometry:

- Regarding the PD, their results are not so different, but still the one with the less complex inlet geometry is also the one with a lower back-pressure.
- In terms of TL:
  - neither for ATD1 nor for ATD4 any significant changes due to the flow could be observed except for the usual increase in the overall attenuation level associated with the dissipative effects of the increasing flow.
  - In terms of the relative importance of the attenuation achieved, it was found that the shapes are all very similar, at least up to 1000 Hz. ATD4 reaches the highest attenuation, likely because of its higher volume together with the presence of a DPF. ATD1, which includes a GPF, follows a similar trend, but with significantly lower attenuation values.

On the modelling assessment

The 1D methodology, that started to take form with the assessment of devices from the simple geometry category was extended and adjusted to also cover devices with realistic geometries. Those from the intermediate complexity category served to expand it.

Similarly to results obtained for simple geometry devices, the developed models were found capable of producing excellent PD results and satisfactory TL results, fairly accurate for low frequencies (up to the $500 - 700$ Hz) and at least indicative for higher frequencies. 3D CFD results provided complementary information as well, and coupled 1D-3D modelling was found to be capable of improving the base 1D; however, such approach might still be regarded as a last resort when very detailed results are needed, as the adaptation required for the coupling is extensive when compared to individual 1D modelling, even if the computation time is greatly reduced in comparison with a complete 3D CFD simulation.

The Very Early Life of GPF

The opportunity to help fill an identified knowledge gap regarding the changes in back-pressure and sound attenuation taking place during the first few cycles of use –a period often referred to as the early service life– on devices containing GPF monoliths was seized. Understanding such changes can lead to a revision of the boundary conditions to take into account for ATD, silencing elements and therefore complete exhaust line design.

To account for these effects, two states or conditions were distinguished, "new" and "clean". "New" stands for never-used, and "clean" refers to the state reached after some usage, with no soot cake layer due to regeneration, and still without significant ash accumulation. Using resources available in the following manner the matter was investigated:

1. ATD1 was selected as test subject, as it contains a GPFc that was received sealed from factory, in the ideal "new" condition, and was already characterized in such state.

2. An engine test bench, conveniently with the native engine of the device mounted, was used for the device to urdergo the equivalent

of a few hours and kilometers of use, approximately equivalent to those of a brand-new car when reaching the final costumer out of the car dealer.

3. At this point, the device is expected to have reached the "clean" condition, as it is known to undergo a deep-bed filtration process that partially fills substrate pores with a certain amount of soot, which becomes in practice immune to regeneration, thus defining the effective base substrate microstructure and cleanness of the WF monolith and in consequence of the whole system.

4. The CFTB and ITR facilities were used again to characterize the device now in the "clean" condition. As a precaution, only the direct position, no-flow test was performed to avoid affecting the deposited soot in any way. Inverse response was estimated from reciprocity properties [40].

5. 1D models, two sets of models were prepared to represent the clean condition, one considering a uniform load distribution and the other considering a non-uniform one. The new state was represented by the previously developed model.

6. The linear approach of the decomposition analysis was applied to both the experimental and the modelling results, in an attempt to identify the role of reactive and dissipative effects on wave propagation, as they may contribute significantly to important simplifications in the design of the exhaust line downstream of the ATS.

Findings of this assessment, separated by the steady or unsteady behaviour studied, include:

- The steady flow results showed hints of the influence of in-pore soot deposition on the dissipative behaviour of the ATS.
  - The pressure drop of the device increased slightly with the use.
  - The substrate pore diameter was the model parameter chosen to represent the deep-bed filtration in "clean" condition,

keeping the rest of the model parameters at the same value as for the "new" condition.

  - For both conditions qualitatively good results were obtained, with a tendency to slightly overestimate at low to mid mass flows, and underestimate at high mass flows, the pressure drop.
  - As the influence of usage is also more apparent in the modelled results, all this might indicate that the effect of load distribution across the wall-flow filter may have a noticeable influence on the overall pressure drop.

- For the unsteady behaviour, two power ratios (reflected and dissipated) were used to highlight the relative importance of reactive and dissipative effects, both in the experimental and in the modelled results. In the case of the reflective/reactive contribution, the main conclusions drawn from the experiments were:
  - The effect of usage showed noticeable influence on the reactive behaviour of the ATS.
  - Overall trends were maintained in terms of peaks and troughs, with the "clean" condition showing less pronounced fluctuations up to 1200 Hz, and quite close to the "new" condition above that frequency, which can be related to higher frequencies being more sensitive to geometrical traits than to microstructure.

- From the modelling work the following points are worth mentioning;
  - The models are able to capture the overall shape of the frequency dependence (if not its details) for frequencies below 1000 Hz, as well as some other aspects above that value. Additionally, the values of the two highest peaks are quite close to their experimental counterparts.
  - The model was able to reproduce qualitatively the effects of usage, showing that the "clean" condition is more reflective at high frequencies. Even if the effect is less pronounced than that observed in the experiments, it can be stated that the

model provides significant results from the point of view of reactive mechanisms.

- In the case of the dissipative contribution, the main experimental outcomes were:
  - The effect of usage induces relatively small differences for frequencies above 1000 Hz, and regardless of the usage effect, the attenuation is dominated by dissipative effects.
  - The usage smooths out the curve for frequencies below 1000 Hz, most notably at the frequencies of the peaks of the reflected power ratio.
  - Overall, dissipation is higher in "clean" conditions, as one could expect.
- From the modelling results, one may conclude that:
  - The description of the dissipative behaviour provided by the model was rather poor, most notably in the case of the "new" condition, where results are much smoother than the experimental ones.
  - The effect of usage, if a uniform loading distribution is assumed, is represented by an almost constant increase in dissipation in comparison with the "new" condition, whereas the consideration of a non-uniform distribution introduces some frequency-dependent features, thus supporting the assumption that the non-uniform distribution of the loading across the wall-flow filter has a significant impact on the dissipation, even if it is not equally noticeable in steady conditions.
- As an overall conclusion, it appears that accounting for these effects, even if approximately, may provide significant advantages from the point of view of exhaust line design.

Validation of methodology with most complex devices

- Contrary to the devices from the simple and intermediate geometry complexity categories, the experimental characterization of

these devices was limited. The PD was measured as usual, but only no-flow measurements were taken for TL.

- Also, the computational modelling from previously assessed devices was guided and investigated with the experimental results as benchmarks. Now the models were prepared strictly following the steps and guides of the developed 1D modelling methodology and its components; for example, tuning with the recommended seed values, and only when the results of those models were available the results were compared.

- PD results could still be improved by fine tuning, but as a first approximation the results with seed tuning parameters can be regarded as acceptable and more than indicative.

- Similarly, TL results could probably still be improved, for example by using the GEM3D or the 3D CFD approach first, but being the result of an unrevised first attempt and iteration based only on the methodology they can be regarded as acceptable.

7.2 Future Works

Apart from improving the modelling methodology or the models with further updates of the commercially available software, as it could be evidenced from improving pre-existing models in GT 7.5, passing through several editions all the way to v2021, this is likely to be the last or among the last research related to acoustic of after-treatment and exhaust lines of Internal Combustion Engines. However, as techniques and technologies are being inherited by hybrid, electric and alternative powertrains, it is possible that the methodologies, analyses and complements produced within this thesis could be adapted and somehow implemented in other areas giving rise to future related works.

Bibliography

[1] AJ Torregrosa, A Broatch, P Quintero, Á Redondo, and F Morin. Assessment of the fluid-dynamic and acoustic behaviour of a swirl static mixer for after-treatment systems. *Applied Acoustics*, 186 (108446), 2022.

[2] A.J Torregrosa, J. De la Morena, E.J Sanchis, Á. Redondo, and E. Servetto. A study of the early life of gasoline particulate filters: Reactive and dissipative acoustic effects. *Part D: Journal of Automobile Engineering*, update(update), 2022.

[3] A. J. Torregrosa, P. Piqueras, J. Sanchis, E., and Á. Redondo. On the applicability of cold acoustic measurements to high-amplitude hot pulsating flows. *Acoustics Australia*, 51:115–128, 2022.

[4] Lesme Corredor, José Avendaño, R. Bello, Á Redondo, J. Calle, and J. Viloria. Industrial energetic districts: Impact analysis on the global energy efficiency and business competitiveness. In *E3S Web of Conferences*, volume 64, page 08007. EDP Sciences, 2018.

[5] Álvaro Rafael Redondo Navarro. Experimental characterization and improved modelling methodology for simple geometry after-treatment devices focused on pressure drop and transmission loss, 2021.

[6] Gautam Kalghatgi. Development of fuel/engine systems—the way forward to sustainable transport. *Engineering*, 5(3):510–518, 2019.

[7] ExxonMobil. 2022 outlook for energy, a perspective to 2050, 2022.

[8] bp British Petroleum. Statistical review of world energy 2022, 2022.

[9] International Energy Agency. World energy outlook 2022, 2022.

[10] Pierre Gadonneix, Abubakar Sambo, Liu Tie'nan, Arup Roy Choudhury, Johannes Teyssen, José Antonio Vargas Lleras, Abbas Ali Naqi, Kevin Meyers, Heon Cheol Shin, Marie-José Nadeau, et al. Global transport scenarios 2050. *World Energy Council*, 456, 2011.

[11] Gautam Kalghatgi. Is it really the end of internal combustion engines and petroleum in transport? *Applied energy*, 225:965–974, 2018.

[12] Eunji Yoo, Myoungsoo Kim, and Han Ho Song. Well-to-wheel analysis of hydrogen fuel-cell electric vehicle in korea. *International Journal of Hydrogen Energy*, 43(41):19267–19278, 2018.

[13] José Ramón Serrano. Imagining the future of the internal combustion engine for ground transport in the current context, 2017.

[14] Carla Tagliaferri, Sara Evangelisti, Federica Acconcia, Teresa Domenech, Paul Ekins, Diego Barletta, and Paola Lettieri. Life cycle assessment of future electric and hybrid vehicles: A cradle-to-grave systems engineering approach. *Chemical Engineering Research and Design*, 112:298–309, 2016.

[15] Takayuki Ogata, Mikio Makino, Takashi Aoki, Takehide Shimoda, Kyohei Kato, Takahiko Nakatani, Koji Nagata, Claus Dieter Vogt, Yoshitaka Ito, and Dominic Thier. Particle number emission reduction for gdi engines with gasoline particulate filters. Technical Report 2017–01–2378, SAE Technical Paper, 2017.

[16] Yong Qian, Zhiyong Wu, Jinjing Guo, Zilong Li, Chenxu Jiang, and Xingcai Lu. Experimental studies on the key parameters controlling the combustion and emission in premixed charge compression ignition concept based on diesel surrogates. *Applied Energy*, 235:233–246, 2019.

[17] E Jiaqiang, Mengyuan Zhao, Qingsong Zuo, Bin Zhang, Zhiqing Zhang, Qingguo Peng, Dandan Han, Xiaohuan Zhao, and Yuanwang Deng. Effects analysis on diesel soot continuous regeneration performance of a rotary microwave–assisted regeneration diesel particulate filter. *Fuel*, 260:116353, 2020.

[18] Zhijun Li, Boxi Shen, Yanke Zhang, Xiangjin Kong, and Shilong Li. Simulation of deep–bed filtration of a gasoline particulate filter with inhomogeneous wall structure under different particle size distributions. *International Journal of Engine Research*, page 1468087421992216, 2021.

[19] Pingen Chen and Junmin Wang. Nonlinear model predictive control of integrated diesel engine and selective catalytic reduction system for simultaneous fuel economy improvement and emissions reduction. *Journal of Dynamic Systems, Measurement, and Control*, 137(8), 2015.

[20] David W. Kapsos, Cary D. Bremigan, Mark P. Adams, and Patrick M. Klein. Exhaust aftertreatment system with spiral mixer, may 11 2010. US Patent 7,712,305.

[21] Euijoon Shim, Hyunwook Park, and Choongsik Bae. Comparisons of advanced combustion technologies (hcci, pcci, and dual-fuel pcci) on engine performance and emission characteristics in a heavy-duty diesel engine. *Fuel*, 262:116436, 2020.

[22] Benjamin Pla, Pedro Piqueras, Pau Bares, and André Aronis. Simultaneous no x and nh 3 slip prediction in a scr catalyst under real driving conditions including potential urea injection failures. *International Journal of Engine Research*, 23(7):1213–1225, 2022.

[23] J. M. Desantes, A. J. Torregrosa, A. Broatch, and H. Climent. Silencing capabilities of non–silencer elements: An underused potential? In *Proc. of the 4th Styrian Noise, Vibration and Harshness Congress 2006*, Graz, Austria, 2006.

[24] H Weltens, H Bressler, and P Krause. Influence of catalytic converters on acoustics of exhaust systems for european cars. *SAE transactions*, pages 1186–1200, 1991.

[25] RJ Astley and A Cummings. Wave propagation in catalytic converters: Formulation of the problem and finite element to solution scheme. *Journal of Sound and vibration*, 188(5):635–657, 1995.

[26] J-G Ih, C-M Park, and H-J Kim. A model for sound propagation in capillary ducts with mean flow. *Journal of Sound and Vibration*, 190(2):163–175, 1996.

[27] K-W Jeong and J-G Ih. A numerical study on the propagation of sound through capillary tubes with mean flow. *Journal of sound and vibration*, 198(1):67–79, 1996.

[28] A Lorea and V Sacca. Close coupled catalyst solution and its effects on exhaust noise control. In *European Conference on Vehicle Noise and Vibration, Held 12-13th May 1998, IMECHE Headquarters, London, UK. IMECHE Conference Transactions 1998–5*, 1998.

[29] A. Selamet, S.H. Yönak, J.M. Novak, and M. Khan. The effect of vehicle exhaust system components on flow losses and noise in spark ignition engines. Technical Report 951260, SAE Technical Paper, 1995.

[30] A Selamet, V Kothamasu, JM Novak, and RA Kach. Experimental investigation of in–duct insertion loss of catalysts in internal combustion engines. *Applied Acoustics*, 60(4):451–487, 2000.

[31] Sabry Allam and Mats Åbom. Acoustic modelling and testing of diesel particulate filters. *Journal of Sound and Vibration*, 288 (1–2):255–273, 2005.

[32] Sabry Allam and Mats Åbom. Sound propagation in an array of narrow porous channels with application to diesel particulate filters. *Journal of Sound and Vibration*, 291(3–5):882–901, 2006.

[33] Sabry Allam and Mats Åbom. Modeling and testing of after–treatment devices. *Journal of Vibration and Acoustics*, 128(3): 347–356, 2006.

[34] Yasser ElNemr. *Acoustic modeling and testing of exhaust and intake system components*. PhD thesis, KTH Royal Institute of Technology, 2011.

[35] Sara Elsaadany. *Investigation and optimization of the acoustic performance of exhaust systems*. PhD thesis, KTH Royal Institute of Technology, 2012.

[36] Sinem Ozturk and Haluk Erol. On acoustics of diesel particulate filters. In *Proceedings of the 22nd International Congress on Acoustics ICA2016*, number 336 in ICA2016, 2016.

[37] Jiri Navratil, Warren Seeley, Peng Wang, and Shriram Siravara. Catalyst and dpf acoustic transmission loss benchmark study. Technical Report 2017–01–1798, SAE Technical Paper, 2017.

[38] Xianjun Hou, Songze Du, Zien Liu, Jin Guo, and Zengke Li. A transfer matrix approach for structural–acoustic correspondence analysis of diesel particulate filter. *Advances in Mechanical Engineering*, 9(9):1687814017722495, 2017.

[39] AJ Torregrosa, FJ Arnau, P Piqueras, EJ Sanchis, and H Tartoussi. Phenomenological methodology for assessing the influence of flow conditions on the acoustic response of exhaust aftertreatment systems. *Journal of Sound and Vibration*, 396:289–306, 2017.

[40] AJ Torregrosa, P Piqueras, EJ Sanchis, S Guilain, and M Dubarry. Assessment of acoustic reciprocity and conservativeness in exhaust aftertreatment systems. *Journal of Sound and Vibration*, 436:46–61, 2018.

[41] Merriam-Webster. Acoustics. in merriam-webster.com dictionary. `https://www.merriam-webster.com/dictionary/acoustics`, 2023. Online; Retrieved February 10, 2023.

[42] World Health Organization et al. *Burden of disease from environmental noise: Quantification of healthy life years lost in Europe*. World Health Organization. Regional Office for Europe, 2011.

[43] María Dolores Redel-Macías, Pilar Aparicio-Martinez, Sara Pinzi, Pedro Arezes, and Antonio José Cubero-Atienza. Monitoring sound and its perception during the lockdown and de-escalation of covid-19 pandemic: A spanish study. *International Journal of Environmental Research and Public Health*, 18(7):3392, 2021.

[44] Manchar Lal Munjal. *Acoustics of ducts and mufflers with application to exhaust and ventilation system design*. John Wiley & Sons, 1987.

[45] Francisco Payri González and José Mª Desantes Fernández. *Motores de combustión interna alternativos*. Editorial Universitat politécnica de valencia, 2011.

[46] N Serhan, A Tsolakis, and FJ Martos. Effect of propylene glycol ether fuelling on the different physico–chemical properties of the emitted particulate matters: Implications of the soot reactivity. *Fuel*, 219:1–11, 2018.

[47] Jeongwoo Lee, Sunyoup Lee, and Seokhwan Lee. Experimental investigation on the performance and emissions characteristics of ethanol/diesel dual–fuel combustion. *Fuel*, 220:72–79, 2018.

[48] Md Nurun Nabi and MG Rasul. Influence of second generation biodiesel on engine performance, emissions, energy and exergy parameters. *Energy conversion and management*, 169:326–333, 2018.

[49] Chenxu Jiang, Zilong Li, Yong Qian, Xiaole Wang, Yahui Zhang, and Xingcai Lu. Influences of fuel injection strategies on combustion performance and regular/irregular emissions in a turbocharged gasoline direct injection engine: Commercial gasoline versus multi–components gasoline surrogates. *Energy*, 157:173–187, 2018.

[50] Magdi K Khair. A review of diesel particulate filter technologies. Technical Report 2003–01–2303, SAE Technical Paper, 2003.

[51] Makoto Ootake, Terunori Kondou, Mamoru Ikeda, Masano Daigo, Masahiko Nakano, Jin Yokoyama, and Manabu Miura. Develop-

ment of diesel engine system with dpf for the european market. Technical Report 2007–01–1061, SAE Technical Paper, 2007.

[52] Ingo Mikulic, Reggie Zhan, and Scott Eakle. Dependence of fuel consumption on engine backpressure generated by a dpf. Technical Report 2010–01–0535, SAE Technical Paper, 2010.

[53] Leslie Bromberg, Daniel Ross Cohn, and V Wong. Regeneration of diesel particulate filters with hydrogen rich gas. Technical report, MIT Plasma Science and Fusion Center, 2005.

[54] Alexander G. Sappok and Victor W. Wong. Detailed chemical and physical characterization of ash species in diesel exhaust entering aftertreatment systems. Technical Report 2007–01–0318, SAE Technical Paper, 2007.

[55] Yujun Wang, Carl J Kamp, Yuesen Wang, Todd J Toops, Changsheng Su, Ruoqian Wang, Jian Gong, and Victor W Wong. The origin, transport, and evolution of ash in engine particulate filters. *Applied Energy*, 263:114631, 2020.

[56] Renbi Bai and Chi Tien. Effect of deposition in deep–bed filtration: determination and search of rate parameters. *Journal of colloid and interface science*, 231(2):299–311, 2000.

[57] Shinji Yamaguchi, Shuji Fujii, Ryuji Kai, Makoto Miyazaki, Yukio Miyairi, Shinichi Miwa, and P Busch. Design optimization of wall flow type catalyzed cordierite particulate filter for heavy duty diesel. Technical Report 2005–01–0666, SAE Technical Paper, 2005.

[58] Chi Tien and Renbi Bai. An assessment of the conventional cake filtration theory. *Chemical Engineering Science*, 58(7):1323–1336, 2003.

[59] Pushkar Tandon, Achim Heibel, Jeanni Whitmore, Naveen Kekre, and Kranthi Chithapragada. Measurement and prediction of filtration efficiency evolution of soot loaded diesel particulate filters. *Chemical Engineering Science*, 65(16):4751–4760, 2010.

[60] Luciana Lisi, Gianluca Landi, and Valeria Di Sarli. The issue of soot–catalyst contact in regeneration of catalytic diesel particulate filters: A critical review. *Catalysts*, 10(11):1307, 2020.

[61] T Kuwahara, S Nishii, T Kuroki, and M Okubo. Complete regeneration characteristics of diesel particulate filter using ozone injection. *Applied energy*, 111:652–656, 2013.

[62] T Maunula, P Matilainen, M Louhelainen, P Juvonen, and T Kinnunen. Catalyzed particulate filters for mobile diesel applications. Technical Report 2007–01–0041, SAE Technical Paper, 2007.

[63] Barry WL Southward, Stephan Basso, and Marcus Pfeifer. On the development of low pgm content direct soot combustion catalysts for diesel particulate filters. Technical Report 2010–01–0558, SAE Technical Paper, 2010.

[64] Mengting Yu, Dan Luss, and Vemuri Balakotaiah. Regeneration modes and peak temperatures in a diesel particulate filter. *Chemical engineering journal*, 232:541–554, 2013.

[65] Arun Cherkkil and Ajay Rathor. Design and optimization of a muffler integrated with an adaptive quarter wave tube for noise reduction in commercial vehicles. Technical Report 2020–01–0507, SAE Technical Paper, 2020.

[66] C Jiang, TW Wu, MB Xu, and CYR Cheng. Bem modeling of mufflers with diesel particulate filters and catalytic converters. *Noise Control Engineering Journal*, 58(3):243–250, 2010.

[67] X Hua, DW Herrin, TW Wu, and T Elnady. Simulation of diesel particulate filters in large exhaust systems. *Applied acoustics*, 74 (12):1326–1332, 2013.

[68] Gianluca Montenegro, Angelo Onorati, Augusto Della Torre, and Antonio J Torregrosa. The 3dcell approach for the acoustic modeling of after–treatment devices. *SAE International Journal of Engines*, 4(2):2519–2530, 2011.

[69] Giovanni Ferrara, Giovanni Vichi, Giulio Lenzi, Davide Biliotti, et al. Acoustic characterization of automotive mufflers–part i:

Test rig design and evaluation of acoustic properties. Technical Report 2012–01–0800, SAE Technical Paper, 2012.

[70] Julien Drant, Philippe Micheau, and Alain Berry. Active noise control of higher modes in a duct using near field compensation and a ring of harmonic acoustic pneumatic sources. *Applied Acoustics*, 188:108583, 2022.

[71] M Åbom. Measurement of the scattering–matrix of acoustical 2–ports. *Mechanical Systems and Signal Processing*, 5(2):89–104, 1991.

[72] JY Chung and DA Blaser. Transfer function method of measuring in–duct acoustic properties. ii. experiment. *The Journal of the Acoustical Society of America*, 68(3):914–921, 1980.

[73] Ragnar Glav, Hans Boden, and Mats Åbom. An acoustic model for automobile catalytic converters. In *Inter–Noise*, volume 88, pages 1261–1266, 1988.

[74] KS Peat. A first aproximation to the effects of mean flow on sound propagation through cylindrical capillary tubes. *Journal of sound and vibration*, 175(4):475–489, 1994.

[75] A Selamet, V Easwaran, JM Novak, and RA Kach. Wave attenuation in catalytic converters: reactive versus dissipative effects. *The Journal of the Acoustical Society of America*, 103(2):935–943, 1998.

[76] Ashutosh Katari, Mukaram Syed, Mark Sickels, Tom Wahl, and Sivanandi Rajadurai. Effect of aspect ratio on pressure drop and acoustics in diesel particulate filters. Technical Report 2004–01–0695, SAE Technical Paper, 2004.

[77] Jürgen Schnitzler. Particulate matter and nox exhaust aftertreatment systems. *FEV Motorentechnik GmbH*, 2006.

[78] Stephen B England, Christopher J Rutland, David E Foster, and Yongsheng He. Investigation of the effect of dpf loading and passive regeneration on engine performance and emissions using an

integrated system simulation. Technical Report 2006–01–0263, SAE Technical Paper, 2006.

[79] Zhenhua Guo and Zhaoyan Zhang. Multi–dimensional modeling and simulation of wall–flow diesel particulate filter during loading and regeneration. Technical Report 2006–01–0265, SAE Technical Paper, 2006.

[80] Gao Wenzhi, Feng Liming, Niu Wenbo, and Wang Hui. Theoretical and experimental investigations on diesel particulate filters. *Noise control engineering journal*, 56(4):282–287, 2008.

[81] Naohisa Ohyama, Tomohiko Nakanishi, and Shigeki Daido. New concept catalyzed dpf for estimating soot loadings from pressure drop. Technical Report 2008–01–0620, SAE Technical Paper, 2008.

[82] Samir Bensaid, DL Marchisio, D Fino, G Saracco, and V Specchia. Modelling of diesel particulate filtration in wall–flow traps. *Chemical Engineering Journal*, 154(1–3):211–218, 2009.

[83] Nalini Kanta Mukherjee. *Flow–Acoustic Analysis of Diesel Particulate Filter and Air Filter*. PhD thesis, Indian Institute of Science Bangalore, 2009.

[84] Ewa Bardasz, Derek Mackney, Nigel Britton, Gunter Kleinschek, Klas Olofsson, Ian Murray, and Andrew P Walker. Investigations of the interactions between lubricant–derived species and aftertreatment systems on a state–of–the–art heavy duty diesel engine. *SAE transactions*, pages 1821–1839, 2003.

[85] Hisaki Toorisaka, Jinichi Minamikawa, Hironori Narita, Toshikatsu Muramatsu, Testuichi Kominami, and Takeshi Sone. Dpr developed for extremely low pm emissions in production commercial vehicles. *SAE transactions*, pages 447–456, 2004.

[86] Gerd Gaiser and Patrick Mucha. Prediction of pressure drop in diesel particulate filters considering ash deposit and partial regenerations. Technical Report 2004–01–0158, SAE Technical Paper, 2004.

[87] T Ishizawa, H Yamane, H Satoh, K Sekiguchi, M Arai, N Yoshimoto, and T Inoue. Investigation into ash loading and its relationship to dpf regeneration method. *SAE international journal of commercial vehicles*, 2(2009–01–2882):164–175, 2009.

[88] D Fino, N Russo, F Millo, DS Vezza, F Ferrero, and A Chianale. New tool for experimental analysis of diesel particulate filter loading. *Topics in Catalysis*, 52(13–20):2083, 2009.

[89] Magín Lapuerta, Rosario Ballesteros, and Francisco J Martos. A method to determine the fractal dimension of diesel soot agglomerates. *Journal of Colloid and Interface Science*, 303(1):149–158, 2006.

[90] G Chiatti, O Chiavola, and G Falcucci. Soot morphology effects on dpf performance. Technical Report 2009–01–1279, SAE Technical Paper, 2009.

[91] Joshua T Hicks, William E Hill, and Adam J Kotrba. Dpf acoustic performance: an evaluation of various substrate materials and soot conditions. Technical Report 2011–01–2198, SAE Technical Paper, 2011.

[92] Christopher Depcik, Bailey Spickler, and Anmesh Gaire. Revisiting the single equation pressure drop model for particulate filters. *SAE International Journal of Engines*, 11(2018–01–0952):1421–1446, 2018.

[93] AJ Torregrosa, JR Serrano, FJ Arnau, and P Piqueras. A fluid dynamic model for unsteady compressible flow in wall–flow diesel particulate filters. *Energy*, 36(1):671–684, 2011.

[94] F Payri, JM Desantes, and A Broatch. Modified impulse method for the measurement of the frequency response of acoustic filters to weakly nonlinear transient excitations. *The Journal of the Acoustical Society of America*, 107(2):731–738, 2000.

[95] FK Bannister and GF Mucklow. Wave action following sudden release of compressed gas from a cylinder. *Proceedings of the Institution of Mechanical Engineers*, 159(1):269–300, 1948.

[96] Raimo Kabral, F Auriemma, M Knutsson, and M Åbom. A new type of compact silencer for high frequency noise. In *Online Proceedings of the 9th International DAAAM Baltic Conference, ISSN*, pages 2346–6138, 2014.

[97] C. L. Morfey. Sound transmission and generation in ducts with flow. *Journal of Sound and Vibration*, 14(1):37–55, 1971.

[98] G Piñero, L Vergara, JM Desantes, and A Broatch. Estimation of velocity fluctuation in internal combustion engine exhaust systems through beamforming techniques. *Measurement science and technology*, 11(11):1585, 2000.

[99] Jannis Gikadi, Moritz Schulze, J Schwing, Stephan Foeller, and Thomas Sattelmayer. Linearized navier–stokes and euler equations for the determination of the acoustic scattering behaviour of an area expansion. In *18th AIAA/CEAS Aeroacoustics Conference (33rd AIAA Aeroacoustics Conference)*, page 2292, 2012.

[100] Ying Guan, Kai H Luo, and Tong Q Wang. Sound transmission in a lined annular duct with mean swirling flow. In *Noise Control and Acoustics Division Conference*, volume 48396, pages 135–144, 2008.

[101] AJ Torregrosa, A Broatch, J García-Tíscar, and F Roig. Experimental verification of hydrodynamic similarity in hot flows. *Experimental Thermal and Fluid Science*, 119:110220, 2020.

[102] Hermann von Helmholtz. Handbuch der physiologischen optik [handbook of physiological optics]. *Leipzig, Germany: Leopold Voss*, 1867.

[103] John William Strutt. Baron rayleigh, the theory of sound. *London, Macmillan and co*, 1:370, 1877.

[104] V Pagneux and A Maurel. Scattering matrix properties with evanescent modes for waveguides in fluids and solids. *The Journal of the Acoustical Society of America*, 116(4):1913–1920, 2004.

[105] VH Gupta. On independence of reciprocity symmetry and conservativeness of one-dimensional linear systems. *Journal of sound and vibration*, 179(3):547–552, 1995.

[106] V Easwaran, VH Gupta, and ML Munjal. Relationship between the impedance matrix and the transfer matrix with specific reference to symmetrical, reciprocal and conservative systems. *Journal of Sound and Vibration*, 161(3):515–525, 1993.

[107] Marco Piumetti, Bart van der Linden, Michiel Makkee, Paolo Miceli, Debora Fino, Nunzio Russo, and Samir Bensaid. Contact dynamics for a solid–solid reaction mediated by gas–phase oxygen: Study on the soot oxidation over ceria–based catalysts. *Applied Catalysis B: Environmental*, 199:96–107, 2016.

[108] F Payri, JM Desantes, and AJ Torregrosa. Acoustic boundary condition for unsteady one–dimensional flow calculations. *Journal of Sound and Vibration*, 188(1):85–110, 1995.

[109] Thomas Morel, John Silvestri, Karl-Alfred Goerg, and Rolf Jebasinski. Modeling of engine exhaust acoustics. Technical Report 1999–01–1665, SAE Technical Paper, 1999.

[110] Ghazanfar Mehdi, Song Zhou, Yuanqing Zhu, Ahmer Hussain Shah, and Kishore Chand. Numerical investigation of scr mixer design optimization for improved performance. *Processes*, 7(3): 168, 2019.

[111] Ligang Tan, Pengfei Feng, Shubao Yang, Yage Guo, Shaochun Liu, and Ziwen Li. Cfd studies on effects of scr mixers on the performance of urea conversion and mixing of the reducing agent. *Chemical Engineering and Processing–Process Intensification*, 123:82–88, 2018.

[112] Joel Michelin, Frederic Guilbaud, Alain Guil, Ian Newbigging, Manuel Jean, Martina Reichert, Mario Balenovic, and Zafar Shaikh. Advanced compact scr mixer: Bluebox. Technical Report 2014–01–1531, SAE Technical Paper, 2014.

[113] M Börnhorst and O Deutschmann. Advances and challenges of ammonia delivery by urea-water sprays in scr systems. *Progress in Energy and Combustion Science*, 87:100949, 2021.

[114] Federico Millo, Mahsa Rafigh, Debora Fino, and Paolo Miceli. Application of a global kinetic model on an scr coated on filter (scr-f) catalyst for automotive applications. *Fuel*, 198:183–192, 2017.

[115] Ying-jie Chen, Pi-qiang Tan, Li-shuang Duan, Yang Liu, Di-ming Lou, and Zhi-yuan Hu. Emission characteristics and performance of scr coated on dpf with different soot loads. *Fuel*, 330:125712, 2022.

[116] Hyung Jun Kim, Seongin Jo, Sangil Kwon, Jong-Tae Lee, and Suhan Park. Nox emission analysis according to after-treatment devices (scr, lnt+ scr, sdpf), and control strategies in euro-6 light-duty diesel vehicles. *Fuel*, 310:122297, 2022.

[117] Ming Chen and Shazam Williams. Modelling and optimization of scr–exhaust aftertreatment systems. Technical Report 2005–01–0969, SAE Technical Paper, 2005.

[118] Srikanth Tummala and Athanasios Dimopoulos. Mixer for after–treatment system, nov 15 2017. GB Patent 2,550,173.

[119] Thomas Gschwind. Mixer for aftertreatment of exhaust gases, nov 5 2015. US Patent 2015/0315943 A1.

[120] Pier Mario Cornaglia and Giorgio Villata. Static mixer for the treatment of exhaust gases and manufacturing method thereof, feb 17 2015. US Patent 8,956,040.

[121] C. Raymond Cheng and Thomas E. Page. Exhaust aftertreatment mixer with stamped muffler flange, may 19 2009. US Patent 7,533,520.

[122] Clark Paterson and Dan B Mastbergen. Low pressure drop mixer for radial mixing of internal combustion engine exhaust flows, combustor incorporating same, and methods of mixing, jun 11 2013. US Patent 8,459,017.

[123] Young Jin Cho and Ji Woong Park. Static mixer or mixing urea aqueous solution and engine exhaust gas, may 2 2013. US 20130104531A1.

[124] Z. Gerald Liu, Michael T. Zuroski, Cary D. Bremigan, Kenneth J. Kicinski, and C. Raymond Cheng. Exhaust aftertreatment device, including chemical mixing and acoustic effects, apr 20 2004. US Patent 6,722,123.

[125] Georg Wirth and Felix Neumann. Static mixer and exhaust gas treatment device, sep 14 2010. US Patent 7,793,494.

[126] Yong Yi and Jinhui Sun. Scr reductant mixer, jan 29 2013. US Patent 8,359,832.

[127] Holger Gentgen. Static mixer for an exhaust gas system of an internal combustion engine, aug 12 2014. US Patent 8,801,267.

[128] Jeffrey Denton. Dual auger mixing system, Aug 25 2016. US Patent 2016/0243510 A1.

[129] Eberspacher Exhaust Technology GmbH & Co. KG. Mixer, jul 25 2019. US Patent 20190226379A1.

[130] LLC Faurecia Emissions Control Technologies, USA. Mixer with swirl box for a vehicle exhaust system, may 19 2016. US Patent 2016138454A1.

[131] Jin-Won Seo, Kyu-Ik Lee, Jeong-Taek Oh, Yun-Ho Choi, Jong-Hwa Lee, and Jin-Il Park. The study on the effects of mixer configurations on fluid mixing characteristics in scr systems. *Transactions of the Korean Society of Automotive Engineers*, 16(6): 192–199, 2008.

[132] Chaofeng Zhang, Chuan Sun, Meiping Wu, and Kai Lu. Optimisation design of scr mixer for improving deposit performance at low temperatures. *Fuel*, 237:465–474, 2019.

[133] A Blinov, N Malastowski, and A Bykov. Performance evaluation of static mixers in the urea injection pipe for scr systems. In *International Conference on Industrial Engineering*, pages 1465–1473. Springer, 2019.

[134] Chuang Zhao, Diming Lou, Yunhua Zhang, Kai Lu, and Shusen Liu. Application study on a new hybrid canning structure of after–treatment system for diesel engine. *Energies*, 13(3):734, 2020.

[135] A. J. Torregrosa, A. Broatch, V. Bermúdez, and I. Andrés. Experimental assessment of emission models used for ic engine exhaust noise prediction. *Experimental Thermal and Fluid Science*, 30(2): 97–107, 2005.

[136] Florian R Menter. Two–equation eddy–viscosity turbulence models for engineering applications. *AIAA journal*, 32(8):1598–1605, 1994.

[137] Antonio Torregrosa, Antonio Gil, Pedro Quintero, Antonio Ammirati, Hervé Denayer, and Wim Desmet. Prediction of flow induced vibration of a flat plate located after a bluff wall mounted obstacle. *Journal of Wind Engineering and Industrial Aerodynamics*, 190:23–39, 2019.

[138] Andrii Rogovyi, Serhii Khovanskyi, Iryna Hrechka, and Anatoly Gaydamaka. Studies of the swirling submerged flow through a confuser. In *Design, Simulation, Manufacturing: The Innovation Exchange*, pages 85–94. Springer, 2020.

[139] CA Gilkeson, VV Toropov, HM Thompson, MCT Wilson, NA Foxley, and PH Gaskell. Dealing with numerical noise in cfd–based design optimization. *Computers & Fluids*, 94:84–97, 2014.

[140] Zhe Zhang, Heiki Tiikoja, Mats Åbom, and Hans Bodén. Experimental analysis of whistle noise in a particle agglomeration pipe. In *Noise Control and Acoustics Division Conference*, volume 51425, page V001T06A002. American Society of Mechanical Engineers, 2018.

[141] Mikael Karlsson and Mats Åbom. On the use of linear acoustic multiports to predict whistling in confined flows. *Acta acustica united with Acustica*, 97(1):24–33, 2011.

[142] Luc Jaouen and Fabien Chevillotte. Length correction of 2d discontinuities or perforations at large wavelengths and for linear

acoustics. *Acta Acustica united with Acustica*, 104(2):243–250, 2018.

[143] Sandeep Viswanathan, David Rothamer, Stephen Sakai, Mitchell Hageman, David Foster, Todd Fansler, and Michael Andrie. Effect of particle size distribution on the deep–bed capture efficiency of an exhaust particulate filter. *Journal of Engineering for Gas Turbines and Power*, 137(10), 2015.

[144] Sandeep Viswanathan, David A Rothamer, David E Foster, Todd D Fansler, Alla Zelenyuk, Mark L Stewart, and David M Bell. Evolution of deep–bed filtration of engine exhaust particulates with trapped mass. *International Journal of Engine Research*, 18(5–6):543–559, 2017.

[145] José Ramón Serrano, Héctor Climent, Pedro Piqueras, and Emanuele Angiolini. Filtration modelling in wall–flow particulate filters of low soot penetration thickness. *Energy*, 112:883–898, 2016.